

**ELM Suppression and Pedestal Structure in I-Mode Plasmas on
Alcator C-Mod**

by

John Reel Walk, Jr.

S.B. Physics & Mathematics (2010)
Massachusetts Institute of Technology

Submitted to the Department of Nuclear Science and Engineering
in partial fulfillment of the requirements for the degree of

Doctor of Philosophy in Applied Plasma Physics

at the

MASSACHUSETTS INSTITUTE OF TECHNOLOGY

June 2014

© Massachusetts Institute of Technology 2014. All rights reserved.

Author
.....

Department of Nuclear Science and Engineering
July 5, 2014

Certified by.....
.....

Jerry W. Hughes
Research Scientist, Plasma Science and Fusion Center
Thesis Supervisor

Certified by.....
.....

Dennis G. Whyte
Professor, Department of Nuclear Science and Engineering
Thesis Reader

Accepted by.....
.....

Mujid S. Kazimi
TEPCO Professor of Nuclear Engineering
Chair, Department Committee on Graduate Students

ELM Suppression and Pedestal Structure in I-Mode Plasmas on Alcator C-Mod
by
John Reel Walk, Jr.

Submitted to the Department of Nuclear Science and Engineering
on July 5, 2014, in partial fulfillment of the
requirements for the degree of
Doctor of Philosophy in Applied Plasma Physics

Abstract

High-performance operation in tokamaks is characterized by the formation of a *pedestal*, a region of suppressed transport and steep gradients in density, temperature, and pressure near the plasma edge. The pedestal height is strongly correlated with overall fusion performance, as a substantial pedestal supports the elevated core pressure necessary for the desired fusion reaction rate and power density. However, stationary operation requires some relaxation of the particle transport barrier, to avoid the accumulation of impurities (e.g., helium “fusion ash,” plasma-facing surface materials) in the plasma. Moreover, the formation of the pedestal introduces an additional constraint: the steep gradients act as a source of free energy for Edge-Localized Mode (ELM) instabilities, which in on ITER- or reactor-scale devices can drive large, explosive bursts of particle and energy transport leading to unacceptable levels of heat loading and erosion damage to plasma-facing materials. As such, the suppression, mitigation, or avoidance of large ELMs is the subject of much current research.

In light of this, a firm physical understanding of the pedestal structure and stability against the ELM trigger is essential for the extrapolation of high-performance regimes to large-scale operation, particularly in operating scenarios lacking large, deleterious ELMs. This thesis focuses on the *I-mode*, a novel high-performance regime pioneered on the Alcator C-Mod tokamak. I-mode is unique among high-performance regimes in that it appears to decouple energy and particle transport, reaching H-mode levels of energy confinement with the accompanying temperature pedestal while maintaining a L-mode-like density profile and particle transport. I-mode exhibits three attractive properties for a reactor regime: (1) I-mode appears to be inherently free of large ELMs, avoiding the need for externally-applied ELM control. (2) The lack of a particle transport barrier maintains the desired level of impurity flushing from the plasma, avoiding excessive radiative losses. (3) Energy confinement in I-mode presents minimal degradation with input heating power, contrary to that found in H-mode.

This thesis presents the results from a combined empirical and computational study of the pedestal on C-Mod. Analysis methods are first implemented in ELMy H-mode base cases on C-Mod – in particular, the EPED model based on the combined constraints from peeling-balloonning MHD instability and kinetic-balloonning turbulence is tested on C-Mod. Empirical results in ELMy H-mode are consistent with the physics assumptions used in EPED, with the pedestal pressure gradient constrained by $\nabla p \sim I_p^2$ expected from the balloonning stability limit. To lowest-order approximation, ELMy H-mode pedestals are limited in $\beta_{p,ped}$, with the attainable beta set by shaping – within this limit, an inverse relationship between pedestal density and temperature is seen. The pedestal width is found to be described by the scaling $\Delta_\psi = G\beta_{p,ped}^{1/2}$ expected from the KBM limit, where $G(\nu, \epsilon, \dots)$ is a weakly varying function with $\langle G \rangle = 0.0857$. No systematic secondary scalings with field, gyroradius, shaping, or collisionality are observed. The EPED

model, based on these assumptions, correctly predicts the pressure pedestal width and height to within a systematic $\sim 20\%$ uncertainty.

Empirical scalings in I-mode highlight the operational differences from conventional H-modes. The temperature and pressure pedestal exhibit a positive trend with current, similar to H-mode (although I-mode pedestal temperature typically exceeds that found in comparable H-modes) – however, the temperature and pressure respond significantly more strongly to heating power, with $T_{e,95} \sim P_{net}/\bar{n}_e$ and $p_{95} \sim P_{net}$. The I-mode density profile is set largely independently of the temperature pedestal (unlike ELMy H-mode), controlled by operator fueling. Given sufficient heating power to maintain a consistent P_{net}/\bar{n}_e , temperature pedestals are matched across a range of fueling levels. This indicates a path to readier access and increased performance in I-mode, with the mode accessed at moderate density and power, after which the pedestal pressure is elevated with matched increases in fueling and heating power. Global performance metrics in I-mode are competitive with H-mode results on C-Mod, and are consistent with the weak degradation of energy confinement with heating power.

I-mode pedestals are also examined against the physics basis for the EPED model. Peeling-balloonning MHD stability is calculated using the ELITE code, finding the I-mode pedestal to be strongly stable to the MHD modes associated with the ELM trigger. Similarly, modeling of the KBM using the infinite-n ballooning mode calculated in BALOO as a surrogate for the threshold indicates that the I-mode pedestal is stable to kinetic-balloonning turbulence, consistent with the observed lack of a trend in the pedestal width with $\beta_{p,ped}$. This is found to be the case even in I-modes exhibiting small, transient ELM-like events. The majority of these events are triggered by the sawtooth heat pulse reaching the edge, and do not negatively perturb the temperature pedestal – it is proposed, then, that these events are not true peeling-balloonning-driven ELMs, but rather are an ionization front in the SOL driven by the sawtooth heat pulse. There are transient ELM events showing the characteristic temperature pedestal crash indicating a true ELM – the steady I-mode pedestals around these isolated events are also modeled to be P-B and KBM stable, although more detailed modeling of these events is ongoing.

Thesis Supervisor: Jerry W. Hughes
Research Scientist, Plasma Science and Fusion Center

Thesis Reader: Dennis G. Whyte
Professor, Department of Nuclear Science and Engineering

A dedication goes here maybe?

ACKNOWLEDGMENTS

Acknowledgements go here.

CONTENTS

1	INTRODUCTION	17
1.1	Plasmas for Fusion	18
1.1.1	Plasma Parameters	18
1.1.2	Fusion Fuels	19
1.2	Magnetic Confinement	22
1.2.1	Basic Principles	22
1.2.2	Toroidal Configurations	25
1.3	Alcator C-Mod	29
1.4	Confinement & Transport	32
1.4.1	Global Confinement	32
1.4.2	Transport Barriers	34
1.5	Goals & Outline	36
2	HIGH-PERFORMANCE REGIMES	43
2.1	ELMy H-Mode	44
2.1.1	ELMy H-Mode Operation	44
2.1.2	Edge-Localized Modes & Pedestal Limits	47
2.1.3	Active ELM Control	49
2.1.4	Prospects for ELMy H-Mode	50
2.2	ELM-Free H-Mode	50
2.3	ELM-Suppressed H-Modes	52
2.3.1	QH-Mode	52
2.3.2	EDA H-Mode	53
2.4	I-Mode	56
2.4.1	Access and Operation	57
2.4.2	Global Performance & Edge Behavior	58
2.4.3	Edge Fluctuations – the Weakly-Coherent Mode	60
3	PEDESTAL MODELING AND THEORY	75
3.1	Early Models	75
3.1.1	Empirical Observations	75
3.1.2	Neutral Penetration & the Density Pedestal	76
3.1.3	Ion-Orbit Loss & Gyroradius Models	77
3.2	MHD Stability: Peeling-Ballooning Modes	79
3.2.1	Pressure-Driven Modes	80
3.2.2	Current-Driven Modes	83
3.2.3	Coupled Modes – the ELITE Code	85
3.3	Kinetic-Ballooning Turbulence Modeling	91
3.3.1	The Ballooning-Critical Pedestal Technique	92
3.4	The EPED Model	93
3.4.1	EPED with Semi-Empirical Width Constraint	95
3.4.2	EPED with First-Principles Width Constraint	96

3.4.3	EPED Model Implementation & ITER Predictions	96
4	ELMY H-MODES ON C-MOD	107
4.1	ELMy H-Mode Access & Experimental Arrangement	107
4.2	ELM Cycle Synchronization	112
4.3	Engineering Parameter Scan	114
4.3.1	I_p Scan	114
4.4	EPED Model Predictions	117
4.4.1	Pedestal Height	118
4.4.2	Pedestal Width	119
4.5	Pedestal Width Response	123
4.5.1	Alternate Width Models	123
4.5.2	Normalized Pedestal Width	124
4.6	Conclusions	127
5	I-MODE PEDESTAL SCALINGS & CONFINEMENT	133
5.1	Access and Experimental Setup	134
5.2	Pedestal Responses	136
5.2.1	Pedestal Temperature	136
5.2.2	Pedestal Response to Fueling	138
5.2.3	Pressure Pedestal Scalings and Performance	140
5.3	Pedestal Widths	142
5.3.1	Kinetic-Ballooning Limited Pedestals	142
5.3.2	Local Physics Parameters	143
5.3.3	Stiff Gradient Limits	146
5.4	Global Behavior, Performance, & Confinement	147
5.4.1	Confinement Scaling Laws	150
5.5	Conclusions	152
6	I-MODE PEDESTAL STABILITY MODELING	159
6.1	MHD Stability – ELITE	159
6.1.1	ELITE Implementation	160
6.1.2	I-Mode ELITE Calculations	162
6.2	Kinetic-Ballooning Mode Stability	165
6.3	Intermittent ELMs in I-Mode	167
6.4	Summary & Discussion	173
7	CONCLUSIONS	179
A	DIAGNOSTICS	183
A.1	Thomson Scattering	183
A.1.1	Principles of Thomson Scattering	184
A.1.2	Edge Thomson Scattering on C-Mod	192
A.2	Fast Diagnostics	194
A.2.1	Electron-Cyclotron Emission	195
A.2.2	H_α Emission	197
A.3	Fluctuation Diagnostics	197

- A.3.1 Reflectometry 197
- A.3.2 Gas-Puff Imaging 198

B HIGH-RESOLUTION PEDESTAL DATABASE 201

LIST OF FIGURES

Figure 1.1	Binding energy per nucleon versus atomic mass number.	20
Figure 1.2	Normalized fusion reaction rate coefficients versus plasma temperature.	21
Figure 1.3	Gyro orbits in an applied magnetic field.	23
Figure 1.4	Geometry of a toroidal plasma.	25
Figure 1.5	Schematic of a tokamak coil configuration and plasma.	27
Figure 1.6	Tokamak cross-section with shaping parameter definitions.	28
Figure 1.7	Cutaway view of the Alcator C-Mod tokamak, cryostat and support structure.	30
Figure 1.8	Labeled cross-section of the C-Mod vacuum vessel.	31
Figure 1.9	Diffusion coefficients and plasma profiles for a “toy model” diffusion equation.	35
Figure 2.1	Characteristic traces of a steady ELMy H-mode.	45
Figure 2.2	ELMy H-mode pedestal density and temperature on a fixed- $\beta_{p,ped}$ line.	45
Figure 2.3	Characteristic traces of transient ELM-free H-modes.	51
Figure 2.4	Characteristic traces of an EDA H-mode on C-Mod.	54
Figure 2.5	C-Mod cross-sections illustrating magnetic configurations suitable for I-mode access.	57
Figure 2.6	Characteristic traces for a typical I-mode, and comparisons of I-mode pedestal profiles to L- and H-modes.	59
Figure 2.7	Impurity confinement time versus normalized confinement for L-, I-, and H-mode.	60
Figure 2.8	Fluctuations from the WCM in I-mode.	61
Figure 3.1	Schematic of the $n \rightarrow \infty$ ballooning and peeling instabilities.	84
Figure 3.2	Schematic of finite- n coupled peeling-balloonning instabilities.	86
Figure 3.3	Mode structure for $n = 30$ model calculated by ELITE.	88
Figure 3.4	Schematic of peeling-balloonning MHD stability space.	90
Figure 3.5	Illustration of the peeling-balloonning MHD and KBM constraints used in the EPED model.	95

Figure 3.6	EPED predictions versus measured pedestal height and width. 97
Figure 4.1	C-Mod cross-section comparing typical and ELMy H-mode shaping. 108
Figure 4.2	Example time window for ELMy H-mode study, showing TS timebase. 109
Figure 4.3	Comparison of pedestal fits for individual frames versus ensemble average. 110
Figure 4.4	Example pedestal illustrating the mtanh fitting function. 111
Figure 4.5	Comparison of measured n_e and T_e pedestal widths. 112
Figure 4.6	Comparison of directly measured pressure pedestal width versus EPED pedestal width. 112
Figure 4.7	Comparison of pressure pedestal height between ensemble-averaged and ELM-synced profiles. 113
Figure 4.8	Comparison of pressure at the 95% flux surface between ensemble-averaged and ELM-synced profiles. 113
Figure 4.9	Plasma current scalings of the density, temperature, and pressure pedestals. 115
Figure 4.10	Pedestal density versus temperature normalized to poloidal field. 116
Figure 4.11	Pedestal pressure versus $I_p \sqrt{T_{e,95}}$ 116
Figure 4.12	Pedestal pressure versus $I_p \sqrt{n_{e,95} T_{e,95}}$ 116
Figure 4.13	ELITE calculation of P-B stability in a C-Mod ELMy H-mode. 117
Figure 4.14	Pressure pedestal height predicted by EPED versus measured (ensemble-averaged) height. 118
Figure 4.15	Pressure pedestal height predicted by EPED versus measured ELM-synced pedestal height. 119
Figure 4.16	Ensemble-averaged Δ_ψ versus $\beta_{p,\text{ped}}$. 120
Figure 4.17	Comparison of EPED-predicted pedestal width and height with corresponding experimental points. 120
Figure 4.18	Comparison of ensemble-averaged and ELM-synced pedestal width and height, compared to the KBM constraint. 121
Figure 4.19	ELM-synced pedestals with data binned by $\beta_{p,\text{ped}}$, fitted to $\Delta_\psi \sim \beta_{p,\text{ped}}^{1/2}$. 121
Figure 4.20	Measured ensemble-averaged pedestal width versus EPED predictions. 122
Figure 4.21	Measured ELM-synced pedestal width versus EPED predictions. 122
Figure 4.22	Δ_{n_e} versus $n_{e,\text{ped}}$ 123
Figure 4.23	Δ_{T_e} and Δ_p versus $\rho_{i,\text{pol}}$ 124

- Figure 4.24 Scaling of the normalized pedestal width with applied toroidal field. 125
- Figure 4.25 Scalings of normalized pedestal width with shaping parameters. 125
- Figure 4.26 Scaling of normalized pedestal width with pedestal collisionality. 126
- Figure 4.27 Scaling of normalized pedestal width with normalized pedestal ion gyroradius. 126
- Figure 4.28 EPED predictions versus measured pressure pedestal heights. 128
- Figure 5.1 Characteristic traces for a typical I-mode, and comparisons of I-mode pedestal profiles to L- and H-modes. 134
- Figure 5.2 I-mode edge safety collisionality and safety factor. 135
- Figure 5.3 Density and power range for I-mode access 135
- Figure 5.4 Pedestal temperature vs. plasma current for I-mode and ELM My H-mode. 137
- Figure 5.5 Pedestal temperature vs. heating power per particle for an example current slice. 138
- Figure 5.6 Pedestal density response to current and fueling. 139
- Figure 5.7 Density and temperature pedestals at matched current and field with varying fueling and heating power – matched P_{net}/\bar{n}_e maintains the T_e pedestal. 139
- Figure 5.8 Pedestal pressure versus plasma current in I-mode and ELM My H-mode. 140
- Figure 5.9 Pedestal pressure vs. heating power for an example current slice. 141
- Figure 5.10 Stored energy versus pedestal pressure. 141
- Figure 5.11 Pressure gradient vs. plasma current for I-mode and ELM My H-mode. 142
- Figure 5.12 Pedestal width vs. poloidal beta in I-mode and ELM My H-mode. 143
- Figure 5.13 Temperature and pressure pedestal width vs. poloidal gyroradius. 144
- Figure 5.14 Temperature and pressure pedestal widths vs. pedestal collisionality. 144
- Figure 5.15 Temperature and pressure pedestal widths vs. edge safety factor. 144
- Figure 5.16 Temperature and pressure pedestal width vs. power-per-particle through the pedestal. 145
- Figure 5.17 I-mode pedestal temperature gradient versus pedestal temperature. 146

Figure 5.18	I-mode pedestal pressure gradient versus pedestal pressure. 146
Figure 5.19	Density, temperature, and pressure profiles in I-mode and EDA H-mode. 148
Figure 5.20	Normalized beta vs. H_{98} for I-mode and ELMy H-mode. 148
Figure 5.21	I-mode stored energy vs. heating power times plasma current. 149
Figure 5.22	Stored energy versus fueling in I-mode and H-mode. 149
Figure 5.23	Power-law fit to I-mode τ_E with full parameter set. 152
Figure 5.24	Power-law fit to I-mode τ_E , with poorly-fitted parameters excluded. 153
Figure 5.25	Power-law fit to I-mode τ_E , with fixed $R^2\sqrt{\epsilon}$ size scaling. 153
Figure 5.26	Power-law fit to I-mode τ_E extrapolated to larger devices. 154
Figure 6.1	I-mode pedestal MHD stability contour generated by ELITE. 161
Figure 6.2	Pedestal profiles in I-mode and ELMy H-mode. 162
Figure 6.3	I-mode pedestal MHD stability contour generated by ELITE – low-field case exhibiting ELM-like events. 163
Figure 6.4	Normalized pedestal temperature and pressure versus density. 164
Figure 6.5	Infinite-n ballooning MHD prediction, overlaid on ELITE result (fig. 6.1). 165
Figure 6.6	Infinite-n ballooning MHD prediction, overlaid on ELITE result (fig. 6.3). 166
Figure 6.7	Density and temperature profiles in I-mode, showing the modification of the temperature pedestal by the sawtooth heat pulse. 168
Figure 6.8	Peeling-balloonning MHD and KBM stability in I-mode, showing modification by sawtooth heat pulse. 168
Figure 6.9	ELM traces for H-mode and I-mode. 169
Figure 6.10	I-mode with a brief H-mode terminated by an ELM, as well as sawtooth-triggered ELM-like events. 170
Figure 6.11	I-mode pedestal stability contour generated by ELITE – case exhibiting a non-sawtooth-triggered ELM 172
Figure 6.12	Infinite-n ballooning MHD prediction, overlaid on ELITE result (fig. 6.11) 173
Figure A.1	Coordinate system for Thomson scattering. 184

Figure A.2	Angular dependences in Thomson scattering geometry. 186
Figure A.3	Spectral functions normalized to density and laser power. 191
Figure A.4	Collection optics for core and edge Thomson scattering systems. 193
Figure A.5	Normalized spectral response functions of the edge TS polychromator. 194

LIST OF TABLES

Table 1.1	Summary of Alcator C-Mod typical operating parameters. 31
Table 2.1	Typical operating parameters of tokamaks noted in this thesis, along with references to overviews of each machine. 44
Table 5.1	Parameters for power-law scalings of I-mode energy confinement time. 151
Table B.1	SQL database parameters. 202

INTRODUCTION

The population of the earth is projected to increase substantially over the next half-century, potentially reaching as high as 10 billion globally by 2050 [1]. At the same time, any attempt to increase the quality of life of the existing population will necessarily involve increased energy consumption per capita, with a greater fraction of the earth approaching “first-world” consumption levels [2]. As such, worldwide energy consumption will likely continue to increase in the next few decades [3, 4]

This increase in energy demand occurs in parallel with increased pressure on traditional energy sources. Fossil fuels (oil, coal, and natural gas), while reliable sources of base-load power, nevertheless face issues. Oil faces increasing cost and technical difficulty in capturing dwindling available reserves, as well as the potential for serious ecological damage from accidents (e.g., the Deepwater Horizon offshore rig accident in 2010). Coal, while more readily available (an estimated 257 billion tons of recoverable reserves in the US, lasting roughly 240 years at current consumption [4, 5]), releases particulate matter into the atmosphere, with serious consequences both to the environment and to human health, as well as the greenhouse gases tied to deleterious climate change.

Renewable energy sources have a certain “green” appeal, providing power generation free of pollution and carbon emissions, and are in many cases scalable and near cost-competitive with fossil-fuel sources – however, each is subject to limitations on their implementation. Solar and wind power suffer from a large degree of variability in their output, necessitating a combination of expensive energy storage methods or (often fossil-fuel based) backup production to handle shortfalls. Hydroelectric and geothermal power are suitable for base-load power production, but are strictly limited in their implementation by geographic concerns – bluntly, there are relatively few locations where hydro or geothermal power generation is feasible, and many of these have already been developed.

Conventional – that is, fission-based – nuclear power can also supply carbon-free base-load power, with fuel reserves lasting through the next century. While nuclear power does suffer from the potential for extremely serious accidents (Fukushima, Chernobyl) it has, on a per-energy-produced basis, a remarkably good safety record. Public perception of nuclear power nevertheless hinges on the threat of serious accidents, limiting both the expansion of nuclear power to meet increasing demand and the development of safe long-term handling

of existing nuclear waste, as well as, ironically, preventing the replacement of an aging reactor fleet with newer, safer designs.

Fusion, the nuclear process driving stellar cores, is a potentially highly attractive option for satisfying the world's growing energy needs in an efficient, environmentally-sound manner. A fusion reactor would supply base-load power using only a small amount of an effectively inexhaustible fuel (readily available for harvesting from seawater), with no greenhouse gas emissions or high-level radioactive waste, and the physical impossibility of a major "meltdown" accident. However, fusion remains in the experimental stage, with significant technical hurdles remaining before the development of a prototype fusion power plant. This thesis will attempt to contribute to the understanding of one of these hurdles. Further reading on the development of fusion energy is available to the interested reader in several excellent references. [6, 7, 8] •

1.1 PLASMAS FOR FUSION

A *plasma* is a gas to which sufficient energy has been applied to strip some or all of the electrons from the nuclei of its constituent atoms. In a plasma, ions and electrons freely interact with one another, behaving as coupled fluids. Plasmas of interest for fusion research are comprised of light elements (typically hydrogen or helium), and are at extremely high temperatures, in excess of 100 million Kelvin (10 – 20 keV). As these conditions are far in excess of the ionization energy for these elements, the plasma is dominated by collisions between its charged particles, rather than interactions with bound electron states.

1.1.1 *Plasma Parameters*

As the plasma is composed of free charged particles, it responds strongly to electric and magnetic fields. In the presence of a DC electric field (externally applied, or generated by an imbalance of positive and negative charge in the plasma), the plasma will rearrange itself to screen out the field. This effect breaks down at short length scales, at which there are insufficient numbers of charge carriers to rearrange and counter the field – the characteristic scale for this effect is the Debye Length, given by

$$\lambda_D = \sqrt{\frac{\epsilon_0 T}{n e^2}} \quad (1.1)$$

At size scales significantly larger than λ_D , this will enforce an approximately balanced electric charge in the plasma, termed "quasi-

“neutrality”. This is reflected in the number densities of electrons and multiple ion species j , each with charge Z_j , by the relation

$$n_e = \sum_j n_j Z_j \quad (1.2)$$

In a multiple-ion species plasma, we may also define an effective ion charge

$$Z_{\text{eff}} = \frac{1}{n_e} \sum_j n_j Z_j^2 \quad (1.3)$$

The electrostatic force driving this charge redistribution induces a “ringing” oscillation in the plasma, at the characteristic plasma frequency ω_p :

$$\omega_p = \sqrt{\frac{n e^2}{\epsilon_0 m_e}} \quad (1.4)$$

This natural oscillation in the plasma also has the effect of screening AC electric fields varying at frequencies $\omega < \omega_p$.

Coulomb collisions between charged particles in the plasma tend to drive magnetically-confined plasmas into thermal equilibrium, with the velocity distribution for a species given by the Maxwellian

$$f(v) = n \left(\frac{m}{2\pi T} \right)^{3/2} \exp \left(-\frac{mv^2}{2T} \right) \quad (1.5)$$

These collisions also cause the plasma to emit a continuous spectrum of Bremsstrahlung radiation. For a plasma in thermal equilibrium, integration over the full spectrum gives for the total radiated power

$$P_{\text{Brems}} = (5.35 \times 10^{-37}) n_e^2 Z_{\text{eff}} \sqrt{T} \quad (1.6)$$

representing a consistent source of heat loss from the plasma.

1.1.2 Fusion Fuels

Fusion collectively refers to the class of nuclear reactions merging lighter nuclei into a single heavier element. While fusion reactions for elements lighter than iron are generally exothermic, as they form nuclei with greater binding energy per nucleon (see fig. 1.1), the most common and readily attainable involve isotopes of hydrogen or helium, the most promising candidates for which are shown below.



Figure 1.1: Binding energy per nucleon versus atomic mass number, with notable isotopes marked. Reactions forming nuclei with higher binding energy are exothermic – thus, fusion of elements lighter than ^{56}Fe or fission of elements heavier than ^{56}Fe releases energy. [9]



Here D and T indicate nuclei of deuterium and tritium, two heavy isotopes of hydrogen (one proton plus one and two neutrons, respectively). The fusion reaction rate R_f is given by

$$R_f = n_1 n_2 \langle \sigma v \rangle_{1,2} \quad (1.11)$$

where n_1 and n_2 indicate the densities of the two fuel ions (e.g., for deuterium-tritium fuel $n_1 n_2 = n_D n_T$, while for pure-deuterium fuel $n_1 n_2 = \frac{1}{2} n_D^2$ to remove double-counting of fuel ions) and $\langle \sigma v \rangle_{1,2}$ is a rate parameter incorporating the energy-dependent reaction cross-section averaged over the Maxwellian fuel distribution (eq. (1.5)). In practice, the energy-dependent cross-section is empirically determined – measured rate parameters $\langle \sigma v \rangle$ for the fuels of interest are shown in fig. 1.2.



Figure 1.2: Reaction rate normalized to fuel density, expressed as the rate coefficient $\langle\sigma v\rangle$, for fusion fuels as a function of temperature. Notably, deuterium-tritium fusion exhibits a higher peak reaction rate, as well as reaching that peak at a lower temperature, than other fuels.

Pure deuterium fuel (reactions shown in eqs. (1.7) and (1.8)) is attractive from a research standpoint, due to the abundance and ease of use of deuterium. Deuterium is a stable nucleus, obviating the need for radiation safety in the fuel system, and is naturally occurring in relative abundance (approximately 1/6420 of hydrogen nuclei on earth are deuterium [10]), allowing harvesting of deuterium fuel from seawater. However, pure-deuterium reactions suffer from low energy output per reaction and a significantly lower reaction rate at feasible plasma conditions compared to other fuel options (see fig. 1.2), setting high performance requirements for a putative DD-burning reactor.

The $D - {}^3He$ reaction (eq. (1.9)) exhibits several desirable properties, namely an impressive energy yield per reaction, and the fact that the reaction produces only charged particles rather than the high-energy neutrons found in $D - D$ and $D - T$ reactions, which can cause significant damage to reactor materials (note, however, that a $D - {}^3He$ plasma will also undergo neutronic $D - D$ fusion at a meaningful rate). However, as with $D - D$ fuel, the $D - {}^3He$ reaction suffers from a lower reaction rate at attainable conditions, as well as the fact that Helium-3 does not occur in economically usable quantities on Earth. While off-planet sources of Helium-3 exist (for example, a useful quantity is present in the lunar regolith [11] and in the

atmospheres of some gas giants [12]), this fuel remains the subject of speculation.

The deuterium-tritium reaction (eq. (1.10)) is considered the most promising for a first-generation fusion reactor, due to its high energy output per reaction and favorable reaction cross-section – the rate parameter $\langle\sigma v\rangle_{DT}$ reaches its peak at a lower temperature, and reaches a greater absolute level than other fusion fuels. However, D – T operation is limited both by fuel sources, and reaction products. D – T fusion produces a 14 MeV neutron, carrying roughly 80% of the energy released by the fusion reaction, which can damage unshielded reactor materials. Moreover, while deuterium is stable and readily available, tritium is radioactive with a short half-life (roughly 12.3 years), so it is not naturally occurring in meaningful quantities on earth. A reactor will solve both of these problems with a *neutron blanket*, a neutron-absorbing structure surrounding the plasma. This provides the necessary shielding for sensitive reactor components. The heat generated in the blanket from neutron absorption will also be drawn off in a steam cycle to drive turbines, generating electricity from the reactor. Finally, seeding the blanket with lithium allows the following reactions with fusion neutrons:



the Lithium-6 reaction (eq. (1.12)) absorbs “slow” neutrons (that is, neutrons that have thermalized to the blanket temperature via collisions) to produce tritium, plus additional heat. Lithium-7 (eq. (1.13)) is more likely to capture fast neutrons to produce tritium in an endothermic reaction; however, the reaction also acts as a neutron multiplier, as a free neutron is maintained through the reaction. Using blankets enriched with ^6Li , coupled with neutron multipliers, a reactor will target an over-unity tritium breeding ratio, with > 1 tritons produced per neutron entering the blanket (i. e., per tritium consumed in a fusion reaction). •

1.2 MAGNETIC CONFINEMENT

1.2.1 Basic Principles

The temperatures in excess of 100 million Kelvin necessary for fusion in a plasma are incompatible with any contact between solid reactor materials and the hot core of the plasma. Magnetic confinement relies on the strong response of the charged particles composing the plasma to magnetic fields, rather than a material wall, to retain the thermal pressure (~ 10 atm for a reactor) from the plasma. The response of

Figure 1.3: Electron and ion gyro orbits in an applied magnetic field. Note that, due to the charge dependence in the Lorentz Force (eq. (1.14)), electrons and ions orbit in opposite directions relative to the magnetic field.



a charged particle to electric and magnetic fields is governed by the Lorentz force,

$$\vec{F} = q \left(\vec{E} + \vec{v} \times \vec{B} \right) \quad (1.14)$$

In a strong background magnetic field, the particle will move on a helical path along the field line. The $\vec{v} \times \vec{B}$ factor in the Lorentz Force causes the particle to experience no magnetic force parallel to the field, while velocity perpendicular to the field generates a force proportional to the velocity times the magnetic field, directed perpendicular to both – thus the particle freely streams parallel to the field, but is trapped in a circular orbit perpendicular to it, termed “gyro motion”, shown in fig. 1.3. The particle will orbit at the cyclotron frequency,

$$\omega_c = \frac{qB}{m} \Rightarrow \omega_{ce} = \frac{eB}{m_e}, \quad \omega_{ci} = \frac{ZeB}{m_i} \quad (1.15)$$

for electrons and ions of charge Z , respectively (note that for brevity we indicate the magnitude of vectors as scalar variables, e.g., $B = |\vec{B}|$). A particle with velocity perpendicular to the magnetic field v_\perp (formally, $v_\perp = |\vec{v} \times \vec{B}|/B$) orbits at its gyroradius,

$$\rho = \frac{v_\perp}{\omega_c} = \frac{mv_\perp}{qB} \quad (1.16)$$

For a thermalized plasma, the perpendicular velocity will, on average, be the thermal velocity $v_t = \sqrt{2T/m}$, thus

$$\rho = \frac{\sqrt{2mT}}{qB} \quad (1.17)$$

The introduction of a nonzero electric field drives additional motion for the particle in the form of a drift velocity – the guiding center (that is, the average point about which the orbital motion of the particle gyrates) will shift with a bulk velocity (see [6, § 8.4] for derivation)

$$\vec{v}_d = \frac{\vec{E} \times \vec{B}}{B^2} \quad (1.18)$$

independent of particle charge, mass, or energy.

This restriction of particle motion perpendicular to field lines to short length scales (at fusion-relevant temperatures and magnetic fields, the gyroradius is typically $\sim 10^{-5}$ m for electrons and $\sim 10^{-3}$ m for ions) compared to the size of the plasma is central to the concept of magnetic confinement. In the perpendicular direction, this scale restriction of particle motion permits a fluid treatment of the dynamics of the plasma. Further simplification of the fluid model (see [13, § 2.3] for detailed derivation) leads to the theory of *magnetohydrodynamics* (MHD), the “workhorse” model describing plasma behavior. A basic equilibrium in a confined plasma is described in MHD by the simple relation

$$\nabla p = \vec{j} \times \vec{B} \quad (1.19)$$

in which the outward force due to the plasma pressure gradient is balanced by an inward force from the interplay between magnetic fields and electric currents (expressed by the current density j). This interplay is readily illustrated in the simple one-dimensional case of an infinite straight cylinder of plasma – in this case, the radially-outward ∇p force may be balanced by an axial current in the \hat{z} direction with an azimuthal $\hat{\theta}$ magnetic field (z -pinch), an azimuthal current and axial field (θ -pinch), or a superposition of the two (screw pinch). However, all three of these options suffer from a lack of parallel confinement – as the magnetic field does not restrict the free-streaming parallel motion of the plasma, these linear concepts (when reduced to a physical, non-infinite size!) suffer from plasma losses at the ends of the cylinder. Despite efforts to restrict the parallel motion in a linear device (e.g., the *magnetic mirror*, which pinches the magnetic field at the cylinder ends in order to reflect the parallel motion of particles with a force due to the field gradient [14]), end losses in linear de-

vices proved incompatible with steady-state fusion conditions. The clear solution, then, was to close the magnetic geometry such that the magnetic field lines have no ends: a *torus*.

1.2.2 Toroidal Configurations

Figure 1.4: Example geometry of a circular-cross-section tokamak plasma, describing a torus of major radius R_0 and minor radius a , with poloidal coordinate θ and toroidal coordinate Φ . Tokamak configurations are characterized by an applied toroidal field B_T with a toroidal plasma current I_p , which in turn generates a poloidal magnetic field B_p .



An example toroidal geometry is shown above in fig. 1.4. In comparison to the previous straight cylindrical geometry, the radial coordinate is replaced by a *minor radius* r , measured from the center of the plasma column to its edge ($r = a$), while the *major radius* R_0 denotes the radius of the torus itself measured from its center axis (Z in fig. 1.4) to the plasma axis. The azimuthal cylindrical coordinate is replaced by the poloidal coordinate θ , wrapping immediately about the plasma column. The axial coordinate in the cylindrical system is replaced by the toroidal angle Φ wrapping around the center axis of the torus and describing a circuit along the plasma column. As with the straight cylindrical case, the magnetic geometry may be described with toroidal and poloidal currents and magnetic fields balancing radially-outward thermal pressure.

However, introducing toroidal effects into the magnetic geometry gives rise to additional drift velocities, causing the guiding centers of

particle gyro-orbits to shift (see [6, § 8.5-7]). Spatial variation in the magnetic field strength causes the ∇B drift, given by

$$\vec{v}_{\nabla B} = \frac{v_{\perp}^2}{2\omega_c} \frac{\vec{B} \times \nabla B}{B^2} \quad (1.20)$$

while the toroidal twist in the magnetic field causes the curvature drift,

$$\vec{v}_k = \frac{v_{\parallel}^2}{\omega_c} \frac{\vec{R}_c \times \vec{B}}{R_c^2 B} \quad (1.21)$$

where v_{\parallel} is the particle velocity parallel to the magnetic field, ω_c is the species cyclotron frequency (eq. (1.15)), and \vec{R}_c is the radius of curvature of the field. In the case of an applied toroidal magnetic field, these drifts are directed vertically in the \hat{Z} direction, and are directed oppositely for electrons and ions due to the charge dependence in ω_c . The electric field resulting from this charge separation drives an outward $\vec{E} \times \vec{B}$ drift (see eq. (1.18)), breaking confinement. This effect is countered by the addition of a poloidal field, which adds a helical twist to the guiding-center path to average out the separation due to particle drifts. Concepts aiming for steady-state magnetic confinement of a plasma typically rely on generating this twist, termed the *rotational transform*, to maintain stable confinement.

One of the most successful implementations of this concept for Magnetic Fusion Energy (MFE) is the *tokamak* [7] (a Russian acronym from *тороидальная камера с магнитными катушками*, *toroidalnaya kamera s magnetnymi katushkami*, “toroidal chamber with magnetic coils”). The tokamak design is characterized by a strong toroidal magnetic field (variously denoted B_T or B_Φ) applied by external coils, with a poloidal field (B_p or B_θ) primarily generated by a current (termed the *plasma current* I_p). A schematic of the plasma and coil arrangement for a tokamak is shown in fig. 1.5. By generating the rotational transform to the magnetic field using the plasma current, the tokamak design utilizes relatively simple planar magnetic coils, avoiding the significantly more complex three-dimensional coils used to generate the helical field in a *stellarator* (the major competing design concept [15]). However, the necessity for large (> 1 MA) plasma currents presents a significant engineering and physics challenge. It is straightforward to generate the plasma current through a simple transformer action from a central solenoid in the torus (depicted in fig. 1.5) – however, this AC-current-driven transformer action necessarily limits tokamaks to pulsed operation. Generation of non-inductive DC current drive [16], via RF [17, 18] or particle beams [19], is an active area of research in tokamak physics and engineering, but is outside the scope of this thesis.



Figure 1.5: Schematic of a tokamak configuration, showing the plasma and magnetic coils. The applied toroidal magnetic field is generated by the toroidal field coils (shown in blue). A toroidal plasma current is generated by the center transformer, in turn generating a poloidal magnetic field (shown in green). These combine to form the helical magnetic field. The plasma shape and equilibrium is adjusted with the outer poloidal field coils (gray).

Due to its regular, planar magnetic coils and continuous plasma current, tokamak equilibria are characterized by rotational symmetry (to good approximation) about the center axis of the torus (*axisymmetry*). Solutions to the MHD equilibrium equation, eq. (1.19), thus reduce to a two-dimensional equation in R and Z (as $\partial/\partial\Phi \rightarrow 0$), given by the Grad-Shafranov Equation [13, 20, 21]:

$$\begin{aligned}\Delta^*\psi &= -\mu_0 R^2 \frac{dp}{d\psi} - \frac{1}{2} \frac{dF^2}{d\psi} \\ \Delta^*\psi &= R^2 \nabla \cdot \left(\frac{1}{R^2} \nabla \psi \right) = R \frac{\partial}{\partial R} \left(\frac{1}{R} \frac{\partial \psi}{\partial R} \right) + \frac{\partial^2 \psi}{\partial Z^2}\end{aligned}\quad (1.22)$$

Figure 1.6: Cross-section of a plasma on the Alcator C-Mod tokamak, illustrating closed magnetic flux surfaces (light blue), the last closed flux surface (red), and surfaces with open magnetic field lines (dark blue). Definitions for plasma shaping parameters elongation κ , and upper and lower triangularity δ_u , δ_l are shown at right.



where $F = RB_\phi$ encodes the toroidal field and p is the thermal pressure. The poloidal field (equivalently, the plasma current profile) is described by the poloidal magnetic flux ψ ,

$$\psi = \frac{1}{2\pi} \int \vec{B}_p \cdot d\vec{S} \quad (1.23)$$

where \vec{S} is a surface with one edge along the magnetic axis. In eq. (1.22), ψ is treated as both an dependent parameter encoding the current, and as an independent variable – a consequence of Grad-Shafranov is that a number of parameters of interest, including pressure and current density, are *flux functions*, constant on a surface of constant ψ , and thus can be expressed as functions of ψ alone, e.g. $p = p(\psi)$. Moreover, magnetic field lines lie within surfaces of constant flux, with helical structure encoded by the flux function $q(\psi)$, termed the *safety factor*, given for a circular cross-section by

$$q = \frac{rB_\Phi}{RB_\theta} \quad (1.24)$$

As the plasma temperature rapidly equilibrates along field lines, the temperature is also a flux function to good approximation. It is useful, then, to picture the confined plasma as a series of closed, nested surfaces of constant ψ , on which the plasma is trapped (see fig. 1.6). In practice, these contours are calculated via a numerical solution of eq. (1.22) by an equilibrium solver such as the EFIT code [22]. For flux functions (i. e., constant parameters on these flux surfaces), this explic-

itly removes the dependence on the poloidal angle θ – the poloidal flux ψ is thus a useful one-dimensional abscissa derived directly from the magnetic geometry (thus independent of the physical scale of the tokamak and useful for cross-machine comparisons) for the profiles of most parameters of interest, and shall be used thus for the balance of this thesis.

Using outer poloidal field coils (shown in fig. 1.5), the tokamak operator may push the plasma into a non-circular shape, with beneficial effects on plasma performance and stability. In general, flux surfaces sufficiently far from the plasma core will not close on themselves, instead intersecting the wall; the boundary between closed, nested surfaces and these open surfaces is termed the *last closed flux surface* or LCFS. With sufficient shaping, the operator may generate a null point, the *X-point*, in the LCFS where the poloidal field is zero, splitting the LCFS (also called the *separatrix* in such configurations) into a minimally open surface with “legs” contacting the wall. This magnetic configuration is illustrated in fig. 1.6, along with a diagram defining the typical plasma shaping parameters: elongation κ and upper and lower triangularity δ_u , δ_l . As the plasma diffuses outwards, it eventually crosses the LCFS and enters open flux surfaces in the *scrape-off layer* (SOL). The plasma then streams freely along these open magnetic field lines until it contacts the wall. By maintaining an X-point, the operator may steer this plasma exhaust into a section of the tokamak, the *divertor* [23, 24, 25], that is designed to handle this high heat flux – a necessary feature to handle reactor-scale exhaust in a tokamak.

1.3 ALCATOR C-MOD

The data presented in this thesis were collected on the Alcator C-Mod tokamak [26, 27] at the MIT Plasma Science and Fusion Center. The Alcator tokamak experiments were designed as compact, high-field tokamaks. Despite its small physical size (67 cm major radius, 22 cm minor radius, considerably smaller than other major experiments), Alcator C-Mod plasmas are capable of approaching ITER- and reactor-relevant densities ($> 1 \times 10^{20} \text{ m}^{-3}$) and pressures ($> 1 \text{ atm}$). This compact design is enabled by a very high toroidal magnetic field driven by liquid-Nitrogen-cooled copper coils, reaching as high as 8.1 T, with typical operation near 5.5 T, allowing reactor-relevant research in a small, cost-effective machine. C-Mod plasmas are primarily heated by RF heating in the ion-cyclotron range of frequencies (ICRF) [28], with up to 6 MW of heating power, with an additional $\sim 1 \text{ MW}$ of lower-hybrid resonance (LHRF) power used for heating and non-inductive current drive [29], providing exceptionally high power density in the $\sim 1.1 \text{ m}^3$ plasma. A cutaway view of C-Mod, including support structures and the concrete “igloo” housing the

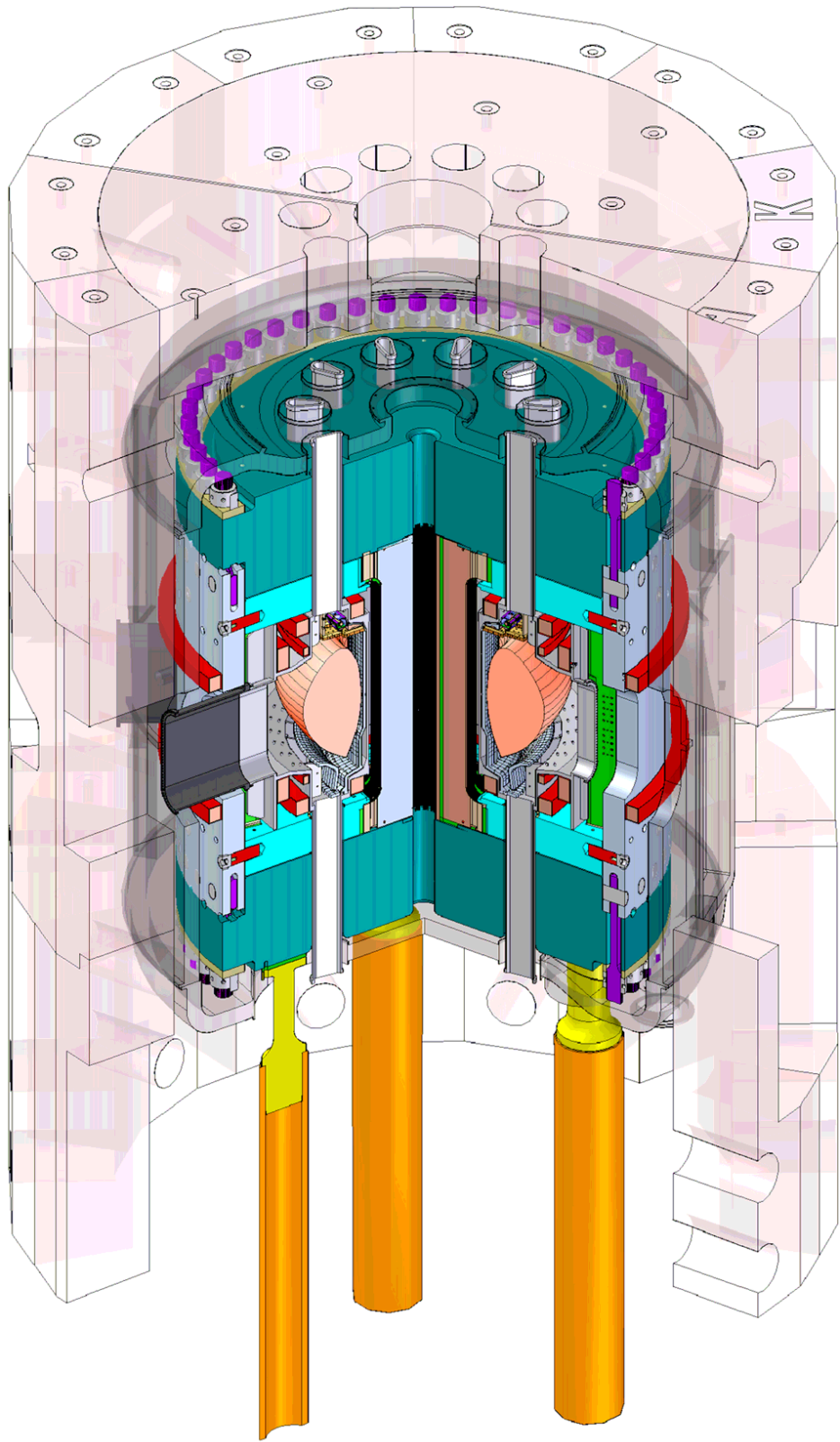


Figure 1.7: Cutaway view of the Alcator C-Mod tokamak, including cryostat and ancillary structures, illustrating the extensive support structures necessary for compact, high-field operation.



Figure 1.8: Cross-section of the C-Mod vacuum vessel, cryostat and diagnostic access ports, with toroidal-field and equilibrium-field magnetic coils labeled. Also shown is the plasma position in a typical LSN shape, with strike points in the lower divertor shown..

cooling systems, is visible in fig. 1.7. A detailed and annotated view of the C-Mod cross-section is shown in fig. 1.8.

Due to their high plasma pressure and power density, C-Mod plasmas must exhaust a large heat flux, reaching levels comparable to that anticipated for ITER [30, 31, 32]. To handle this heat flux, C-Mod operates entirely with high-Z metal materials (primarily Molybdenum and Tungsten) for all plasma-facing surfaces. In addition to its high heat tolerance and low erosion rates due to plasma contact, metal walls provide relatively low retention of fuel gas at the edge – metal walls are thus the leading candidate for ITER- and reactor-scale plasma-facing components.

The presence of a full high-Z lower divertor and upper strike plate, as well as metal limiter walls, gives C-Mod great flexibility in attainable plasma shapes – plasmas may be run in a lower-single null (LSN) shape with the plasma exhaust striking the lower divertor (shown in fig. 1.8, upper-single null (USN) ex-

Table 1.1: Summary of Alcator C-Mod typical operating parameters.

parameter	range
major radius	0.67 m
minor radius	0.22 m
toroidal field	3 – 8.1 T
plasma current	≤ 2 MA
plasma density	$\leq 5 \times 10^{20} \text{ m}^{-3}$
central temperature	≤ 8 keV
plasma pressure	≤ 2 atm
ICRF power	6 MW
LHFR power	1 MW

hausting into the upper strike plate, or in a limited shape where the scrape-off layer directly impinges on the plasma-facing wall. •

1.4 CONFINEMENT & TRANSPORT

1.4.1 Global Confinement

The rate at which a fusion plasma bleeds off heat is described by a characteristic time scale, the energy confinement time τ_E . From basic power balance for the total plasma stored energy W_p ,

$$\frac{dW_p}{dt} = P_{in} - P_{out} = P_{tot} - \frac{W_p}{\tau_E} \quad (1.25)$$

where $P_{in} = P_{tot}$ is the total input heating power, from Ohmic heating $P_{Ohm} = I_p^2 R_{plasma}$, RF or beam auxiliary heating power P_{aux} , or self-heating of the plasma from fusion reactions. In the case of the latter, note that as fusion neutrons are immediately lost into the blanket, only the energy carried by *charged* fusion products contributes to fusion self-heating: in the case of D – T fusion we denote this as the alpha heating power $P_\alpha = 1/5 \times P_{fusion}$ for the energy carried by the ${}^4\text{He}$ nucleus. It is common to encapsulate these heat source and sink terms into a single “loss” power,

$$P_{loss} = P_{Ohm} + P_{aux} + P_{fusion} - \frac{dW_p}{dt} = P_{tot} - \frac{dW_p}{dt} \quad (1.26)$$

While P_{loss} is commonly used as a parameter of merit for confinement studies, it is also important to account for the radiated power P_{rad} , the heat loss due to radiative (primarily Bremsstrahlung) rather than transport-driven effects encoded by W_p/τ_E . This is expressed in the net power,

$$\begin{aligned} P_{net} &= P_{Ohm} + P_{aux} + P_{fusion} - P_{rad} - \frac{dW_p}{dt} \\ P_{net} &= P_{loss} - P_{rad} \end{aligned} \quad (1.27)$$

The radiative power loss is commonly difficult to consistently determine experimentally, and is only partially subject to operator control, as the radiation is due both to intrinsic impurities from plasma-facing materials and intentionally-introduced high-Z impurities for radiation control. As such, P_{loss} is typically used for a simply relation for the experimental energy confinement time,

$$\tau_E = \frac{W_p}{P_{loss}} \quad (1.28)$$

Nevertheless an understanding of the radiated power is necessary for reactor operation. Radiated power from the core is deleterious to performance, driving decreased τ_E at higher radiated-power fractions $P_{\text{rad}}/P_{\text{tot}}$ [33]. Edge radiation, conversely, is essential for reactor operation to reduce the heat loads incident on the divertor, with edge radiated power fractions in excess of 50% predicted to be necessary for ITER [30]. In practice, the physics determining energy confinement are extremely complex; as such, working models for calculating τ_E from bulk parameters typically require an empirical power-law scaling.

A closer examination of the power balance equation, eq. (1.25), reveals an important figure of merit. For a DT-burning fusion reactor, steady-state operation with plasma temperatures sustained by fusion self-heating (termed “ignition”) is highly desirable. At these conditions, the heating power is dominated by P_α ; for steady-state operation ($dW_p/dt \rightarrow 0$), eq. (1.25) reduces to

$$\frac{W_p}{\tau_E} = P_\alpha \quad (1.29)$$

The alpha heating power is simply the fusion reaction rate $R_f = n_D n_T \langle \sigma v \rangle_{DT}$ times the energy carried by charged particles from a single reaction, $E_\alpha = 1/5 \times E_{\text{fusion}} = 3.5 \text{ MeV}$. Quasineutrality (eq. (1.2)) requires $n_e \approx n_D + n_T$. As the reaction rate is optimized for a 50-50 fuel mix, the alpha heating power is given by

$$P_\alpha = \frac{1}{4} n_e^2 \langle \sigma v \rangle E_\alpha \quad (1.30)$$

The stored energy is defined by

$$W_p = \frac{3}{2} p_{\text{thermal}} \quad (1.31)$$

with the thermal pressure in the plasma given by

$$p_{\text{thermal}} = n_e T_e + n_D T_D + n_T T_T = 2n_e T_e \quad (1.32)$$

assuming the condition above on the electron and ion densities, and assuming temperature equilibration $T_e \approx T_D \approx T_T$. This, then, implies $W_p = 3n_e T_e$ (a convenient expression, as electron quantities are typically more readily measured in plasma experiments). Power balance at ignition then requires

$$\frac{3n_e T_e}{\tau_E} = \frac{1}{4} n_e^2 \langle \sigma v \rangle E_\alpha \quad (1.33)$$

thus simplifying to the Lawson Criterion [34]

$$n_e \tau_E = \frac{12 T_e}{\langle \sigma v \rangle E_\alpha} \quad (1.34)$$

Multiplying both sides by $2T_e$ gives the “triple product,”

$$2n_e T_e \tau_E = p \tau_E = \frac{24 T_e^2}{\langle \sigma v \rangle E_\alpha} \quad (1.35)$$

an important figure of merit for a reactor that is optimized for D – T fusion at $T_e \approx 15$ keV with a value of $p \tau_E \approx 8.3$ atm · s, setting target parameters for a fusion reactor [15].

However, the maximum attainable thermal pressure in a tokamak is limited by a global MHD stability limit expressed in terms of [7, § 6.16]

$$\beta = \frac{2\mu_0 p}{B^2} \quad (1.36)$$

the ratio of thermal pressure to magnetic pressure $B^2/2\mu_0$ (equivalently, the ratio of thermal and magnetic stored energy) – a normalization that also falls naturally out of solutions to the MHD equilibrium, eq. (1.19). Thus for a given B_T , set by design and operational limits, there is a maximum obtainable pressure, necessitating increased energy confinement – that is, higher values for τ_E – to reach the triple-product target for ignition.

1.4.2 Transport Barriers

Global improvement to energy confinement may be achieved through local modification of the transport of energy or particles out of the plasma, achieved via regions termed *transport barriers*. While the physics driving the formation of transport barriers is not entirely understood, the effect is evidently caused by sheared flows in the plasma – these break up the turbulent “eddies” driving much of the energy or particle transport through the plasma, locally reducing transport drive in the sheared region.

The effect on the transport is clearly evident from a diffusive transport model, given by

$$\frac{\partial Q}{\partial t} = \nabla \cdot (D_Q \nabla Q) + R_Q \quad (1.37)$$

for a general parameter $Q(\vec{x}, t)$ with accompanying diffusion coefficient $D_Q(Q, \vec{x}, t)$ and net source/sink term $R_Q(Q, \vec{x}, t)$. We may con-

sider a one-dimensional “toy model” of diffusion with a simple constant source term, given in steady state by

$$\frac{d}{dx} \left(D_Q \frac{dQ}{dx} \right) + R_Q = 0 \quad (1.38)$$

The solution to this model for two sample diffusion coefficients is given in fig. 1.9. A simple constant diffusion coefficient D_Q produces a profile with weak slope, whereas an order-of-magnitude drop in D_Q near the edge (consistent with experimentally-observed values of diffusion coefficients in transport barriers) produces a region with a steep gradient in Q compared to the flat- D_Q solution, despite identical source terms R_Q . Experimentally, reductions in the particle transport coefficient D_n or the heat transport coefficient χ due to sheared flows correspond to steep-gradient regions in density or temperature, characteristic of the transport barrier.

Of particular interest is the *edge transport barrier*, also termed the *pedestal* [33, 35]. A number of high-performance tokamak regimes have been established, exploiting the formation of a pedestal to suppress transport and boost global energy confinement to levels necessary to reach the triple-product target (eq. (1.35)) for an ignited plasma. The understanding of these high-performance regimes, commonly referred to as “high-confinement” or H-modes, and their extrapolation to ITER and reactor-scale devices has been a major focus of recent tokamak research.

However, the formation of the pedestal also presents challenges that must be addressed for reactor-scale operation. Increased particle confinement causes the plasma to retain impurities – particularly ionized wall materials – along with fuel ions. Low-Z impurities, particularly the ${}^4\text{He}$ “fusion ash”, tend to slow the fusion reaction rate due to fuel dilution, while high-Z impurities drive elevated radiative losses (note the strong charge dependence for Bremsstrahlung radiation, eq. (1.6)). This ultimately leads to a *radiative collapse* [27, 33], dropping the plasma out of H-mode – thus, stationary (i.e., non-transient) operation in H-mode requires a means to regulate particle confinement and flush impurities from the plasma core.

The steep gradient in the plasma pressure generated in the pedestal has been shown to drive *Edge-Localized Modes* (ELMs) [36], instabilities

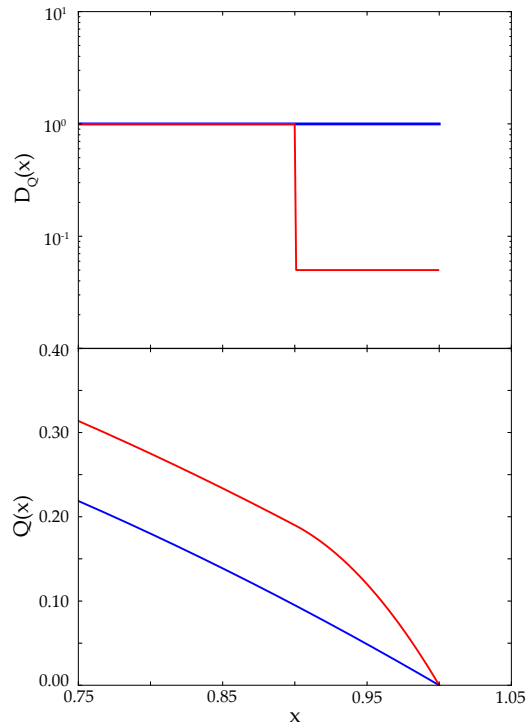


Figure 1.9: Diffusion coefficients and plasma profiles for a “toy model” 1D diffusion equation with a general parameter $Q(x)$ and accompanying diffusion coefficient $D_Q(x)$.

that cause the pedestal to periodically “crash,” expelling particles and energy into the scrape-off layer. The smaller ELM bursts found in existing experiments provide the desired level of particle transport for stationary operation – thus ITER operation is designed considering an H-mode with ELMs as the baseline for operation [37, 38]. However, on ITER-scale devices the heat pulses from ELMs drive unacceptable levels of transient thermal loading and erosion damage to wall and divertor materials [39, 40]. As such, high-performance operation on ITER- or reactor-scale devices requires mitigation or elimination of large, deleterious ELMs, either through externally-applied controls or physics-based stabilization.

1.5 GOALS & OUTLINE

This thesis will present results in the *I-mode*, a novel high-performance regime pioneered on Alcator C-Mod. I-mode is notable for its apparent decoupling of energy and particle transport, reaching H-mode-like energy confinement while maintaining L-mode levels of particle and impurity transport, achieving the desired flushing of impurities from the plasma. This is manifested in the edge with the formation of an H-mode-like temperature pedestal without the accompanying density pedestal found in conventional H-modes. I-mode also appears to be naturally free of large ELMs, avoiding the need for complex externally-applied controls, and to exhibit highly favorable scalings of energy confinement with heating power.

A firm understanding of the structure and stability of the pedestal is essential to extend I-mode operation to larger devices. This thesis will describe a combined approach to the understanding of the pedestal in I-mode, using both direct observations of pedestal structure and numerical modeling of the pedestal stability against MHD triggers for large, deleterious ELMs. The applicability of I-mode to reactor operation can thereby be evaluated. The balance of this thesis is arranged as follows:

CHAPTER 2: HIGH-PERFORMANCE REGIMES

An overview of existing results in established H-mode regimes, including observed pedestal behaviors. A detailed introduction to I-mode physics and operation is also included.

CHAPTER 3: PEDESTAL MODELING AND THEORY

An introduction to the theory of the MHD and turbulent instabilities governing the pedestal and driving large ELMs, and the numerical modeling approaches used in their analysis.

CHAPTER 4: ELMY H-MODES ON C-MOD

The results of recent experiments on C-Mod testing a unified model for pedestal structure in ELMy H-mode, the approach to which is also applied to I-mode pedestals.

CHAPTER 5: I-MODE PEDESTAL SCALINGS

New results from dedicated pedestal experiments in I-mode examining the response of pedestal structure to engineering and physics parameters, and potential extrapolations of pedestal structure and performance to larger devices.

CHAPTER 6: I-MODE PEDESTAL STABILITY MODELING

Numerical modeling results for the stability of I-mode pedestals against identified ELM triggers, and correlations to the generally observed lack of ELMs in I-mode.

CHAPTER 7: CONCLUSIONS

A summary of the results presented in this thesis and some directions for future work.

An overview of the diagnostics used in the experiments presented here is also given in appendix A. A summary of the pedestal database used in these experiments is given in appendix B. *

BIBLIOGRAPHY

- [1] United Nations. *World Population Prospects: The 2010 Revision. Comprehensive Tables*, volume 1. United Nations, 2010.
- [2] J. Klugman et al. *Human development report 2011. Sustainability and Equity: A Better Future for All*, 2011.
- [3] H. Gruenspecht. *International energy outlook 2011. Center for Strategic and International Studies*, 2010.
- [4] B.P. Global. *Statistical review of world energy 2010*.
- [5] U.S. Energy Information Administration. *Annual coal report 2012*, 2013.
- [6] J.P. Freidberg. *Plasma Physics and Fusion Energy*. Cambridge books online. Cambridge University Press, 2007.
- [7] J. Wesson. *Tokamaks*. International Series of Monographs on Physics. Oxford University Press, 2011.
- [8] F.F. Chen. *Introduction to Plasma Physics and Controlled Fusion*. Springer, 1984.
- [9] K.S. Krane. *Introductory Nuclear Physics*. Wiley, 1987.
- [10] W.M. Haynes. *CRC Handbook of Chemistry and Physics, 93rd Edition*. Taylor & Francis, 2012.
- [11] Jeffrey R. Johnson, Timothy D. Swindle and Paul G. Lucey. *Estimated solar wind-implanted helium-3 distribution on the moon*. *Geophysical Research Letters*, 26(3):385–388, 1999.
- [12] B. Palaszewski. *Atmospheric mining in the outer solar system*. In *41st American Institute of Aeronautics and Astronautics Joint Propulsion Conference and Exhibit*, 2005.
- [13] Jeffrey P. Freidberg. *Ideal Magnetohydrodynamics*. Springer, 1987.
- [14] J. Kesner, R.S. Post, B.D. McVey and D.K. Smith. *A tandem mirror with axisymmetric central-cell ion confinement*. *Nuclear Fusion*, 22(4):549, 1982.
- [15] Dale Meade. *50 years of fusion research*. *Nuclear Fusion*, 50(1):014004, 2010.
- [16] Egbert Westerhof. *Non-inductive current drive*. *Fusion Science and Technology*, 61:312–319, 2012.

- [17] Paul T. Bonoli. **Review of recent experimental and modeling progress in the lower hybrid range of frequencies at ITER relevant parameters.** *AIP Conference Proceedings*, 1580(1):15–24, 2014.
- [18] R. Prater. **Heating and current drive by electron cyclotron waves.** *Physics of Plasmas*, 11(5):2349–2376, 2004.
- [19] C. Gormezano, A.C.C. Sips, T.C. Luce, S. Ide, A. Becoulet et al. **Chapter 6: Steady state operation.** *Nuclear Fusion*, 47(6):S285, 2007.
- [20] H. Grad and H. Rubin. MHD equilibrium in an axisymmetric toroid. In *Proceedings of the 2nd U.N. Conference on the Peaceful Uses of Atomic Energy*, volume 31, page 190, 1958.
- [21] V.D. Shafranov. Grad-Shafranov equation for MHD equilibrium in a torus. *Soviet Physics, Journal of Experimental and Theoretical Physics*, 26:682, 1960.
- [22] L.L. Lao, H. St. John, R.D. Stambaugh, A.G. Kellman and W. Pfeiffer. **Reconstruction of current profile parameters and plasma shapes in tokamaks.** *Nuclear Fusion*, 25(11):1611, 1985.
- [23] B. Lipschultz, X. Bonnin, G. Counsell, A. Kallenbach, A. Kukushkin et al. **Plasma–surface interaction, scrape-off layer and divertor physics: implications for ITER.** *Nuclear Fusion*, 47(9):1189, 2007.
- [24] B. Lipschultz, B. LaBombard, J. L. Terry, C. Boswell and I. H. Hutchinson. **Divertor physics research on Alcator C-Mod.** *Fusion Science and Technology*, 51:369–380, 2007.
- [25] P. Titus, R. Vieira, B. LaBombard, B. Lipschultz, S. Wolfe et al. **Conceptual design of a new outer divertor for C-Mod.** *Fusion Science and Technology*, 56(1):101–106, 2009.
- [26] I. H. Hutchinson, R. Boivin, F. Bombarda, P. Bonoli, S. Fairfax et al. **First results from Alcator C-Mod.** *Physics of Plasmas*, 1(5):1511–1518, 1994.
- [27] M. Greenwald, N. Basse, P. Bonoli, R. Bravenec, E. Edlund et al. **Confinement and transport research in Alcator C-Mod.** *Fusion Science and Technology*, 51(3):266–287, 2007.
- [28] Y Takase, R L Boivin, F Bombarda, P T Bonoli, C L Fiore et al. **Survey of ICRF heating experiments and enhanced performance modes in Alcator C-Mod.** *Plasma Physics and Controlled Fusion*, 38(12):2215, 1996.
- [29] J.R. Wilson, R. Parker, M. Bitter, P.T. Bonoli, C. Fiore et al. **Lower hybrid heating and current drive on the Alcator C-Mod tokamak.** *Nuclear Fusion*, 49(11):115015, 2009.

- [30] A. Loarte, B. Lipschultz, A.S. Kukushkin, G.F. Matthews, P.C. Stangeby et al. **Chapter 4: Power and particle control.** *Nuclear Fusion*, 47(6):S203, 2007.
- [31] J. L. Terry, B. LaBombard, B. Lipschultz, M. J. Greenwald, J. E. Rice et al. **The scrape-off layer in Alcator C-Mod: Transport, turbulence, and flows.** *Fusion Science and Technology*, 51(3):342–356, 2007.
- [32] B. LaBombard, J. L. Terry, J. W. Hughes, D. Brunner, J. Payne et al. **Scaling of the power exhaust channel in Alcator C-Mod.** *Physics of Plasmas*, 18(5):056104, 2011.
- [33] M. Greenwald, R.L. Boivin, F. Bombarda, P.T. Bonoli, C.L. Fiore et al. **H-mode confinement in Alcator C-Mod.** *Nuclear Fusion*, 37(6):793, 1997.
- [34] J D Lawson. **Some criteria for a power producing thermonuclear reactor.** *Proceedings of the Physical Society. Section B*, 70(1):6, 1957.
- [35] F. Wagner, G. Becker, K. Behringer, D. Campbell, A. Eberhagen et al. **Regime of improved confinement and high beta in neutral-beam-heated divertor discharges of the ASDEX tokamak.** *Physical Review Letters*, 49(19):1408–1412, Nov 1982.
- [36] H Zohm. **Edge localized modes (ELMs).** *Plasma Physics and Controlled Fusion*, 38(2):105, 1996.
- [37] ITER Physics Expert Group on Confinement, Transport and ITER Physics Expert Group on Confinement Modelling and Database and ITER Physics Basis Editors. **Chapter 2: Plasma confinement and transport.** *Nuclear Fusion*, 39(12):2175, 1999.
- [38] M. Shimada, D.J. Campbell, V. Mukhovatov, M. Fujiwara, N. Kirneva et al. **Chapter 1: Overview and summary.** *Nuclear Fusion*, 47(6):S1, 2007.
- [39] A Loarte, G Saibene, R Sartori, D Campbell, M Becoulet et al. **Characteristics of type I ELM energy and particle losses in existing devices and their extrapolation to ITER.** *Plasma Physics and Controlled Fusion*, 45(9):1549, 2003.
- [40] G Federici, A Loarte and G Strohmayer. **Assessment of erosion of the ITER divertor targets during type I ELMs.** *Plasma Physics and Controlled Fusion*, 45(9):1523, 2003.

2

HIGH-PERFORMANCE REGIMES

The development of magnetic-confinement fusion into an economical form of power generation is characterized by two seemingly contrary requirements: first, a high level of energy confinement is necessary to reach the desired level of self-heating of the plasma by fusion products, satisfying triple-product requirements (eq. (1.35)). At the same time, particle transport must be sufficient to avoid the deleterious effects of accumulated helium “fusion ash” and other impurities on fusion performance – particularly important in the case of the high-Z impurities from the metal plasma-facing walls necessary for reactor-scale devices [1, 2, 3].

A number of operating scenarios, collectively termed “high confinement” or H-modes[4, 5], satisfying these requirements have been developed. The “low confinement” or L-mode operating baseline of energy confinement is characterized through an extensive multi-machine scaling study [6] by the ITER-89 scaling,

$$\tau_{E,ITER89} = 0.048 \times \bar{n}_e^{0.1} M^{0.5} I_p^{0.85} R^{1.2} a^{0.3} \kappa^{0.5} B_T^{0.2} P_{aux}^{-0.5} \quad (2.1)$$

in which \bar{n}_e is the line-averaged density (10^{20} m^{-3}), M is the atomic mass (amu), I_p is the plasma current (MA), B_T is the toroidal field (T), R and a are the major and minor radii in m (see fig. 1.4), κ is the elongation (see fig. 1.6), and P_{aux} is the externally-applied heating power (MW). Compared to this baseline, H-modes represent a significant improvement in performance, with confinement – here represented in a normalized sense by the H-factor, i.e.,

$$H_{89} = \frac{\tau_E}{\tau_{E,ITER89}} \quad (2.2)$$

improved by roughly a factor of two compared to L-mode [7].

This improvement in confinement is due to the formation of a *pedestal*, a transport barrier (see section 1.4.2) at the edge that greatly slows the transport of particles and/or energy out of the plasma, and accordingly forms a steep-gradient region in density and/or temperature at the edge. Pedestal formation is achieved through strongly sheared flows in the plasma edge, driven in part by a radial electric field (the “ E_r well”) and the resulting $\vec{E} \times \vec{B}$ flows in the pedestal. While this flow is difficult to model due to the short scale lengths inherent to the pedestal [8, 9], the role of edge E_r and flows has been extensively studied both from an experimental [10, 11, 12, 13] and a

theoretical [14, 15, 16, 17, 18] standpoint, as has the role of other edge fluctuations coupling into these flows in driving the transition into H-mode [19]. As the pedestal structure is known to set a strong constraint on the overall performance in high-confinement regimes [20], as well as determining the edge stability and heat exhaust properties of the regime, a firm understanding of the pedestal is essential for extrapolation of a high-performance regime to ITER and beyond.

This chapter provides an overview and comparison of different classes of established H-mode operation, particularly regarding their behaviors in the high energy confinement and low particle confinement required for a reactor. Additionally, observations of Edge-Localized Modes (ELMs) [21] are addressed. We then introduce the access conditions, operation, and global characteristics of *I-mode* – an alternate high-performance regime with a number of favorable characteristics for reactor operation, and the subject of the majority of this thesis.

Table 2.1: Typical operating parameters of tokamaks noted in this thesis, along with references to overviews of each machine. *Note:* all ITER values are projected.

Device	R/a [m]	I _p [MA]	B _T [T]	⟨n _e ⟩ [10 ¹⁹ m ⁻³]	T _{i0} [keV]	refs.
C-Mod (USA)	0.67/0.22	≤ 2	3 – 8.1	≤ 50	≤ 8	[22, 23, 24]
DIII-D (USA)	1.67/0.67	1 – 3	2.2	6	5 – 10	[25, 26, 27]
ASDEX-U (GER)	1.65/0.5	~ 1	3.9	7.5	2 – 3	[28, 29, 30]
JET (UK)	3.4/0.9	3 – 4	3.8	5	10 – 20	[31, 32]
JT-60U (JAP)	3.4/0.9	3 – 4	4.8	5	10 – 20	[33, 34]
JFT-2M (JAP)	1.3/0.35	0.5	2.2	5	1 – 2	[35, 36]
ITER*	6.2/2.0	15	5.3	≤ 10	10 – 20	[37, 38, 39]

2.1 ELMY H-MODE

2.1.1 ELMY H-Mode Operation

The first H-modes, observed in high-power experiments on ASDEX [4, 5], exhibited a prompt decrease by roughly a factor of two in both particle and energy transport [4]. The H-mode transition is marked by high edge temperatures and strong gradients – the first H-modes were observed in divertor experiments on ASDEX, as the diverted configuration allows higher edge temperatures than are attainable in limited plasmas [5]. Unlike ELM-free H-modes, however, the confinement is periodically degraded by *Edge-Localized Modes* (ELMs), intermittent “crashes” in the pedestal expelling particles and energy into the SOL, with repetition rates ranging from a few ELM cycles per second to over 100 Hz, which drives sufficient particle transport to flush impurities from the plasma and allow stationary operation

Figure 2.1: Characteristic traces of a steady ELMY H-mode (section 2.1). Density and radiated power rise after the L-H transition, but stabilize as the periodic relaxation of the pedestal regulates and flushes impurities from the plasma. ELM bursts are visible as spikes on the edge D_α signal.



Figure 2.2: ELMY H-mode pedestals from pedestal similarity experiments on Alcator C-Mod and DIII-D. Pedestal densities and temperatures are shown normalized to poloidal field (which accounts for differences in plasma current) such that hyperbolae in the parameter space are curves of constant poloidal beta. ELMY H-mode pedestals are, to lowest order, constrained to a curve of fixed $\beta_{p,\text{ped}}$.



[5, 21]. The ELMY H-mode forms a strong pedestal in both density and temperature – due to profile stiffness in the core, the pedestal supports high temperatures and pressures and good global performance [7, 40, 41]. Moreover, the ELMY H-mode is readily attainable on all major tokamak experiments at a broad range of collisionalities and operating densities, although ELMY H-modes on C-Mod require an atypical shape [42, 43]. Here we define the collisionality (normalized collision frequency) by [44],

$$\begin{aligned} \nu^* &= \frac{\nu_{\text{eff}}}{\nu_{\text{bounce}}} = \frac{qR\nu_{ei}}{\varepsilon^{3/2}\nu_{Th,e}} \\ &= (6.921 \times 10^{-18}) \frac{Rqn_e Z_{\text{eff}} \ln \Lambda_e}{\varepsilon^{3/2} T_e^2} \end{aligned} \quad (2.3)$$

with electron density n_e in m^{-3} and temperature in eV, major radius R in m, and with the Coulomb logarithm defined by $\ln \Lambda_e = 24 - \ln(\sqrt{n_e}/T_e)$. Typically the pedestal collisionality is calculated by evaluating n_e , T_e , and q at the 95% flux surface. The operating density range is expressed in terms of the Greenwald density limit [45],

$$n_{Gr} = \frac{I_p}{\pi a^2} \quad f_{Gr} = \frac{\bar{n}_e}{n_{Gr}} \quad (2.4)$$

with I_p in MA and a in m yielding density in 10^{20} m^{-3} . ELMY H-mode operation is possible with Greenwald fractions ranging from $f_{Gr} \sim 0.3 - 1.0$, although confinement degrades as f_{Gr} approaches unity [2, 46]. As such, the ELMY H-mode is considered the baseline for ITER operation [37, 38]. Analysis of a multi-machine database [47] led to the development of the ITER98y2 H-mode confinement scaling [38],

$$\tau_{ITER98y2} = 0.0562 \times \bar{n}_e^{0.41} M^{0.19} I_p^{0.93} R^{1.39} a^{0.58} \kappa^{0.78} B_T^{0.15} P_{loss}^{-0.69} \quad (2.5)$$

$$H_{98} = \frac{\tau_E}{\tau_{E,ITER98y2}} \quad (2.6)$$

in which \bar{n}_e is the line-averaged density (10^{19} m^{-3}), M is the atomic mass (amu), I_p is the plasma current (MA), B_T is the toroidal field (T), R and a are the major and minor radii in m (see fig. 1.4), κ is the elongation (see fig. 1.6), and P_{loss} is the heating power defined in eq. (1.26) (MW).

Due to the importance of pedestal structure on overall performance [20], a number of models for the pedestal width and height in ELMY H-mode have been proposed. The ELMY H-mode pedestal has been observed to be limited in pressure gradient [48, 49] – as the pedestal

width on a given machine typically varies only over a small range [41, 50], this constitutes (to lowest order approximation) a limit on the attainable pedestal height. Models based on gyroradius limits, and their expected effects on the growth rates of turbulent modes compared to the $\vec{E} \times \vec{B}$ shearing rate, have been proposed [51, 52]. However, this has been discounted in favor of a model based on poloidal beta limits, $\beta_p = 2\mu_0 p/B_p^2$, both by experiments varying density and temperature at fixed p_{ped} [53] and by isotope-mass-difference experiments [54] (both of which vary the gyroradius without varying $\beta_{p,ped}$). These models are described in more detail in section 3.1.

On existing machines, ELMs provide sufficient impurity transport to allow stationary operation without seriously impacting energy confinement [55]. However, the transient power load from the ELM heat pulse is consistently observed to be 20 – 30% of the input heating power [56], resulting in ELM energy losses reaching 2 – 6% of the total stored energy – on ITER, this results in heat pulses as high as 80 MJ reaching the divertor plate [40, 57]. As wall materials are generally limited to ELM heat loads of ~ 10 MJ per ELM [58], uncontrolled large ELM pulses can seriously exceed tolerances for ITER plasma-facing wall and divertor materials [58, 59]. Thus, avoiding or mitigating large, deleterious ELMs is essential for ITER operation.

2.1.2 Edge-Localized Modes & Pedestal Limits

Early phenomenological experiments on DIII-D and ASDEX [21, 40, 48] classified ELMs into three broad categories:

TYPE-I

Large, discrete ELMs. Repetition rate f_{ELM} rises with increasing heating power. The ELM crash is preceded by broadband electromagnetic and density fluctuations. Type-I ELMy pedestals are modeled to be at or near the ballooning stability boundary (described below).

TYPE-II

Smaller and faster than type-I, often termed “grassy ELMs.” No discernable f_{ELM} dependence on heating power. Found in strongly shaped plasmas between the first and second-stable regions for ballooning MHD.

TYPE-III

Small ELMs, f_{ELM} decreases with increasing heating power. Exhibit a coherent magnetic precursor fluctuation before the ELM crash. Found only below a threshold pedestal temperature, typically at levels of heating power just above the L-H threshold, given by [60] (where \bar{n}_e is in 10^{20} m^{-3} , B_T in T, and S is the plasma surface area in m^2):

$$\begin{aligned} P_{\text{thres}} &= 0.0488 \times \bar{n}_e^{0.717} B_T^{0.803} S^{0.941} \\ S &= (2\pi)^2 a R \sqrt{\kappa} \end{aligned} \quad (2.7)$$

Early investigation of the ELM pedestal, particularly in large type-I ELMs, associated the pedestal limit with a “ballooning” MHD instability – these MHD modes are driven unstable by strong pressure gradients in the edge, expressed in terms of the parameter α_{MHD} for a general toroidal equilibrium [61],

$$\alpha_{\text{MHD}} = -\frac{2}{(2\pi)^2} \frac{\partial V}{\partial \psi} \sqrt{\frac{V}{2\pi^2 R}} \mu_0 \frac{dp}{d\psi} \quad (2.8)$$

This reduces to a more intuitive form for a cylindrical plasma [62],

$$\alpha_{\text{MHD}} = -\frac{2Rq^2}{B_T^2} \nabla p \quad (2.9)$$

with the q^2/B_T^2 factor effectively expressing the scaling as $\alpha_{\text{MHD}} \sim \nabla p / B_p^2$. Type-I ELM H-mode pedestals are typically found to be near a critical value for α_{MHD} dependent on the plasma shape [53] – stronger shaping is associated with slower ELM frequencies and greater stabilization of type-I ELMs, consistent with ballooning MHD [21, 46, 49]. Due to the restricted width range for the pedestal on a given machine [41, 50], the α_{MHD} limit reduces, to good approximation, to a limit on β_p at the pedestal top [46, 49]. For example, points at matched shaping, field and current across a DIII-D/C-Mod similarity experiment, shown in fig. 2.2, lie on a fixed $n_e T_e$ line. The transition from type-I to type-III ELMs with increasing density and decreasing temperature [46], or alternately the transition from type-III ELMs just above the L-H transition to type-I ELMs with increasing heating power [48], is consistent with the transition from a resistive mode for type-III ELMs to the ideal MHD modes identified with type-I ELMs.

A naive ballooning MHD analysis, however, does not accurately capture the ELM H-mode pedestal – parallel observations of MHD stability in early ELM H-modes also identified current-driven kink/peeling modes as a potential limiting instability, particularly at low collisionality [40, 48, 51]. This is particularly true in light of the *bootstrap current*, an effect by which gradients in the plasma self-generate an electric current, given by [44]

$$j_{\text{boot}} = I(\psi) p_e(\psi) \left[\alpha \frac{dn_e}{d\psi} + \beta \frac{dT_e}{d\psi} + \gamma \frac{dT_i}{d\psi} \right] \quad (2.10)$$

where $I(\psi) = RB_\phi$ is a flux function encoding the field, $p_e(\psi)$ is the electron pressure, and α , β , and γ are coefficients determined by the collisionality and trapped-particle fraction, ordered $\alpha > \beta > \gamma$. Due to the strong density and temperature gradients in the pedestal, the local current density may be large enough for current-driven kink/peeling modes to be a concern.

MHD models built on coupled peeling and ballooning MHD modes, as well as diamagnetic effects stabilizing ballooning modes with high toroidal mode number n [40], have been developed [63, 64] and successfully capture the MHD limits of the ELMY H-mode. Moreover, turbulence studies based on the kinetic ballooning mode (KBM) [65] predict that the KBM will limit the pressure gradient and width such that the pedestal width scales with $\beta_{p,ped}$ in a manner consistent with experimental observations, $\Delta_{ped} \sim \beta_{p,ped}^{1/2}$ [66]. Turbulent fluctuations with an onset soon after the inter-ELM pressure pedestal gradient saturation have been observed [67], but a definitive analysis is still ongoing. A self-consistent model including both the MHD and turbulent constraints, EPED [68], has been implemented and tested in multi-machine analyses [69], including on DIII-D [70], C-Mod [71], and KSTAR [72]. The constraints of this model are discussed in detail in chapter 3.

2.1.3 Active ELM Control

In light of the potential deleterious effects of large ELMs on ITER-scale devices [58, 59], mitigating or preventing large type-I ELMs in H-mode is of prime concern. One engineering solution for active ELM control is the application of a *resonant magnetic perturbation* (RMP) [73, 74, 75]. Small perturbations (less than 1/1000 the magnitude of the background magnetic field), for example those driven by an $n = 3$ coil set on DIII-D [73] or a variable $n = 3, 4, 6$ set on MAST [76], are sufficient to completely suppress ELMs, as on DIII-D and ASDEX Upgrade, or mitigate them, as on MAST [76]. The physics mechanism underlying the RMP is unclear; it is proposed by Snyder *et al.* [70] that stochastic magnetic islands in the pedestal limit the inward growth of the pedestal such that the MHD stability boundary is not reached. In cases of ELM mitigation, Chapman *et al.* [77] propose that modification of the edge rotation shear or 3D effects destabilize the ELM before reaching conditions for a large, deleterious ELM event. Due to its resonant nature, the RMP effect is strongly sensitive to the edge safety factor q , limiting the potential profiles possible for RMP ELM control [74].

Rather than attempting to eliminate the ELM instability, it is also possible to “smooth out” the ELM heat pulse using pellet pacing [78]. Generally, the transient ELM power $P_{ELM} \sim f_{ELM} \Delta W_{ELM}$ is roughly fixed - thus smaller, faster ELMs expel the less energy per ELM for

the same average power. By triggering smaller, faster ELMs the heat load can be smoothed to a level closer to steady-state heat loads tolerable to divertor materials, rather than large transient heat pulses. In pellet pacing, the sharp density increase locally introduced in the pedestal by the pellet triggers a high- n ballooning mode, resulting in a small ELM. Experiments, e. g., on DIII-D [78], ASDEX Upgrade [79], and JET [80], including with the ITER-like metal wall [81], have demonstrated suitable ELM mitigation through pellet pacing. However, the feasibility of pellet pacing on ITER, as well as the potential for non-axisymmetric heat loading in the divertor due to the localized nature of the pellet perturbation, remain open questions.

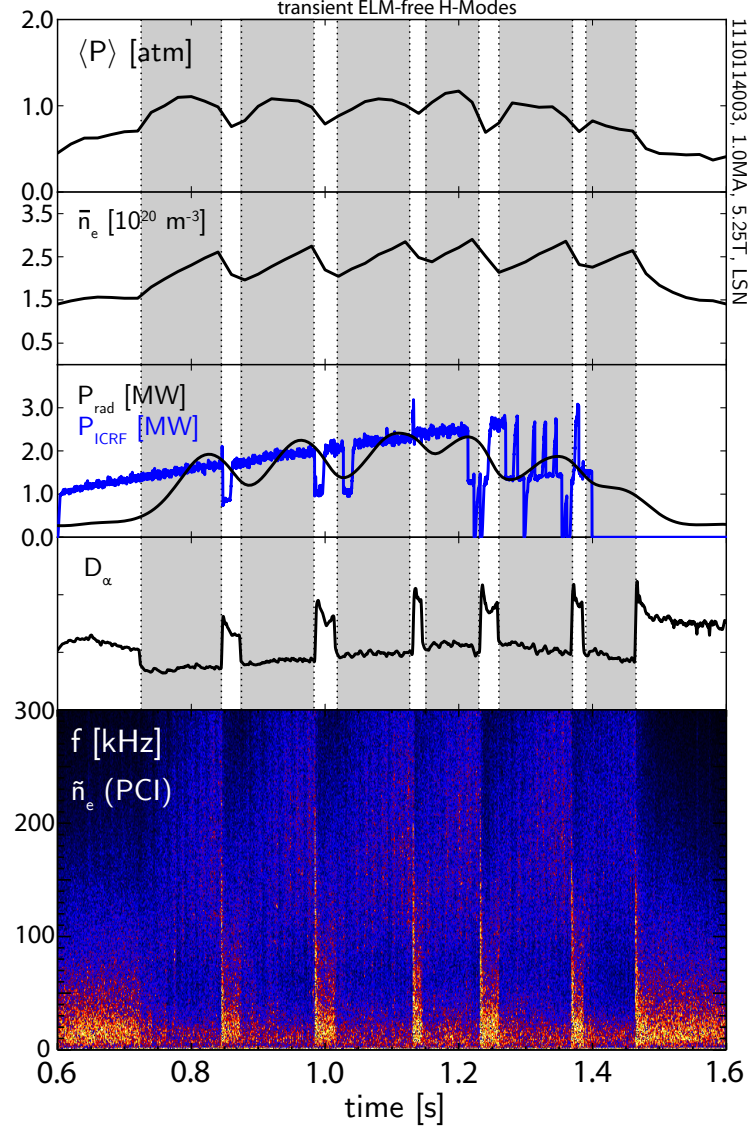
2.1.4 Prospects for ELMy H-Mode

Though ELMy H-mode represents the most readily attainable high-performance regime, its applicability to ITER-scale devices hinges on the limitation, mitigation, or elimination of large ELMs and the associated heat loads on wall and divertor surfaces. ELM losses from type-I ELMs tend to be smaller for a given $\beta_{p,ped}$ at higher density and lower temperature, ultimately transitioning to type-III ELMs [49], however these plasmas tend to exhibit lower global confinement [46]. Type-II ELMs may provide the necessary near-continuous heat exhaust, but access to the regime is narrow and highly sensitive to shaping [56]. Alternately, ELM heat loading in type-I regimes may be controlled or suppressed via engineering solutions (i. e., RMP or pellet pacing) – but these are similarly limited in availability, and are of uncertain extrapolation to ITER-scale devices. Thus, recent efforts have also placed great emphasis on high-performance regimes that are naturally free of large ELMs. •

2.2 ELM-FREE H-MODE

Under a broad range of conditions, the plasma may enter a transient *ELM-free H-mode*, in which an H-mode forms without exhibiting large edge-localized modes (ELMs) [21, 82]. ELM-free H-modes exhibit high levels of both energy and particle confinement ($H_{89} \sim 2$), resulting in strong density and temperature pedestals [83, 84]. The plasma stored energy, global pressure, and density rise monotonically after the L-H transition (shown in fig. 2.3), as does the edge pressure gradient [85]. This, however, is unsustainable – the increased particle confinement causes impurities to accumulate in the plasma, increasing the power lost to radiative effects. Above $P_{rad}/P_{in} \sim 0.5$ confinement degrades due to cooling at the edge, and the H-mode terminates as the radiated power approaches the total heating power, an event termed the “radiative collapse” [7].

Figure 2.3: Characteristic traces of transient ELM-free H-modes, highlighted on the traces (section 2.2). After the L-H transition, density and thermal pressure (and therefore fusion reaction rate and stored energy) rise, while turbulent particle transport is reduced, as seen by the drop in edge D_α light and suppression of turbulence. However, radiated power rises due to impurity accumulation – when radiated power reaches a level comparable to total heating power, the plasma drops back into L-mode.



As a result, the ELM-free H-mode is an inherently transient state for the plasma – the excessive particle confinement and resulting radiative losses tend to drop the plasma back into L-mode although under certain conditions the edge pressure gradient may grow sufficiently to instead transition into an ELMy H-mode [85]. As an H-L back-transition can release energy and particles on a scale in excess of even large type-I ELMs, these transient states must be avoided similarly to uncontrolled ELMy H-modes. This demonstrates the necessity of some form of regulation of the particle confinement in high-performance regimes to control and flush impurities from the plasma, allowing stationary operation without reaching an ELMing limit. •

2.3 ELM-SUPPRESSED H-MODES

In addition to H-modes exhibiting ELMs, classes of H-mode have been established capable of stationary operation with acceptable levels of particle transport (avoiding the radiative collapse and subsequent transient nature found in classical ELM-free H-modes) without exhibiting the bursty heat and particle transport driven by ELMs. Rather, the pedestal is regulated by a continuous fluctuation localized in the pedestal. The characteristics of two, the Quiescent H-mode (QH-mode) and Enhanced D _{α} (EDA) H-mode, are presented here.

2.3.1 QH-Mode

The *Quiescent H-mode* (QH-mode) was first observed on DIII-D [86, 87], and subsequently achieved on ASDEX Upgrade [88], JT-60U [89], and JET [90]. In QH-mode operation, following a brief ELM-free or ELMing phase after the L-H transition, the plasma enters a state with steady averaged density and radiated power, indicating a lack of serious impurity accumulation, despite lacking ELM-mediated transport (evident from divertor D _{α} light, which is “quiescent” compared to the characteristic spikes driven by ELMs). Although QH-mode requires lower densities (average density reduced by roughly a factor of two from comparable ELMy H-modes) with cryopumping for density control, access is otherwise robust, with successful operation across a broad range of shaping, safety factor, current and field [86]. The regime is capable of stationary operation, with the mode sustained for most of the current flat-top on DIII-D ($\sim 25\tau_E$) with very good confinement – in cases with an internal transport barrier in addition to the pedestal (termed the “Quiescent Double Barrier” or QDB regime [91, 92, 93]) a confinement metric of $\beta_N H_{89} \sim 7$ was reached (albeit for a briefer period, $\sim 5\tau_E$), compared to $\beta_N H_{89} \sim 4$ found in ELMy H-modes on DIII-D [92]. Here we use the normalized pressure metric [94]

$$\beta_N = \beta \frac{a B_T}{I_p} \quad (2.11)$$

in m · T · MA⁻¹. Similarly competitive confinement between QH-mode and ELMy H-mode is seen on ASDEX Upgrade and JET, although the mode on JT-60U is out-performed by ELMy H-mode [95]. The pedestal density is reduced (comparable to the reduction in globally-averaged density) in QH-mode compared to ELMy H-mode, and excess fueling to the edge by gas puffing, pellet fueling, or wall outgassing destroys the QH-mode. However, pedestal temperatures are typically somewhat higher [92], thus the mode is found at ITER-relevant low collisionalities. Pedestal pressure gradients are compa-

rable to those found in ELMy H-mode [86]. A particularly strong E_r well (2 – 3 times deeper than in comparable ELMy H-modes) is also observed in the QH-mode pedestal [93].

In place of bursty ELM transport, the pedestal in QH-mode is continuously regulated by the *Edge Harmonic Oscillation* (EHO), an MHD mode observed in density, temperature, and magnetic fluctuations [86]. The EHO is made up of distinct harmonics with toroidal mode numbers $n \sim 1 - 10$; these harmonics are directly observed in the particle flux at the divertor, indicating that the EHO is responsible for density regulation in QH-mode [92]. MHD modeling approaches similar to those described in chapter 3 indicate that the EHO is a saturated peeling mode [70, 96, 97]. This is consistent with the low pedestal collisionality in the QH-mode pedestal (lower collisionalities and higher bootstrap currents tends to drive the pedestal towards the peeling side of the peeling-balloonning MHD boundary, as described in chapter 3), and with the observed localization of the EHO in the region of strongest E_r and rotation shear [91]. The saturated mode is driven by the strong rotation shear in the edge – while this typically destabilizes low- n MHD modes, in the case of the EHO the magnetic component of the mode couples to the vacuum-vessel wall as the rotation spins up, providing the drag force necessary to saturate the mode at finite amplitude [98]. This prevents a rapidly-growing edge instability, thus providing the ELM suppression in QH-mode [70].

Historically, QH-mode operation has required significant neutral-beam inputs directed counter the plasma current direction, providing the necessary rotation [86]. However, counter-current beam operation drives significant fast-ion losses into the outer wall, necessitating operation with a large outer gap to avoid wall outgassing. More recent experiments have successfully generated QH-modes with co-current beam injection [98] and with torque from non-axisymmetric magnetic fields [99, 100]. The latter is of particular importance, as it is not expected that the NBI systems on ITER will drive sufficient torque to produce QH-mode [99]. In addition to the requirement for externally-supplied torque to maintain the mode, QH-mode suffers from accumulation of high-Z impurities – while lower-Z ions are flushed from the plasma by the EHO, high-Z impurities tend to accumulate in the core [90, 92], which may present difficulties attaining QH-mode on metal-walled machines where high-Z impurities dominate. Nevertheless QH-mode is a potentially attractive option for a reactor regime, provided high-density operation with sufficient high-Z impurity control is attainable.

2.3.2 EDA H-Mode

The *Enhanced D _{α} H-mode* (EDA H-mode) is a high-performance regime discovered and explored on the Alcator C-Mod tokamak [101, 102,

Figure 2.4: Characteristic traces of an EDA H-mode on C-Mod (section 2.3.2). Following a brief ELM-free phase, the plasma density and radiated power stabilizes at a sustainable level. The edge transport barrier is regulated by the continuous QCM fluctuation rather than bursty ELM transport.



[103]. Along with transient ELM-free H-modes, the EDA regime is the customary approach to H-mode operation on C-Mod, unlike other major tokamak experiments; the Type-I ELMMy H-mode commonly found on other devices requires an atypical shaping to more easily reach the stability boundary associated with the ELM trigger on C-Mod [43]. In EDA operation, the L-H transition is followed by a rise in radiated power and density similar to an ELM-free H-mode. However, shortly thereafter the H-mode stabilizes at steady density [101], with the radiated power held at $P_{\text{rad}}/P_{\text{in}} \sim 30\%$ [104], allowing steady operation (maintained for most of the steady current phase, $\sim 10\tau_E$) and good performance, with $H_{89} \sim 1.9$, $H_{98} \sim 1$ [102]. Notably, empirical scalings in EDA H-mode (see section 3.1.1) indicate energy confinement with potentially weaker degradation of τ_E with input heating power compared to that predicted by the ITER98y2 scaling [103, 105, 106]. Rather than bursty ELM transport, the EDA pedestal

is regulated continuously, with divertor D_α signals (indicative of the particle exhaust from the plasma) recovering to near L-mode levels after an initial drop at the L-H transition. Access to EDA H-mode is strongly favored by higher collisionality, $\nu^* > 1$ (see eq. (2.3)), and edge safety factor [105, 107] and by strong shaping [107]. Although a higher collisionality is observed to be required at lower values of q_{95} , a collisionality threshold alone is insufficient to explain EDA access [105]. Instead, EDA and ELM-free H-modes are separated in a phase space of collisionality ν^* and normalized pressure gradient α_{MHD} (see eq. (2.8)) – however, the transition between the two regimes is soft, with the EDA smoothly appearing at higher pressure gradients and collisionalities rather than exhibiting a sharp transition [108].

While the pedestal pressure in EDA H-mode is comparable to that in ELM_y H-mode, the pedestal profiles in EDA tend towards higher density and lower temperature, yielding the elevated pedestal collisionality favoring EDA access. The pedestal appears to be limited by transport effects rather than macroscopic stability – the pedestal is modeled to be stable to ideal MHD effects [43, 107], despite exhibiting a $\nabla p \sim I_p^2$ trend expected from a ballooning instability [106]. High pedestal density results in strong ionization in the scrape-off layer and an edge that is relatively opaque to neutrals [23, 109]. As a result, the density will rise until the transport saturates – additional fueling through the edge triggers minimal response, while a density drop is countered by increased particle confinement to recover the density, resulting in pedestal and global density values set by the plasma current, with weak dependence on other engineering parameters [110].

The regulation of the pedestal in EDA H-mode is provided by the *Quasi-Coherent Mode* (QCM), a field-aligned electromagnetic fluctuation localized in the steep-gradient region of the pedestal [102, 111, 112]. The QCM is a fairly narrow-band ($\delta f/f \sim 10\%$) mode strongly visible in density and magnetic fluctuations, with a centroid frequency ranging from 50 – 200 kHz and a fairly short poloidal wavelength, $k_\theta \sim 1.5 \text{ cm}^{-1}$ [111]. QCM fluctuations are visible in the density flux to the divertor, indicating that the QCM fluctuation is directly responsible for the particle transport through the EDA H-mode pedestal [23, 111]. Numerical modeling of the EDA H-mode pedestal suggests a resistive ballooning mode (the collisional analogue to the ideal ballooning MHD mode found in ELM_y H-modes, described in section 3.2.1) for the QCM [108, 113]. This is consistent with experimental observations of the EDA pedestal – the requirement of high collisionality (the QCM disappears below $\nu^* \sim 0.1$) suggests a resistive effect [43], while the favored high edge pressure gradient (α_{MHD}) suggests a ballooning instability. At high power and high edge pressure gradient, the QCM is replaced by small, high-frequency ELMs [107, 108, 112], potentially indicating that the pedestal is “burn-

ing through” the resistive-ballooning regulation of the pedestal and reaching the ideal MHD boundary associated with the ELM trigger.

The EDA H-mode presents another potential route to reactor-scale operation with naturally-suppressed large ELMs. The regime is robustly accessible on C-Mod using only RF heating with no external momentum sources or non-axisymmetric magnetic coils, with good confinement and acceptable levels of impurity accumulation and radiated power consistent with high performance [114]. Moreover, there is an extensive body of research studying the EDA H-mode on a machine with all-metal walls, with ITER-relevant heat flux and edge neutral behavior [23, 109], and with similar electron-ion equilibration to that expected for ITER [13]. However, the necessary collisionality near the pedestal top ($\nu^* > 1$) for the QCM fluctuation is significantly higher than the expected levels for the ITER pedestal ($\nu^* < 0.1$), an apparent challenge to EDA H-mode access on ITER. •

2.4 I-MODE

In order for an H-mode regime to achieve stationary operation, there must be some form of relaxation of the density transport barrier – either by intermittent bursts of transport due to ELMs, or through a continuous fluctuation regulating the particle confinement (as in the EDA and QH-modes). However, each of these regimes faces some level of increased particle confinement relative to L-mode, as well as difficulties inherent in their operation – large ELMs are incompatible with reactor-scale operation due to the large pulsed heat loads on wall and divertor materials [58, 59], while alternate H-modes pose sometimes-onerous operational constraints. Recent work on Alcator C-Mod has demonstrated a novel high-confinement regime, termed the *I-mode*, which is unique in that it appears to decouple energy and particle transport, forming an H-mode-like temperature pedestal with the accompanying improvement in energy confinement, while maintaining an L-mode density profile and particle transport level. I-mode exhibits several highly attractive properties for a reactor regime:

1. The lack of a particle transport barrier or density pedestal maintains the desired level of impurity flushing from the plasma, avoiding excessive radiative losses
2. I-mode appears to be generally stable against large ELMs, avoiding the excessive pulsed heat loads found in ELMs (of critical importance for ITER-scale devices) without externally-applied engineering controls
3. appears to exhibit much weaker degradation of confinement with increased heating power

Figure 2.5: C-Mod cross-sections illustrating magnetic configurations suitable for I-mode access. Either upper-null operation in the normal field direction, or lower-null with field and current reversed provides ion ∇B drift away from the X-point. This configuration is unfavorable for the H-mode threshold, but allows for easier access to I-mode.



A firm understanding of the structure and stability of the I-mode pedestal is essential for the extrapolation of I-mode operation to larger devices, and will form the balance of this thesis.

2.4.1 Access and Operation

It has been long established that the orientation of the X-point (described in section 1.2.2) relative to the vertical particle drifts (particularly the ∇B drift, eq. (1.20)) in the plasma column has a strong effect on plasma behavior, particularly flows in the edge [109, 115, 116, 117]. Notably, in cases where the ion ∇B drift is directed towards the X-point, the power threshold to access conventional H-modes is reduced by roughly a factor of two [56, 118, 119] (thus for the balance of this section we refer to this configuration as the “favorable ∇B drift direction”). In experiments in the unfavorable drift configuration (that is, ion ∇B drift away from the X-point), however, a transitional state was observed in L-H threshold experiments in which energy confinement improved before the formation of a classical H-mode. This transient state, termed the “improved L-mode” on ASDEX [120], was later identified as a sustainable, distinct operating regime, termed I-mode, on Alcator C-Mod [13, 121, 122].

I-mode access is fairly robust, provided the appropriate drift configuration is held – this can be achieved either by running an upper-null shape, or by reversing the field (as well as the plasma current, to maintain magnetic-field helicity) and running in a standard LSN shape [123], shown in fig. 2.5. Upper-null operation allows a broader range of plasma shapes, but suffers from poorer diagnostic coverage and

power handling due to the SOL flux impinging on a flat strike plate rather than the full lower divertor [123, 124]. Short I-mode periods have also been observed in the favorable-drift configuration in a modified plasma shape used for ELMy H-mode experiments on C-Mod, but these transitioned quickly into H-mode and will not be considered for the balance of this thesis [43, 124]. In either the forward-field USN or reversed-field LSN shape, I-mode access is favored by higher heating powers, low collisionality, and strong shaping [121]; as with all C-Mod operation, I-mode is accessible with purely RF heating, without external sources of momentum input [125]. Unlike H-modes on C-Mod, I-mode operation is also largely insensitive to wall conditions due to the low impurity confinement [123].

Initially, access to I-mode was available within a relatively narrow window in density and heating power – I-mode attempts with insufficient density were aborted by core radiation from high-Z impurities generated by interactions between fast ions and the wall, while high-density or high-power cases tended to transition into an ELM-free H-mode [121]. However, more recent experiments have greatly expanded both the available density and heating power range in I-mode, particularly by fueling into established I-modes to maintain sufficiently low density at the L-I transition [125]. As of the most recent campaign, I-modes can be sustained for the current flat-top ($\sim 20\tau_E$) up to the maximum available RF heating power [123, 125].

2.4.2 Global Performance & Edge Behavior

I-mode is characterized by H-mode-like normalized energy confinement ($H_{98} \sim 1$) while maintaining an L-mode density profile and particle transport level. While the pedestal density is generally reduced compared to H-mode, $n_{e,ped} \sim 1 \times 10^{20} \text{ m}^{-3}$, pedestal temperatures are typically higher than H-modes at comparable power. Due to profile stiffness in the core, this results in very high core temperatures, and global-average pressures near the C-Mod H-mode record¹ ($\sim 1.5 \text{ atm}$ in I-mode, compared to $\sim 1.8 \text{ atm}$ in H-mode) [122]. Notably, scalings of stored energy against RF power in I-mode indicate only weak degradation of energy confinement with heating power, contrary to the $\tau_E \sim P^{-0.5}$ (L-mode) or $\tau_E \sim P^{-0.69}$ (ELMy H-mode) trends from multi-machine scalings [6, 38] – a potentially highly-favorable result for extrapolation to ITER-scale devices. Particle and impurity confinement, on the other hand, is minimal, limiting radiative losses to $\sim 25\%$ of heating power, well below H-mode levels [121]. Impurity confinement times and accumulation are measured to be at L-mode levels on laser blow-off [126] and charge-exchange [13, 127] diagnostics. Initial studies of the I-mode threshold indicate that the mode should be accessible on ITER at reduced den-

¹ and therefore the all-tokamak record thermal pressure

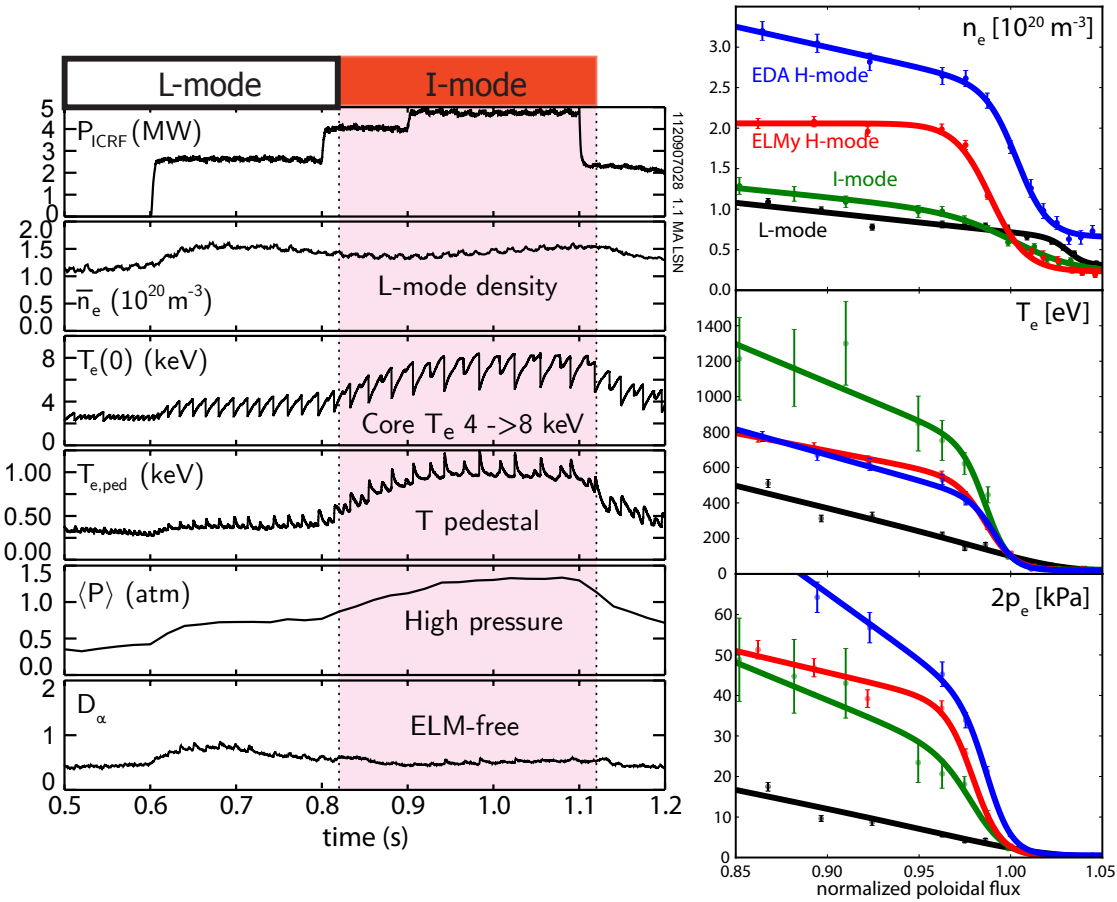


Figure 2.6: (left) Characteristic traces for a typical I-mode. At the L-I transition, the core and edge temperature rise over several sawtooth cycles before reaching a steady level; global confinement and pressure rise accordingly. However, the density remains at L-mode levels, and no ELMs are exhibited. (right) Edge profiles for density, temperature, and pressure in L-, I-, and H-mode. The I-mode (green) retains an density profile comparable to the L-mode (black), unlike the ELMy (red) and EDA (blue) H-modes which form a strong density pedestal. However, the I-mode forms a higher temperature pedestal than either H-mode. As a result, the I-mode reaches comparable pedestal pressures to the H-modes while retaining L-mode particle transport.

sity ($\sim 4 \times 10^{19} \text{ m}^{-3}$), then fueled after the transition up to a $Q = 10$ scenario [24, 125]. Ready fueling control in such a scenario would be critical, as density is the primary engineering “knob” for fusion power in predominantly self-heated fusion plasmas [123].

The lack of a particle transport barrier in I-mode drives significantly different edge behavior compared to H-mode – the reduced ∇n_e in the pedestal reduces both the overall pressure gradient and the bootstrap current drive (eq. (2.10)), which has a stabilizing effect on both ballooning and kink/peeling edge MHD modes [43]. The SOL heat flux channel in I-mode also appears to be significantly wider than in comparable H-modes [121, 125]. Energy transport suppression in I-mode appears along with the expected E_r well at the edge, which is similar in depth and $\vec{E} \times \vec{B}$ shearing rate to some EDA H-modes, albeit weaker than that found in H-modes with the highest τ_E [127, 128].

Figure 2.7: Impurity confinement time τ_I measured by laser blow-off [126] versus normalized confinement H_{98} for L-mode, I-mode, and H-mode. I-mode exhibits H-mode-like energy confinement, increased by roughly a factor of two over L-mode. However, I-mode retains L-mode levels of particle and impurity transport, readily flushing heavy impurities from the plasma. EDA H-mode exhibits strongly increased particle confinement, while transient ELM-free H-modes increase their particle confinement to the point of radiative collapse (see section 2.2).



I-modes exhibit toroidal rotation levels comparable to H-mode, consistent with a ∇T_e scaling for rotation velocity [129], which may contribute to edge shearing in I-mode [127].

Notably, the edge behavior across the L-I transition is distinct from more conventional L-H transitions. The L-H transition is rapid both in the bifurcation in measured transport (< 1 ms on C-Mod) and in pedestal development (~ 20 ms, comparable to τ_E) – the L-I transition, however, may exhibit a comparable bifurcation in transport (see fig. 2.8), but develops the pedestal significantly more slowly, with a steady increase in edge temperature lasting up to ~ 150 ms $\gg \tau_E$ [121, 127]. The L-I transition appears to be tied to sawtooth heat pulses reaching the edge – with each heat pulse, the edge temperature “ratchets” upward, reaching a steady I-mode over several sawtooth cycles [122, 123]. The L-I transition is seen to be more rapid at higher levels of RF heating power and lower q_{95} [121]. Both factors are associated with larger sawtooth crashes, consistent with a transient heat pulse driving the transition [123].

2.4.3 Edge Fluctuations – the Weakly-Coherent Mode

As with other high-performance regimes, the I-mode pedestal exhibits broadband suppression of turbulence at moderate frequencies (20 – 150 kHz). In its place, the I-mode pedestal exhibits a broad electromagnetic fluctuation termed the *Weakly-Coherent Mode* [121]. The WCM is primarily observed as a density and magnetic fluctuation,



Figure 2.8: Measurements of \dot{n}_e fluctuations from the WCM in I-mode. (left) Reflectometer measurements in the pedestal region, showing the transition from broadband L-mode turbulence to the WCM, and subsequent fluctuation suppression as the plasma transitions into an ELM-free H-mode. Edge T_e measurements are also shown, tracking the formation of the characteristic I-mode temperature pedestal. Note the dynamics of the L-I transition – while the edge temperature increases steadily over several sawtooth periods, the turbulence suppression and formation of the WCM is more rapid, with the mode spinning up in frequency as the I-mode is established. (right) Gas-puff imaging measurements of the WCM, averaged over the I-mode. The mode is restricted in k -space to $k_\theta \sim 2 \text{ cm}^{-1}$, but is broad in frequency. Also shown is the $k_\theta = 0$, $f \sim 10 \text{ kHz}$ signal of the GAM coupled to the WCM [130].

although temperature fluctuations associated with the mode are also observed (albeit at an amplitude reduced by roughly an order of magnitude) [124, 130, 131]. Due to its prominence in the I-mode edge and similarity to the quasi-coherent mode (QCM) found in the EDA H-mode, the WCM is a prime candidate for pedestal regulation in I-mode, driving enhanced particle transport – initial observations indicate a correlation between particle flux through the LCFS and the (normalized) WCM amplitude [124], although a firm characterization of the effect of the WCM on the particle transport is ongoing.

The WCM is found at fairly short poloidal wavelength, $k_\theta \sim 1.5 \text{ cm}^{-1}$, similar to the QCM [124]. Compared to the QCM, however, the WCM is significantly less coherent – $\delta f/f \sim 50\%$, compared to $\sim 10\%$ for the QCM – and exists at a higher frequency ($200 - 400 \text{ kHz}$) and phase velocity [122, 130]. While the radial location and extent of the WCM has not yet been definitively determined, it has been localized within the last $\sim 2 \text{ cm}$ of the LCFS by O-mode reflectometry [124] and gas-puff imaging [130, 132]. The onset of the WCM is immediate and contemporaneous with the turbulence suppression in the L-I transition, unlike the formation of the T_e pedestal, which typically requires several sawtooth cycles to form [132]. However, the WCM can “dither” for several sawtooth heat pulses in marginal I-modes, and typically spins up in frequency as the mode is established (contrary to the behavior observed in the QCM) [122, 132]. Notably, the WCM appears to be coupled to Geodesic Acoustic Modes (GAMs) [133] in

the plasma edge. GAM dynamics have been associated with the L-H transition on other tokamaks [19, 134], but GAMs are not seen in H-modes on C-Mod – however, persistent GAMs co-existing with the mean flow in the edge are consistently seen in I-mode [130].

The nature of the WCM is, as of this writing, an open question – several candidate instabilities have been proposed, including a branch of the kinetic-balloonning mode [65] or the heavy-particle mode [135, 136], but the underlying instability in the WCM remains unknown. Experiments probing the behavior of the WCM, as well as theoretical work in understanding its underlying physics, is ongoing. ★

BIBLIOGRAPHY

- [1] A. Loarte, B. Lipschultz, A.S. Kukushkin, G.F. Matthews, P.C. Stangeby et al. **Chapter 4: Power and particle control.** *Nuclear Fusion*, 47(6):S203, 2007.
- [2] E. Joffrin, M. Baruzzo, M. Beurskens, C. Bourdelle, S. Brezinsek et al. **First scenario development with the JET new ITER-like wall.** *Nuclear Fusion*, 54(1):013011, 2014.
- [3] R Neu, ASDEX Upgrade Team, EU PWI Taskforce and JET EFDA Contributors. **Preparing the scientific basis for an all metal ITER.** *Plasma Physics and Controlled Fusion*, 53(12):124040, 2011.
- [4] F. Wagner, G. Becker, K. Behringer, D. Campbell, A. Eberhagen et al. **Regime of improved confinement and high beta in neutral-beam-heated divertor discharges of the ASDEX tokamak.** *Physical Review Letters*, 49(19):1408–1412, Nov 1982.
- [5] M Keilhacker, G Becker, K Bernhardi, A Eberhagen, M ElShaer et al. **Confinement studies in L and H-type ASDEX discharges.** *Plasma Physics and Controlled Fusion*, 26(1A):49, 1984.
- [6] P.N. Yushmanov, T. Takizuka, K.S. Riedel, O.J.W.F. Kardaun, J.G. Cordey et al. **Scalings for tokamak energy confinement.** *Nuclear Fusion*, 30(10):1999, 1990.
- [7] M. Greenwald, R.L. Boivin, F. Bombarda, P.T. Bonoli, C.L. Fiore et al. **H-mode confinement in Alcator C-Mod.** *Nuclear Fusion*, 37(6):793, 1997.
- [8] Grigory Kagan and Peter J Catto. **Neoclassical ion heat flux and poloidal flow in a tokamak pedestal.** *Plasma Physics and Controlled Fusion*, 52(5):055004, 2010.
- [9] Matt Landreman and Darin R Ernst. **Local and global Fokker–Planck neoclassical calculations showing flow and bootstrap current modification in a pedestal.** *Plasma Physics and Controlled Fusion*, 54(11):115006, 2012.
- [10] R. J. Groebner, K. H. Burrell and R. P. Seraydarian. **Role of edge electric field and poloidal rotation in the L-H transition.** *Physical Review Letters*, 64(25):3015–3018, Jun 1990.
- [11] Keith H. Burrell. **Tests of causality: Experimental evidence that sheared $E \times B$ flow alters turbulence and transport in tokamaks.** *Physics of Plasmas*, 6(12):4418–4435, 1999.

- [12] P. W. Terry. **Suppression of turbulence and transport by sheared flow.** *Reviews of Modern Physics*, 72:109–165, Jan 2000.
- [13] R. M. McDermott, B. Lipschultz, J. W. Hughes, P. J. Catto, A. E. Hubbard et al. **Edge radial electric field structure and its connections to H-mode confinement in Alcator C-Mod plasmas.** *Physics of Plasmas*, 16(5):056103, 2009.
- [14] K. C. Shaing and E. C. Crume. **Bifurcation theory of poloidal rotation in tokamaks: A model for L-H transition.** *Physical Review Letters*, 63(21):2369–2372, Nov 1989.
- [15] H. Biglari, P. H. Diamond and P. W. Terry. **Influence of sheared poloidal rotation on edge turbulence.** *Physics of Fluids B: Plasma Physics*, 2(1):1–4, 1990.
- [16] Y. B. Kim, P. H. Diamond and R. J. Groebner. **Neoclassical poloidal and toroidal rotation in tokamaks.** *Physics of Fluids B: Plasma Physics*, 3(8):2050–2060, 1991.
- [17] A S Ware, P W Terry, P H Diamond and B A Carreras. **Transport reduction via shear flow modification of the cross phase.** *Plasma Physics and Controlled Fusion*, 38(8):1343, 1996.
- [18] K H Burrell, T N Carlstrom, E J Doyle, D Finkenthal, P Gohil et al. **Physics of the L-mode to H-mode transition in tokamaks.** *Plasma Physics and Controlled Fusion*, 34(13):1859, 1992.
- [19] L. Schmitz, L. Zeng, T. L. Rhodes, J. C. Hillesheim, E. J. Doyle et al. **Role of zonal flow predator-prey oscillations in triggering the transition to H-mode confinement.** *Physical Review Letters*, 108:155002, Apr 2012.
- [20] J.E. Kinsey, G.M. Staebler, J. Candy, R.E. Waltz and R.V. Budny. **ITER predictions using the GYRO verified and experimentally validated trapped gyro-Landau fluid transport model.** *Nuclear Fusion*, 51(8):083001, 2011.
- [21] H Zohm. **Edge localized modes (ELMs).** *Plasma Physics and Controlled Fusion*, 38(2):105, 1996.
- [22] I. H. Hutchinson, R. Boivin, F. Bombarda, P. Bonoli, S. Fairfax et al. **First results from Alcator C-Mod.** *Physics of Plasmas*, 1(5):1511–1518, 1994.
- [23] M. Greenwald, N. Basse, P. Bonoli, R. Bravenec, E. Edlund et al. **Confinement and transport research in Alcator C-Mod.** *Fusion Science and Technology*, 51(3):266–287, 2007.
- [24] M. Greenwald, A. Bader, S. Baek, H. Barnard, W. Beck et al. **Overview of experimental results and code validation activities at Alcator C-Mod.** *Nuclear Fusion*, 53(10):104004, 2013.

- [25] J.L. Luxon. **A design retrospective of the DIII-D tokamak.** *Nuclear Fusion*, 42(5):614, 2002.
- [26] J.L. Luxon, T.C. Simonen, R.D. Stambaugh and the DIII-D Team. **Overview of the DIII-D fusion science program.** *Fusion Science and Technology*, 48(2):807–827, October 2005.
- [27] J.L. Luxon. **A brief introduction to the DIII-D tokamak.** *Fusion Science and Technology*, 48(2):828–833, October 2005.
- [28] A. Herrmann and O. Gruber. **Chapter 1: ASDEX upgrade - introduction and overview.** *Fusion Science and Technology*, 44(3):569–577, November 2003.
- [29] F. Ryter, A. Stäbler and G. Tardini. **Chapter 5: Core energy transport in conventional scenarios in ASDEX Upgrade.** *Fusion Science and Technology*, 44(3):618–635, November 2003.
- [30] U. Stroth, J. Adamek, L. Aho-Mantila, S. Äkäslompolo, C. Amador et al. **Overview of ASDEX upgrade results.** *Nuclear Fusion*, 53(10):104003, 2013.
- [31] D.C. McDonald, Y. Andrew, G.T.A. Huysmans, A. Loarte, J. Onenga et al. **Chapter 3: ELMY H-mode operation on JET.** *Fusion Science and Technology*, 53(4):891–957, May 2008.
- [32] F. Romanelli and JET EFDA Contributors. **Overview of the JET results with the ITER-like wall.** *Nuclear Fusion*, 53(10):104002, 2013.
- [33] Y. Kamada, T. Fujita, S. Ishida, M. Kikuchi, S. Ide et al. **Fusion plasma performance and confinement studies on JT-60 and JT-60U.** *Fusion Science and Technology*, 42(2,3):185–254, November 2002.
- [34] A. Kitsunezaki, M. Shimizu, H. Ninomiya, M. Kuriyama and the JT-60 Team. **JT-60 program.** *Fusion Science and Technology*, 42(2,3):179–184, September 2002.
- [35] Y. Kusama, M. Yamamoto and the JFT-2M Group. **JFT-2M program.** *Fusion Science and Technology*, 49(2):89–95, February 2006.
- [36] Y. Miura, M. Mori, T. Shoji, H. Matsumoto, K. Kamiya et al. **Studies of improved confinement in JFT-2M.** *Fusion Science and Technology*, 49(2):96–121, February 2006.
- [37] M. Shimada, D.J. Campbell, V. Mukhovatov, M. Fujiwara, N. Kirneva et al. **Chapter 1: Overview and summary.** *Nuclear Fusion*, 47(6):S1, 2007.

- [38] ITER Physics Expert Group on Confinement, Transport and ITER Physics Expert Group on Confinement Modelling and Database and ITER Physics Basis Editors. **Chapter 2: Plasma confinement and transport.** *Nuclear Fusion*, 39(12):2175, 1999.
- [39] E.J. Doyle, W.A. Houlberg, Y. Kamada, V. Mukhovatov, T.H. Osborne et al. **Chapter 2: Plasma confinement and transport.** *Nuclear Fusion*, 47(6):S18, 2007.
- [40] W Suttrop. **The physics of large and small edge localized modes.** *Plasma Physics and Controlled Fusion*, 42(5A):A1, 2000.
- [41] P.A. Schneider, E. Wolfrum, R.J. Groebner, T.H. Osborne, M.N.A. Beurskens et al. **Analysis of temperature and density pedestal gradients in AUG, DIII-D and JET.** *Nuclear Fusion*, 53(7):073039, 2013.
- [42] J. Hughes, P. Snyder, X. Xu, J. Walk, E. Davis et al. **Pedestal stability and transport on the Alcator C-Mod tokamak: Experiments in support of developing predictive capability.** In *24th IAEA Fusion Energy Conference*, 2012.
- [43] J.W. Hughes, P.B. Snyder, J.R. Walk, E.M. Davis, A. Diallo et al. **Pedestal structure and stability in H-mode and I-mode: a comparative study on Alcator C-Mod.** *Nuclear Fusion*, 53(4):043016, 2013.
- [44] O. Sauter, C. Angioni and Y. R. Lin-Liu. **Neoclassical conductivity and bootstrap current formulas for general axisymmetric equilibria and arbitrary collisionality regime.** *Physics of Plasmas*, 6(7):2834–2839, 1999.
- [45] M. Greenwald, J.L. Terry, S.M. Wolfe, S. Ejima, M.G. Bell et al. **A new look at density limits in tokamaks.** *Nuclear Fusion*, 28(12):2199, 1988.
- [46] G. Saibene, L.D. Horton, R. Sartori, B. Balet, S. Clement et al. **The influence of isotope mass, edge magnetic shear and input power on high density ELMy H modes in JET.** *Nuclear Fusion*, 39(9):1133, 1999.
- [47] J.P. Christiansen, J.G. Cordey, K. Thomsen, A. Tanga, J.C. DeBoo et al. **Global energy confinement H-mode database for ITER.** *Nuclear Fusion*, 32(2):291, 1992.
- [48] J W Connor. **Edge-localized modes - physics and theory.** *Plasma Physics and Controlled Fusion*, 40(5):531, 1998.
- [49] H Urano, W Suttrop, L D Horton, A Herrmann, J C Fuchs et al. **Energy and particle losses during type-I ELMy H-mode in ASDEX Upgrade.** *Plasma Physics and Controlled Fusion*, 45(9):1571, 2003.

- [50] C.F. Maggi. Progress in understanding the physics of the H-mode pedestal and ELM dynamics. *Nuclear Fusion*, 50(6):066001, 2010.
- [51] R. J. Groebner and T. H. Osborne. Scaling studies of the high mode pedestal. *Physics of Plasmas*, 5(5):1800–1806, 1998.
- [52] M. N. A. Beurskens, T. H. Osborne, P. A. Schneider, E. Wolfrum, L. Frassinetti et al. H-mode pedestal scaling in DIII-D, ASDEX Upgrade, and JET. *Physics of Plasmas*, 18(5):056120, 2011.
- [53] T H Osborne, R J Groebner, L L Lao, A W Leonard, R Maingi et al. H-mode pedestal characteristics, ELMs, and energy confinement in ITER shape discharges on DIII-D. *Plasma Physics and Controlled Fusion*, 40(5):845, 1998.
- [54] H. Urano, T. Takizuka, Y. Kamada, N. Oyama, H. Takenaga et al. Dimensionless parameter dependence of H-mode pedestal width using hydrogen and deuterium plasmas in JT-60U. *Nuclear Fusion*, 48(4):045008, 2008.
- [55] B.W. Rice, K.H. Burrell, J.R. Ferron, C.M. Greenfield, G.L. Jackson et al. Progress towards sustainment of advanced tokamak modes in DIII-D. *Nuclear Fusion*, 39(11Y):1855, 1999.
- [56] W. Suttrop, A. Herrmann, F. Ryter and J. Stober. Chapter 6: H-mode and pedestal physics in ASDEX Upgrade. *Fusion Science and Technology*, 44(3):636–649, November 2003.
- [57] A.W. Leonard, A. Herrmann, K. Itami, J. Lingertat, A. Loarte et al. The impact of ELMs on the ITER divertor. *Journal of Nuclear Materials*, 266–269(o):109 – 117, 1999.
- [58] G Federici, A Loarte and G Strohmayer. Assessment of erosion of the ITER divertor targets during type I ELMs. *Plasma Physics and Controlled Fusion*, 45(9):1523, 2003.
- [59] A Loarte, G Saibene, R Sartori, D Campbell, M Becoulet et al. Characteristics of type I ELM energy and particle losses in existing devices and their extrapolation to ITER. *Plasma Physics and Controlled Fusion*, 45(9):1549, 2003.
- [60] Y R Martin, T Takizuka and the ITPA CDBM H-mode Threshold Database Working Group. Power requirement for accessing the H-mode in ITER. *Journal of Physics: Conference Series*, 123(1):012033, 2008.
- [61] R. L. Miller, M. S. Chu, J. M. Greene, Y. R. Lin-Liu and R. E. Waltz. Noncircular, finite aspect ratio, local equilibrium model. *Physics of Plasmas*, 5(4):973–978, 1998.

- [62] J. W. Connor, R. J. Hastie and J. B. Taylor. **Shear, periodicity, and plasma ballooning modes.** *Physical Review Letters*, 40:396–399, Feb 1978.
- [63] P. B. Snyder, H. R. Wilson, J. R. Ferron, L. L. Lao, A. W. Leonard et al. **Edge localized modes and the pedestal: A model based on coupled peeling–ballooning modes.** *Physics of Plasmas*, 9(5):2037–2043, 2002.
- [64] A D Turnbull, L L Lao, T H Osborne, O Sauter, E J Strait et al. **Edge localized modes in DIII-D high performance discharges.** *Plasma Physics and Controlled Fusion*, 45(10):1845, 2003.
- [65] W.M. Tang, J.W. Connor and R.J. Hastie. **Kinetic-balloonning-mode theory in general geometry.** *Nuclear Fusion*, 20(11):1439, 1980.
- [66] P. B. Snyder and G. W. Hammett. **Electromagnetic effects on plasma microturbulence and transport.** *Physics of Plasmas*, 8(3):744–749, 2001.
- [67] A. Diallo, W. Hughes, J. M. Greenwald, B. LaBombard, E. Davis et al. **Observation of edge instability limiting the pedestal growth in tokamak plasmas.** *Physical Review Letters*, 112:115001, Mar 2014.
- [68] P. B. Snyder, R. J. Groebner, A. W. Leonard, T. H. Osborne and H. R. Wilson. **Development and validation of a predictive model for the pedestal height.** *Physics of Plasmas*, 16(5):056118, 2009.
- [69] R.J. Groebner, C.S. Chang, J.W. Hughes, R. Maingi, P.B. Snyder et al. **Improved understanding of physics processes in pedestal structure, leading to improved predictive capability for ITER.** *Nuclear Fusion*, 53(9):093024, 2013.
- [70] P. B. Snyder, T. H. Osborne, K. H. Burrell, R. J. Groebner, A. W. Leonard et al. **The EPED pedestal model and edge localized mode-suppressed regimes: Studies of quiescent H-mode and development of a model for edge localized mode suppression via resonant magnetic perturbations.** *Physics of Plasmas*, 19(5):–, 2012.
- [71] J.R. Walk, P.B. Snyder, J.W. Hughes, J.L. Terry, A.E. Hubbard et al. **Characterization of the pedestal in Alcator C-Mod ELM-ing H-modes and comparison with the EPED model.** *Nuclear Fusion*, 52(6):063011, 2012.
- [72] Hyunsun Han, Ohjin Kwon and J. Y. Kim. **Predictive modeling of pedestal structure in KSTAR using EPED model.** *Physics of Plasmas*, 20(10):–, 2013.

- [73] T. E. Evans, R. A. Moyer, P. R. Thomas, J. G. Watkins, T. H. Osborne et al. **Suppression of large edge-localized modes in high-confinement DIII-D plasmas with a stochastic magnetic boundary.** *Physical Review Letters*, 92:235003, Jun 2004.
- [74] R. A. Moyer, T. E. Evans, T. H. Osborne, P. R. Thomas, M. Be-
coulet et al. **Edge localized mode control with an edge resonant
magnetic perturbation.** *Physics of Plasmas*, 12(5):–, 2005.
- [75] T E Evans, R A Moyer, K H Burrell, M E Fenstermacher, I Joseph et al. **Edge stability and transport control with resonant mag-
netic perturbations in collisionless tokamak plasmas.** *Nature
Physics*, 2:419 – 423, 2006.
- [76] A Kirk, I T Chapman, J Harrison, Yueqiang Liu, E Nardon et al. **Effect of resonant magnetic perturbations with toroidal mode
numbers of 4 and 6 on edge-localized modes in single null H-
mode plasmas in MAST.** *Plasma Physics and Controlled Fusion*, 55(1):015006, 2013.
- [77] I T Chapman, A Kirk, C J Ham, J R Harrison, Y Q Liu et al. **Towards understanding edge localised mode mitigation by res-
onant magnetic perturbations in MAST.** *Physics of Plasmas*, 57(5):294, 2012.
- [78] L. R. Baylor, N. Commaux, T. C. Jernigan, S. J. Meitner, S. K. Combs et al. **Reduction of edge localized mode intensity on
DIII-D by on-demand triggering with high frequency pellet in-
jection and implications for ITER.** *Physics of Plasmas*, 20(8):–, 2013.
- [79] P.T. Lang, A. Burckhart, M. Bernert, L. Casali, R. Fischer et al. **ELM pacing and high-density operation using pellet injection
in the ASDEX Upgrade all-metal-wall tokamak.** *Nuclear Fusion*, 54(8):083009, 2014.
- [80] P.T. Lang, A. Alonso, B. Alper, E. Belonohy, A. Boboc et al. **ELM
pacing investigations at JET with the new pellet launcher.** *Nu-
clear Fusion*, 51(3):033010, 2011.
- [81] P.T. Lang, D. Frigione, A. Gáraud, T. Alarcon, P. Bennett et al. **ELM pacing and trigger investigations at JET with the new
ITER-like wall.** *Nuclear Fusion*, 53(7):073010, 2013.
- [82] W Suttrop, O Gruber, B Kurzan, H D Murmann, J Neuhauser et al. **Effect of plasma shape variation on ELMs and H-mode
pedestal properties in ASDEX upgrade.** *Plasma Physics and Con-
trolled Fusion*, 42(5A):A97, 2000.
- [83] A E Hubbard. **Physics and scaling of the H-mode pedestal.** *Plasma Physics and Controlled Fusion*, 42(5A):A15, 2000.

- [84] T Hatae, Y Kamada, S Ishida, T Fukuda, T Takizuka et al. **Characteristics of edge pedestal width in JT-60U ELM-free H-mode plasmas.** *Plasma Physics and Controlled Fusion*, 40(6):1073, 1998.
- [85] P Breger, C Flewin, K-D Zastrow, S J Davies, N C Hawkes et al. **Plasma-edge gradients in L-mode and ELM-free H-mode JET plasmas.** *Plasma Physics and Controlled Fusion*, 40(3):347, 1998.
- [86] K H Burrell, M E Austin, D P Brennan, J C DeBoo, E J Doyle et al. **Quiescent H-mode plasmas in the DIII-D tokamak.** *Plasma Physics and Controlled Fusion*, 44(5A):A253, 2002.
- [87] R.J. Groebner, D.R. Baker, K.H. Burrell, T.N. Carlstrom, J.R. Ferron et al. **Progress in quantifying the edge physics of the H-mode regime in DIII-D.** *Nuclear Fusion*, 41(12):1789, 2001.
- [88] W Suttrop, M Maraschek, G D Conway, H-U Fahrbach, G Haas et al. **ELM-free stationary H-mode plasmas in the ASDEX Upgrade tokamak.** *Plasma Physics and Controlled Fusion*, 45(8):1399, 2003.
- [89] Y Sakamoto, H Shirai, T Fujita, S Ide, T Takizuka et al. **Impact of toroidal rotation on ELM behaviour in the H-mode on JT-60U.** *Plasma Physics and Controlled Fusion*, 46(5A):A299, 2004.
- [90] W. Suttrop, V. Hynönen, T. Kurki-Suonio, P.T. Lang, M. Maraschek et al. **Studies of the 'quiescent H-mode' regime in ASDEX Upgrade and JET.** *Nuclear Fusion*, 45(7):721, 2005.
- [91] K. H. Burrell, M. E. Austin, D. P. Brennan, J. C. DeBoo, E. J. Doyle et al. **Quiescent double barrier high-confinement mode plasmas in the DIII-D tokamak.** *Physics of Plasmas*, 8(5):2153–2162, 2001.
- [92] E J Doyle, L R Baylor, K H Burrell, T A Casper, J C DeBoo et al. **The quiescent double barrier regime in the DIII-D tokamak.** *Plasma Physics and Controlled Fusion*, 43(12A):A95, 2001.
- [93] C M Greenfield, K H Burrell, E J Doyle, R J Groebner, W P West et al. **The quiescent double barrier regime in DIII-D.** *Plasma Physics and Controlled Fusion*, 44(5A):A123, 2002.
- [94] F Troyon, R Gruber, H Saurenmann, S Semenzato and S Succi. **MHD-limits to plasma confinement.** *Plasma Physics and Controlled Fusion*, 26(1A):209, 1984.
- [95] N Oyama, P Gohil, L D Horton, A E Hubbard, J W Hughes et al. **Pedestal conditions for small ELM regimes in tokamaks.** *Plasma Physics and Controlled Fusion*, 48(5A):A171, 2006.

- [96] P.B. Snyder, K.H. Burrell, H.R. Wilson, M.S. Chu, M.E. Fenstermacher et al. **Stability and dynamics of the edge pedestal in the low collisionality regime: physics mechanisms for steady-state ELM-free operation.** *Nuclear Fusion*, 47(8):961, 2007.
- [97] T H Osborne, P B Snyder, K H Burrell, T E Evans, M E Fenstermacher et al. **Edge stability of stationary ELM-suppressed regimes on DIII-D.** *Journal of Physics: Conference Series*, 123(1):012014, 2008.
- [98] K. H. Burrell, T. H. Osborne, P. B. Snyder, W. P. West, M. E. Fenstermacher et al. **Quiescent H-mode plasmas with strong edge rotation in the cocurrent direction.** *Physical Review Letters*, 102:155003, Apr 2009.
- [99] A.M. Garofalo, W.M. Solomon, J.-K. Park, K.H. Burrell, J.C. DeBoo et al. **Advances towards QH-mode viability for ELM-stable operation in ITER.** *Nuclear Fusion*, 51(8):083018, 2011.
- [100] K.H. Burrell, A.M. Garofalo, W.M. Solomon, M.E. Fenstermacher, D.M. Orlov et al. **Quiescent H-mode operation using torque from non-axisymmetric, non-resonant magnetic fields.** *Nuclear Fusion*, 53(7):073038, 2013.
- [101] M. Greenwald, R. Boivin, P. Bonoli, R. Budny, C. Fiore et al. **Characterization of enhanced D _{α} high-confinement modes in Alcator C-Mod.** *Physics of Plasmas*, 6(5):1943–1949, 1999.
- [102] A. E. Hubbard, R. L. Boivin, R. S. Granetz, M. Greenwald, J. W. Hughes et al. **Pedestal profiles and fluctuations in C-Mod enhanced D-alpha H-modes.** *Physics of Plasmas*, 8(5):2033–2040, 2001.
- [103] Jerry W. Hughes. *Edge Transport Barrier Studies On the Alcator C-Mod Tokamak*. PhD thesis, Massachusetts Institute of Technology, 2005.
- [104] A. E. Hubbard, R. L. Boivin, R. S. Granetz, M. Greenwald, I. H. Hutchinson et al. **Measurements of the high confinement mode pedestal region on Alcator C-Mod.** *Physics of Plasmas*, 5(5):1744–1751, 1998.
- [105] J. W. Hughes, D. A. Mossessian, A. E. Hubbard, B. LaBombard and E. S. Marmar. **Observations and empirical scalings of the high-confinement mode pedestal on Alcator C-Mod.** *Physics of Plasmas*, 9(7):3019–3030, 2002.
- [106] J. W. Hughes, B. LaBombard, D. A. Mossessian, A. E. Hubbard, J. Terry et al. **Advances in measurement and modeling of the high-confinement-mode pedestal on the Alcator C-Mod tokamak.** *Physics of Plasmas*, 13(5):056103, 2006.

- [107] D A Mossessian, P B Snyder, M Greenwald, J W Hughes, Y Lin et al. **H-mode pedestal characteristics and MHD stability of the edge plasma in Alcator C-Mod.** *Plasma Physics and Controlled Fusion*, 44(4):423, 2002.
- [108] J. W. Hughes, A. E. Hubbard, D. A. Mossessian, B. LaBombard, T. M. Biewer et al. **H-mode pedestal and L-H transition studies on Alcator C-Mod.** *Fusion Science and Technology*, 51(3):317–341, 2007.
- [109] A. E. Hubbard, J. W. Hughes, I. O. Bespamyatnov, T. Biewer, I. Cziegler et al. **H-mode pedestal and threshold studies over an expanded operating space on Alcator C-Mod.** *Physics of Plasmas*, 14(5):056109, 2007.
- [110] J.W. Hughes, B. LaBombard, J. Terry, A. Hubbard and B. Lipschultz. **Edge profile stiffness and insensitivity of the density pedestal to neutral fuelling in Alcator C-Mod edge transport barriers.** *Nuclear Fusion*, 47(8):1057, 2007.
- [111] J.L. Terry, N.P. Basse, I. Cziegler, M. Greenwald, O. Grulke et al. **Transport phenomena in the edge of Alcator C-Mod plasmas.** *Nuclear Fusion*, 45(11):1321, 2005.
- [112] D. A. Mossessian, P. Snyder, A. Hubbard, J. W. Hughes, M. Greenwald et al. **High-confinement-mode edge stability of Alcator C-mod plasmas.** *Physics of Plasmas*, 10(5):1720–1726, 2003.
- [113] A. Mazurenko, M. Porkolab, D. Mossessian, J. A. Snipes, X. Q. Xu et al. **Experimental and theoretical study of quasicoherent fluctuations in enhanced D_α plasmas in the Alcator C-Mod tokamak.** *Physical Review Letters*, 89:225004, Nov 2002.
- [114] J.W. Hughes, A. Loarte, M.L. Reinke, J.L. Terry, D. Brunner et al. **Power requirements for superior H-mode confinement on Alcator C-Mod: experiments in support of ITER.** *Nuclear Fusion*, 51(8):083007, 2011.
- [115] B. LaBombard, J.E. Rice, A.E. Hubbard, J.W. Hughes, M. Greenwald et al. **Transport-driven scrape-off-layer flows and the boundary conditions imposed at the magnetic separatrix in a tokamak plasma.** *Nuclear Fusion*, 44(10):1047, 2004.
- [116] C. Fenzi, G. R. McKee, R. J. Fonck, K. H. Burrell, T. N. Carlstrom et al. **Effect of ion ∇B drift direction on density fluctuation poloidal flow and flow shear.** *Physics of Plasmas*, 12(6):062307, 2005.

- [117] B. LaBombard, J. W. Hughes, N. Smick, A. Graf, K. Marr et al. **Critical gradients and plasma flows in the edge plasma of Alcator C-Mod.** *Physics of Plasmas*, 15(5):056106, 2008.
- [118] T N Carlstrom, K H Burrell and R J Groebner. **Comparison of a ∇B drift effect model with measured H-mode power thresholds.** *Plasma Physics and Controlled Fusion*, 40(5):669, 1998.
- [119] R J Groebner and T N Carlstrom. **Critical edge parameters for H-mode transition in DIII-D.** *Plasma Physics and Controlled Fusion*, 40(5):673, 1998.
- [120] F Ryter, W Suttrop, B Brüsehaber, M Kaufmann, V Mertens et al. **H-mode power threshold and transition in ASDEX Upgrade.** *Plasma Physics and Controlled Fusion*, 40(5):725, 1998.
- [121] D.G. Whyte, A.E. Hubbard, J.W. Hughes, B. Lipschultz, J.E. Rice et al. **I-mode: an H-mode energy confinement regime with L-mode particle transport in Alcator C-Mod.** *Nuclear Fusion*, 50(10):105005, 2010.
- [122] A. E. Hubbard, D. G. Whyte, R. M. Churchill, I. Cziegler, A. Dominguez et al. **Edge energy transport barrier and turbulence in the I-mode regime on Alcator C-Mod.** *Physics of Plasmas*, 18(5):056115, 2011.
- [123] A.E. Hubbard, D.G. Whyte, R.M. Churchill, A. Dominguez, J.W. Hughes et al. **Threshold conditions for transitions to I-mode and H-mode with unfavourable ion grad B drift direction.** *Nuclear Fusion*, 52(11):114009, 2012.
- [124] Arturo Dominguez. *Study of Density Fluctuations and Particle Transport at the Edge of I-Mode Plasmas.* PhD thesis, Massachusetts Institute of Technology, 2012.
- [125] A. Hubbard, E. Marmar, S. Baek, I. Cziegler, A. Dominguez et al. **Progress in performance and understanding of steady ELM-free I-modes on Alcator C-Mod.** In *24th IAEA Fusion Energy Conference*, number EX/1-3, 2012.
- [126] N. T. Howard, M. Greenwald and J. E. Rice. **Characterization of impurity confinement on Alcator C-Mod using a multi-pulse laser blow-off system.** *Review of Scientific Instruments*, 82(3):–, 2011.
- [127] Rachael M. McDermott. *Edge Radial Electric Field Studies via Charge Exchange Recombination Spectroscopy on the Alcator C-Mod Tokamak.* PhD thesis, Massachusetts Institute of Technology, 2009.

- [128] C Theiler, R M Churchill, B Lipschultz, M Landreman, D R Ernst et al. Inboard and outboard radial electric field wells in the H- and I-mode pedestal of Alcator C-Mod and poloidal variations of impurity temperature. accepted to *Nuclear Fusion*, 2014.
- [129] J. E. Rice, J. W. Hughes, P. H. Diamond, Y. Kosuga, Y. A. Podpaly et al. Edge temperature gradient as intrinsic rotation drive in Alcator C-Mod tokamak plasmas. *Physical Review Letters*, 106:215001, May 2011.
- [130] I. Cziegler, P. H. Diamond, N. Fedorczak, P. Manz, G. R. Tynan et al. Fluctuating zonal flows in the I-mode regime in Alcator C-Mod. *Physics of Plasmas*, 20(5):–, 2013.
- [131] A.E. White, P. Phillips, D.G. Whyte, A.E. Hubbard, C. Sung et al. Electron temperature fluctuations associated with the weakly coherent mode in the edge of I-mode plasmas. *Nuclear Fusion*, 51(11):113005, 2011.
- [132] Istvan Cziegler. *Turbulence and Transport Phenomena in Edge and Scrape-Off Layer Plasmas*. PhD thesis, Massachusetts Institute of Technology, 2011.
- [133] Niels Winsor, John L. Johnson and John M. Dawson. Geodesic acoustic waves in hydromagnetic systems. *Physics of Fluids*, 11(11):2448–2450, 1968.
- [134] P. Manz, G. S. Xu, B. N. Wan, H. Q. Wang, H. Y. Guo et al. Zonal flow triggers the L-H transition in the Experimental Advanced Superconducting Tokamak. *Physics of Plasmas*, 19(7):–, 2012.
- [135] B. Coppi and T. Zhou. Plasma confinement regimes and collective modes characterizing them. *Physics of Plasmas*, 19(10):102509, 2012.
- [136] B. Coppi and T. Zhou. Interpretation of the I-regime and transport associated with relevant heavy particle modes. *Physics of Plasmas*, 19(1):012302, 2012.

3

PEDESTAL MODELING AND THEORY

While a number of high-performance regimes (described in chapter 2) have been established and are actively explored for tokamak operation, much of the physics governing these regimes is still unknown. In particular, the physics underlying the structure of the pedestal is an area of active research, due in large part to the inherent difficulty in experimentally diagnosing the pedestal plasma as it varies over short scale lengths, and in the wide variability of H-mode behaviors observed in tokamak experiments. Nevertheless confidence in the prediction of pedestal height and stability for ITER- and reactor-scale devices is essential: central temperature and pressure in the plasma are strongly sensitive to pedestal conditions due to core profile stiffness [1, 2], thus fusion power density is controlled by the pressure pedestal structure. Moreover, operation with large, uncontrolled Edge-Localized Modes (ELMs – see section 2.1) can drive transient heat loads exceeding wall material tolerances on ITER-scale devices [3, 4] – an understanding of pedestal stability against ELMs is necessary for ITER operation and beyond. This chapter provides a review of the efforts to date in theory and modeling of the pedestal, including the theoretical models considered in this thesis. •

3.1 EARLY MODELS

Initial efforts in understanding the pedestal took a variety of approaches, including models built from fairly simple *ansätze* for the physics determining the pedestal structure. Several of these approaches are detailed here. Overviews of these models may also be found in [5, 6, §2].

needs better title...

3.1.1 Empirical Observations

Absent a firm understanding of the physics underlying the pedestal structure, experimental efforts have sought to characterize the pedestal in terms of simple scalings with engineering parameters. The pedestal width, in particular, presented significant difficulty in this regard, as it tends to be quite robust, varying only over a narrow range on a given machine [7] – observations on JET [8] and Alcator C-Mod [9, 10] found minimal variation of the pedestal width with plasma current or magnetic field, although a somewhat broader pedestal was observed at low current and with strong shaping on C-Mod [10, 11]. Accordingly, the measured gradients in density, temperature, and pressure

in the steepest region of the pedestal trend linearly with the corresponding value at the pedestal top [8, 10].

Multivariate dependences on engineering parameters may be explored with a reasonably general approach via power-law scalings, fitting pedestal data to scalings with no assumed underlying physics. Suttrop *et al.* [12] found for ASDEX Upgrade pedestals

$$\nabla p \sim B_T^{-0.31} P_{\text{tot}}^{0.16} \langle n_e \rangle^{-0.1} I_p^{2.1} \quad (3.1)$$

A similar approach on C-Mod using an extensive dataset of EDA H-modes [9] found

$$\begin{aligned} n_{e,\text{ped}} &\sim I_p^{0.95} n_{e,L}^{0.39} B_T^{-0.46} \\ T_{e,\text{ped}} &\sim I_p^{0.95} n_{e,L}^{-0.78} B_T^{0.80} P_{\text{net}}^{0.64} \\ p_{e,\text{ped}} &\sim I_p^{1.98} n_{e,L}^{-0.56} P_{\text{net}}^{0.48} \end{aligned} \quad (3.2)$$

(here $n_{e,L}$ is the line-averaged L-mode target density, as pedestal density is not readily controllable in EDA H-mode). However, later studies asserted that the magnetic-field dependence was overstated in the above [13]. While these empirical models perform reasonably well on their respective experimental data, a physics-based understanding of the pedestal structure is necessary to explain results on multiple machines and to confidently extrapolate to ITER-scale operation.

*Hughes 2006 PoP
says field
dependence
overstated, but there
is a field dependence
in Hubbard 2006
PoP*

3.1.2 Neutral Penetration & the Density Pedestal

Given the proximity of the plasma pedestal to neutral gas from fueling apparatus and wall outgassing in the edge, it is logical that the density profile should depend strongly on interaction with and ionization of neutral particles in the pedestal. Based on a relatively simple particle transport model, the pedestal width is expected to scale with the characteristic neutral penetration length before ionization [6, 14]:

$$\lambda_{\text{neutral}} = \frac{v_n}{n_e \langle \sigma v \rangle_{\text{ion}}} \quad (3.3)$$

where v_n is the velocity of neutrals entering the pedestal (set by the neutral thermal temperature in the edge) and $\langle \sigma v \rangle_{\text{ion}}$ is the velocity-averaged ionization cross-section. Given that v_n is set, in the simplest approximation, by the neutral thermal distribution (although a population of the charge-exchanged neutrals retain the ion velocity, such that the neutral temperature does exhibit a trend with ion pedestal temperature in more complex models) and that $\langle \sigma v \rangle_{\text{ion}}$ is roughly constant over the temperatures of interest in the edge [6], therefore

we expect the simple relation $\Delta_n \sim 1/n_{e,ped}$. More complex models for the neutral penetration typically reproduce the dependence on $\lambda_{neutral}$.

However, experimental observations of the density pedestal conflict with these relatively simple predictions. Observations in similarity experiments between DIII-D, JET, and ASDEX Upgrade [15] and between DIII-D and C-Mod [16] were inconsistent with the simple model: although DIII-D data were consistent with the trends found in the model, data from JET were not, and moreover the model predicted an inconsistent scaling between the two machines for pedestal density and width. Likewise, predictions based on pedestal widths set by neutral penetration performed poorly as a predictor for pedestal height in a multi-machine scaling from AUG, DIII-D, JT-60U, and JET [17]. EDA H-modes on Alcator C-Mod show near-complete insensitivity of the density pedestal to neutral interactions – the density pedestal instead saturates to a level dictated by plasma transport (predicted best by $n_{e,ped} \sim I_p$), with fueling via edge gas puffing having little effect on the density pedestal [11, 13].

In addition to significant sensitivity to machine and discharge conditions and wall materials [15], density pedestal behavior appears to be strongly sensitive to magnetic configuration – experiments on MAST [7] found that, while the density pedestal width was poloidally constant in single-null discharges, the density pedestal is measurably broader on the outboard, low-field side in double-null discharges. These results indicate that plasma-neutral interactions in the density pedestal are quite complex, and dependent on poloidal transport behaviors and fueling asymmetries [7]. This remains an important area of research, as ITER is expected to have an edge that is highly opaque to neutrals, complicating the density pedestal structure and fueling scenarios for high-density plasmas [7, 11].

3.1.3 Ion-Orbit Loss & Gyroradius Models

Due to the importance in the edge E_r well in pedestal formation, modeling efforts naturally turned to putative sources for the electric field to explain the pedestal. One suggested source was ion orbit loss across the last closed flux surface, in which the gyro-motion of ions near the edge intersect the SOL or the plasma-facing material surfaces – the charge imbalance induced by this particle “leak” results in a radial electric field [18]. Assuming ion orbit losses drive the E_r well, the $\vec{E} \times \vec{B}$ shear layer width ought to be governed by the banana orbit width, which scales as the poloidal gyroradius $\rho_{i,pol} \sim \sqrt{T_i}/B_p$.

Accounting for the squeezing effect of the radial electric field on the banana orbit width, Shaing [19] gives for the well width

$$\Delta_{\vec{E} \times \vec{B}} \propto \sqrt{\epsilon} \frac{\rho_{i,pol}}{\sqrt{S}}$$

$$S = \left| 1 - \frac{1}{B_p \omega_{ci,p}} \frac{dE_r}{dr} \right| \quad (3.4)$$

where S is the squeezing factor and $\omega_{ci,p}$ is the ion cyclotron frequency evaluated with the poloidal field. The model is further refined by Itoh & Itoh [20] to include the broadening effects of viscosity shear. The predicted trend is observed in ELM-free H-modes on JT-60U [21], with $\Delta \approx 3.3\sqrt{\epsilon}\rho_{i,pol}$; however, as the squeezing factor S is estimated to be near-unity, the pedestal width is broader by a factor of ~ 3.3 than the $\sim \sqrt{\epsilon}\rho_{i,pol}$ banana width. ELMy H-modes on JT-60U exhibit a similar scaling at weak shaping, with a broader pedestal and additional safety factor dependence $\Delta \approx 5\rho_{i,pol}q_{95}^{-0.3}$ at higher triangularity [22].

However, other predictions and experimental observations contradict these results. Depending on the calculation method of growth rate suppression by $\vec{E} \times \vec{B}$ sheared flow, the pedestal width may scale with the gyroradius anywhere from $\Delta \sim (\rho^*)^{1/2}$ to $\Delta \sim \rho^*$, where ρ^* indicates the gyroradius normalized to the plasma minor radius [15, 17]. Alternately, stabilization of drift-ballooning modes leads to a predicted dependence of $\Delta \sim \rho_{i,pol}^{2/3}$ [23]; similarly, diamagnetic stabilization in the pedestal leads to the prediction of $\Delta \sim I_p^2 \rho_{i,pol}^{2/3}$ [24]. Observations on DIII-D [25] found a dependence of $\Delta/R \sim (\rho_{i,pol}/R)^{0.67}$, while observations on ASDEX Upgrade [15, 26] found no gyroradius dependence for the pedestal width.

Distinguishing between these scalings is difficult given the diagnostic complications inherent in pedestal measurements, and the narrow range over which ρ_i or the pedestal and E_r well width vary on a given machine [7, 27]. Moreover, alternate models propose a scaling with poloidal beta at the pedestal top, rather than poloidal gyroradius, with trends of width of $\Delta \sim \beta_{p,ped}^{0.4}$ to $\sim \beta_{p,ped}^{0.5}$ observed on DIII-D [25, 28], JET [7], JT=60U [29], and ASDEX Upgrade [15]. Due to the strong covariance between $\rho_{i,pol} \sim \sqrt{mT}/I_p$ and $\sqrt{\beta_{p,ped}} \sim \sqrt{nT}/I_p$ these trends are quite difficult to separate. However, dedicated experiments to separate the two, either via pumping to vary density and temperature at fixed pressure, exploiting the density dependence in $\beta_{p,ped}$ [25], or via isotope variation targeting the mass dependence in $\rho_{i,pol}$ [29, 30], found the $\beta_{p,ped}$ scaling to be the better predictor, with a weaker secondary gyroradius dependence $\Delta \sim \rho_{i,pol}^{0.2} \beta_{p,ped}^{0.5}$ [7, 29]. The physics underlying the $\Delta \sim \sqrt{\beta_{p,ped}}$ scaling will be discussed in detail in section 3.3. •

3.2 MHD STABILITY: PEELING-BALLOONING MODES

Due to the extremely rapid onset of explosive ELM instabilities, ideal MHD modes were identified early on as candidates for the ELM trigger [31, 32, 33]. In this section, we detail the development of models for the pedestal structure based on the idea that ELM instabilities represent an ultimate limit on the pedestal.

The stability of a plasma may be assessed via a linear perturbation to the customary MHD equations. We consider a first-order perturbation $\vec{\xi}$ to a plasma fluid element – typically the perturbation is considered general in spatial variables, and is taken to be a Fourier harmonic in time, $\vec{\xi} = \vec{\xi}(\psi, \chi, \zeta) \exp(i\omega t)$ where ψ is the flux coordinate, χ is a poloidal angle, and ζ is a toroidal angle. Substituting into the first-order perturbation of the MHD equations results in the simple relation (see [34, §8] for derivation)

$$\rho \frac{d^2 \vec{\xi}}{dt^2} = -\omega^2 \rho \vec{\xi} = \vec{F}(\vec{\xi}) \quad (3.5)$$

where ω is the mode frequency, ρ is the mass density, and \vec{F} is a forcing operator given by

$$\begin{aligned} \vec{F}(\vec{\xi}) &= \frac{1}{\mu_0} (\nabla \times \vec{B}) \times \vec{Q} + \frac{1}{\mu_0} (\nabla \times \vec{Q}) \times \vec{B} + \nabla (\vec{\xi} \cdot \nabla p + \gamma p \nabla \cdot \vec{\xi}) \\ \vec{Q} &= \nabla \times (\vec{\xi} \times \vec{B}) \end{aligned} \quad (3.6)$$

with \vec{Q} for the perturbed magnetic field and γ for the specific heat ratio of the plasma. The usual treatment of this operator leverages the fact that \vec{F} is self-adjoint (i.e., it is its own complex conjugate) – this permits by integration over the plasma volume P in a variational formulation

$$\begin{aligned} \omega^2 &= \frac{\delta W(\vec{\xi}^*, \vec{\xi})}{K(\vec{\xi}^*, \vec{\xi})} \\ \delta W &= -\frac{1}{2} \int_P \vec{\xi}^* \cdot \vec{F}(\vec{\xi}) d^3 \vec{r} \\ K &= \frac{1}{2} \int_P \rho |\vec{\xi}|^2 d^3 \vec{r} \end{aligned} \quad (3.7)$$

This formulation permits the use of the *energy principle*: if the potential energy δW is negative for any displacement (i.e., the perturbation drives the plasma to a more energetically-favorable state) then the mode corresponding to that displacement is unstable, captured by

detail these in intro?

the fact that $\delta W < 0$ requires an imaginary frequency ω (and thus will have an exponentially growing mode).

This permits a conceptually straightforward means to assess mode stability. However, the formulation for δW is highly involved (see [34, §8.8]):

$$\begin{aligned}\delta W &= \delta W_F + \delta W_S + \delta W_V \\ \delta W_F &= \frac{1}{2} \int_P d^3\vec{r} \left[\frac{|\vec{Q}|^2}{\mu_0} + \frac{B^2}{\mu_0} \left| \nabla \cdot \vec{\xi}_\perp + 2\vec{\xi}_\perp \cdot \vec{\kappa} \right|^2 + \gamma p \left| \nabla \cdot \vec{\xi} \right|^2 \right. \\ &\quad \left. - 2 \left(\vec{\xi}_\perp \cdot \nabla p \right) \left(\vec{\kappa} \cdot \vec{\xi}_\perp^* \right) - j_\parallel \left(\vec{\xi}_\perp^* \times \vec{b} \right) \cdot \vec{Q}_\perp \right] \quad (3.8) \\ \delta W_S &= \frac{1}{2} \int_S dS \left| \hat{n} \cdot \vec{\xi}_\perp \right|^2 \hat{n} \cdot \left[\nabla \left(p + \frac{B^2}{2\mu_0} \right) \right] \\ \delta W_V &= \frac{1}{2} \int_V d^3\vec{r} \frac{|B_1|^2}{\mu_0}\end{aligned}$$

for the fluid, surface, and vacuum energy contributions integrated over the plasma volume P , plasma surface S , and vacuum volume V respectively (in the above $\vec{\kappa}$ is the vectorized curvature, \hat{n} is the normal vector to the plasma surface, \vec{b} is the background magnetic field unit vector, and B_1 is the perturbed magnetic field in the vacuum region). The complexity of the stability problem necessitates both a firm theoretical understanding to simplify eq. (3.8) to a tractable form, and numerical approaches to efficiently calculate the stability in experimental plasmas.

3.2.1 Pressure-Driven Modes

Examining the fluid energy formulation δW_F in eq. (3.8), we see two potential sources of instability (that is, negative terms in δW) – these identify the pressure gradient ∇p and the parallel current density j_\parallel as potential sources of free energy to drive unstable modes. We first consider the pressure-gradient-driven modes, dubbed “ballooning modes” for their characteristic perturbation, in which the plasma tends to “bulge” outwards due to the pressure gradient. The mode tends to vary along a field line (with long parallel wavelength, although the most unstable modes have short perpendicular wavelength) such that it is concentrated in regions with the least favorable magnetic curvature, such that the increased stabilizing effect from magnetic field line bending cannot compensate for the destabilizing pressure gradient [34]. These modes were identified early on as a possible ELM trigger: early experiments in ELMy H-mode observed a limit on the pressure gradient preceding the ELM crash [35, 36],

with the value of ∇p at the limit increasing with plasma current and shaping, consistent with ballooning theory (detailed below) [26].

Early studies in ballooning modes by Connor, Hastie, and Taylor [37, 38] focused on the comparatively simple high- n limit. By minimizing δW in terms of displacement parallel to the magnetic field and lying within the flux surface (straightforward due to the slow parallel variation of the ballooning mode), the potential energy may be expressed solely in terms of the displacement normal to the flux surface, ξ_ψ (here expressed for compactness as $X = RB_p \xi_\psi$) in an expansion in powers of $n^{-1/2}$ correct to $O(1/n)$ by

$$\delta W = \pi \iint d\Psi dx \left\{ \frac{JB^2}{R^2 B_p^2} |k_{\parallel} X|^2 + \frac{R^2 B_p^2}{JB^2} \left| \frac{1}{n} \frac{\partial}{\partial \Psi} (JB k_{\parallel} X) \right|^2 - \frac{2J}{B^2} \frac{dp}{d\Psi} \left[|X|^2 \frac{\partial}{\partial \Psi} \left(p + \frac{B^2}{2} \right) - \frac{iF}{JB^2} \frac{\partial}{\partial X} \left(\frac{B^2}{2} \right) \frac{X^*}{n} \frac{\partial X}{\partial \Psi} \right] \right\} \quad (3.9)$$

where J is the Jacobian, satisfying $Jd\chi = dl/B_p$ for a poloidal arc segment dl , $F = RB_T$ encodes the toroidal field (as in the Grad-Shafranov equation, eq. (1.22)) We define the parallel gradient operator k_{\parallel} such that

$$ik_{\parallel} = \frac{1}{JB} \left(\frac{\partial}{\partial \chi} + i n \nu \right) \quad (3.10)$$

and $\nu = JB_T/R$ encodes the rotational transform; this requires for rational surfaces that $n \oint \nu d\chi = 2\pi m$ for integer m, n . In eq. (3.9), the first two terms encode the stabilizing effects of magnetic field line bending; the third defines the destabilizing effect of the pressure gradient, and the fourth contains the effect of curvature, which is stabilizing on the inboard side and destabilizing on the outboard side.

This is solved using the “ballooning transform” formalized in [37], which encodes the periodicity of the magnetic shear by a transform from the periodic poloidal angle χ to an infinite, non-periodic domain y – the rapid variation in X is then contained in an exponential phase factor $\sim \exp(-in \int \nu dy)$, with the mode amplitude in a scale factor $f(\psi, y)$ that is comparatively insensitive to n . The Euler-Lagrange equation minimizing δW in eq. (3.9) is satisfied by an equation of the form

$$\begin{aligned} (L + \Omega^2 M) f &= 0 \\ L &= L_0 + \frac{1}{n^{1/2}} L_1 + \frac{1}{n} L_2 + \dots \\ M &= M_0 + \frac{1}{n^{1/2}} M_1 + \frac{1}{n} M_2 + \dots \end{aligned} \quad (3.11)$$

where Ω^2 is the eigenvalue of the system and L, M are operators based on the plasma equilibrium and normalized pressure gradient α_{MHD} (see eqs. (2.8) and (2.9)), with L acting as a differential operator in y . As with the expansion of the energy-principle formulation, these operators are expressed as an expansion in $n^{-1/2}$. To lowest order (appropriate in the $n \rightarrow \infty$ limit) the system reduces to an eigenvalue problem for the local eigenmode characterized by ω^2 [38], $(L_0 + \omega^2 M_0)f = 0$ – in this case, the modes are perfectly localized on their corresponding rational surfaces and decoupled from modes on other surfaces, yielding an exceedingly simple calculation, given by

$$\begin{aligned} L_0 f &= \frac{\partial}{\partial y} \left\{ \frac{1}{JR^2B_p^2} \left[1 + \left(\frac{R^2B_p^2}{B} \int^y \frac{dv}{d\psi} dy \right)^2 \right] \frac{\partial f}{\partial y} \right\} \\ &\quad + f \left\{ \frac{2J}{B^2} \frac{dp}{d\psi} \frac{\partial}{\partial \psi} \left(p + \frac{B^2}{2} \right) - \frac{F}{B^4} \frac{dp}{d\psi} \left(\int^y \frac{dv}{d\psi} dy \right) \frac{\partial B^2}{\partial y} \right\} \\ M_0 f &= \frac{J}{R^2B_p^2} \left[1 + \left(\frac{R^2B_p^2}{B} \int^y \frac{dv}{d\psi} \right)^2 \right] f \end{aligned} \tag{3.12}$$

This form is used by the BALOO code [38, 39, 40], which efficiently calculates the infinite- n ballooning stability limit. Intuitively, the mode is driven by pressure gradient and stabilized by magnetic shear and favorable curvature, such that the mode is triggered above a critical gradient (couched in terms of α_{MHD}), with the attainable α_c increasing with increased magnetic shear.

While the high- n ballooning formalism described above has been successful for the treatment of core ballooning modes, it is insufficient to accurately model modes in the pedestal. Experimentally, the measured pressure gradient is seen to exceed the limit predicted by infinite- n ballooning calculations [25, 28], indicating that stabilizing effects due to edge current density (primarily from the bootstrap effect) and diamagnetism come into play. Moreover, the assumptions used in the expansion described above break down in the edge. In the conventional theory [37, 38] described above (resulting in eqs. (3.11) and (3.12)), the mode is treated in an expansion in orders of $n^{-1/2}$, in which the lowest order describes a local eigenvalue ω^2 for a given flux surface, the first order $O(n^{-1/2})$ contains the mode phase, and the second order $O(n^{-1})$ describes the Gaussian envelope spanning $\sim n^{1/2}$ rational flux surfaces containing the mode harmonics, as well as the correction to the “true” mode eigenvalue: $\Omega^2 = \omega^2 + O(n^{-1})$ [41, 42]. However, the assumptions inherent in the expansion in $n^{-1/2}$ break down in the edge due to the possibility of a steep pressure gradient out to the separatrix, and the proximity of the mode center to the plasma edge (forbidding Gaussian wave envelopes). A modifica-

tion to the theory [41, 42] instead expands the energy-principle result in orders of $n^{-1/3}$, with the lowest order again determining a local pseudo-eigenvalue ω^2 and the first order $O(n^{-1/3})$ defining the phase, but with the second-order expansion instead defining an Airy function envelope spanning $\sim n^{1/3}$ rational surfaces, consistent with the edge behavior. This also provides a stabilizing $O(n^{-2/3})$ correction to the $n \rightarrow \infty$ theory [41]. There also remains the question of the treatment of current-driven modes, both the “peeling” mode driven by the parallel current density and the “kink” mode driven by the current gradient [43], and their effect on the edge stability.

3.2.2 Current-Driven Modes

In addition to the ballooning instability, edge kink or peeling MHD modes were proposed early on in H-mode experiments as a driver for the ELM instability [32, 44]. Whereas the ballooning modes are primarily driven by the pressure gradient, these modes are primarily driven unstable by the electric current (note the destabilizing term in δW_F in eq. (3.8)) in the case of the peeling mode, or by the current gradient for the kink mode [43]. These fundamentally similar instabilities – the peeling mode is strongly localized in the edge, and is driven by the rapid change in parallel current across the separatrix [41, 43]. The kink mode may be driven in the core or the edge, and tends to twist the plasma into a helix due to $\vec{j} \times \vec{B}$ forces; the peeling mode, on the other hand, is unique to the plasma edge, and tends to peel the plasma edge similar to a tearing mode [42].

clarify

An extension of the analysis resulting in eq. (3.9) [38] included additional terms in δW accounting for the effects of current and current gradient, of the form

$$\pi \iint d\Psi d\chi \left\{ -\frac{X^*}{n} JBk_{\parallel} \left(X \frac{d\sigma}{d\Psi} \right) + \frac{1}{n} \left[P^* JBk_{\parallel} Q + PJBk_{\parallel}^* Q^* \right] \right\} \quad (3.13)$$

where

$$\begin{aligned} P &= \sigma X + \frac{B_p^2}{\nu B^2} \frac{F}{n} \frac{\partial}{\partial \Psi} (JBk_{\parallel}) \\ Q &= \frac{X}{B^2} \frac{dp}{d\Psi} + \frac{F^2}{\nu R^2 B^2} \frac{1}{n} \frac{\partial}{\partial \Psi} (JBk_{\parallel} X) \\ \sigma &= -\frac{F}{B^2} \frac{dp}{d\Psi} - \frac{dF}{d\Psi} = \frac{j_{\parallel}}{B} \end{aligned} \quad (3.14)$$

for parallel current j_{\parallel} . An analysis in the high- n limit following similar methodology to that used in ballooning modes [41] focused on the edge “peeling” modes driven by the parallel current. These modes are resonant in the vacuum on rational surfaces close to the plasma

boundary – at high n , these modes are highly localized on this surface, so through an expansion about this surface Connor *et al.* [41] found for the stability criterion

$$\sqrt{1 - 4D_M} > 1 + \frac{2}{2\pi(dq/d\psi)} \oint \frac{j_{||}B}{R^2B_p^3} dl \quad (3.15)$$

analogous to the Mercier Criterion [45] for interchange-mode stability ($1 - 4D_M > 0$), where D_M is the Mercier parameter given by

$$\begin{aligned} D_M &= -\frac{C_1}{C_2} \\ C_1 &= \frac{p'}{2\pi} \oint \frac{\partial J}{\partial \psi} d\chi - \frac{(p')^2}{2\pi} \oint \frac{J}{B_p^2} d\chi \\ &\quad + Fp' \oint \frac{J}{R^2 B_p^2} d\chi \left[\oint \frac{JB^2}{R^2 B_p^2} d\chi \right]^{-1} \left[\frac{Fp'}{2\pi} \oint \frac{J}{R^2 B_p^2} d\chi - q' \right] \\ C_2 &= 2\pi (q')^2 \left[\oint \frac{JB^2}{R^2 B_p^2} d\chi \right]^{-1} \end{aligned} \quad (3.16)$$

It is clear from eq. (3.15) that the parallel current (on the right hand side) is destabilizing; increased pressure gradient and magnetic shear causes D_M to become more negative (deepening the “magnetic well”), stabilizing the peeling mode [46, 47]. This causes the peeling mode to destabilize below a critical value of the magnetic shear, with this value decreasing with increased pressure gradient.

Figure 3.1: Schematic in $s - \alpha_{MHD}$ space of the infinite- n peeling and ballooning instabilities. The ballooning instability (see section 3.2.1) is destabilized by increasing pressure gradient and stabilized by magnetic shear. A second-stable region for the ballooning mode is found at very high pressure gradient, which can be accessed by increasing the pressure gradient at low magnetic shear. The peeling instability is driven by large edge current density (equivalently, low magnetic shear), and is stabilized by increased pressure gradient.



The shared influence of pressure gradient and magnetic shear for ballooning and peeling modes is conducive to a unified picture of the stability boundaries for these modes, as shown in fig. 3.1. Ballooning

instabilities are driven by pressure gradient and stabilized by magnetic shear, while peeling modes are stabilized by pressure gradient and driven by edge current density, which is tied to the magnetic shear by the relation $s = 2(1 - j_{\parallel}/\langle j \rangle)$ where s is the shear and $\langle j \rangle$ is the volume-averaged pressure [37] (thus magnetic shear is also stabilizing to peeling modes). Notably, the ballooning formalism allows for a second stable region at high pressure gradient, evident in fig. 3.1, that is accessible below a critical value for s [42, 48, 49]. This regime arises due to local effects at the outboard midplane, where the ballooning mode is most unstable – where the $s - \alpha$ paradigm treats the flux-surface-averaged shear, it is the local shear that affects ballooning stability, with unstable modes appearing where local shear is weak or vanishing. In cases with high β (supported by a steep pressure gradient α_{MHD}) the Shafranov shift significantly perturbs the outboard equilibrium; when the average shear is small, this perturbation is sufficient to reverse the shear at the outboard midplane, re-stabilizing the ballooning mode and allowing second-stable access [50]. The separation of the infinite- n ballooning- and peeling-unstable regions is dependent on the stabilizing effects of favorable magnetic curvature, with stronger plasma shaping increasing average favorable curvature and stabilizing the modes, opening the channel in $s - \alpha$ space for second-stable access [46].

check

Although the high- n limit results in a highly tractable model for peeling modes, the approximation does not capture the entirety of current-driven physics in the edge. Low- n kink modes can also destabilize within the pedestal due to the strongly-peaked current density profile due to the bootstrap effect [46]. Moreover, multiple harmonics of the edge kink mode may couple to each other at finite n due to the broader radial extent of the mode, as well as coupling with pressure-driven ballooning modes due to the strong pressure gradient [42, 47]. Unlike the $n \rightarrow \infty$ peeling and ballooning modes, each of which may be formulated with a simple one-dimensional calculation, treatment of the finite- n coupled modes requires a more careful 2D treatment.

3.2.3 Coupled Modes – the ELITE Code

The high- n limits for the ballooning and peeling modes (note here that we refer to all current-driven modes in the edge as “peeling,” in order to distinguish them from core kink modes) yield straightforward, one-dimensional constraints on the MHD stability of the pedestal. However, finite-larmor-radius and diamagnetic effects tend to stabilize high- n modes, making this approximation relatively poor [47] – instead, the pedestal is generally limited by finite modes with toroidal wavenumbers in the range $5 \leq n \leq 40$. In this range, modes are radially broad enough that they are not cleanly localized on the corresponding rational surface, and may couple to other poloidal har-

Figure 3.2: Schematic in $s - \alpha_{\text{MHD}}$ space of finite- n coupled peeling-balloonning instabilities, with the infinite- n decoupled results (see fig. 3.1) shown by the dashed lines. Mode coupling tends to stabilize finite- n ballooning modes. However, the coupled modes can close off access to the second-stable regime; only in cases with very strong “magnetic wells” (typically achieved with extreme plasma shaping) does this access reopen.



monics on nearby rational surfaces [41]. Moreover, pressure-driven ballooning and current-driven peeling modes may couple, generating modes driven by both free-energy sources, with sufficient radial extent to affect the entire pedestal region – driving the large, explosive crashes associated with type-I ELMs [51]. Treatment of these modes requires a full two-dimensional approach. Mirroring the approach shown in fig. 3.1, a schematic illustration of the results from such a 2-D calculation are shown in fig. 3.2. Although finite- n effects tend to stabilize the ballooning mode (infinite- n calculations for the peeling and ballooning modes are shown as the dashed lines), mode coupling tends to close off the access path to the second-stable region [42]. At higher n , the first- and second-stable regions tend to pinch together due to weakened coupling between modes, reopening access to the second-stable region; the modes also decouple more readily in a deeper “magnetic well,” expressed as $d_M = D_M s^2 / \alpha$ to encode the effects of shaping and finite aspect ratio with deep magnetic wells and the accompanying potential for second-stable access most readily attained with strong plasma shaping [46].

We use the “Edge-Localized Instabilities in Tokamak Equilibria” or ELITE code [42, 46, 51] to calculate both the growth rate and eigen-mode structure for these coupled modes. ELITE utilizes the expansion of the free energy in $O(n^{-1})$ found in earlier studies of peeling and ballooning modes (see eqs. (3.9) and (3.13)), with an additional

boundary term for the peeling drive [51, 52], reproduced here for completeness:

$$\delta W = \pi \iint d\Psi d\chi \left\{ \frac{JB^2}{R^2 B_p^2} |k_{\parallel} X|^2 + \frac{R^2 B_p^2}{JB^2} \left| \frac{1}{n} \frac{\partial}{\partial \Psi} (JB k_{\parallel} X) \right|^2 \right. \\ - \frac{2J}{B^2} \frac{dp}{d\Psi} \left[|X|^2 \frac{\partial}{\partial \Psi} \left(p + \frac{B^2}{2} \right) - \frac{iF}{JB^2} \frac{\partial}{\partial \chi} \left(\frac{B^2}{2} \right) \frac{X^*}{n} \frac{\partial X}{\partial \Psi} \right] \\ - \frac{X^*}{n} JB k_{\parallel} \left(X \frac{d\sigma}{d\Psi} \right) + \frac{1}{n} \left[PJB k_{\parallel}^* Q^* + P^* JB k_{\parallel} Q \right] \\ \left. + \frac{\partial}{\partial \Psi} \left[\frac{\sigma}{n} X^* JB k_{\parallel} X \right] \right\} \quad (3.17)$$

with P , Q , and σ as defined in eq. (3.14). Given this formulation, the methodology used in ELITE is straightforward. First, poloidal variation is encoded in a “straight field line” angle ω c[42],

$$\omega = \frac{1}{q} \int^x v \, d\chi \quad (3.18)$$

(recall that the rotational transform and safety factor q are encoded such that $2\pi q = \oint v \, d\chi$). Using this, the perturbation $X = RB_p \xi_{\psi}$ is decomposed into individual poloidal harmonics,

$$X = \sum_m u_m(\psi) e^{-im\omega} \quad (3.19)$$

where at fixed n each u_m describes the eigenmodes centered on rational surfaces determined by each (m, n) pair. It can be shown [51] that this yields the relation

$$JB k_{\parallel} X = \sum_m \left(-\frac{v}{q} \right) (m - nq) u_m(x) e^{-im\omega} \quad (3.20)$$

motivating the introduction of the radial variable $x = m_0 - nq$, where m_0 is the poloidal mode number of an arbitrary reference rational surface (by convention, we use the first rational surface outside the plasma, as was used in the high- n peeling mode in section 3.2.2 [51]). This describes spatial variation over the expected length scale for the radial extent of u_m , and is a straightforward conversion from ψ . It is worth noting that ELITE does not treat the separatrix in its calculations, instead truncating the calculation at an internal surface (typically 99.5 – 99.8% of poloidal flux), which prevents a singularity in x ; although peeling modes are highly unstable at the X-point, high local collisionality prevents the omission from significantly affecting

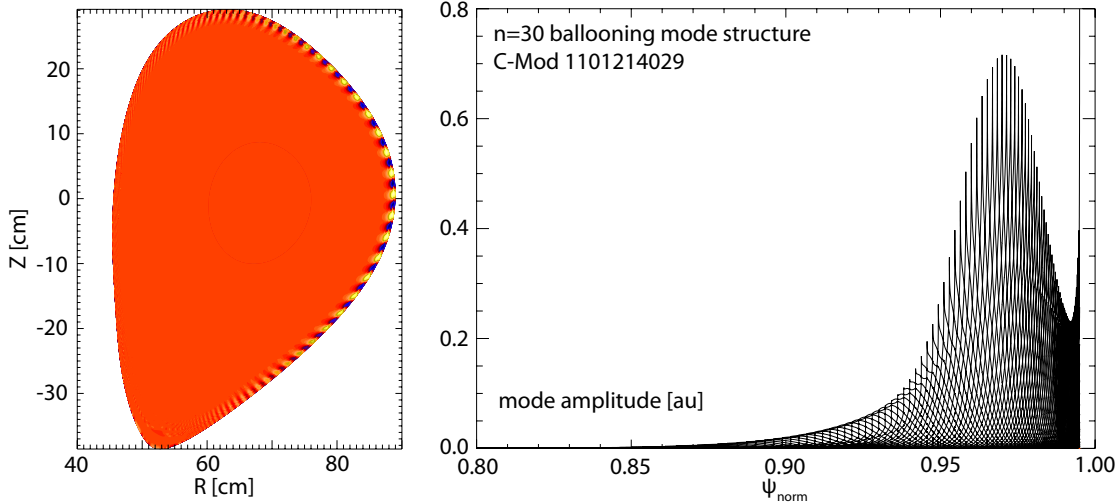


Figure 3.3: Mode structure for an $n = 30$ ballooning mode calculated by ELITE. (left) Contour plot of radial perturbations from the mode. The mode is edge-localized and strongest at the outboard midplane, consistent with an edge ballooning mode. (right) Eigenmode structure of the $n = 30$ mode. Each peak is a poloidal harmonic localized around the rational flux surface determined by the corresponding poloidal mode number m for $n = 30$. The mode is strongest in the steep gradient region, but extends inward due to the comparatively high mode number (eigenmode envelope encompasses $O(n^{1/3})$ flux surfaces). Note that, as ELITE cannot treat the separatrix, the mode calculation truncates at $\psi_{\text{norm}} = 0.995$.

the overall result [53]. The Euler-Lagrange equations minimizing the potential energy may be expressed as a set of coupled second-order ordinary differential equations of the form [52]

$$A_{m,m'}^{(2)} \frac{d^2 u_m}{d\psi^2} + A_{m,m'}^{(1)} \frac{du_m}{d\psi} + A_{m,m'}^{(0)} u_m = 0 \quad (3.21)$$

where the coefficients A are matrix elements describing the coupling between two modes m and m' (see Wilson *et al.* [51] for definitions). Efficient computation of these eigenmodes is assisted by two simplifications: first, while the eigenmodes u_m vary on a very short length scale x , comparable to the spacing between rational surfaces, the equilibrium parameters used in the calculation of the matrix elements A vary more slowly, and can be calculated on a coarser mesh than that needed to evaluate eq. (3.21). Second, this radial localization of u_m means that only harmonics on nearby rational surfaces will strongly couple – other modes can be ignored in the computation to save time [51]. An example of the eigenmode structure for an $n = 30$ ballooning mode is shown in fig. 3.3, with the poloidal variation of the displacement amplitude (strongest at the outboard midplane, as is typical for ballooning modes) shown at left and the radial structure of the modes shown at right.

Absent other considerations, the eigenvalue γ^2 from this ideal MHD calculation describes both the stability of the mode, and its growth

rate – positive growth rates (typically presented with a natural normalization to the Alfvén frequency $\omega_A = v_A/R$, with $v_A = B/\sqrt{\mu_0 \rho}$, arising from the system of equations) indicating an unstable mode. However, a number of studies [24, 54, 55] have noted that this neglects finite-Larmor-radius and diamagnetic effects, which can have a strong stabilizing effect on modes in the pedestal. While a full treatment of the diamagnetic effects requires a fluid treatment not captured by the ideal MHD formalism, the stabilizing effect in the pedestal may be approximated by a nonzero growth-rate threshold for the instability – this is described (*cf.* [46]) by the analytic relation

$$-\gamma_{\text{MHD}}^2 = \omega(\omega - \omega_{*\text{pi}}) \quad (3.22)$$

where γ_{MHD} is the ideal growth rate and $\omega_{*\text{pi}}$ is the diamagnetic frequency given by [54, 56].

$$\begin{aligned} \omega_{*\text{pi}} &= \tau \frac{nq \langle \nabla \psi \rangle}{\rho_0 B_0 \langle r \rangle} \frac{dp}{d\psi} \\ \tau &= \frac{1}{\omega_{Bi}\tau_A} = \frac{1}{eR_0 \sqrt{M/\mu_0 n_i}} \end{aligned} \quad (3.23)$$

where angled brackets indicate a flux-surface average, ω_{Bi} is the ion bounce frequency, τ_A is the Alfvén time, and ρ_0 is the mass density normalized to that on the magnetic axis. eq. (3.22) requires $\gamma > \omega_{*\text{pi}}/2$ for instability; as the diamagnetic frequency is mode-number-dependent (roughly $\omega_{*\text{pi}} \sim n\omega_A$ [47]) this provides the expected improved stabilization of higher- n ballooning modes in the ELITE formalism. However, the diamagnetic frequency is expected to vary strongly on short length scales in the pedestal due to the pressure-gradient dependence [33], with the result of the peeling-balloonning stability calculation depending significantly on the treatment approach for this variation.

Sequences of ELITE calculations are capable of effectively characterizing the stability space for a pedestal – this is customarily expressed in terms of normalized pressure gradient (α_{MHD}) and normalized pedestal current ($\gamma = 2j_{||}/\langle j \rangle$, such that $s = 2 - \gamma$) in place of the less-intuitive magnetic shear s , as shown in fig. 3.4. This shape is, at a glance, similar to first-stable regime in fig. 3.2 (albeit mirrored along the vertical axis). However, the shape of the stability boundary is modified by the effects of collisionality on the MHD stability [56]. At low collisionality, the bootstrap current is quite high for given pedestal gradients. The enhanced edge current drives particularly unstable peeling modes, with the most unstable modes at lower n , setting the upper-left boundary of the stable region. Higher collisionality suppresses the edge current density, leaving ballooning modes the

clarify?

Figure 3.4: Schematic of the stability space to coupled peeling-balloonning MHD modes, set by the edge pressure gradient and current density.

Ballooning modes are driven by pressure gradient but stabilized by magnetic shear driven by edge currents, while kink/peeling modes are current-driven but stabilized by pressure gradients. Ref to Snyder?



most unstable. A simplistic calculation finds that ballooning modes are consistently more unstable at higher n – however, higher- n modes are strongly stabilized by diamagnetic effects [36], thus moderate $n \sim 10 - 40$ ballooning modes limit high-collisionality pedestals [47], found at the right-side, high- α_{MHD} boundary. In moderate-collisionality, high-performance discharges (such that both edge pressure gradient and bootstrap current are high) coupled peeling-balloonning modes with $n \sim 5 - 15$, found in the “nose” of the stability boundary, limit the pedestal. These coupled modes may extend comparatively far into the plasma, leading to large, explosive ELMs on instability [51]. However, as discussed above strong shaping inhibits this mode coupling, extending the “nose” of the stability boundary to high pressure gradient and current; with extreme shaping, second-stable access may open for a broad range of n , opening the stability boundary to second-stable access [57]. In practice, the stability boundary is well-characterized by calculations spanning $5 \leq n \leq 35$ – higher n are suppressed by diamagnetic effects, while $n < 5$ peeling modes are difficult to distinguish from core kink modes due to their broad radial extent, and are rarely more unstable than $n > 5$ [56].

ELITE calculations have been benchmarked against a number of other codes [53], including GATO [58], MISHKA [54, 59], MARG2D [60, 61], and KINX [62, 63]. Notably, GATO calculations extend to lower n than are suitable in ELITE, and KINX calculations include treatment of the separatrix – however, ELITE calculations show good agreement across a broad range in toroidal mode number. ELITE has been broadly successful in capturing the limiting physics of ELMy H-mode [47], although nonlinear calculations are necessary to capture the dynamics of the ELM crash itself [64]. Moreover, other H-

mode regimes are well-described by peeling-balloon physics – the EDA H-mode [16, 65] and QH-mode [66] are modeled to be stable just below the ballooning and peeling sides of the boundary, respectively, with ELMs appearing as the pedestal crosses the ideal MHD limit. RMP ELM-suppressed H-modes are similarly calculated to be peeling-balloon stable, with ELMs appearing as the pedestal crosses the boundary when the RMP coils are switched off [56]. The peeling-balloon boundary is evidently a useful figure of merit in general for H-mode pedestals.

•

3.3 KINETIC-BALLOONING TURBULENCE MODELING

Following the L-H transition, the $\vec{E} \times \vec{B}$ flows associated with the formation of the pedestal and transition to high confinement should continue to rise, due to the strong increase in the diamagnetic term due to the pedestal [56]. However, the pedestal gradient appears to be limited, even before the onset of an ELM – thus, there must be a mechanism limiting the pedestal prior to the onset of the ideal MHD instability (section 3.2). As the $\vec{E} \times \vec{B}$ flow strongly suppresses long-wavelength turbulence, short-wavelength turbulent modes appear to be an ideal candidate. Electron-temperature-gradient (ETG) modes at short wavelengths is more likely to modify the interplay between density and temperature in the pedestal [56] – instead, the recent efforts have focused on the kinetic-balloon mode (KBM) for a constraint on the pressure pedestal.

The KBM arises from the introduction of kinetic effects in an extension of the high- n ideal ballooning MHD formalism, introduced in section 3.2.1 [67]. Although the initial assumptions for each are quite different – the ideal MHD energy principle (eq. (3.9)) requires high collisionality for the coupled fluid treatment, the kinetic-energy formulation treating a collisionless plasma with trapped-particle effects results in a very similar fluid-like relation [67]. Earlier gyrokinetic studies focused on electrostatic fluctuations, of which the ion-temperature gradient (ITG) mode is dominant; however, the introduction of magnetic fluctuations both modifies ITG dynamics, and allows for the formation of the electromagnetic KBM fluctuation [68]. In regimes with high β or steep pressure gradients – in short, exactly the plasmas of concern for high-performance regimes – electrostatic simplifications to gyrokinetic turbulence break down, necessitating treatment of the KBM in modeling [68, 69].

Gyrokinetic and gyrofluid simulations using the necessary electromagnetic treatment [68, 70, 71, 72] found the onset of a distinct turbulent mode at high beta, overtaking the usually-dominant ITG and trapped-electron mode (TEM) turbulence at low and moderate beta, respectively. Above this threshold in β (more properly, a threshold in α_{MHD}), simulations using the GYRO code [73] found that the mode

onset was highly stiff – that is, the growth rate of the mode increases extremely quickly even in plasmas just above the onset threshold [72] – and is insensitive to $\vec{E} \times \vec{B}$ shear, such that the mode drives transport levels sufficient to constrain the pedestal gradient near the critical α_{MHD} [56]. Moreover, gyrofluid simulations found that the KBM is destabilized near the infinite- n ideal ballooning limit – in cases with a flat temperature profile, the onset is precisely matched to the calculated MHD limit, while the inclusion of a finite temperature gradient somewhat reduced the onset α_{MHD} due to ion drift resonance effects [68]. This motivates the use of more straightforward high- n MHD calculations (see section 3.2.1) to calculate the KBM threshold for the purposes of this thesis, rather than complex gyrokinetic/gyrofluid simulations.

The stiff onset of the kinetic-balloonning mode, and accompanying limits to the pedestal pressure gradient, allows for a heuristic scaling for the pedestal width [56]. To good approximation, the critical gradient is simply given by $\alpha_c \sim \beta_{p,\text{ped}}/\Delta$ for the poloidal beta at the pedestal top and the pedestal width Δ expressed in (normalized) poloidal flux – thus we require $\Delta \sim \beta_{p,\text{ped}}/\alpha_c$. As with ideal MHD ballooning modes, the KBM is sensitive to magnetic shear. However, at the outboard midplane (where magnetic curvature is least favorable) the local shear is such that the critical α_c increases with decreasing shear, $\alpha_c \sim 1/s^{1/2}$. In the pedestal, we expect the shear to trend as $1/\langle j \rangle$, which to lowest-order approximation is simply $1/\beta_{p,\text{ped}}$ as the current in the pedestal is bootstrap-dominated. This implies $\alpha_c \sim \beta_{p,\text{ped}}^{1/2}$ and therefore $\Delta \sim \beta_{p,\text{ped}}^{1/2}$. This trend is in accordance with experimental observations on DIII-D [25], JT-60U [29, 74], ASDEX Upgrade [15, 75] and Alcator C-Mod [76]. Moreover, the growth of the pedestal between ELMs appears to maintain a limited pressure gradient [7, 77], and pedestal fluctuations saturate early in the ELM cycle [78], consistent with the idea that KBM turbulence constrains the pedestal indepedent of explosive ELM-driven transport.

*not sure I follow
phil's reasoning here*

3.3.1 The Ballooning-Critical Pedestal Technique

The arguments detailed above lead to an intuitive expression for the pedestal width and height based on KBM limits, $\Delta \sim \beta_{p,\text{ped}}^{1/2}$. However, full quantification of the KBM constraint from first principles requires a more detailed treatment. The analogous onset of the KBM to the infinite- n ideal ballooning MHD mode allows a computationally-efficient approach to the turbulence threshold.

The KBM is an approximately local effect due to its short scale length – as such, no single calculated mode can describe the destabilization of the entire pedestal without a highly involved nonlocal calculation of the stability across the pedestal profile. A far more efficient and straightforward model can be developed using the “balloon-

ing critical pedestal” (BCP) technique [79, 80], which finds the point where half of the pedestal is locally at or beyond criticality for the KBM. At fixed pedestal width, the height is incremented to increase the pressure gradient, following the same approach as the peeling-balloonning calculation. At each increment, the stability of the pedestal to high- n ideal ballooning MHD modes is calculated, e. g., using the BALOO code [38, 39]. As the infinite- n modes calculated by BALOO are also perfectly localized on the corresponding rational flux surfaces, the code finds unstable surfaces in the pedestal region and the width of the pedestal covered by these surfaces. When half of the pedestal width is thus unstable, the KBM threshold is said to have been reached. This approach is highly numerically efficient – as the ballooning MHD criterion reduces in the infinite- n limit to a straightforward one-dimensional eigenvalue problem [38] that can be computed efficiently – and fairly robust, although it does require the unstable region of the pedestal to be well-defined and bounded (typically the “middle half” of the pedestal, where the pressure gradient is steepest). This assumption can break down at very strong shaping or low aspect ratio [80].

3.4 THE EPED MODEL

In light of the importance of the pedestal structure for optimized fusion performance – both by maximizing fusion power density via the pressure pedestal height constraint on core profiles [81], and by avoiding or mitigating large, damaging ELMs [3, 4] – a predictive understanding of the pedestal is highly desirable for planned operations on ITER and beyond. Models based on peeling-balloonning MHD instability, particularly the ELITE code (section 3.2.3), have proven quite successful at capturing the limiting physics of the ELMy H-mode pedestal. However, these calculations typically rely on experimental profiles and magnetic equilibria reconstructed after the fact, and as such cannot by themselves provide predictive capability. Similarly, the constraint set by kinetic-balloonning mode (KBM) turbulence (section 3.3) corresponds well with pedestal observations in profiles with steep pressure gradients in the pedestal, but cannot by itself uniquely constrain the pedestal structure. The EPED series of models, developed by Snyder *et al.* [80], combines these two constraints into a single predictive model for the ELMy H-mode pedestal.

To incorporate predictive capability into the peeling-balloonning MHD stability model calculated by ELITE (section 3.2.3), the EPED model must characterize peeling-balloonning stability as accurately as possible using only parameters known prior to the plasma discharge, set by operator control; however, as discussed in section 3.2.3, the inherent nonlocality of the problem still requires two-dimensional MHD calculation. To that end, the model employs a set of model Miller

equilibria [48], up/down-symmetric equilibria allowing for plasma elongation and triangularity defined with analytic plasma profiles such that the essential physics in the pedestal (namely, the pressure gradient and bootstrap current profiles) is nearly matched to experimental conditions [56]. Using this setup, the model equilibria may be defined by a small set of scalar parameters for use in ELITE: major and minor radius R and a , elongation and shaping κ, δ (recall that in these up/down-symmetric equilibria $\delta_l = \delta_u = \delta$), plasma current I_p , and applied field B_T , set the magnetic equilibrium when combined with the target global normalized pressure (typically the Troyon normalized β_N [82]). Global beta also impacts the pedestal stability via the beneficial effect of increased Shafranov shift in the core on MHD stability [66]. The EPED model additionally takes as inputs for the ELITE calculation the density at the pedestal top $n_{e,ped}$ and the pedestal width Δ in normalized poloidal flux (note that the density and temperature profiles are defined to have the same width) to constrain the pressure and current profiles, with the current calculated from the density and temperature profiles from the analytic Sauter formula, eq. (2.10) [83].

The calculation of the peeling-balloonning stability boundary is straightforward – at a fixed pedestal width, the pressure pedestal height (and, accordingly, the MHD instability drives from the edge pressure gradient and current density) is increased in increments until the stability boundary is reached [56]. The interdependence between pedestal width and height is determined by repeating the calculation at a range of pedestal widths, determining a relation between the pressure pedestal width and height for a given model equilibrium. To lowest order, the MHD limit is a limit on ∇p , leading one to expect a linear relation between the pedestal width and height. However, non-local effects on the MHD stability – in particular, the broader, lower- n modes destabilized by wider pedestals leading to reduced maximum α_{MHD} at wider Δ [55] – reduces the linear dependence, leading to a rough scaling of $p_{ped} \sim \Delta^{3/4}$ set by the peeling-balloonning stability boundary [53].

On its own, the peeling-balloonning MHD constraint defines the pedestal height as a function of width, necessitating a second constraint to allow a unique predictive solution. The Kinetic Ballooning Mode (KBM), described in section 3.3, limits the pedestal gradient with a relation $p_{ped} \sim \Delta^2$ (more precisely, $\Delta \sim \beta_{p,ped}^{1/2}$). This constraint is sufficiently distinct from that enforced by peeling-balloonning MHD that only a single nontrivial solution satisfying both exists – thereby uniquely predicting the pedestal width and height. An example of the prediction at the intersection of the P-B and KBM constraints, along with the corresponding experimental result [80], is shown in fig. 3.5.

Figure 3.5: Illustration of the peeling-balloonning MHD and kinetic-balloonning turbulent constraints used in the EPED model. The peeling-balloonning constraint, calculated by ELITE, results in a trend roughly of $p_{\text{ped}} \sim \Delta_{\psi}^{3/4}$, while the KBM width constraint calculated via the balloonning-critical pedestal (BCP) technique sets $p_{\text{ped}} \sim \Delta_{\psi}^2$. The unique solution to these constraints is the EPED prediction for the pedestal width and height. The prediction is here shown compared to the measured pedestal from DIII-D shot 132003 (reproduced from [80]) [get permission](#)



3.4.1 EPED with Semi-Empirical Width Constraint

The simplest version of the EPED series, EPED1 [56], takes advantage of the dominant scaling of the width with $\beta_{\text{p,ped}}$ in the KBM constraint, described in section 3.3: as little secondary variation of the width beyond $\Delta \sim \beta_{\text{p,ped}}^{1/2}$ is seen with other expected controlling parameters, e.g., ν^* , ρ^* or ρ_{pol}^* , $n_{e,\text{ped}}$ [56] (cf. section 3.1, particularly section 3.1.3), the constraint is reduced to a single relation $\Delta = c\beta_{\text{p,ped}}^{1/2}$ with a fitted value for c . For historical reasons based on DIII-D data, EPED1 uses $c = 0.076$, although a newer multi-machine fit produces $c = 0.084$ [80].

To calculate the threshold for the peeling-balloonning MHD instability, the growth rate as calculated by ELITE must be balanced against against the inherent stabilizing effect of plasma diamagnetism in the pedestal, as described in section 3.2.3. The effect of diamagnetic stabilization may be approximated by a threshold in the growth rate, $\gamma > \omega_{*\text{pi}}/2$ for the diamagnetic frequency $\omega_{*\text{pi}}$. In the EPED1 model $\omega_{*\text{pi}}$ is taken to be constant across the pedestal, with a value set to the half-maximum calculated for the analytic pedestal structure used by the model equilibrium [56]. Although this is a comparatively rough approximation of the diamagnetic effect in the pedestal, it can be calculated with very high computational efficiency.

Both the KBM and P-B constraints calculated in EPED1 use significant simplifications. Nevertheless, the model is capable of producing predictions with a systematic $\pm 15 - 20\%$ uncertainty across a range of parameters [56, 79]. The simplicity and efficiency of the calculations used allow EPED1 to be tested against very large pedestal datasets [80].

3.4.2 EPED with First-Principles Width Constraint

Although the bulk of the variation in the KBM-constrained pedestal width is captured by the $\beta_{p,ped}$ scaling, it is nevertheless desirable to account for its effects on the scale factor of the trend – more properly, the weakly-varying function $G(v^*, \varepsilon, \dots)$ such that $\Delta = G\beta_{p,ped}^{1/2}$ – allowing EPED to make first-principles predictions (in that the constraint is not dependent on a scale factor set by fitted data).

The EPED1.6 implementation [79, 80] achieves this by directly calculating the KBM constraint via the “ballooning critical pedestal” (BCP) technique, described in section 3.3.1. By performing this calculation across a range of pedestal widths and fitting the result against $\beta_{p,ped}$, a first-principles calculation of the KBM pedestal constraint is generated and paired with the peeling-balloonning MHD result [80]. While this approach is more computationally expensive than the fixed scaling used in EPED1, the BCP calculation allows the effects of collisionality and shaping on the KBM threshold to be properly accounted for – this manifests in a range of scale factors, $\langle G \rangle \approx 0.07 - 0.1$, that are comparable to the fitted result used in EPED1, but are specific to discharge characteristics.

The simple diamagnetic stabilization model used in EPED1, described above, also fails to capture important physics in the pedestal – the model assumes a constant diamagnetic frequency ω_{*pi} for the stabilization of the peeling-balloonning modes, while in fact the diamagnetic frequency varies rapidly over the pedestal [79]. EPED1.6 replaces this with an “effective” diamagnetic frequency ω_{*eff} , based on a fit to calculations of the diamagnetic stabilization of peeling-balloonning modes in the fluid code BOUT++ [84, 85, 86]. This provides stronger stabilization of higher- n ($n > \sim 12$) modes at higher collisionality than that found in the simple linear model [77, 80], a correction that is particularly necessary for the comparatively high-collisionality pedestals in ELMy H-modes on C-Mod [77].

3.4.3 EPED Model Implementation & ITER Predictions

The EPED model has been extensively tested on numerous machines, particularly on DIII-D [80, 87], JT-60U [53], C-Mod [88], and KSTAR [89]. The model has also been tested on NSTX [87], with limited success due to breakdown of the assumptions inherent to the KBM constraint at small aspect ratio [53]. Given the proximity of the pedestal to the peeling-balloonning MHD and KBM turbulence limits in most high-performance regimes, it is expected that EPED predictions are viable as a figure of merit for H-mode operation on ITER [80, 90].

Notably, EPED predictions for ITER (shown compared to results from DIII-D and C-Mod [77] in fig. 3.6) predict pedestal pressures of $\beta_{N,ped} \sim 0.6 - 0.7$, corresponding to $p_{ped} \sim 90 \text{ kPa}$, at a pedestal width of

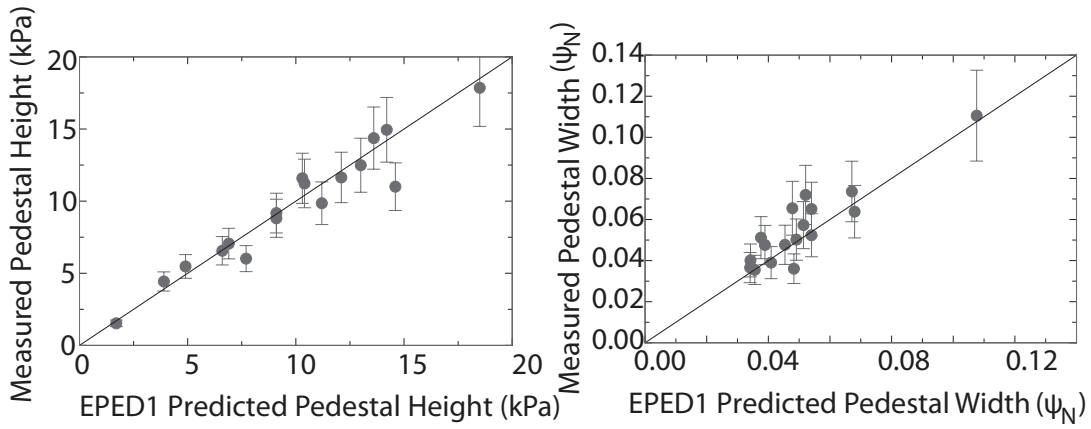


Figure 3.6: EPED1 predictions versus measured pressure pedestal height and width on a range of DIII-D discharges [56]. permission

$\Delta \sim 4\%$ [53, 80]. This is within a factor of $\sim 2 - 3$ of the range of experimental results on which EPED has been tested [77, 88], and is consistent with the planned $Q = 10$ operation on ITER assuming sufficient optimization of core and pedestal profiles [80, 90]. Although development is ongoing for the EPED model series, it has demonstrated viable predictive capability for H-mode pedestals in a variety of conditions for conventional-aspect-ratio tokamaks. *

BIBLIOGRAPHY

- [1] M. Greenwald, N. Basse, P. Bonoli, R. Bravenec, E. Edlund et al. **Confinement and transport research in Alcator C-Mod.** *Fusion Science and Technology*, 51(3):266–287, 2007.
- [2] A. E. Hubbard, R. L. Boivin, R. S. Granetz, M. Greenwald, I. H. Hutchinson et al. **Measurements of the high confinement mode pedestal region on Alcator C-Mod.** *Physics of Plasmas*, 5(5):1744–1751, 1998.
- [3] A Loarte, G Saibene, R Sartori, D Campbell, M Becoulet et al. **Characteristics of type I ELM energy and particle losses in existing devices and their extrapolation to ITER.** *Plasma Physics and Controlled Fusion*, 45(9):1549, 2003.
- [4] G Federici, A Loarte and G Strohmayer. **Assessment of erosion of the ITER divertor targets during type I ELMs.** *Plasma Physics and Controlled Fusion*, 45(9):1523, 2003.
- [5] A E Hubbard. **Physics and scaling of the H-mode pedestal.** *Plasma Physics and Controlled Fusion*, 42(5A):A15, 2000.
- [6] Jerry W. Hughes. *Edge Transport Barrier Studies On the Alcator C-Mod Tokamak.* PhD thesis, Massachusetts Institute of Technology, 2005.
- [7] C.F. Maggi. **Progress in understanding the physics of the H-mode pedestal and ELM dynamics.** *Nuclear Fusion*, 50(6):066001, 2010.
- [8] P Breger, C Flewin, K-D Zastrow, S J Davies, N C Hawkes et al. **Plasma-edge gradients in L-mode and ELM-free H-mode JET plasmas.** *Plasma Physics and Controlled Fusion*, 40(3):347, 1998.
- [9] J. W. Hughes, D. A. Mossessian, A. E. Hubbard, B. LaBombard and E. S. Marmar. **Observations and empirical scalings of the high-confinement mode pedestal on Alcator C-Mod.** *Physics of Plasmas*, 9(7):3019–3030, 2002.
- [10] J. W. Hughes, A. E. Hubbard, D. A. Mossessian, B. LaBombard, T. M. Biewer et al. **H-mode pedestal and L-H transition studies on Alcator C-Mod.** *Fusion Science and Technology*, 51(3):317–341, 2007.
- [11] J.W. Hughes, B. LaBombard, J. Terry, A. Hubbard and B. Lipschultz. **Edge profile stiffness and insensitivity of the density**

- pedestal to neutral fuelling in Alcator C-Mod edge transport barriers.** *Nuclear Fusion*, 47(8):1057, 2007.
- [12] W Suttrop, M Kaufmann, H J de Blank, B Brüsehaber, K Lackner et al. **Identification of plasma-edge-related operational regime boundaries and the effect of edge instability on confinement in ASDEX Upgrade.** *Plasma Physics and Controlled Fusion*, 39(12):2051, 1997.
- [13] J. W. Hughes, B. LaBombard, D. A. Mossessian, A. E. Hubbard, J. Terry et al. **Advances in measurement and modeling of the high-confinement-mode pedestal on the Alcator C-Mod tokamak.** *Physics of Plasmas*, 13(5):056103, 2006.
- [14] M.A. Mahdavi, T.H. Osborne, A.W. Leonard, M.S. Chu, E.J. Doyle et al. **High performance H mode plasmas at densities above the Greenwald limit.** *Nuclear Fusion*, 42(1):52, 2002.
- [15] M. N. A. Beurskens, T. H. Osborne, P. A. Schneider, E. Wolfrum, L. Frassinetti et al. **H-mode pedestal scaling in DIII-D, ASDEX Upgrade, and JET.** *Physics of Plasmas*, 18(5):056120, 2011.
- [16] D. A. Mossessian, P. Snyder, A. Hubbard, J. W. Hughes, M. Greenwald et al. **High-confinement-mode edge stability of Alcator C-mod plasmas.** *Physics of Plasmas*, 10(5):1720–1726, 2003.
- [17] T. Onjun, G. Bateman, A. H. Kritz and G. Hammett. **Models for the pedestal temperature at the edge of H-mode tokamak plasmas.** *Physics of Plasmas*, 9(12):5018–5030, 2002.
- [18] K. C. Shaing, E. C. Crume and W. A. Houlberg. **Bifurcation of poloidal rotation and suppression of turbulent fluctuations: A model for the L-H transition in tokamaks.** *Physics of Fluids B: Plasma Physics*, 2(6):1492–1498, 1990.
- [19] K. C. Shaing. **Poloidal magnetic field dependence of the edge electric field layer width in the H mode in tokamaks.** *Physics of Fluids B: Plasma Physics*, 4(2):290–291, 1992.
- [20] Kimitaka Itoh and Sanae-I Itoh. **The role of the electric field in confinement.** *Plasma Physics and Controlled Fusion*, 38(1):1, 1996.
- [21] T Hatae, Y Kamada, S Ishida, T Fukuda, T Takizuka et al. **Characteristics of edge pedestal width in JT-60U ELM-free H-mode plasmas.** *Plasma Physics and Controlled Fusion*, 40(6):1073, 1998.
- [22] Y Kamada, T Hatae, T Fukuda and T Takizuka. **Growth of the edge pedestal in JT-60U ELMy H-mode.** *Plasma Physics and Controlled Fusion*, 41(11):1371, 1999.

- [23] H R Wilson and J W Connor. Ballooning instabilities, poloidal flow and the temperature pedestal at the tokamak edge. In *Proceedings of the 24th European Physical Society Conference on Controlled Fusion and Plasma Physics*, volume 21A of *Europhysics Conference Abstracts*, pages 289–292, Geneva, 1997.
- [24] B. N. Rogers and J. F. Drake. Diamagnetic stabilization of ideal ballooning modes in the edge pedestal. *Physics of Plasma*, 6(7):2797–2801, 1999.
- [25] T H Osborne, R J Groebner, L L Lao, A W Leonard, R Maingi et al. H-mode pedestal characteristics, ELMs, and energy confinement in ITER shape discharges on DIII-D. *Plasma Physics and Controlled Fusion*, 40(5):845, 1998.
- [26] W Suttrop, O Gruber, B Kurzan, H D Murmann, J Neuhauser et al. Effect of plasma shape variation on ELMs and H-mode pedestal properties in ASDEX upgrade. *Plasma Physics and Controlled Fusion*, 42(5A):A97, 2000.
- [27] P. Gohil, K.H. Burrell and T.N. Carlstrom. Parametric dependence of the edge radial electric field in the DIII-D tokamak. *Nuclear Fusion*, 38(1):93, 1998.
- [28] R. J. Groebner and T. H. Osborne. Scaling studies of the high mode pedestal. *Physics of Plasmas*, 5(5):1800–1806, 1998.
- [29] H. Urano, T. Takizuka, Y. Kamada, N. Oyama, H. Takenaga et al. Dimensionless parameter dependence of H-mode pedestal width using hydrogen and deuterium plasmas in JT-60U. *Nuclear Fusion*, 48(4):045008, 2008.
- [30] G. Saibene, L.D. Horton, R. Sartori, B. Balet, S. Clement et al. The influence of isotope mass, edge magnetic shear and input power on high density ELMMy H modes in JET. *Nuclear Fusion*, 39(9):1133, 1999.
- [31] F. Wagner, G. Becker, K. Behringer, D. Campbell, A. Eberhagen et al. Regime of improved confinement and high beta in neutral-beam-heated divertor discharges of the ASDEX tokamak. *Physical Review Letters*, 49(19):1408–1412, Nov 1982.
- [32] M Keilhacker, G Becker, K Bernhardi, A Eberhagen, M ElShaer et al. Confinement studies in L and H-type ASDEX discharges. *Plasma Physics and Controlled Fusion*, 26(1A):49, 1984.
- [33] G T A Huysmans. ELMs: MHD instabilities at the transport barrier. *Plasma Physics and Controlled Fusion*, 47(12B):B165, 2005.
- [34] Jeffrey P. Freidberg. *Ideal Magnetohydrodynamics*. Springer, 1987.

- [35] Y Kamada, R Yoshino, Y Neyatani, M Sato, S Tokuda et al. **Onset condition for ELMs in JT-60U.** *Plasma Physics and Controlled Fusion*, 38(8):1387, 1996.
- [36] W Suttrop. **The physics of large and small edge localized modes.** *Plasma Physics and Controlled Fusion*, 42(5A):A1, 2000.
- [37] J. W. Connor, R. J. Hastie and J. B. Taylor. **Shear, periodicity, and plasma ballooning modes.** *Physical Review Letters*, 40:396–399, Feb 1978.
- [38] J. W. Connor, R. J. Hastie and J. B. Taylor. **High mode number stability of an axisymmetric toroidal plasma.** *Proceedings of the Royal Society of London. A. Mathematical and Physical Sciences*, 365(1720):1–17, 1979.
- [39] R.L. Miller and J.W. Van Dam. **Hot particle stabilization of ballooning modes in tokamaks.** *Nuclear Fusion*, 27(12):2101, 1987.
- [40] R. L. Miller, Y. R. Lin-Liu, A. D. Turnbull, V. S. Chan, L. D. Pearlstein et al. **Stable equilibria for bootstrap-current-driven low aspect ratio tokamaks.** *Physics of Plasmas*, 4(4):1062–1068, 1997. BALOO code.
- [41] J. W. Connor, R. J. Hastie, H. R. Wilson and R. L. Miller. **Magnetohydrodynamic stability of tokamak edge plasmas.** *Physics of Plasmas*, 5(7):2687–2700, 1998.
- [42] H. R. Wilson, J. W. Connor, A. R. Field, S. J. Fielding, R. L. Miller et al. **Ideal magnetohydrodynamic stability of the tokamak high-confinement-mode edge region.** *Physics of Plasmas*, 6(5):1925–1934, 1999.
- [43] H R Wilson, S C Cowley, A Kirk and P B Snyder. **Magnetohydrodynamic stability of the H-mode transport barrier as a model for edge localized modes: an overview.** *Plasma Physics and Controlled Fusion*, 48(5A):A71, 2006.
- [44] H Zohm. **Edge localized modes (ELMs).** *Plasma Physics and Controlled Fusion*, 38(2):105, 1996.
- [45] Claude Mercier. **A necessary condition for hydromagnetic stability of plasma with axial symmetry.** *Nuclear Fusion*, 1(1):47, 1960.
- [46] P. B. Snyder, H. R. Wilson, J. R. Ferron, L. L. Lao, A. W. Leonard et al. **Edge localized modes and the pedestal: A model based on coupled peeling–ballooning modes.** *Physics of Plasmas*, 9(5):2037–2043, 2002.

- [47] P.B. Snyder, H.R. Wilson, J.R. Ferron, L.L. Lao, A.W. Leonard et al. **ELMs and constraints on the H-mode pedestal: peeling-balloonning stability calculation and comparison with experiment.** *Nuclear Fusion*, 44(2):320, 2004.
- [48] R. L. Miller, M. S. Chu, J. M. Greene, Y. R. Lin-Liu and R. E. Waltz. **Noncircular, finite aspect ratio, local equilibrium model.** *Physics of Plasmas*, 5(4):973–978, 1998.
- [49] J W Connor. **Edge-localized modes - physics and theory.** *Plasma Physics and Controlled Fusion*, 40(5):531, 1998.
- [50] J.M. Greene and M.S. Chance. **The second region of stability against ballooning modes.** *Nuclear Fusion*, 21(4):453, 1981.
- [51] H. R. Wilson, P. B. Snyder, G. T. A. Huysmans and R. L. Miller. **Numerical studies of edge localized instabilities in tokamaks.** *Physics of Plasmas*, 9(4):1277–1286, 2002.
- [52] A. Dowsett, P. B. Snyder and H. R. Wilson. **ELITE and extension to low toroidal mode number.** In *26th Meeting of the ITPA Pedestal & Edge Physics Topical Group*, 2014.
- [53] P.B. Snyder, N. Aiba, M. Beurskens, R.J. Groebner, L.D. Horton et al. **Pedestal stability comparison and ITER pedestal prediction.** *Nuclear Fusion*, 49(8):085035, 2009.
- [54] G. T. A. Huysmans, S. E. Sharapov, A. B. Mikhailovskii and W. Kerner. **Modeling of diamagnetic stabilization of ideal magnetohydrodynamic instabilities associated with the transport barrier.** *Physics of Plasmas*, 8(10):4292–4305, 2001.
- [55] P B Snyder and H R Wilson. **Ideal magnetohydrodynamic constraints on the pedestal temperature in tokamaks.** *Plasma Physics and Controlled Fusion*, 45(9):1671, 2003.
- [56] P. B. Snyder, R. J. Groebner, A. W. Leonard, T. H. Osborne and H. R. Wilson. **Development and validation of a predictive model for the pedestal height.** *Physics of Plasmas*, 16(5):056118, 2009.
- [57] A D Turnbull, L L Lao, T H Osborne, O Sauter, E J Strait et al. **Edge localized modes in DIII-D high performance discharges.** *Plasma Physics and Controlled Fusion*, 45(10):1845, 2003.
- [58] L.C. Bernard, F.J. Helton and R.W. Moore. **GATO: An MHD stability code for axisymmetric plasmas with internal separatrices.** *Computer Physics Communications*, 24(3–4):377 – 380, 1981.
- [59] A. B. Mikhailovskii, G. T. A. Huysmans, W. Kerner and S. E. Sharapov. **Optimization of computational MHD normal-mode analysis for tokamaks.** *Plasma Physics Reports*, 23(10):844–857, 1997.

- [60] Nobuyuki Aiba, Shinji Tokuda, Tomoko Ishizawa and Masao Okamoto. **Extension of the Newcomb equation into the vacuum for the stability analysis of tokamak edge plasmas.** *Computer Physics Communications*, 175(4):269 – 289, 2006.
- [61] Nobuyuki Aiba, Shinji Tokuda, Takaaki Fujita, Takahisa Ozeki, Ming S. Chu et al. **Numerical method for the stability analysis of ideal MHD modes with a wide range of toroidal mode numbers in tokamaks.** *Plasma and Fusion Research*, 2:010, 2007.
- [62] L. Degtyarev, A. Martynov, S. Medvedev, F. Troyon, L. Villard et al. **The KINX ideal MHD stability code for axisymmetric plasmas with separatrix.** *Computer Physics Communications*, 103(1):10–27, 1997.
- [63] S Yu Medvedev, A A Martynov, Y R Martin, O Sauter and L Villard. **Edge kink/ballooning mode stability in tokamaks with separatrix.** *Plasma Physics and Controlled Fusion*, 48(7):927, 2006.
- [64] P. B. Snyder, H. R. Wilson and X. Q. Xu. **Progress in the peeling-ballooning model of edge localized modes: Numerical studies of nonlinear dynamics.** *Physics of Plasmas*, 12(5):–, 2005.
- [65] D A Mossessian, P B Snyder, M Greenwald, J W Hughes, Y Lin et al. **H-mode pedestal characteristics and MHD stability of the edge plasma in Alcator C-Mod.** *Plasma Physics and Controlled Fusion*, 44(4):423, 2002.
- [66] P.B. Snyder, K.H. Burrell, H.R. Wilson, M.S. Chu, M.E. Fenstermacher et al. **Stability and dynamics of the edge pedestal in the low collisionality regime: physics mechanisms for steady-state ELM-free operation.** *Nuclear Fusion*, 47(8):961, 2007.
- [67] W.M. Tang, J.W. Connor and R.J. Hastie. **Kinetic-ballooning-mode theory in general geometry.** *Nuclear Fusion*, 20(11):1439, 1980.
- [68] P. B. Snyder and G. W. Hammett. **Electromagnetic effects on plasma microturbulence and transport.** *Physics of Plasmas*, 8(3):744–749, 2001.
- [69] Philip B. Snyder. **Gyrofluid Theory and Simulation of Electromagnetic Turbulence and Transport in Tokamak Plasmas.** PhD thesis, Princeton University, 1999.
- [70] F Jenko and W Dorland. **Nonlinear electromagnetic gyrokinetic simulations of tokamak plasmas.** *Plasma Physics and Controlled Fusion*, 43(12A):A141, 2001.
- [71] Bruce D Scott. **Computation of electromagnetic turbulence and anomalous transport mechanisms in tokamak plasmas.** *Plasma Physics and Controlled Fusion*, 45(12A):A385, 2003.

- [72] J. Candy. **Beta scaling of transport in microturbulence simulations.** *Physics of Plasmas*, 12(7):–, 2005.
- [73] J. Candy and R.E. Waltz. **An eulerian gyrokinetic-maxwell solver.** *Journal of Computational Physics*, 186(2):545–581, 2003.
- [74] N. Oyama, Y. Sakamoto, A. Isayama, M. Takechi, P. Gohil et al. **Energy loss for grassy ELMs and effects of plasma rotation on the ELM characteristics in JT-60U.** *Nuclear Fusion*, 45(8):871, 2005.
- [75] O. Gruber, H.-S. Bosch, S. Günter, A. Herrmann, A. Kallenbach et al. **Overview of ASDEX Upgrade results.** *Nuclear Fusion*, 39(9Y):1321, 1999.
- [76] B. LaBombard, J. W. Hughes, N. Smick, A. Graf, K. Marr et al. **Critical gradients and plasma flows in the edge plasma of Alcator C-Mod.** *Physics of Plasmas*, 15(5):056106, 2008.
- [77] J.W. Hughes, P.B. Snyder, J.R. Walk, E.M. Davis, A. Diallo et al. **Pedestal structure and stability in H-mode and I-mode: a comparative study on Alcator C-Mod.** *Nuclear Fusion*, 53(4):043016, 2013.
- [78] A. Diallo, W. Hughes, J. M. Greenwald, B. LaBombard, E. Davis et al. **Observation of edge instability limiting the pedestal growth in tokamak plasmas.** *Physical Review Letters*, 112:115001, Mar 2014.
- [79] P.B. Snyder, R.J. Groebner, J.W. Hughes, T.H. Osborne, M. Beurskens et al. **A first principles predictive model of the pedestal height and width: Development, testing, and ITER optimization with the EPED model.** In *IAEA FEC Proceedings, Daejon, Korea, October 2010.* THS/1-1. IAEA FEC, 2010. THS/1-1.
- [80] P.B. Snyder, R.J. Groebner, J.W. Hughes, T.H. Osborne, M. Beurskens et al. **A first-principles predictive model of the pedestal height and width: development, testing and ITER optimization with the EPED model.** *Nuclear Fusion*, 51(10):103016, 2011.
- [81] J.E. Kinsey, G.M. Staebler, J. Candy, R.E. Waltz and R.V. Budny. **ITER predictions using the GYRO verified and experimentally validated trapped gyro-Landau fluid transport model.** *Nuclear Fusion*, 51(8):083001, 2011.
- [82] F. Troyon, R. Gruber, H. Saurenmann, S. Semenzato and S. Succi. **MHD-limits to plasma confinement.** *Plasma Physics and Controlled Fusion*, 26(1A):209, 1984.
- [83] O. Sauter, C. Angioni and Y. R. Lin-Liu. **Neoclassical conductivity and bootstrap current formulas for general axisymmetric**

- equilibria and arbitrary collisionality regime.** *Physics of Plasmas*, 6(7):2834–2839, 1999.
- [84] B. D. Dudson, M. V. Umansky, X. Q. Xu, P. B. Snyder and H. R. Wilson. **BOUT++: a framework for parallel plasma fluid simulations.** *Computer Physics Communications*, 180:1467–1480, 2009.
- [85] X. Q. Xu, B. Dudson, P. B. Snyder, M. V. Umansky and H. Wilson. **Nonlinear simulations of peeling-balloonning modes with anomalous electron viscosity and their role in edge localized mode crashes.** *Physical Review Letters*, 105:175005, Oct 2010.
- [86] T.Y. Xia, X.Q. Xu and P.W. Xi. **Six-field two-fluid simulations of peeling-balloonning modes using BOUT++.** *Nuclear Fusion*, 53(7):073009, 2013.
- [87] R.J. Groebner, C.S. Chang, J.W. Hughes, R. Maingi, P.B. Snyder et al. **Improved understanding of physics processes in pedestal structure, leading to improved predictive capability for ITER.** *Nuclear Fusion*, 53(9):093024, 2013.
- [88] J.R. Walk, P.B. Snyder, J.W. Hughes, J.L. Terry, A.E. Hubbard et al. **Characterization of the pedestal in Alcator C-Mod ELMing H-modes and comparison with the EPED model.** *Nuclear Fusion*, 52(6):063011, 2012.
- [89] Hyunsun Han, Ohjin Kwon and J. Y. Kim. **Predictive modeling of pedestal structure in KSTAR using EPED model.** *Physics of Plasmas*, 20(10):–, 2013.
- [90] P. B. Snyder, T. H. Osborne, K. H. Burrell, R. J. Groebner, A. W. Leonard et al. **The EPED pedestal model and edge localized mode-suppressed regimes: Studies of quiescent H-mode and development of a model for edge localized mode suppression via resonant magnetic perturbations.** *Physics of Plasmas*, 19(5):–, 2012.

4

ELMY H-MODES ON C-MOD

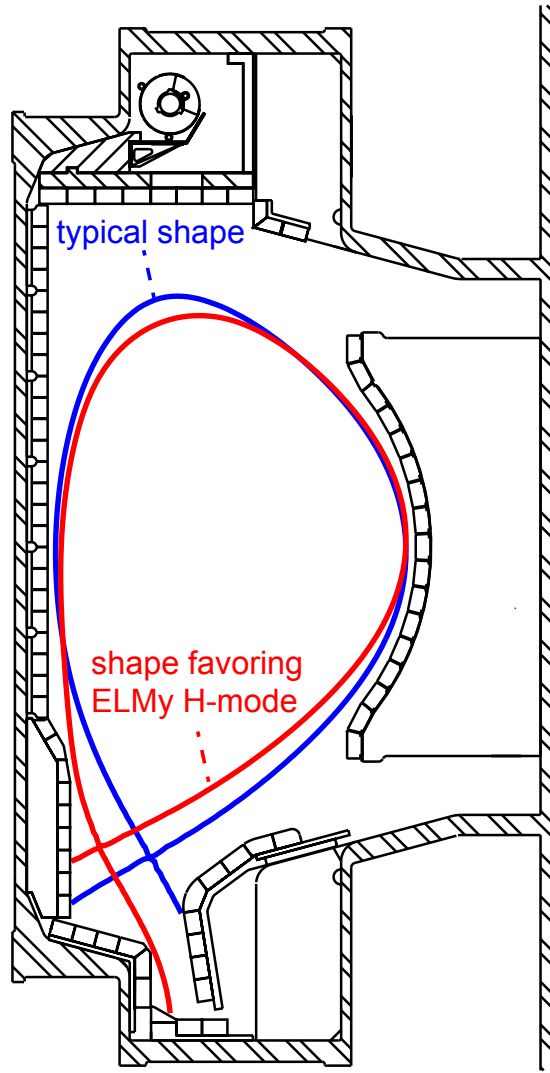
The ELMY H-mode [1, 2], described in section 2.1, is the most commonly accessed high-performance regime on major tokamak experiments. The bursty transport driven by ELMs provides sufficient relaxation of the particle confinement in H-mode to allow stationary operation without excessive impurity accumulation; as such, the ELMY H-mode is considered the baseline operating regime for ITER [3, 4]. However, on ITER-scale devices the pulsed heat loading associated with ELMs drives unacceptable levels of erosion and damage to plasma-facing wall and divertor materials [5, 6].

In light of the impact of large, deleterious ELMs on the ITER wall, and the profound impact of pedestal height on overall plasma performance [7, 8], a firm understanding of the physics governing the pedestal in high-performance regimes and their extrapolation to reactor-scale devices is of paramount importance to fusion research leading up to ITER operation. To that end, a Joint Research Target combining theory, experiment, and modeling efforts in the ELMY H-mode pedestal was undertaken [9, 10]. Notably, this effort saw the development of the EPED model [11, 12, 13], described in section 3.4, which predicts the pressure pedestal width and height preceding the ELM crash through a combination of constraints based on peeling-balloonning MHD instability [14, 15, 16] (section 3.2) and kinetic ballooning turbulence [17] (section 3.3). This chapter details the contributions from Alcator C-Mod to this joint effort [18] both in empirical studies of the ELMY H-mode pedestal, and in the implementation of the EPED model. C-Mod ELMY H-modes greatly expand the parameter space in which the EPED model is tested, reaching within a factor of two of the target pedestal pressure for ITER. The techniques developed in this analysis will subsequently be applied to I-mode pedestals in chapters 5 and 6.

4.1 ELMY H-MODE ACCESS & EXPERIMENTAL ARRANGEMENT

Typical H-modes on Alcator C-Mod do not exhibit the large Type-I ELMs customarily seen on other devices [20]. Instead, ELM-free H-modes tend to form at lower collisionalities, with high-density operation tending towards the continuously-regulated EDA H-mode rather than exhibiting discrete ELMs (see sections 2.2 and 2.3.2). However, by operating in a modified shape (see fig. 4.1) with low elongation, $\kappa \sim 1.4 - 1.55$, and low upper triangularity ($\delta_u \sim 0.15$) paired with high lower triangularity ($\delta_l > 0.75$) and a strike point on the diver-

Figure 4.1: C-Mod cross-section comparing the typical plasma shape (blue) to the altered shape favoring ELMy H-mode operation (red), developed in joint experiments with the JFT-2M tokamak [19]. ELMy H-mode access is favored by high lower triangularity and an outer strike point in the divertor slot, coupled with very low upper triangularity and elongation. This is thought to reduce the required edge pressure gradient and current to reach the peeling-balloonning boundary.



tor floor, regular ELMy H-mode operation is attainable. This comparatively weak shaping, developed in similarity experiments with the JFT-2M tokamak [21, 22], reduces the necessary pressure gradient and bootstrap current to reach the ideal peeling-balloonning MHD stability boundary (described in section 3.2), triggering the ELM. In this shape, new experiments on C-Mod [18] attained ELMy H-modes across a broad range in current (400 – 1100 kA) and field (3.5 – 8 T) with high-resolution pedestal data.

Pedestal profiles are taken with the edge Thomson scattering system, detailed in appendix A.1.2. The pedestal data is taken over steady ELMing phases to minimize the effects of random scatter in the data – an example of such a window, with line-averaged density \bar{n}_e , core and edge T_e , and divertor D_α signal (indicative of the ELM crash), is shown in fig. 4.2, with a comparison of the individual-frame fits to the ensemble shown in fig. 4.3. Strictly, models of the pedestal structure in ELMy H-mode predict the pedestal immediately preceding

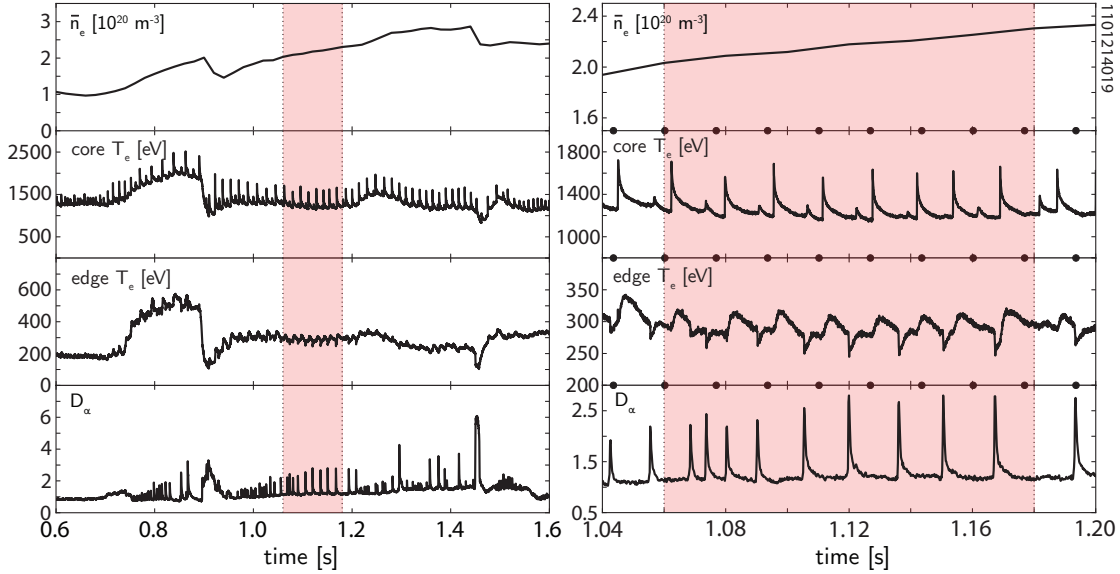


Figure 4.2: Example ELMy H-mode window (highlighted). Phases for study are selected for steady density (\bar{n}_e shown in the top trace), temperature (ECE T_e signals shown for the interior, at $r/a \sim 0.5$, and pedestal), and ELM cycles (D_α signal shown). The same modeling window is shown zoomed-in at the right. Note the strong perturbation to the edge temperature due to both the sawtooth crash and the ELM, while the interior temperature is perturbed only by the sawtooth (note that this trace is outside the sawtooth inversion radius). Thomson scattering frames are indicated by the black ticks on the axes – the ELM cycle is at a comparable frequency, ~ 60 Hz, to the TS system frame rate. This presents a difficulty for selecting data masked to the “peak” of the ELM cycle, necessitating long, steady ELMing phases for study.

the ELM crash, when the pedestal is most unstable to the ELM trigger. However, ELMs on C-Mod typically cycle at $60 - 100$ Hz, comparable to the repetition rate of the Thomson scattering system (as shown in figs. 4.2 and 4.3). This presents difficulties in resolving the pedestal with multiple frames per ELM and binning the data to the peaks of the ELM cycle. In most cases, pedestals are prepared in a single “ensemble average” utilizing all TS data in the window; in certain cases, a statistical set is also constructed using time slices during the last 20% of the ELM cycle as is typical for other machines. The results from this correction are discussed in section 4.2.

The electron density, temperature, and pressure profiles are fitted using a modified hyperbolic-tangent fit developed in [23]. In a general x, y space, the fitting function is expressed by

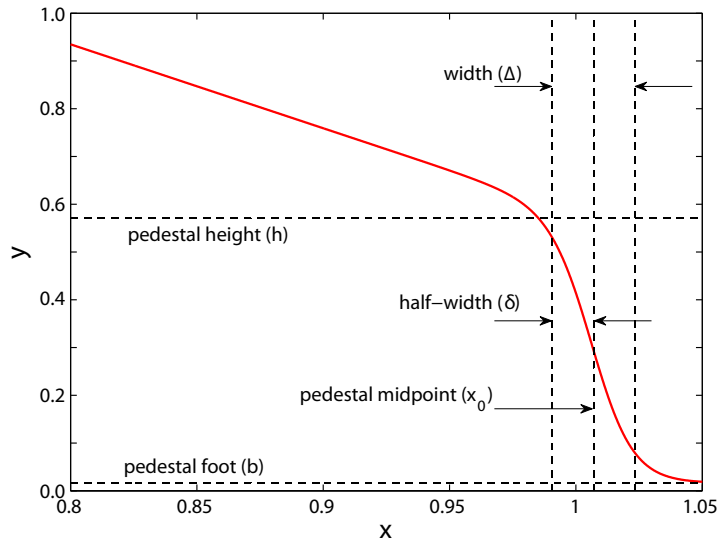
$$\begin{aligned} z &= \frac{x_0 - x}{\delta} \\ \text{mtanh}(\alpha, z) &= \frac{(1 + \alpha z)e^z - e^{-z}}{e^z + e^{-z}} \\ y &= \frac{h + b}{2} + \frac{h - b}{2} \text{mtanh}(\alpha, z) \end{aligned} \quad (4.1)$$

where x_0 is the pedestal midpoint, h and b are the height and baseline, and δ is the half-width (we use $\Delta = 2\delta$ as the “pedestal width”).



Figure 4.3: Comparison of fits for the n_e , T_e , and p_e pedestal width and height from Thomson scattering. Individual frames of data are shown as black points, with their average shown by the black line (errorbars indicated by the dashes). The ensemble-averaged fit is shown in red. The ensemble fit captures the average behavior in a steady ELMing phase well, while suppressing the random scatter found in individual frames of TS data. For comparison, ELM crash times in the window are indicated by vertical dashed lines.

Figure 4.4: Example pedestal illustrating the mtanh function used for pedestal fitting (eq. (4.1)), defining the parameters: height h , baseline b , midpoint x_0 , half-width δ /full width Δ . The inboard slope is characterized by the parameter α .



The inboard slope is encoded by the parameter α , with the multiplicative factor $1 + \alpha z$ providing an approximately linear profile inboard from the steep-gradient region ($z \gg 0$). This definition provides a smooth, continuous definition for the pedestal gradient throughout the profile, given by

$$\begin{aligned} \frac{dy}{dx} &= -\frac{h-b}{2\delta} \left[\frac{1 + \frac{\alpha}{4} (1 + 2z + e^{2z})}{\cosh^2(z)} \right] \\ \frac{dy}{dx} &\rightarrow -\frac{h-b}{2\delta} \left(1 + \frac{\alpha}{2} \right) \quad \text{as } x \rightarrow x_0, z \rightarrow 0 \\ \frac{dy}{dx} &\rightarrow -\frac{h-b}{2\delta} \alpha \quad \text{for } z \gg 0 \end{aligned} \tag{4.2}$$

with the peak gradient found analytically at x_0 ($z = 0$). Recent H-mode studies use the fitting parameter h as the figure-of-merit for the pedestal height; however, it is also common to express the pedestal height in terms of the evaluated value of the fit at the 95% poloidal flux surface. For the purposes of this document we denote the height taken from the fitting parameter h by the subscript ped , and values taken at the 95% flux surface by the subscript 95 .

Due to the ready availability of high-resolution electron density and temperature diagnostics, for the purposes of this section we assume equal ion and electron pressures, $p = 2n_e T_e$ (a viable approximation on C-Mod due to the relatively low impurity content found in ELMY H-modes, $Z_{\text{eff}} \sim 2$, and rapid ion-electron equilibration in H-mode pedestals on C-Mod [24]). All profiles are prepared using normalized poloidal flux for the abscissa, facilitating comparison to



Figure 4.5: Comparison of the measured pedestal widths for the n_e and T_e pedestals, differentiated for the low-, standard-, and high-field H-mode cases. Pedestal widths are similar for density and temperature, although on average the density pedestal is slightly wider. The error-weighted centroid of the dataset is shown by the star.



Figure 4.6: Comparison of the directly-measured pressure pedestal width and the EPED width Δ_Ψ , defined as the average of Δ_{n_e} and Δ_{T_e} . The widths trend quite closely to one another, although Δ_Ψ is systematically somewhat wider.

results from other machines and to the EPED model. For the purposes of the EPED model we also prepare an averaged width, defined by

$$\delta_\Psi = \frac{\delta_{n_e} + \delta_{T_e}}{2} \quad \Delta_\Psi = 2\delta_\Psi \quad (4.3)$$

a practice adopted in order to include in multi-machine studies devices in which the density and temperature profile measurements are generated by distinct diagnostics (rather than taking both from the Thomson scattering system, as is customary on C-Mod) and to more closely match the assumption of $\Delta_T = \Delta_n$ used in model profiles in EPED. As the density and temperature widths are quite close (although the density pedestal is, on average, slightly wider, as shown in fig. 4.5, with an average ratio of $\Delta_{T_e}/\Delta_{n_e} = 1.051$), the difference between Δ_Ψ and the directly-measured Δ_{P_e} is minimal – as shown in fig. 4.6, the two widths are well-correlated, with Δ_Ψ systematically slightly wider. ●

4.2 ELM CYCLE SYNCHRONIZATION

The common practice for modeling the ELMy H-mode pedestal is to take profile data immediately preceding the ELM crash (commonly, data from the last 20% of the ELM cycle), as this most closely corresponds to the pedestal profile at the stability limit associated with the ELM trigger. However, as the ELM cycle in H-mode on C-Mod is typically at a comparable repetition rate to the Thomson Scattering system (60 Hz), this practice is only possible on a subset of discharges,

with sufficiently long, steady H-mode phases, such that a sufficient number of frames in the desired time window can be found.

Figure 4.7: Comparison of the pressure pedestal height p_{ped} between the ensemble-averaged and ELM-synchronized profiles. On average, ELM synchronization results in a 10.8% increase in measured pedestal pressure, consistent with ELM losses observed on other machines. At lower pressures, ELMs are typically small enough that the perturbation is minimal; however, the distinction becomes important for the highest-pressure ELMs on C-Mod.



Figure 4.8: Comparison of the pressure at the 95% flux surface, p_{95} , between the ensemble-averaged and ELM-synchronized profiles. On average, ELM synchronization results in a 7.6% increase in the measured pressure. This is consistent with the ELM perturbation to the pedestal being largely restricted to the pedestal just within the steep-gradient region, with decreasing perturbation further into the plasma from the pedestal.



A comparison between the ensemble-averaged and ELM-synchronized pressure pedestals (pedestal height p_{ped} and the pressure at the 95% flux surface p_{95}) are shown in figs. 4.7 and 4.8. ELM synchronization finds an average 10.8% increase in the measured pressure p_{ped} , with a slightly lesser increase of 7.6% in p_{95} . This is consistent with the perturbation to the pressure pedestal by the ELM observed on other machines [5, 25]. The weaker perturbation due to the ELM crash observed at the 95% flux surface is also consistent with previous ELM observations – the ELM crash typically alters the pressure profile only in a region just inside the steep-gradient region, with minimal perturbation to profiles in the plasma interior.

4.3 ENGINEERING PARAMETER SCAN

The ELMY H-mode experiments presented here significantly expanded the parameter range available for the regime on Alcator C-Mod, including a broad scan in plasma current ($400 - 1100$ kA) and toroidal magnetic field (3.5, 5.4, 8.0 T), as well as a secondary scan of elongation ($1.45 < \kappa < 1.55$) and collisionality ($0.25 < \nu_{95}^* < 6$). This study entailed a factor of ~ 7 sweep in pedestal pressure – notably, this expanded the range of pressure pedestals tested against the EPED model to within a factor of two of the target pedestal thermal pressure for ITER [12].

4.3.1 I_p Scan

Trends of the density, temperature, and pressure pedestal widths and heights with plasma current are shown in fig. 4.9. Previous experiments in EDA H-modes [26] demonstrated a robust linear dependence of the pedestal density on plasma current; density is less constrained by current ELMY H-mode (fig. 4.9, (b)). A weak positive trend of the pedestal temperature (fig. 4.9, (d)) is seen, but is insufficient as a unique predictor. The combined pressure pedestal ($p = 2n_e T_e$) exhibits a $p_{95} \sim I_p$ trend, with some scatter.

The density and temperature pedestal widths individually show no systematic dependence on the plasma current. In the combined pressure pedestal width an inverse trend $\Delta_p \sim I_p^{-1}$ is discernable, although the pressure width varies little over the range of 3-5% of poloidal flux.

These observations are generally consistent with historical observations of the ELMY H-mode pedestal – the combined $p_{ped} \sim I_p$ and $\Delta_p \sim I_p^{-1}$ trends indicate a pressure gradient limit, $\nabla p \sim I_p^2$, consistent with pedestals limited by ballooning MHD instability, as described in section 3.2. Moreover, the pressure pedestal width trend is consistent with the previously-observed constraint from kinetic-balloonng turbulence, $\Delta_p \sim \beta_{p,ped}^{1/2} \sim \sqrt{p_{ped}}/I_p$, with the scatter in $\Delta_p \sim I_p^{-1}$ due to pressure variation. Previous experiments in EDA H-mode [27] have observed a trend of $p_{ped} \sim I_p^2$ with no dependence of the pedestal width on current; however, this is consistent with the ballooning limit of $\nabla p \sim I_p^2$, and may be attributed to the small range over which the pedestal width varies on a given machine. In the C-Mod cases as well, the pedestal width varies over a sufficiently small range that, to lowest order, the ballooning limit may be approximated as a limit on β_p at the pedestal top. This is shown in fig. 4.10 (see also fig. 2.2), showing the pedestal density versus temperature normalized to the poloidal field. This normalization accounts for plasma-current differences between points, as well as rendering hyperbolae in the parameter space as contours of fixed $\beta_{p,ped}$. At a given shaping, ELMY H-



Figure 4.9: Plasma current scalings of the density, temperature, and pressure pedestal widths and heights. Magnetic-field sets are differentiated by color. While the density and temperature pedestals independently show little systematic dependence of their widths on plasma current, the pressure pedestal width exhibits a $\Delta_{ped} \sim I_p^{-1}$ trend. The n_e and T_e pedestal heights both positively trend with current, although with significant scatter – inverse trends between the two are consistent with the zero'th-order approximation of MHD-limited ELMy pedestals lying on a curve of fixed $\beta_{p,ped}$ for a given shaping/field configuration. The pressure pedestal height shows a trend of $p_{ped} \sim I_p$, such that the pressure pedestal is consistent with the expected $\nabla p \sim I_p^2$ scaling.

Figure 4.10: Pedestal density vs. temperature normalized to poloidal field (accounting for variation in plasma current) such that hyperbolae in the parameter space are curves of fixed $\beta_{p,ped}$. At a given shaping, ELMY H-mode pedestals are to lowest order constrained to fixed $\beta_{p,ped}$, with stronger shaping allowing greater attainable β_p .

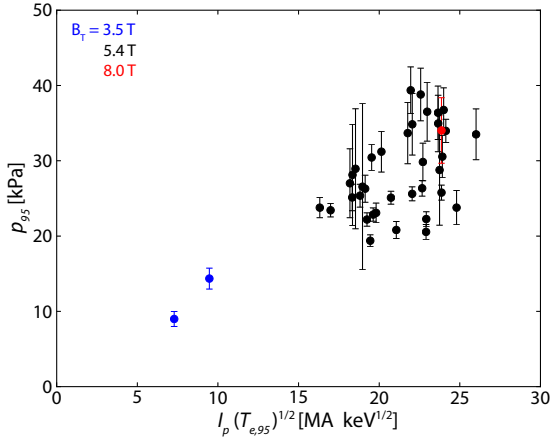
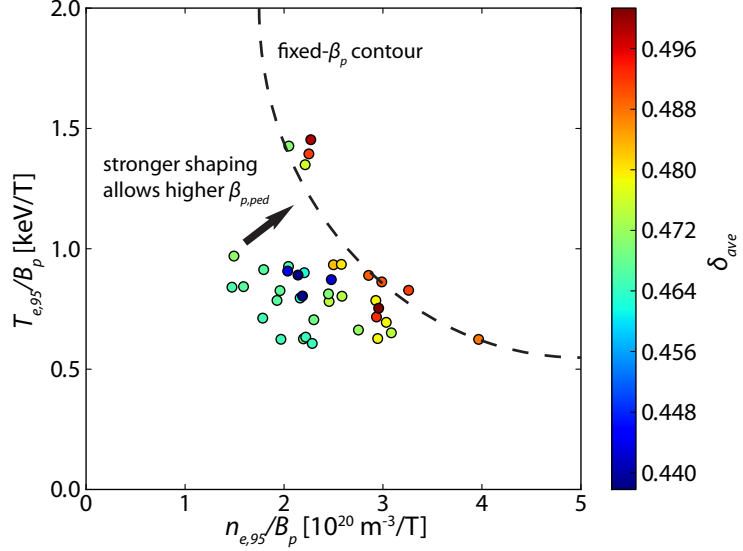


Figure 4.11: Pedestal pressure versus $I_p \sqrt{T_{e,95}}$ – effectively, the $p_{ped} \sim I_p^2 \rho_{i,pol}$ scaling predicted in [28].

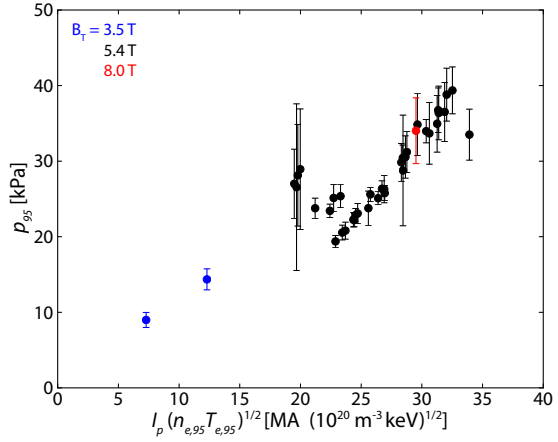


Figure 4.12: Pedestal pressure versus $I_p \sqrt{n_{e,95} T_{e,95}}$ – effectively, the $p_{ped} \sim I_p^2 \sqrt{\beta_{p,ped}}$ scaling predicted for a KBM-limited pedestal.

modes lie roughly on a contour of fixed $\beta_{p,ped}$, with stronger shaping allowing a higher attainable poloidal beta.

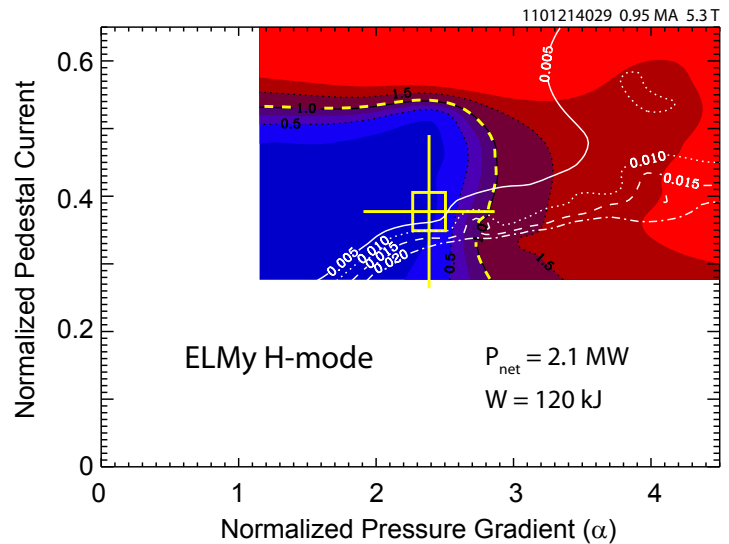
Pre-EPED models accounting for pressure-gradient limits assumed the pressure pedestal height would be governed simply by $p_{ped} \sim \nabla p \times \Delta_p$, with ∇p limited by MHD stability and a separate constraint for the pedestal width. The ballooning limit was couched by Saibene *et al.* [29] as $\nabla p \sim I_p^2 f_{sh}$, where f_{sh} is a function describing the edge magnetic shear. Taking the pedestal width to be governed by poloidal gyroradius $\rho_{i,pol} \sim \sqrt{T_e}/I_p$ (as was done by Saibene *et al.*), this predicts $p_{ped} \sim I_p \sqrt{T_{e,ped}}$, as shown in fig. 4.11. However, the putative scaling of the pedestal width on $\rho_{i,pol}$ is readily conflated with the KBM-limited trend of pedestal width with $\beta_{p,ped}^{1/2} \sim \sqrt{n_e T_e}/I_p$. Assuming a $\beta_{p,ped}$ limit on the pedestal width,

we predict $p_{ped} \sim I_p \sqrt{n_{e,ped} T_{e,ped}}$, shown in fig. 4.12 to be a significantly better predictor of the pedestal height.

4.4 EPED MODEL PREDICTIONS

The EPED model, described in section 3.4, combines pedestal limits based on coupled peeling-balloonning MHD instabilities [14, 15, 16] and kinetic-balloonning mode turbulence [17]. An example of MHD and KBM calculations of the type used by EPED is shown in fig. 4.13. The red-blue contour indicates the peeling-balloonning stability calculated by ELITE (described in section 3.2.3), with the yellow dash indicating the stability boundary – in this case, the pedestal is limited by intermediate-n balloonning modes (see fig. 3.4), as is expected at the higher collisionality typically seen on C-Mod. White contours indicate the KBM stability calculated by BALOO (see section 3.3). To within error bars, the ELMY H-mode pedestal is at both the peeling-balloonning and kinetic-balloonning stability boundaries, as is expected for pedestals at the ELM threshold. Calculations of this type are shown in more detail in chapter 6.

Figure 4.13: Calculation of the peeling-balloonning MHD stability contour from ELITE for an ELMY H-mode pedestal on C-Mod. To within error bars, the pedestal lies on the peeling-balloonning boundary. The comparatively higher collisionality typical of C-Mod H-mode pedestals pushes the MHD behavior of the pedestal towards higher-n, pure-balloonning modes, although moderate-n coupled modes in the “nose” of the stability contour are also common.



These models set two distinct constraints on the pedestal width and height, with peeling-balloonning MHD predicting $p_{ped} \sim \Delta^{3/4}$ and kinetic-balloonning turbulence predicting $p_{ped} \sim \Delta^2$ (see fig. 3.5). The unique intersection of these two constraints provides a predictive value for the pedestal width and height. The most recent version of the model, EPED1.63, utilizes a modified gyrokinetic calculation compared to the standard EPED1.6 (section 3.4.2) to more accurately constrain the diamagnetic stabilization of higher-n peeling-balloonning modes, necessary for the balloonning modes that typically limit the pedestal on C-Mod due to the high collisionality. A comparison be-

tween the observed and predicted pedestal parameters is presented here.

4.4.1 Pedestal Height

A comparison between the pressure pedestal height predicted by EPED1.63 and the observed height is shown in fig. 4.14. While most measured pedestals lie within the $\pm 20\%$ expected error in the EPED prediction (indicated by the grey band in fig. 4.14), the EPED model systematically over-predicts the pedestal pressure, corresponding on average ratio of measured to predicted pedestal heights of 0.835 ± 0.036 , indicated by the red dashed line.

Figure 4.14: Pressure pedestal height predicted by EPED1.63 versus the measured (ensemble-averaged) pedestal height, color-coded by magnetic field set. The grey band indicates perfect agreement, $\pm 20\%$ typical prediction accuracy for EPED. The EPED model systematically over-predicts the pedestal pressure, with an average match of 0.835 ± 0.036 (indicated by the red line).



The discrepancy between the predicted and measured pedestal heights may be attributed (at least in part) to the use of pedestal measurements averaged across the entire ELM cycle (“ensemble-averaged”). As discussed in section 4.2, models of the pedestal structure (including EPED) most closely correspond to the pedestal structure immediately preceding the ELM crash, where the pedestal is most unstable to the ELM trigger. A subset of ELMy H-modes are prepared with ELM-synchronized data, shown in fig. 4.15 with the corresponding ensemble-averaged points for comparison. The prediction accuracy is substantially improved, with an average ratio of measured to predicted pedestal heights of 0.934 ± 0.066 , well within the anticipated $\pm 20\%$ accuracy of the EPED prediction. As expected, the modification to the measured pedestal pressure by ELM synchronization is minimal at lower pedestal pressures, but becomes substantial at higher pedestal pressures (> 35 kPa) as ELM losses increase proportionally with the pedestal stored energy.

Figure 4.15: Pressure pedestal height predicted by EPED1.63 versus measured, ELM-synchronized pedestal height (red, with corresponding ensemble-average points shown in black). The grey band indicates perfect agreement, $\pm 20\%$ typical prediction accuracy for EPED. ELM synchronization brings the measured pedestal height into better agreement with EPED predictions, with a correspondence of 0.934 ± 0.066 (indicated by the red dash).



The EPED model still systematically slightly over-predicts the pedestal pressure, however – this is potentially due to the strong sensitivity of the stability calculation to diamagnetic effects, which tend to stabilize higher- n ballooning modes. As diamagnetic effects are substantial in the relatively collisional pedestal found in H-modes on C-Mod, a careful accounting of these effects is necessary for accurate prediction – use of a slightly weaker diamagnetic stabilization model brings the prediction into generally better agreement with C-Mod data.

4.4.2 Pedestal Width

While historically a number of models for the pedestal width (see section 3.1) have been examined, the most uniformly successful has been an expected scaling of pedestal width with poloidal beta at the pedestal top ($\beta_{p,ped}$), observed on several machines [9], and shown to follow from a critical-gradient limit in the edge pressure profile established by kinetic-balloonning mode (KBM) turbulence. Including magnetic shear stabilization, this takes the form $\Delta = c\beta_{p,ped}^{1/2}$, where c is, strictly, a weakly-varying function of a number of plasma parameters [11]. This constraint on the pedestal width and height is utilized in the EPED model, coupled with peeling-balloonning MHD stability limits to set a unique constraint on the pedestal structure at the ELM crash.

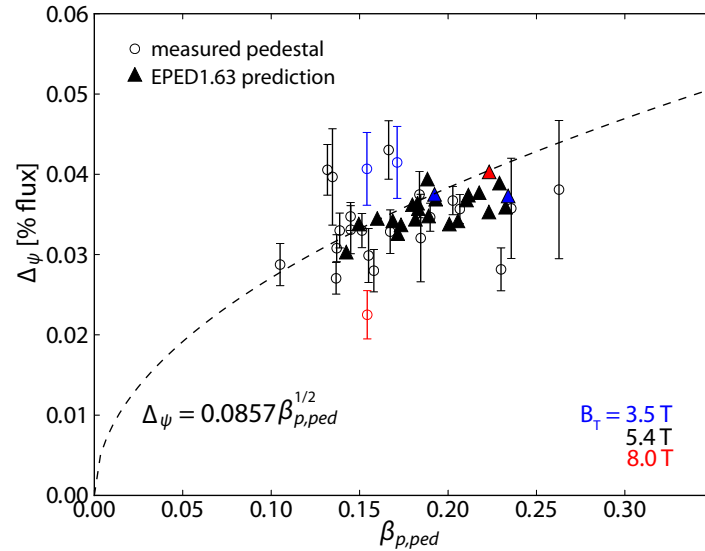
An evaluation of this scaling with ensemble-averaged data is shown in fig. 4.16, with a fitted scale factor of $\langle c \rangle = 0.0857 \pm 0.0024$, consistent with previously-observed scalings. The earliest versions of the EPED model used this simple constraint as the second condition on the pedestal width and height, using an experimentally-determined fixed scale factor. The newest version of the model self-consistently

calculates the scale factor from gyrokinetic considerations of the KBM turbulence; however, the result is quantitatively similar. A comparison of the experimental versus the EPED1.63-predicted pedestals in $\Delta_\psi - \beta_{p,ped}$ space is shown in fig. 4.17.

Figure 4.16: Ensemble-averaged EPED width Δ_ψ (eq. (4.3)) versus $\beta_{p,ped}$, color-coded by field set. The expected scaling from the KBM limit, $\Delta_\psi = c\beta_{p,ped}^{1/2}$, is shown with a scale factor of 0.0857, consistent with observations in previous experiments.



Figure 4.17: Comparison of EPED1.63-predicted pedestal width Δ_ψ and height $\beta_{p,ped}$ with the corresponding ensemble-averaged experimental points, with the KBM scaling $\Delta_\psi = c\beta_{p,ped}^{1/2}$. Though the EPED predictions were calculated with a self-consistent treatment of the scale factor c as a weakly-varying function of plasma parameters, the result is quantitatively similar to the simple fixed scale factor.



Application of the ELM synchronization technique does not significantly alter this result, although the pedestal pressure (i.e., $\beta_{p,ped}$) is significantly increased in the last 20% of the ELM cycle. Recent research in the inter-ELM development of the pedestal suggests that the KBM saturates early in the ELM cycle, clamping the pedestal to the $\beta_{p,ped}^{1/2}$ limit – the pedestal is then thought to evolve along this limit until the peeling-balloonning boundary is also reached, triggering the ELM. Observations on DIII-D [30] are consistent with this picture, and with both the pedestal width and height growing at clamped gra-

Figure 4.18: Comparison of ensemble-averaged (black) and ELM-synchronized (Red) pedestal width and height, compared to the KBM constraint. The $\Delta_\psi = 0.0857\beta_{p,ped}^{1/2}$ scaling found in the ensemble-averaged case is shown in black, while the minor modification of $\Delta_\psi = 0.0896\beta_{p,ped}^{1/2}$ for the ELM-synced cases is shown in red.



Figure 4.19: ELM-synchronized pedestals, with data binned by $\beta_{p,ped}$ for clarity. The data are fitted by $\Delta_\psi = (0.0851 \pm 0.003)\beta_{p,ped}^{1/2}$ (black), or by $\Delta_\psi = (0.0824 \pm 0.015)\beta_{p,ped}^{0.49 \pm 0.11}$ using a more general power law.



dient prior to the ELM. Similarly, observations on C-Mod observed a fluctuation consistent with the KBM saturating early in the ELM cycle [31], although the pressure pedestal height appeared to saturate earlier in the ELM cycle [19]. Consistent with this, ELM-synchronized pedestals exhibit wider, taller pedestals on average (see also fig. 4.21 for pedestal widths), with a similar constraint imposed by the KBM compared to the ensemble-averaged result.

A comparison of the ensemble-averaged and ELM-synced pedestals in $\Delta_\psi - \beta_{p,ped}$ space is shown in fig. 4.18, with the ELM-synced pedestals fitted to a scale factor $\langle c \rangle = 0.0896 \pm 0.0034$. The data may be clarified significantly by taking an error-weighted average within fixed bins in $\beta_{p,ped}$ as well, shown in fig. 4.19, which tends to reduce the influence of strongly-outlying points on the fit. Again, the fit is

Figure 4.20: Measured EPED pedestal width $\Delta_\psi = (\Delta_{n_e} + \Delta_{T_e})/2$ in ensemble-averaged pedestals versus EPED1.63-predicted pedestal widths. Magnetic-field groups are indicated by color. The dashed line indicates perfect agreement with EPED prediction. Pedestal widths are robust on C-Mod, restricted to $\sim 2 - 5\%$ of poloidal flux. The EPED model reproduces this trait within expected prediction error.

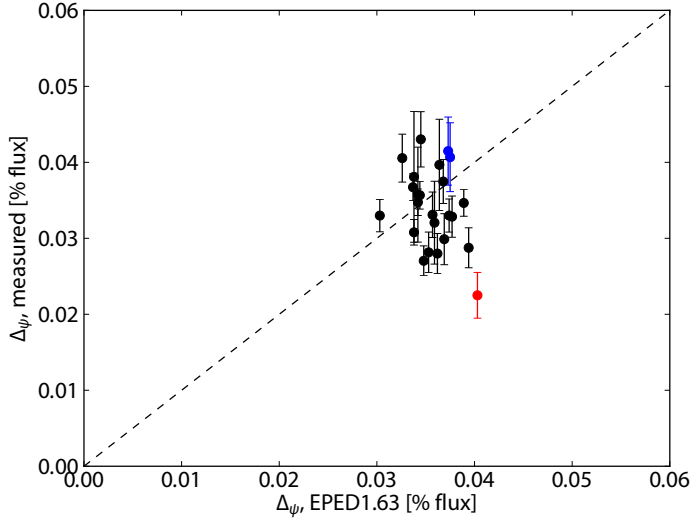
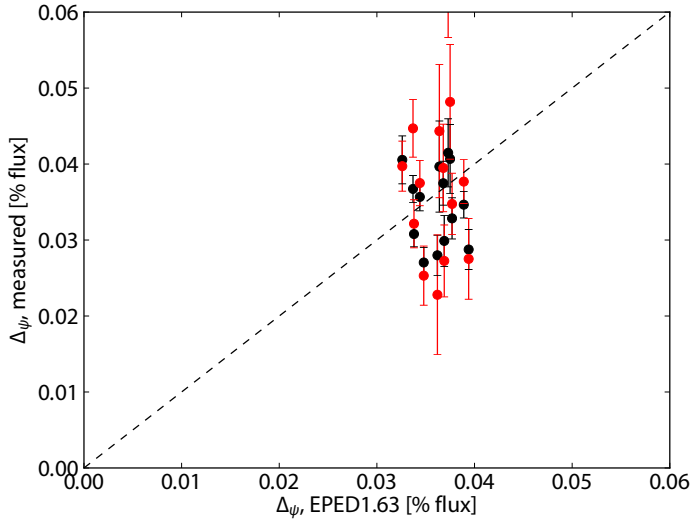


Figure 4.21: Measured pedestal width Δ_ψ versus EPED1.63 predicted width. Ensemble-averaged points are shown in black, while corresponding ELM-synchronized points are shown in red. ELM-synced pedestals are typically somewhat wider, although still lie within the $\pm 20\%$ expected error for EPED.



quantitatively very similar – the data fit well to $\Delta_\psi = c\beta_{p,ped}^{1/2}$ with $\langle c \rangle = 0.0851 \pm 0.003$. Alternately, we may use a more general power-law fit $\Delta_\psi = c_1 \beta_{p,ped}^{c_2}$, with which we find $\langle c_1 \rangle = 0.0824 \pm 0.015$ and $\langle c_2 \rangle = 0.49 \pm 0.11$, closely reproducing the $\beta_{p,ped}^{1/2}$ model. The fitting results are quite consistent across these methods, demonstrating the robustness of the KBM model for the pedestal width and its insensitivity to the details of data preparation.

Prediction of the pedestal width is difficult, given the robust width of the pressure pedestal (typically 3-5% of poloidal flux space, corresponding to ~ 5 mm on C-Mod). The EPED model correctly recovers this robustness (within the expected $\pm 20\%$ prediction error), as shown in fig. 4.20. As seen in fig. 4.18, ELM-synchronized pedestals are typically somewhat wider than their ensemble-averaged counterparts, commensurate with the increased $\beta_{p,ped}$ at the maximum of

Figure 4.22: Density pedestal width versus pedestal density. Contrary to expectations from neutral-penetration models (see section 3.1.2), there is little systematic variation of the density pedestal width and height.



the ELM cycle while the pedestal structure is limited throughout most of the ELM cycle by KBM turbulence. A comparison of the ELM-synced pedestal widths versus EPED1.63 prediction is shown in fig. 4.21.

4.5 PEDESTAL WIDTH RESPONSE

4.5.1 Alternate Width Models

Early models for the pedestal width (see section 3.1) led to several easily-testable predictions – first, neutral-penetration models (section 3.1.2) predict a scaling of the density pedestal $\Delta n_e \sim 1/n_{e,ped}$, while transport-driven models predict temperature/pressure pedestal widths limited by poloidal gyroradius, or equivalently the banana orbit width (section 3.1.3). The density pedestal width is shown against pedestal density in fig. 4.22 – while there is high scatter in the data, with both the pedestal density and measured width Δn_e spanning more than a factor of two in variation, the densest region in the dataset shows a weak positive trend between density pedestal width and height. This is directly contrary to the predictions from simple neutral-penetration models; however, it is consistent with previous observations in EDA H-mode [27]. The measured temperature and pressure widths ΔT_e and Δp_e are shown against $\rho_{i,pol}$ (the ion gyroradius evaluated with the poloidal field) in fig. 4.23. In the case of the temperature pedestal width, no systematic variation with $\rho_{i,pol}$ is seen. A possible weak trend for the pressure pedestal width is seen, with comparable spread to that seen in the pressure pedestal width versus $\beta_{p,ped}$. However, as there is significant covariance between $\rho_{i,pol} \sim \sqrt{T_e}/I_p$ and $\beta_{p,ped} \sim \sqrt{n_e T_e}/I_p$, and the width scaling with $\beta_{p,ped}$ is seen to be a superior

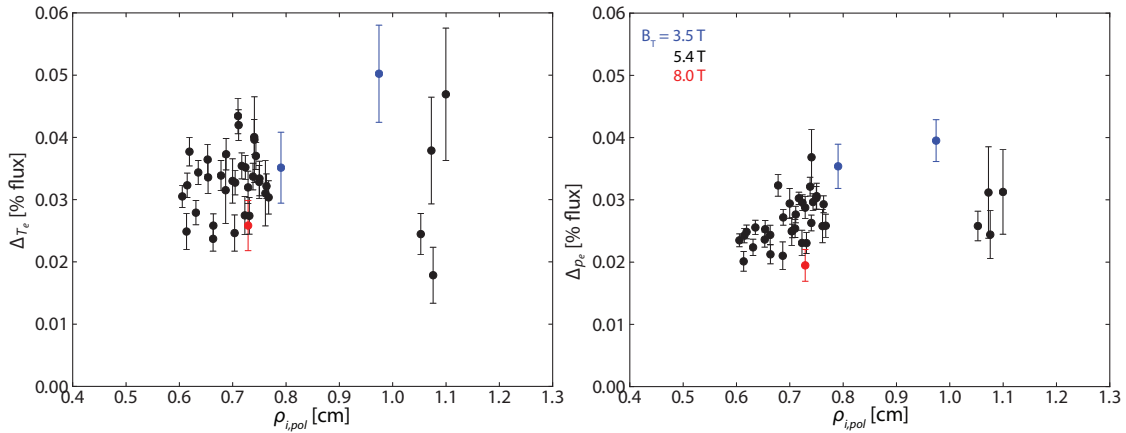


Figure 4.23: Temperature and pressure pedestal widths versus poloidal gyroradius. The temperature pedestal width shows no systematic variation with $\rho_{i,\text{pol}}$. A weak trend is possible in the pressure pedestal width, comparable to the the trend of $\Delta_p \sim \beta_{p,\text{ped}}^{1/2}$ (due to the strong covariance between $\rho_{i,\text{pol}}$ and $\beta_{p,\text{ped}}$). However, this trend is overruled in favor of a poloidal beta scaling by other observations.

predictor (see fig. 4.12) this model should be discarded in favor of the $\Delta \sim \beta_{p,\text{ped}}^{1/2}$ scaling from KBM physics. This is consistent with results from experiments designed to distinguish between $\rho_{i,\text{pol}}$ and $\beta_{p,\text{ped}}$ dependencies via isotope variation to exploit the mass dependence in $\rho_{i,\text{pol}}$ [32] or pumping experiments to independently vary pedestal density and temperature at fixed pressure [33, 34].

4.5.2 Normalized Pedestal Width

As detailed in section 4.4.2, the scale factor in the dominant width scaling in ELMY H-mode, $\Delta \sim \beta_{p,\text{ped}}^{1/2}$, is most properly a weakly varying function of plasma shaping, collisionality, and other dimensionless parameters: $\Delta_\psi = G(\nu^*, \varepsilon, \dots) \beta_{p,\text{ped}}^{1/2}$ [12] (cf. section 3.3). These secondary dependencies in G may be examined by normalizing the pedestal width (here we use the EPED width, Δ_ψ , from eq. (4.3)) to the fitted scaling $\Delta_\psi = 0.0857 \beta_{p,\text{ped}}^{1/2}$ (see fig. 4.16).

Normalized pedestal widths are shown against the range in toroidal fields in fig. 4.24. The high scatter in the normalized pedestal widths at standard field (5.4 T), along with the difficulty in attaining usable datapoints at low and high field, renders it difficult to conclusively establish a secondary scaling of the pedestal width with toroidal field. The broader pedestal at lower field is qualitatively consistent with modeling efforts [34, 35]; however, the observation of broader pedestals at low current [26] complicates this observation due to the strong co-variance between field and current in the 3.5 T range.

Similarly, normalized pedestal widths are shown against the plasma shaping parameters – upper and lower triangularity δ_u , δ_l , average triangularity $\delta_{\text{ave}} = (\delta_l + \delta_u)/2$, and elongation κ – in fig. 4.25. No

Figure 4.24: Scalings of the pedestal width Δ_ψ , normalized to the dominant scaling $\Delta_\psi = 0.0857\beta_{p,ped}^{1/2}$, with the applied toroidal field B_T . Although the high scatter at standard B_T and the sparsity of data at low and high field makes a conclusive scaling difficult, there is some indication of an inverse relation of pedestal width with toroidal field.

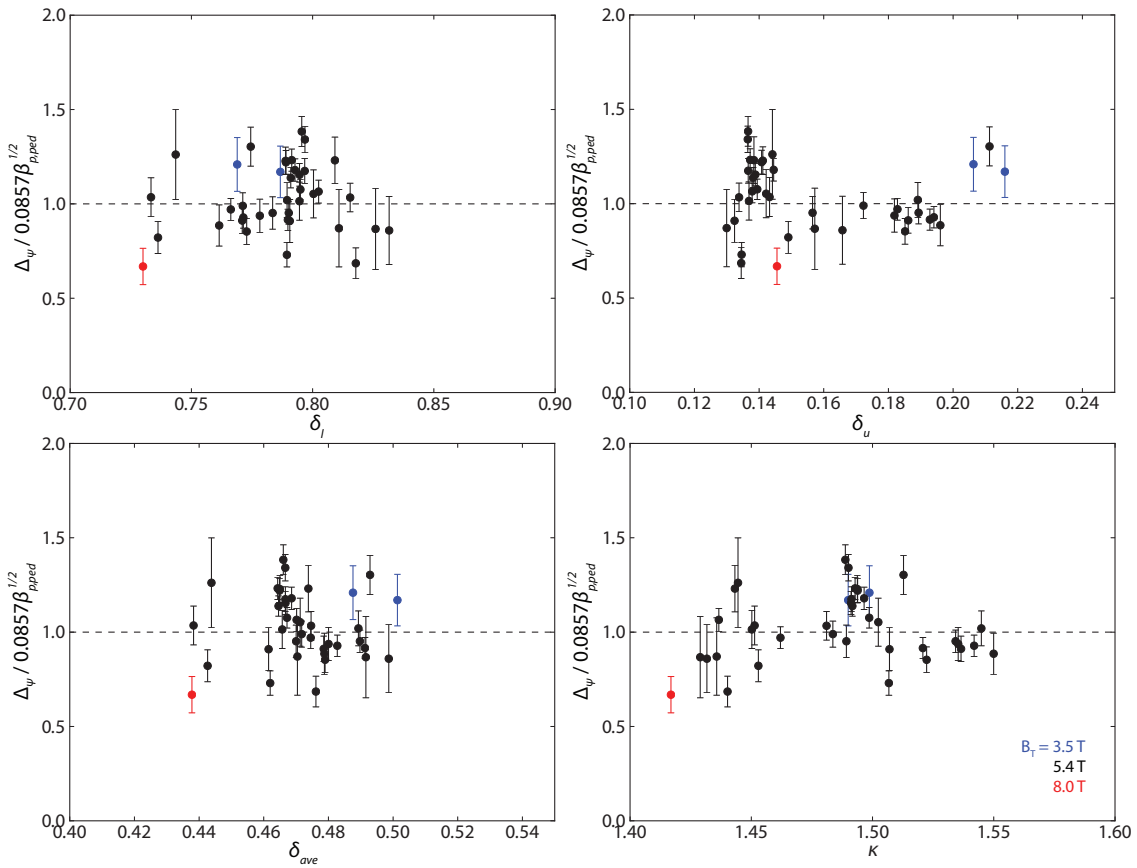
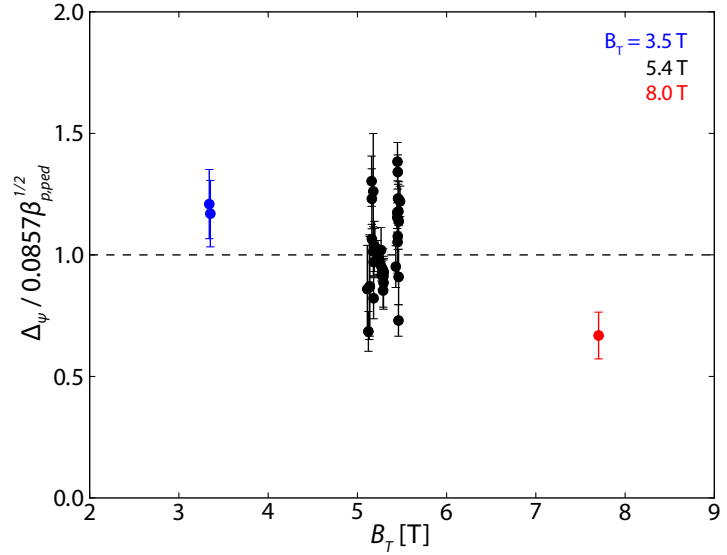


Figure 4.25: Scalings of the pedestal width Δ_ψ normalized to the dominant scaling $\Delta_\psi = 0.0857\beta_{p,ped}^{1/2}$, with plasma shaping: upper, lower, and average triangularity (δ_l , δ_u , $\delta_{ave} = (\delta_u + \delta_l)/2$), and elongation κ . No strong trend with shaping parameters is seen – rather, the influence of plasma shaping is exhibited by increased $\beta_{p,ped}$ and pedestal width due to increased stability of peeling-balloonning MHD.

Figure 4.26: Scaling of the normalized pedestal width $\Delta_\psi / 0.0857 \beta_{p,ped}^{1/2}$ versus pedestal collisionality v_{95}^* . Low, standard, and high-field sets are indicated in blue, black, and red respectively. No systematic variation is observed.



Figure 4.27: Scaling of the normalized pedestal width $\Delta_\psi / 0.0857 \beta_{p,ped}^{1/2}$ with normalized pedestal gyroradius ρ_{95}^* . Low, standard, and high-field sets are indicated in blue, black, and red respectively. No systematic variation is seen.



clear secondary dependence of the normalized pedestal width (that is, in the scale function $G(v^*, \varepsilon, \dots)$) is seen in shaping: δ_l , δ_{ave} , and κ exhibit no trend, while δ_u is unclear with the broadest widths (compared to the $\sim 0.0857 \beta_{p,ped}^{1/2}$ fit) at both the low and high extremes of the range in δ_u . Rather, the shaping dependence manifests as increased poloidal beta, and secondarily pedestal width, at stronger shaping – increased shaping is known to have a stabilizing effect on ballooning MHD modes, increasing the normalized pressure gradient α_{MHD} at which the instability is triggered. However, as the shaping range available for ELMY H-modes on C-Mod is restricted, weak dependences of the pedestal width on shaping may go undetected.

Pedestal collisionality v_{95}^* is anticipated as a controlling term in the scale function G , due both to its role in controlling ionization rate

and neutral penetration, and its influence on bootstrap current density and the accompanying MHD effects in the pedestal. However, across a broad range on collisionality, $0.25 < \nu_{95}^* < 6$, no systematic variation in the normalized pedestal width is seen (see fig. 4.26). The highest collisionality points were obtained in cold, low-field discharges, possibly conflating the elevated pedestal width (relative to the $\sim 0.0857\beta_{p,ped}^{1/2}$ fit) with possible broadening at reduced B_T .

While a primary dependence of the pedestal width on the gyroradius is ruled out (see the discussion in section 4.5.1 and fig. 4.12), a secondary gyroradius dependence in addition to the β_p scaling is still possible – for example, $\Delta_{ped} \sim \rho_{i,pol}^{0.2} \beta_{p,ped}^{0.5}$ found by Urano *et al.* [32]. However, when the scale function G is examined via trends of the normalized pedestal width versus normalized gyroradius ρ_{95}^* , shown in fig. 4.27, no systematic dependence is seen. Notably, the strong outlier for ρ^* – the high- B_T case, shown to have a narrow pedestal compared to the expected scaling – is nevertheless within the range of normalized width for the bulk of the dataset. As such, no distinct dependence of the normalized width (equivalently, $G(\nu^*, \varepsilon, \dots)$) can be discerned from the data. •

4.6 CONCLUSIONS

ELMy H-mode experiments on C-Mod reach the highest magnetic field and pedestal thermal pressure of any tokamak, reaching within a factor of ~ 2 of the target pressure for ITER (see fig. 4.28). As part of a DOE Joint Research Target [9], these experiments tested the EPED model series [11] for ELMy H-mode pedestal width and height, greatly expanding the parameter space in which the model has been implemented [18]. The newest version of EPED, EPED1.63 (a minor modification to EPED1.6 to account for strong diamagnetic effects on C-Mod) accurately predicts the pressure pedestal height, particularly when pedestal data is masked to time frames immediately preceding ELM crashes – a practice that, despite diagnostic difficulties on C-Mod, produces data most closely corresponding to the pedestal structure at the point of ELM instability. Although systematic prediction of the pedestal width on C-Mod is difficult due to the narrow range over which it varies, the EPED prediction for Δ_ψ matches experimental results to within the expected $\sim 20\%$ error.

The pedestal width is well-described by the prediction used by EPED1.6 based on the KBM, $\Delta_\psi = G(\nu^*, \varepsilon, \dots) \beta_{p,ped}^{1/2}$, where $G(\nu^*, \varepsilon, \dots)$ is a weakly varying function, $G \approx .0857$ – matching the fitted result from multiple machines [9]. Secondary scalings of the pedestal width, discerned by normalizing the pedestal width to the dominant $\beta_{p,ped}$ dependence, with magnetic field, ν^* , ρ^* , and shaping parameters are minimal over the available range in the data set. Conversely, the pedestal width is not well-described by alternate models not based on

Figure 4.28: EPED predictions versus measured pressure pedestal heights from DIII-D and C-Mod, spanning a significant range of pedestal pressures. Notably, C-Mod pressure pedestals reach within a factor of ~ 2 of the predicted ITER pedestal height. Reproduced from [19]



the KBM-driven $\beta_{p,ped}$ dependence: the density pedestal width does not exhibit a $\Delta_{n_e} \sim n_{e,ped}$ trend expected from neutral-penetration models, while the temperature and pressure pedestals do not scale clearly with $\rho_{i,pol}$. The temperature pedestal width shows no trend with poloidal gyroradius, while the pressure pedestal does not show a trend independent of the $\beta_{p,ped}$ scaling ($\rho_{i,pol}$ and $\beta_{p,ped}$ are difficult to discern from one another without careful operational control).

Examined over a broad range in plasma current, the pressure pedestal height exhibits a trend $p_{ped} \sim I_p$, while the pressure pedestal width trends as $\Delta_{p_e} \sim I_p^{-1}$. This is consistent with the expected trend of $\nabla p_{ped} \sim I_p^2$ from ballooning MHD stability. More carefully, the pedestal height is well-predicted by $p_{ped} \sim \nabla p \times \Delta_p$ – taking $\nabla p \sim I_p^2$ from MHD stability and the pedestal width $\Delta_p \sim \beta_{p,ped}^{1/2} \sim \sqrt{n_{e,ped} T_{e,ped}} / I_p$ gives $p_{ped} \sim I_p \sqrt{n_{e,ped} T_{e,ped}}$ (see fig. 4.12), which matches the observed pressure pedestal height quite well.

The results shown in this chapter firmly establish that the pedestal in ELMY H-modes on C-Mod are limited by the physics assumed in the EPED model – namely, peeling-balloonning MHD modes and kinetic-balloonning turbulence. The ELM behavior and pedestal dynamics observed here are of the familiar kind, characteristic of type-I ELMs on larger devices. This places C-Mod on a common physics footing with other machines, and indicates that the approach used in EPED can, with reasonable confidence, be extrapolated to ITER operation. The empirical and computational tests demonstrated in this chapter may also be meaningfully applied to examine the structure and limiting physics of I-mode, shown in chapters 5 and 6. *

BIBLIOGRAPHY

- [1] F. Wagner, G. Becker, K. Behringer, D. Campbell, A. Eberhagen et al. **Regime of improved confinement and high beta in neutral-beam-heated divertor discharges of the ASDEX tokamak.** *Physical Review Letters*, 49(19):1408–1412, Nov 1982.
- [2] M Keilhacker, G Becker, K Bernhardi, A Eberhagen, M ElShaer et al. **Confinement studies in L and H-type ASDEX discharges.** *Plasma Physics and Controlled Fusion*, 26(1A):49, 1984.
- [3] ITER Physics Expert Group on Confinement, Transport and ITER Physics Expert Group on Confinement Modelling and Database and ITER Physics Basis Editors. **Chapter 2: Plasma confinement and transport.** *Nuclear Fusion*, 39(12):2175, 1999.
- [4] M. Shimada, D.J. Campbell, V. Mukhovatov, M. Fujiwara, N. Kirneva et al. **Chapter 1: Overview and summary.** *Nuclear Fusion*, 47(6):S1, 2007.
- [5] A Loarte, G Saibene, R Sartori, D Campbell, M Becoulet et al. **Characteristics of type I ELM energy and particle losses in existing devices and their extrapolation to ITER.** *Plasma Physics and Controlled Fusion*, 45(9):1549, 2003.
- [6] G Federici, A Loarte and G Strohmayer. **Assessment of erosion of the ITER divertor targets during type I ELMs.** *Plasma Physics and Controlled Fusion*, 45(9):1523, 2003.
- [7] J.E. Kinsey, G.M. Staebler, J. Candy, R.E. Waltz and R.V. Budny. **ITER predictions using the GYRO verified and experimentally validated trapped gyro-Landau fluid transport model.** *Nuclear Fusion*, 51(8):083001, 2011.
- [8] E.J. Doyle, W.A. Houlberg, Y. Kamada, V. Mukhovatov, T.H. Osborne et al. **Chapter 2: Plasma confinement and transport.** *Nuclear Fusion*, 47(6):S18, 2007.
- [9] R.J. Groebner, C.S. Chang, J.W. Hughes, R. Maingi, P.B. Snyder et al. **Improved understanding of physics processes in pedestal structure, leading to improved predictive capability for ITER.** *Nuclear Fusion*, 53(9):093024, 2013.
- [10] R. Groebner, C. Chang, P. Diamond, J. Hughes, R. Maingi et al. **Fusion energy science joint facilities and theory research target final report.** Technical report, Department of Energy Office of Science, 2011.

- [11] P. B. Snyder, R. J. Groebner, A. W. Leonard, T. H. Osborne and H. R. Wilson. **Development and validation of a predictive model for the pedestal height.** *Physics of Plasmas*, 16(5):056118, 2009.
- [12] P.B. Snyder, R.J. Groebner, J.W. Hughes, T.H. Osborne, M. Beurskens et al. **A first-principles predictive model of the pedestal height and width: development, testing and ITER optimization with the EPED model.** *Nuclear Fusion*, 51(10):103016, 2011.
- [13] P.B. Snyder, N. Aiba, M. Beurskens, R.J. Groebner, L.D. Horton et al. **Pedestal stability comparison and ITER pedestal prediction.** *Nuclear Fusion*, 49(8):085035, 2009.
- [14] P.B. Snyder, H.R. Wilson, J.R. Ferron, L.L. Lao, A.W. Leonard et al. **ELMs and constraints on the H-mode pedestal: peeling–ballooning stability calculation and comparison with experiment.** *Nuclear Fusion*, 44(2):320, 2004.
- [15] H. R. Wilson, P. B. Snyder, G. T. A. Huysmans and R. L. Miller. **Numerical studies of edge localized instabilities in tokamaks.** *Physics of Plasmas*, 9(4):1277–1286, 2002.
- [16] H R Wilson, S C Cowley, A Kirk and P B Snyder. **Magneto-hydrodynamic stability of the H-mode transport barrier as a model for edge localized modes: an overview.** *Plasma Physics and Controlled Fusion*, 48(5A):A71, 2006.
- [17] P. B. Snyder and G. W. Hammett. **Electromagnetic effects on plasma microturbulence and transport.** *Physics of Plasmas*, 8(3):744–749, 2001.
- [18] J.R. Walk, P.B. Snyder, J.W. Hughes, J.L. Terry, A.E. Hubbard et al. **Characterization of the pedestal in Alcator C-Mod ELMing H-modes and comparison with the EPED model.** *Nuclear Fusion*, 52(6):063011, 2012.
- [19] J.W. Hughes, P.B. Snyder, J.R. Walk, E.M. Davis, A. Diallo et al. **Pedestal structure and stability in H-mode and I-mode: a comparative study on Alcator C-Mod.** *Nuclear Fusion*, 53(4):043016, 2013.
- [20] M. Greenwald, N. Basse, P. Bonoli, R. Bravenec, E. Edlund et al. **Confinement and transport research in Alcator C-Mod.** *Fusion Science and Technology*, 51(3):266–287, 2007.
- [21] J.W. Hughes, A. Loarte, M.L. Reinke, J.L. Terry, D. Brunner et al. **Power requirements for superior H-mode confinement on Alcator C-Mod: experiments in support of ITER.** *Nuclear Fusion*, 51(8):083007, 2011.

- [22] J.L. Terry, I. Cziegler, A.E. Hubbard, J.A. Snipes, J.W. Hughes et al. **The dynamics and structure of edge-localized-modes in Alcator C-Mod.** *Journal of Nuclear Materials*, 363–365(0):994 – 999, 2007.
- [23] R.J. Groebner, D.R. Baker, K.H. Burrell, T.N. Carlstrom, J.R. Ferron et al. **Progress in quantifying the edge physics of the H-mode regime in DIII-D.** *Nuclear Fusion*, 41(12):1789, 2001.
- [24] R. M. McDermott, B. Lipschultz, J. W. Hughes, P. J. Catto, A. E. Hubbard et al. **Edge radial electric field structure and its connections to H-mode confinement in Alcator C-Mod plasmas.** *Physics of Plasmas*, 16(5):056103, 2009.
- [25] H Urano, W Suttrop, L D Horton, A Herrmann, J C Fuchs et al. **Energy and particle losses during type-I ELMMy H-mode in ASDEX Upgrade.** *Plasma Physics and Controlled Fusion*, 45(9):1571, 2003.
- [26] J.W. Hughes, B. LaBombard, J. Terry, A. Hubbard and B. Lipschultz. **Edge profile stiffness and insensitivity of the density pedestal to neutral fuelling in Alcator C-Mod edge transport barriers.** *Nuclear Fusion*, 47(8):1057, 2007.
- [27] J. W. Hughes, D. A. Mossessian, A. E. Hubbard, B. LaBombard and E. S. Marmar. **Observations and empirical scalings of the high-confinement mode pedestal on Alcator C-Mod.** *Physics of Plasmas*, 9(7):3019–3030, 2002.
- [28] M. N. A. Beurskens, T. H. Osborne, P. A. Schneider, E. Wolfrum, L. Frassinetti et al. **H-mode pedestal scaling in DIII-D, ASDEX Upgrade, and JET.** *Physics of Plasmas*, 18(5):056120, 2011.
- [29] G. Saibene, L.D. Horton, R. Sartori, B. Balet, S. Clement et al. **The influence of isotope mass, edge magnetic shear and input power on high density ELMMy H modes in JET.** *Nuclear Fusion*, 39(9):1133, 1999.
- [30] P. B. Snyder, T. H. Osborne, K. H. Burrell, R. J. Groebner, A. W. Leonard et al. **The EPED pedestal model and edge localized mode-suppressed regimes: Studies of quiescent H-mode and development of a model for edge localized mode suppression via resonant magnetic perturbations.** *Physics of Plasmas*, 19(5):–, 2012.
- [31] A. Diallo, W. Hughes, J. M. Greenwald, B. LaBombard, E. Davis et al. **Observation of edge instability limiting the pedestal growth in tokamak plasmas.** *Physical Review Letters*, 112:115001, Mar 2014.

- [32] H. Urano, T. Takizuka, Y. Kamada, N. Oyama, H. Takenaga et al. Dimensionless parameter dependence of H-mode pedestal width using hydrogen and deuterium plasmas in JT-60U. *Nuclear Fusion*, 48(4):045008, 2008.
- [33] T H Osborne, R J Groebner, L L Lao, A W Leonard, R Maingi et al. H-mode pedestal characteristics, ELMs, and energy confinement in ITER shape discharges on DIII-D. *Plasma Physics and Controlled Fusion*, 40(5):845, 1998.
- [34] C.F. Maggi. Progress in understanding the physics of the H-mode pedestal and ELM dynamics. *Nuclear Fusion*, 50(6):066001, 2010.
- [35] C. S. Chang, Seunghoe Ku and H. Weitzner. Numerical study of neoclassical plasma pedestal in a tokamak geometry. *Physics of Plasmas*, 11(5):2649–2667, 2004.

The I-mode [1, 2], introduced in section 2.4, is a novel high-performance regime pioneered on Alcator C-Mod. I-mode is unique in that it appears to decouple energy and particle transport, forming a steep temperature pedestal with H-mode levels of energy confinement without the accompanying density pedestal or suppression of particle transport found in conventional H-modes (see fig. 5.1). I-mode exhibits several highly attractive properties for a putative reactor regime:

1. Due to the lack of particle transport suppression (as is found in H-modes), the I-mode retains L-mode-like impurity confinement times, avoiding the accumulation of deleterious impurities in the plasma, including those from high-Z metal plasma-facing components necessary for reactor operation [3]. This ensures stationary operation without the need for ELMs or continuous fluctuations in the edge to provide the necessary relaxation of the particle confinement.
2. I-mode appears to be naturally stable against large ELMs, avoiding excessive pulsed heat loading to plasma-facing components without externally-applied engineering controls (described in section 2.1.3).
3. Energy confinement in I-mode appears to exhibit little to know degradation with input heating power, in contrast to that found in ELMy H-mode ($\tau_E \sim P^{-0.7}$ from the ITER98y2 analysis [4]), scaling quite favorably to reactor-scale devices.

A firm understanding of the pedestal is essential for the extrapolation of any high-performance regime to ITER- and reactor-scale devices. The pedestal height sets a strong constraint on core temperature and pressure – and therefore overall fusion performance – both by acting as a boundary condition for the plasma profiles, and by supporting steeper core temperature gradients due to profile stiffness [5, 6]. Moreover, the pedestal structure, particularly the steep gradients in density, temperature, and/or pressure, determines stability of the plasma against large, deleterious ELMs (see section 3.2). In this chapter, we review empirical observations of the pedestal in I-mode from a recent series of dedicated experiments, with a focus on high-resolution pedestal profile measurements across a range of plasma parameters. Through this, we examine trends in I-mode pedestal behavior, and their impact on global behavior and performance in I-mode, and possible extrapolations to larger devices.

• *be more specific...
maybe?*

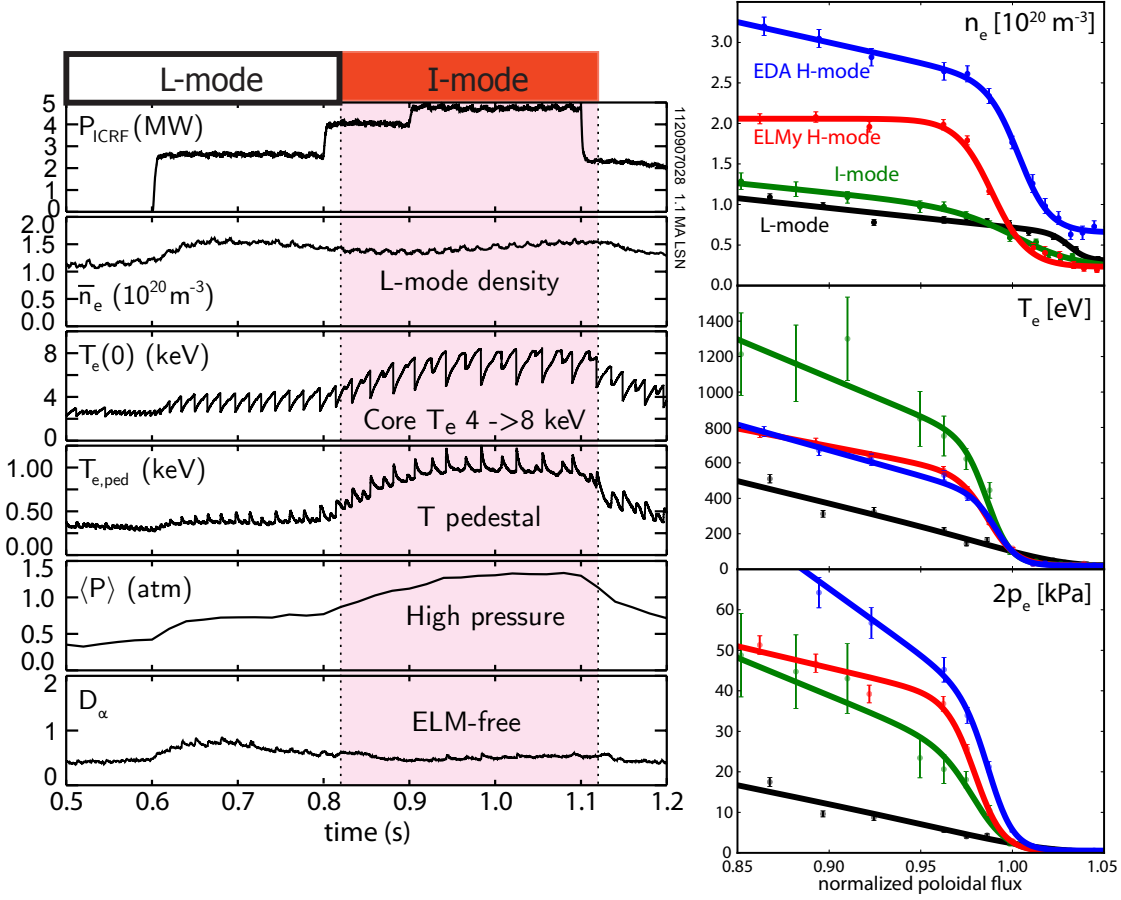


Figure 5.1: (left) Characteristic traces for a typical I-mode. At the L-I transition, the core and edge temperature rise over several sawtooth cycles before reaching a steady level; global confinement and pressure rise accordingly. However, the density remains at L-mode levels, and no ELMs are exhibited. (right) Edge profiles for density, temperature, and pressure in L-, I-, and H-mode. The I-mode (green) retains an density profile comparable to the L-mode (black), unlike the ELMy (red) and EDA (blue) H-modes which form a strong density pedestal. However, the I-mode forms a higher temperature pedestal than either H-mode. As a result, the I-mode reaches comparable pedestal pressures to the H-modes while retaining L-mode particle transport. (repeated from fig. 2.6) **use more minimal, alternate pedestal figure?**

5.1 ACCESS AND EXPERIMENTAL SETUP

All data presented here was taken on the Alcator C-Mod tokamak, described in section 1.3. As described in section 2.4.1, I-mode access hinges primarily on operation with the ion ∇B drift (eq. (1.20)) directed away from the primary X-point in the plasma (the “unfavorable ∇B drift” configuration). Within this requirement, though, I-mode access is fairly robust, with steady I-modes sustained in a variety of shapes – both USN with standard field, and LSN shapes with reversed field to achieve the desired ∇B drift direction (in the latter case, the plasma current is reversed as well to preserve field helicity) – and edge-current profiles, and at low-to-moderate collisionality (eq. (2.3)). The attainable range in q_{95} and v_{95}^* is shown in fig. 5.2. I-mode has been sustained with heating power up to $\sim 2\times$ the L-

Figure 5.2: Range in edge collisionality ν_{95}^* and q_{95} over which I-modes have been accessed. Notably, I-mode operation is naturally favored near ITER targets for these parameters. The subset of this data prepared with high-resolution pedestal profiles, herein termed the “pedestal database”, is also highlighted.

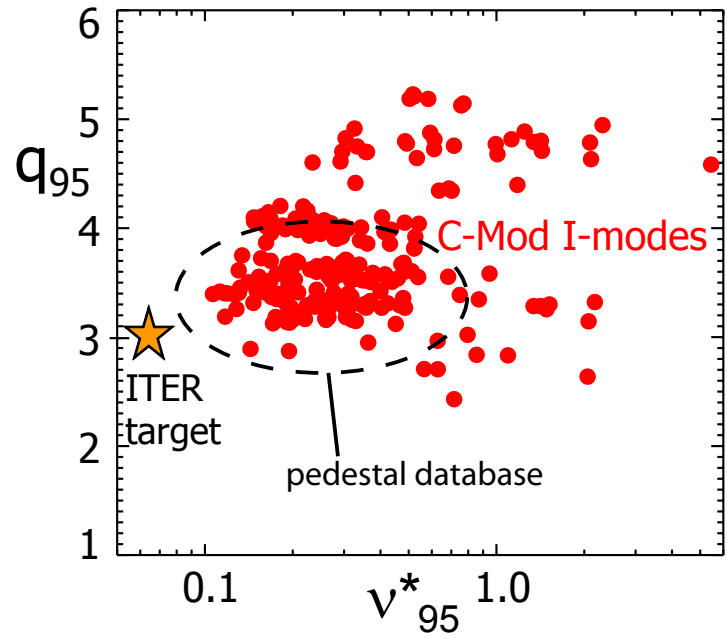
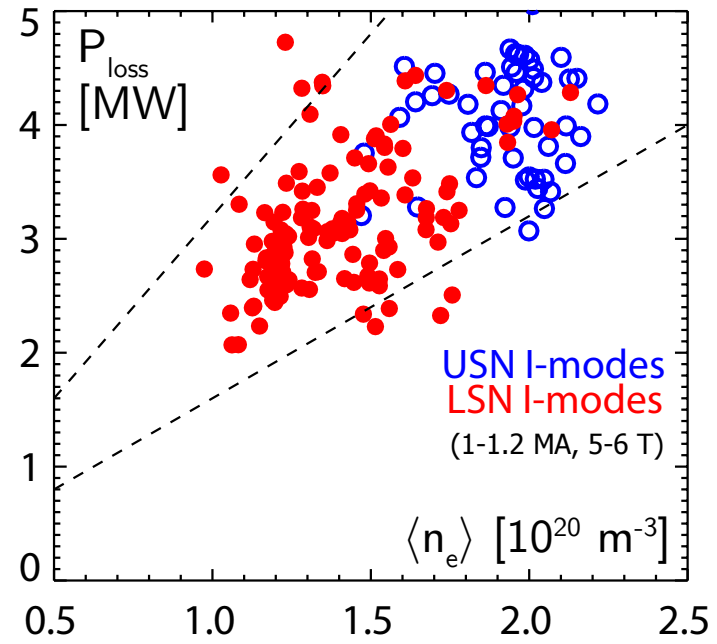


Figure 5.3: Line-averaged density and loss power range for USN and LSN I-modes, illustrating $\sim 2 \times P_{L-I}$ range for 1 – 1.2 MA, 5 – 6 T I-modes. USN shapes are forward-field and LSN-shapes are reversed field, such that all I-modes shown are in the unfavorable drift configuration. swap for plot showing only high-res database, or merge?



I transition threshold power (see fig. 5.3), above which the plasma typically enters an ELM-free H-mode (recall that operating with unfavorable ∇B drift elevates the H-mode threshold power by roughly a factor of two [7, 8, 9]).

I-mode experiments in the most recent run campaigns have focused on reversed-field LSN plasmas, which exhibit the widest access window and avoid difficulties with power handling and edge diagnostics. A subset of results from these experiments have been prepared with high-resolution pedestal measurements, optimized for analysis of the I-mode pedestal structure both from an empirical standpoint and for a computational approach to the pedestal stability; this data, herein termed the “pedestal database” (parameter range highlighted in fig. 5.2) is stored in an SQL database (see appendix B) for easy access and analysis, and will be used for the bulk of the I-mode work in this thesis (chapters 5 and 6). •

5.2 PEDESTAL RESPONSES

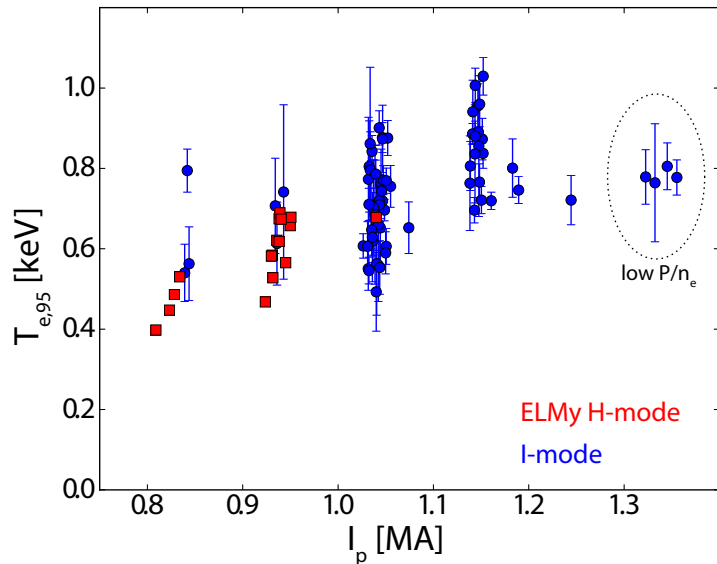
not sure this level of detail is needed

To understand the physics of the I-mode pedestal, it is useful to compare the I-mode to established scalings for baseline H-modes. For the purposes of this discussion, we distinguish between the *MHD-limited* pedestals found in ELMy H-mode (see section 2.1) and the *transport-limited* pedestals in EDA H-mode (see section 2.3.2). The pedestal structure in the MHD-limited case is determined by peeling-balloonning stability, described in section 3.2 – this manifests predominantly as a limit on the pressure gradient due to the instability drive to for the ballooning mode, α_{MHD} (see eqs. (2.8) and (2.9)). This scales as $\alpha_{MHD} \sim \nabla p / B_p^2$, consistent with the observed $\nabla p \sim I_p^2$ dependence observed in experiments [10, 11] (*cf.* chapter 4). To lowest-order approximation, this sets a limit on the pedestal poloidal beta, such that for a given current, field, and shaping configuration the pedestal pressure $p \sim n_e T_e$ is fixed. Altering the density via fueling results in heating or cooling the pedestal to maintain this limit, while attempts to modify the pedestal via heating power alters the energy transport (increasing the ELM frequency $f_{ELM} \sim P$ for large type-I ELMs [12]). In transport-limited EDA H-mode pedestals, on the other hand, the pedestal is controlled in part by the interplay between the strong particle pinch and the continuous outward particle transport driven by the QCM, such that the density tends to lock to a value set by the plasma current. Within this limit, the pedestal temperature (and therefore pressure) responds positively to heating power [13].

5.2.1 Pedestal Temperature

As the I-mode is characterized, in part, by its H-mode-like temperature pedestal and energy confinement, that is a suitable place to be-

Figure 5.4: Pedestal temperature versus plasma current for I-mode and ELM My H-mode. I-mode temperature pedestals meet or exceed H-mode levels, and trend positively with current. The spread in $T_{e,95}$ at a given current point is due to varying power per particle (see fig. 5.5). The highest-current I-modes exhibit temperatures below the bulk trend due to low values of P_{net}/\bar{n}_e , as these I-modes were fueled to comparatively high densities.

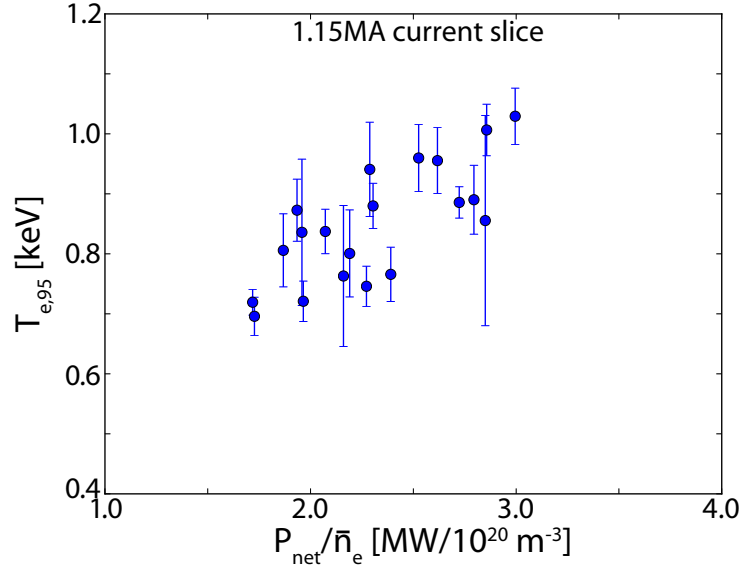


gin an examination of the I-mode pedestal. A scan of plasma current from 0.85 to 1.35 MA reveals a positive trend of the pedestal temperature with plasma current, shown in fig. 5.4 with ELM My H-modes for comparison. The I-mode temperature pedestal meets or exceeds the pedestal T_e found in H-modes. This is highly beneficial for global performance, as the high temperature pedestal coupled with stiff core temperature profiles supports very high (up to 8 keV) core temperatures – with moderately peaked core density profiles, this supports comparable core pressures and fusion reaction rates to H-mode despite the relaxed pedestal.

There is, however, significant scatter at a given point in the I_p scan, due to variation in the input heating power. Examining a single current slice at 1.15 MA, shown in fig. 5.5, we see a strong dependence of the temperature pedestal height on the net heating power (eq. (1.27)), normalized to (line-averaged) density – effectively, the input power per particle. A consistent pattern is observed at other current points. The comparatively suppressed temperatures at the highest-current I-modes is a result of the higher fueling at these points, resulting in lower values of P_{net}/\bar{n}_e .

The temperature pedestal response in I-mode to plasma current is comparable to that seen in the density, temperature, and pressure pedestals in ELM My H-mode (*cf.* fig. 4.9), although the sensitivity of the temperature pedestal in ELM My H-mode is somewhat weaker than in I-mode. The response of the temperature pedestal to heating power is notable: the temperature in ELM My H-mode pedestals is only weakly dependent on power – rather, increased heating power increases the ELM frequency and energy transport to maintain the approximately β_p -limited pedestal (*cf.* figs. 2.2 and 4.10). Transport-limited EDA H-

Figure 5.5: Pedestal temperature $T_{e,95}$ vs. heating power per particle (P_{net}/\bar{n}_e) for the 1.15 MA current slice, illustrating the approximately-linear trend in temperature at fixed current. This behavior is highly beneficial as an external control for the pedestal temperature.



mode pedestals exhibit a similar trend [13], $T_{e,\text{ped}} \sim (P_{\text{net}}/\bar{n}_e)^{0.5 \pm 0.1}$, with the I-mode pedestal responding at least as strongly.

5.2.2 Pedestal Response to Fueling

In contrast to the temperature pedestal (section 5.2.1), the edge density in I-mode exhibits markedly different behavior compared to conventional H-modes. Edge density is set primarily through operator fueling control via gas puffing, maintaining an L-mode-like density profile without the density pedestal found in H-mode. The pedestal response to fueling is shown at right in fig. 5.6. In contrast to transport-limited EDA pedestals, the plasma current is a poor predictor of I-mode pedestal density, with the positive trend (shown at left in fig. 5.6) due to the strong co-variance between I_p and \bar{n}_e .

Given sufficient heating power, temperature pedestals can be maintained with increased density due to the strong response of $T_{e,95}$ to power-per-particle. Example discharges matched in current, field, and shaping are shown in fig. 5.7, spanning a range in fueling and heating power, $\bar{n}_e = 1.0 - 1.7 \times 10^{20} \text{ m}^{-3}$, $P_{\text{net}} = 2.75 - 4.10 \text{ MW}$. Temperature pedestals are matched across all three discharges, using consistent power-per-particle $P_{\text{net}}/\bar{n}_e = 2.4 - 2.7 \text{ MW}/10^{20} \text{ m}^{-3}$.

This behavior is distinct from that found in H-modes on C-Mod. ELM My H-modes at fixed current and shaping exhibit an inverse relationship between pedestal n_e and T_e due to limited pedestal β_p , such that increased fueling tends to cool the pedestal (although the modification of pedestal collisionality also modifies the ELM character). EDA H-modes lack the fueling control found in I-mode, instead railing the pedestal density to a value set by the plasma current, such that the outward transport and strong inward particle pinch are bal-

find cite

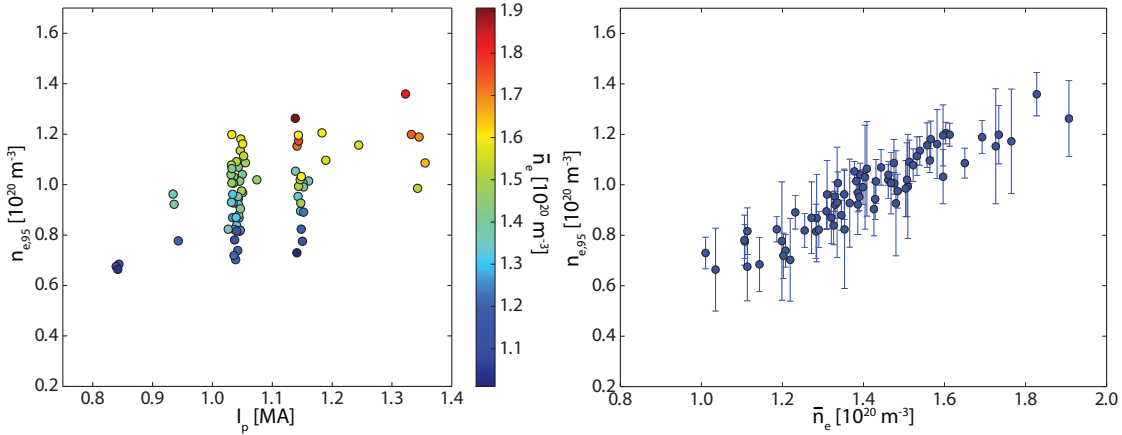
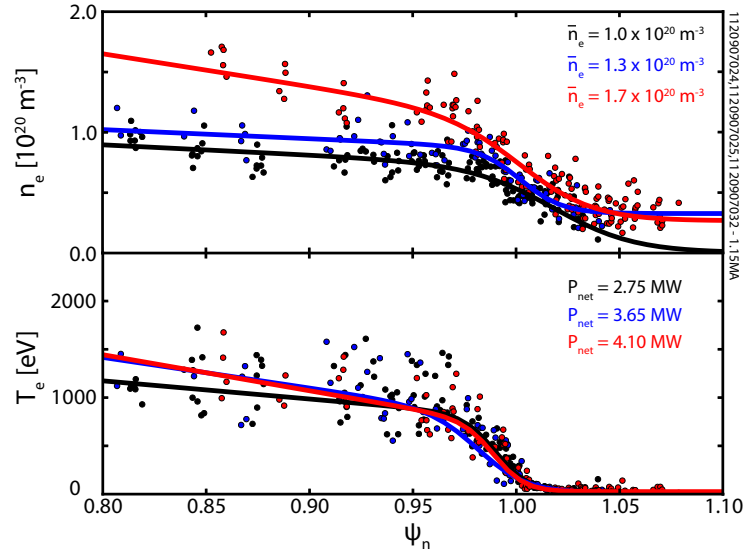


Figure 5.6: Pedestal density as a function of current (left, colored by \bar{n}_e) and line-averaged density (right). The pedestal density is set solely by operator fueling; in contrast the transport-limited pedestals in EDA H-mode, plasma current is a poor predictor of the pedestal density, with the trend due only to the co-variance between I_p and \bar{n}_e .

Figure 5.7: Density and temperature pedestals at matched current, field, and shaping, with varying fueling and heating power levels. The three discharges are fueled to \bar{n}_e of 1.0 (black), 1.3 (blue), and $1.7 \times 10^{20} \text{ m}^{-3}$ (red) respectively, with heating powers of 2.75, 3.65, and 4.10 MW to maintain matched $P_{\text{net}}/\bar{n}_e \sim 2.4 - 2.7$. The constant power-per-particle maintains matched temperature pedestals across the fueling range, indicative of the independent control of pedestal n_e and T_e available in I-mode.



anced. The largely-decoupled behavior of the density and temperature profiles in the edge in I-mode are highly desirable from an operational standpoint – fueling (done entirely via edge gas puffing on C-Mod) and heating power are separated as “knobs” for plasma control, granting significant operational freedom compared to the relatively-constrained H-mode pedestal behavior.

The phenomenon demonstrated in fig. 5.7 is indicative of a path to strongly improved performance in I-mode, increasing pedestal β_p and global confinement via matched increases in fueling and heating power, maintaining the target temperature pedestal with appropriate levels of P_{net}/\bar{n}_e . Recent experiments on C-Mod [14] have successfully applied this approach, reaching elevated density by fueling into

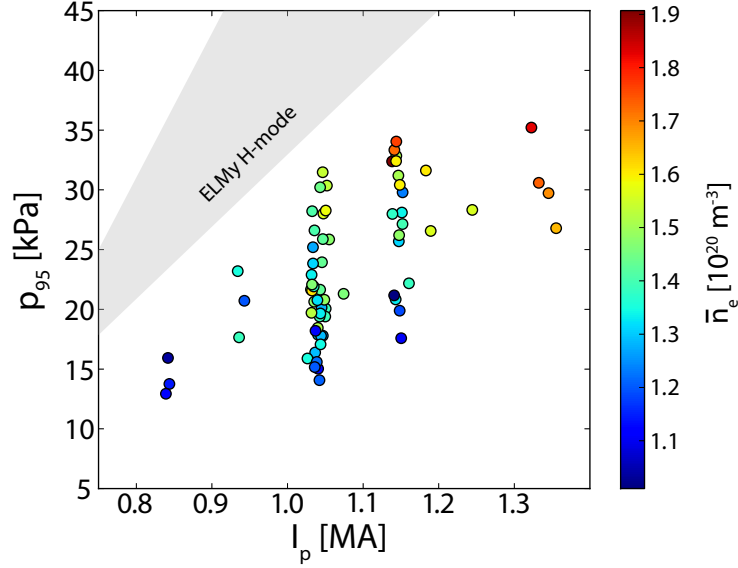
elaborate on neutral opacity, fueling behavior for ITER

an established I-mode despite the application of heating power levels sufficient for a transition to H-mode at a higher starting density.

5.2.3 Pressure Pedestal Scalings and Performance

Despite lacking a density pedestal, I-mode is capable of reaching competitive levels of pedestal thermal pressure, while maintaining favorable behavior in its particle (particularly impurities – see fig. 2.7) transport and temperature pedestal. I-mode pedestal pressure (we use twice the electron pressure from Thomson Scattering here, consistent with $T_i \approx T_e$ measurements in well-equilibrated pedestals on C-Mod [2] and with the relatively low impurity contribution to the pressure, $Z_{\text{eff}} \sim 2$) versus plasma current is shown in fig. 5.8, with additional differentiation by fueling level indicated by color. An increase in pedestal pressure by at least $p_{95} \sim I_p$ is observed, consistent with the scaling of the temperature pedestal $T_e \sim I_p$. The pedestal pressure at a given current is seen to increase strongly with increased fueling, consistent with the maintenance of the temperature pedestal with increased heating power and matched fueling, thus constant levels of P_{net}/\bar{n}_e . I-mode pedestal pressure is reduced from that typically found in H-mode (the typical range in ELM My H-mode is indicated by the shaded region in fig. 5.8). This is due to the reduced pedestal density in I-mode compared to H-mode, as the temperature pedestals found in I-mode typically meet or exceed H-mode levels.

Figure 5.8: Pedestal thermal pressure ($2 \times p_{e,95}$) versus plasma current, colored by fueling level indicated by line-averaged density \bar{n}_e . The shaded region indicates the typical range of pedestal pressures in C-Mod ELM My H-modes. A strong, roughly $p_{95} \sim I_p$ trend in pedestal pressure is observed. At a given current, a strong increase in pedestal pressure with fueling is also observed (note: heating power also varied in these discharges).



The effect of heating power on the pressure pedestal is visible in fig. 5.9, showing the 1.15 MA current slice (see fig. 5.5 for the same). At fixed current, the pressure pedestal scales as $p_{95} \sim P_{\text{net}}$, consistent with the previously observed $T_{e,95} \sim P_{\text{net}}/\bar{n}_e$ trend in the temperature pedestal as $p_{95} \sim n_{e,95} T_{e,95}$. This corresponds to the favorable scal-

Figure 5.9: Pedestal pressure ($2 \times p_{e,95}$) versus net heating power for the 1.15 MA current slice, illustrating the trend $p_{95} \sim P_{\text{net}}$ at fixed current. This is consistent with the power trend in the I-mode temperature pedestal, $T_{e,95} \sim P_{\text{net}}/\bar{n}_e$.

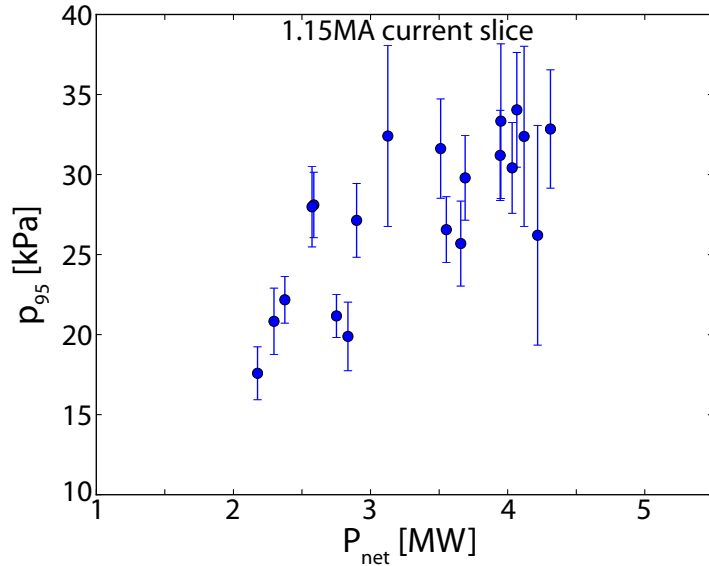
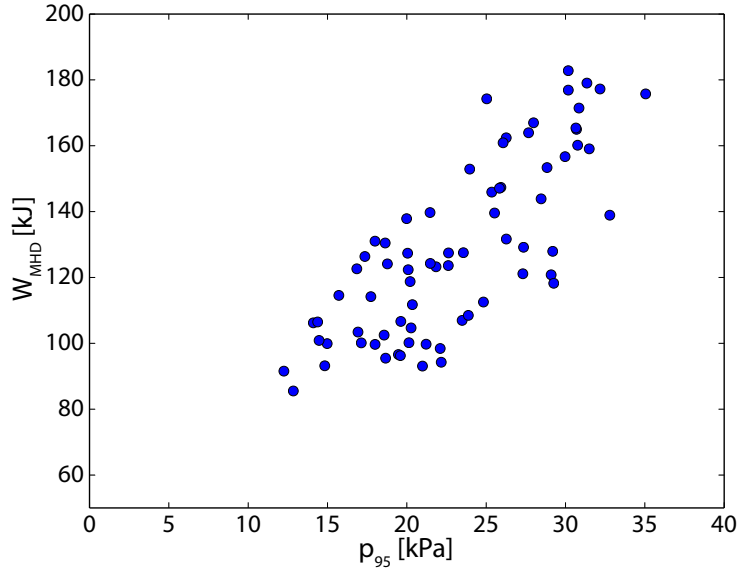


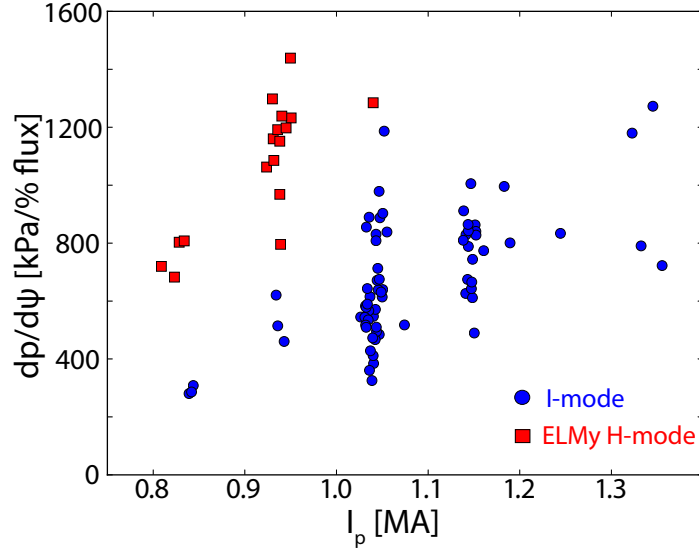
Figure 5.10: I-mode stored energy versus pedestal pressure, confirming the strong dependence of global performance on the pedestal height. *too trivial?*



ing of energy confinement in I-mode with heating power – plasma stored energy is set by heating power and the energy confinement time, $W \sim P\tau_E$, and is strongly influenced by the pedestal pressure (see fig. 5.10). Thus, the trend $p_{95} \sim P_{\text{net}}$ is consistent with little or no degradation of τ_E with heating power, which has been observed in global measurements of I-mode [1, 15], and is distinct from the trend $\tau_E \sim P^{-0.7}$ found for ELMy H-modes [4]. This behavior is quite favorable when scaled to large, high-power machines, particularly in scenarios with a significant degree of fusion self-heating.

Trends in the pressure pedestal in I-mode are also indicative of MHD stability. As shown in fig. 5.11, the peak pressure gradient (identified as the driver for ballooning MHD instabilities, described in section 3.2.1, and the trigger for large ELMs) in I-mode is consistently

Figure 5.11: Peak pressure gradient (measured at the pedestal midpoint) versus plasma current for I-mode and ELMy H-mode. I-mode consistently exhibits a weaker pressure gradient at a given current, as well as scaling more weakly than the $\nabla p \sim I_p^2$ expected from the ballooning MHD stability limits associated with ELMy H-mode.



shallower at a given I_p than comparable ELMy H-modes on C-Mod, due to the flat edge density profile. Moreover, the pedestal pressure gradient scales more weakly than the expected $\nabla p \sim I_p^2$ expected from the ballooning stability boundary [16]. The intuitive conclusion from this is that I-mode is generally stable to the MHD instabilities identified with the ELM trigger – the MHD stability and ELM behavior of I-mode is explored in detail in chapter 6. •

5.3 PEDESTAL WIDTHS

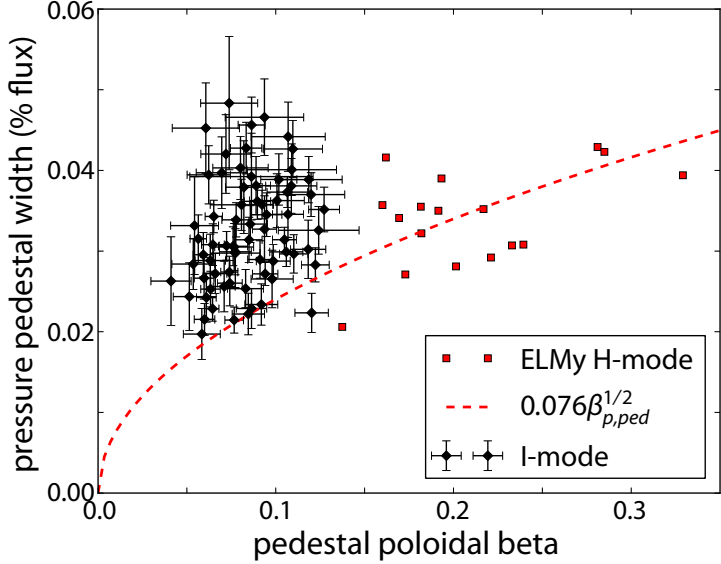
Conventionally, H-mode pedestals are found to be constrained by critical-gradient-driven instabilities, such that the peak ∇p is limited – therefore, the width of the transport barrier sets a constraint on the attainable pedestal height (and thus global performance). Due to the small spatial scales inherent in the pedestal, accurate measurement of the pedestal width has historically been quite difficult, although a number of theoretical models have been proposed and tested against experimental observations, e.g., [17, 18, 19]. This section explores a range of potential explanations for the observed pedestal widths in I-mode.

5.3.1 Kinetic-Ballooning Limited Pedestals

The edge turbulence in I-mode is characterized by a strong reduction in mid-frequency turbulence and the appearance of a higher-frequency ($\sim 200 - 400$ kHz) fluctuation, dubbed the *Weakly-Coherent Mode* or WCM [1, 2, 15, 20, 21, 22]. The WCM appears to be connected to the density pumpout and pedestal regulation in I-mode, with the WCM amplitude shown to be correlated to the particle flux through

not sure I like this
intro

Figure 5.12: Pedestal width versus poloidal beta in I-mode and ELMY H-mode. ELMY H-modes lie on the $\Delta_\psi \sim \beta_{p,ped}^{1/2}$ line predicted for KBM-limited pedestals (see section 4.4.2). I-mode shows no scaling of the pedestal width with β_p , and exhibits pedestals consistently wider than predicted for comparable ELM-limited pedestals.



the LCFS [15]. An understanding of the turbulent behavior in the I-mode pedestal, then, is essential to the extrapolation of I-mode operation to larger devices. Kinetic-balloonning mode (KBM) turbulence, described in section 3.3, is thought to constrain the pedestal in ELMY H-mode, and is therefore an important starting point for investigating the WCM.

The KBM applies a constraint to the pedestal width of the form $\Delta \sim \beta_{p,ped}^{1/2}$, where Δ is the pedestal width in normalized poloidal flux. This trend has been observed on several machines [11, 18, 23], including on C-Mod (see chapter 4). This constraint is used in the EPED model series, described in section 3.4. The simplest implementation of the constraint, used in EPED1 (section 3.4.1) uses a fitted coefficient, $\Delta = 0.076\beta_{p,ped}^{1/2}$ [24]. A comparison of I-mode pedestals against this predictive line, as well as example ELMY H-modes, is shown in fig. 5.12. I-mode pedestals are wider on average than predicted by the KBM-limited ($\sim \beta_{p,ped}^{1/2}$) line, and show no trend of pedestal width with poloidal beta. This suggests that the I-mode pedestal is not constrained by KBM turbulence, consistent with the relaxed pressure gradient found in I-mode – stability against the KBM is examined in more detail in section 6.2.

5.3.2 Local Physics Parameters

While the constraint on the pressure pedestal from kinetic-balloonning turbulence has been the most successful in capturing the limiting physics in ELMY H-modes, a number of other theories (see section 3.1) based on localized physics in the edge have been proposed, with testable trends in the pedestal width. Of particular note are models based on a trend in poloidal gyroradius, described in section 3.1.3,

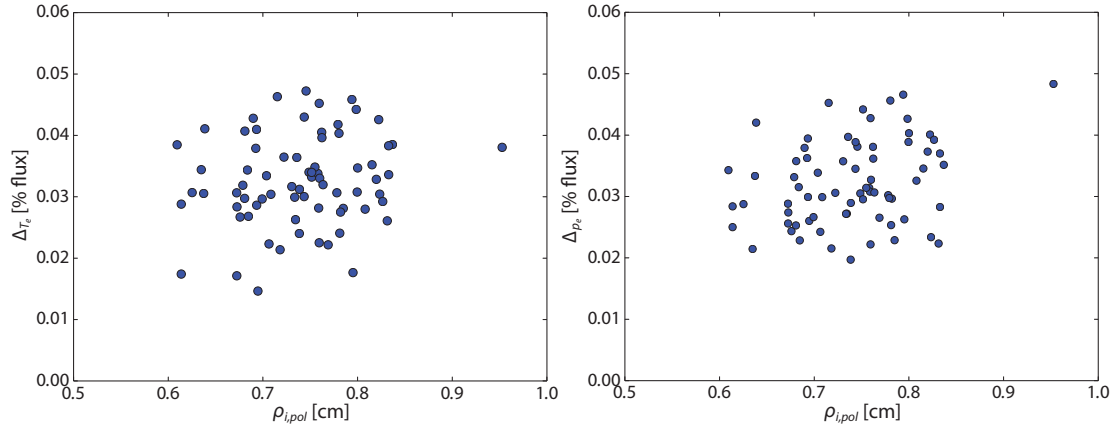


Figure 5.13: Temperature (left) and pressure (right) pedestal widths versus poloidal gyroradius $\rho_{i,\text{pol}}$. No correlation in the pedestal width is seen, contrary to models suggesting a scaling of the sheared-flow layer and pedestal with the gyroradius.

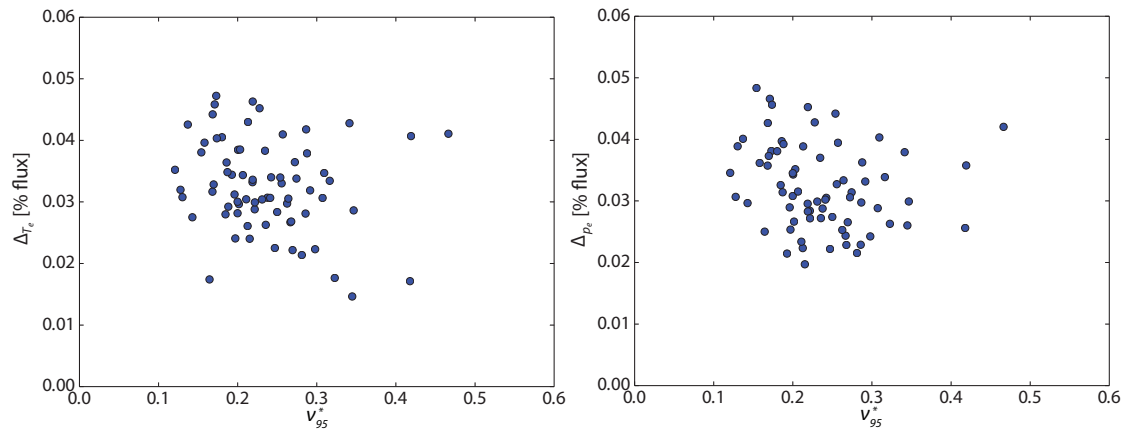


Figure 5.14: Temperature (left) and pressure (right) pedestal widths versus pedestal collisionality v_{95}^* . No correlation is seen.



Figure 5.15: Temperature (left) and pressure (right) pedestal widths versus edge safety factor q_{95} . No correlation is seen.

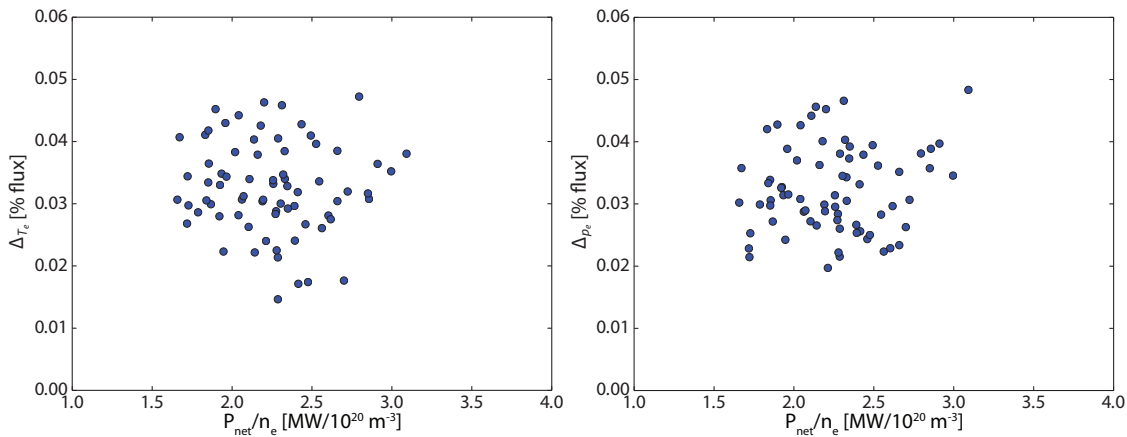


Figure 5.16: Temperature (left) and pressure (right) pedestal widths versus power-per-particle, P_{net}/\bar{n}_e , i.e., the heat flux through the pedestal. No correlation is seen.

operating on the assumption that ion orbit loss in the plasma edge drives the radial electric field responsible for the pedestal formation – thus the size scale of the ion orbit sets the pedestal width. Some experimental observations correlate well to these predictions, although these may be largely incidental due to the strong covariance between $\rho_{i,\text{pol}}$ and $\beta_{p,\text{ped}}$, and have been discounted by dedicated experiments distinguishing the two. However, as the KBM does not appear to limit the I-mode pedestal (see section 5.3.1) gyroradius scalings remain an open avenue. Electron temperature and pressure pedestal widths are shown against $\rho_{i,\text{pol}}$ in fig. 5.13. Both pedestal widths appear quite insensitive to the gyroradius, although due to the correlation between T_e and I_p the range in $\rho_{i,\text{pol}}$ is rather limited.

Similarly, the temperature and pressure pedestal widths are shown against pedestal collisionality ν_{95}^* and edge safety factor q_{95} in fig. 5.14 and fig. 5.15, respectively. The collisionality may be expected to influence the pedestal width both by controlling neutral ionization rates (thus the influence of neutral penetration on the pressure width) and through the bootstrap current in the edge, which enters into the peeling-balloonning MHD stability boundary (see section 3.2). The safety factor is directly tied to the magnetic shear, which is locally stabilizing to MHD modes in the edge. However, as the I-mode pedestal appears to be strongly MHD-stable, as is shown in chapter 6, these should have a minimal effect. In figs. 5.14 and 5.15, no correlation between the pedestal width and either parameter is evident.

In section 5.2.1, it is shown that the temperature pedestal height is strongly dependent on P_{net}/\bar{n}_e , effectively heating power per particle (equivalently, the heat flux through the pedestal). Temperature and pressure pedestal widths are shown against power-per-particle in fig. 5.16. As with the other parameters, the pedestal width is uncorrelated with the heat flux through the pedestal.

elaborate on these
expected
dependences?

arguments for effect
on width?

Figure 5.17: Peak ∇T_e in the I-mode pedestal versus $T_{e,95}$. Hotter pedestals support a steeper gradient in temperature (albeit with significant scatter), consistent with a robust temperature pedestal width.

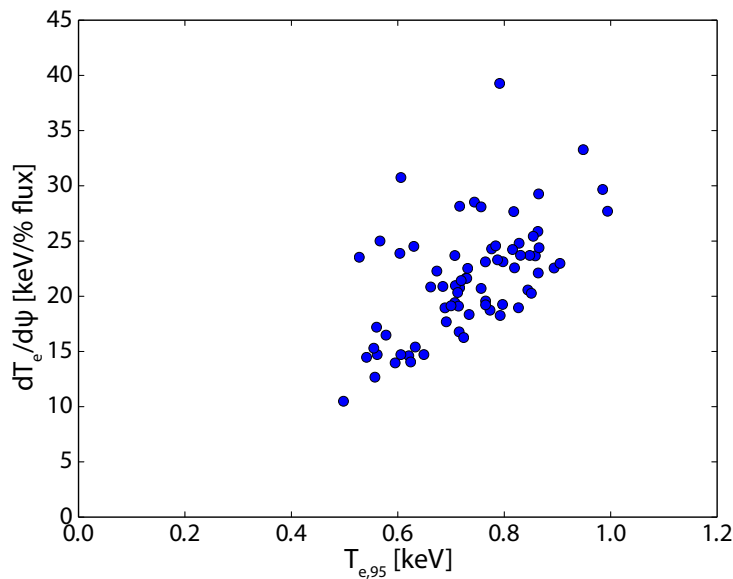
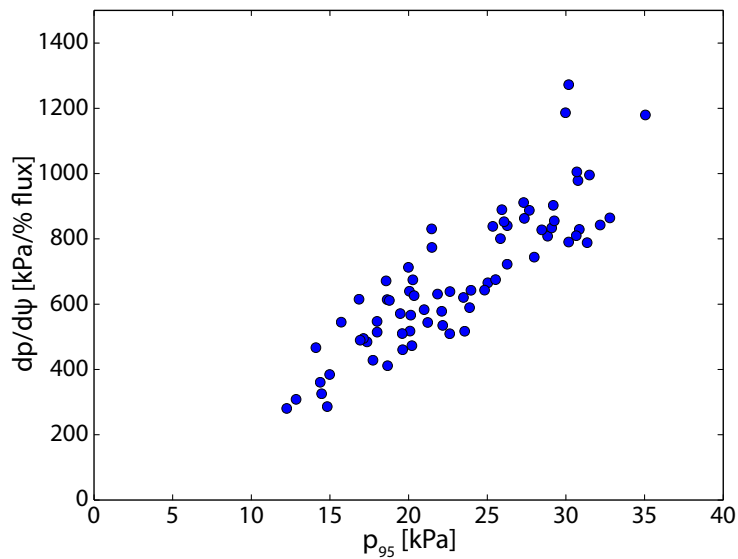


Figure 5.18: Peak ∇p in the I-mode pedestal versus p_{95} . There is a robust linear dependence between the pedestal gradient and height, consistent with a robust pedestal width.



5.3.3 Stiff Gradient Limits

In sections 5.3.1 and 5.3.2, the I-mode pedestal width (both in temperature and pressure) is shown to be insensitive to a number of pedestal parameters. This may be examined directly by viewing the peak pedestal gradient versus its height – to lowest approximation, $\nabla Q \sim Q/\Delta Q$ (where Q is the pedestal quantity, i.e., T_e , p_{tot}). The peak gradients in temperature and pressure are shown against the corresponding 95%-flux values in fig. 5.17 and fig. 5.18, respectively. In both cases, a linear dependence of the gradient on the pedestal-top value is observed, albeit with scatter favoring higher gradients than the linear prediction in the case of the temperature. The pressure gradient is predicted quite well by its 95%-flux value. Similar behavior

has been observed for the electron and ion temperatures in H-mode on AUG and DIII-D, independent of plasma shaping and evidently operating under a separate limit from the ideal-MHD constraint on the pressure pedestal [25]. These trends are consistent with robust pedestal widths, particularly in the pressure pedestal, in I-mode.

note H-mode robust width, ultimate limit on ∇p

5.4 GLOBAL BEHAVIOR, PERFORMANCE, & CONFINEMENT

The pedestal structure of the I-mode is quite desirable for a reactor scenario – due to the strong response of the pedestal temperature to heating power, externally-applied heating power is an effective engineering control for core temperatures, and subsequently fusion reaction rates. The high pedestal temperature, coupled to stiff core temperature profiles (such that a higher temperature supports a steeper marginally-stable ∇T_e), supports very high core temperatures. With a moderate degree of core density peaking, this supports comparable core and volume-averaged pressures to H-mode despite the comparatively relaxed pedestal, supporting beneficial fusion conditions in the core while avoiding stability issues in the pedestal. Example density, temperature, and pressure profiles for I-mode and H-mode cases are shown in fig. 5.19, illustrating the high core pressures attainable in I-mode despite the lower pedestal and reduced density. This is reflected in fig. 5.20, showing the global-averaged normalized beta ($\langle \beta_N \rangle = \langle \beta \rangle a B_T / I_p$) versus the confinement metric H_{98} in I-mode and ELM My H-mode – I-mode reaches comparable levels of β_N while maintaining H-mode-like $H_{98} \sim 1$ at comparable levels to ELM My H-mode, while maintaining desirable impurity confinement and ELM stability behaviors.

density peaking?

Energy confinement in I-mode also appears to lack strong degradation with heating power (cf. the $\tau_E \sim P^{-0.7}$ trend for H-modes, as in eq. (2.5)) – a highly desirable characteristic for large devices. This may be seen intuitively in fig. 5.21. The plasma stored energy trends as $W \sim P \tau_E$; from the H-mode scaling, we expect $\tau_E \sim I_p$. The H-mode confinement scaling, then, predicts $W \sim I_p P_{net}^{0.3}$. However, the stored energy in I-mode trends as $W \sim P_{net} I_p$, indicating that there is little or no (negative) dependence of τ_E on heating power in I-mode. The strong dependence of the stored energy on heating power is reflected in the response of the pressure pedestal to the same, shown in fig. 5.9. The degradation of energy confinement with heating power in H-mode reflects the MHD limits on the pedestal – increased heating power raises the ELM frequency to drive enhanced energy transport, maintaining the pedestal at the MHD limit, which in turn drives the weak increase of stored energy with increased power. The lack of power degradation in I-mode, then, reflects the stability of the pedestal against ELMS.

show EDA?

reword, something about density

Figure 5.19: Profiles in density, temperature, and pressure for I-mode and EDA H-mode. The H-mode case exhibits a very strong density pedestal, with a somewhat reduced temperature pedestal; the I-mode, in contrast, has a significant temperature pedestal with a relaxed density profile. While this typically results in a reduced pedestal pressure in I-mode compared to H-mode, core profile stiffness supports very high central temperatures, such that I-mode exhibits comparable core and average pressure despite the reduced pedestal.

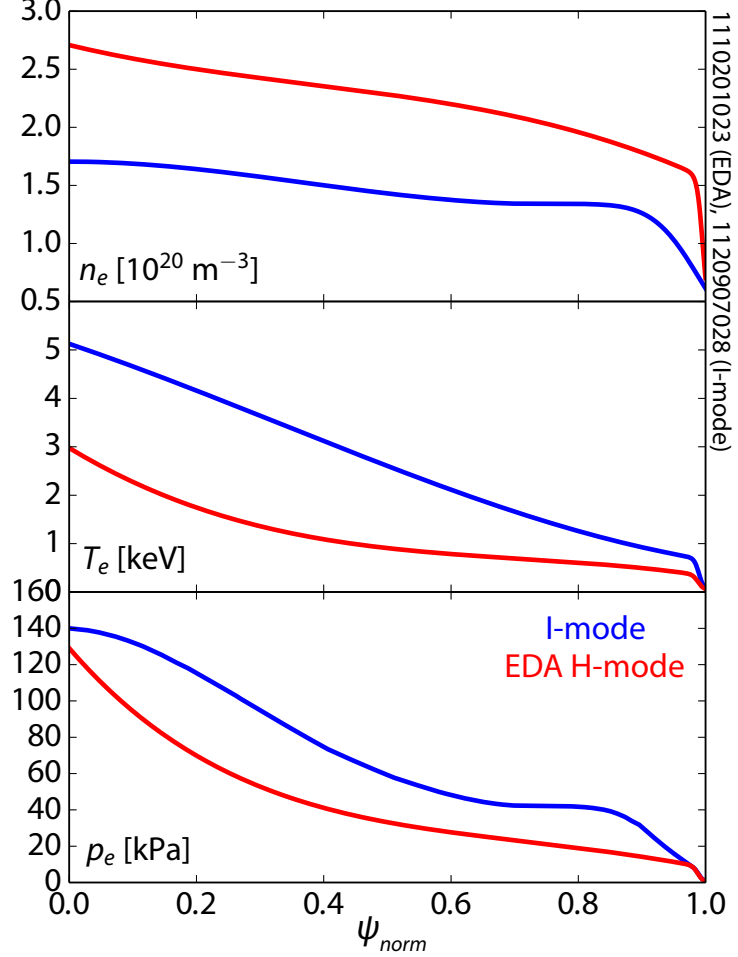


Figure 5.20: Global normalized β_N versus confinement factor H_{98} for I-mode and ELMy H-mode. Despite the relaxed pedestal pressure, I-modes reach comparable average pressures, while maintaining H-mode-like energy confinement.

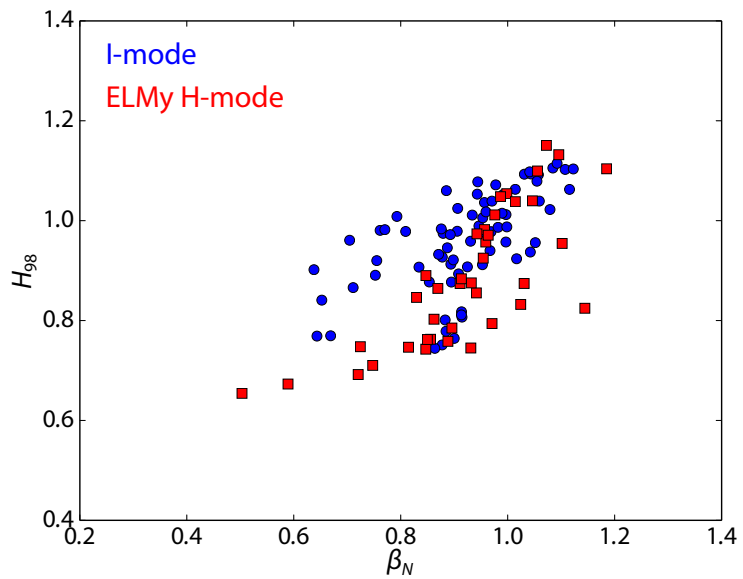


Figure 5.21: I-mode stored energy versus the product of net heating power P_{net} and plasma current I_p . Based on the H-mode confinement scaling, τ_E is expected to scale linearly with I_p , and to show a strong degradation with heating power: $\tau_E \sim I_p \times P_{\text{net}}^{-0.7}$. As the stored energy is given by $W \sim P_{\text{net}}\tau_E$, $W \sim I_p P_{\text{net}}^{0.3}$ is expected. The observed linear trend indicates little-to-no degradation of τ_E in I-mode with heating power.

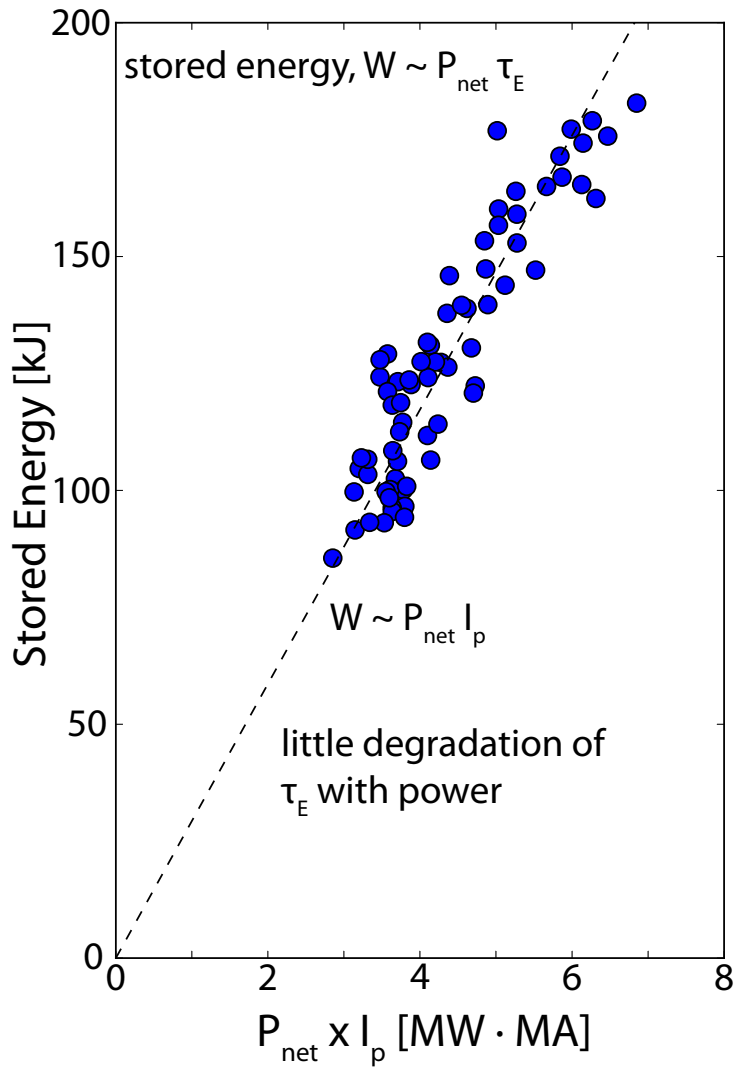
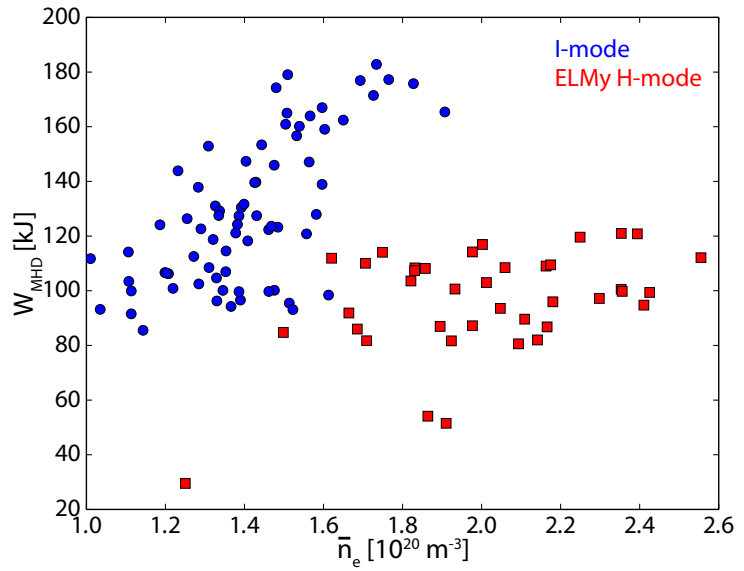


Figure 5.22: Plasma stored energy versus fueling, indicated by \bar{n}_e in I-mode and ELMMy H-mode. I-mode shows no degradation of confinement with fueling, while the H-mode is flat
conjure on this, maybe substitute?



5.4.1 Confinement Scaling Laws

Due to the complexity inherent in modeling global energy transport from first-principles physics, it is common to establish empirical scaling laws for energy confinement using a power-law fit to large datasets. For example, the ITER89 [26] and ITER98 [4] scalings utilized an extensive multi-machine database [27] for L-mode and H-mode confinement. In particular the ITER98y2 scaling (see eq. (2.5)) is a commonly-used baseline for high-performance regimes, particularly in terms of the normalized H_{98} (eq. (2.6)). However, as the ITER98y2 scaling was constructed predominantly with type-I ELM My H-modes (as these customarily are the highest-performance H-modes on most tokamaks), and as such implicitly includes the physics of ELM-limited pedestals. For example, the power-law fit in ITER98y2 includes a strong degradation of confinement with heating power, $\tau_E \sim P^{-0.7}$. This is consistent with the observed weak response of ELMing pedestals with heating power [28], with increased power instead raising the ELM frequency to maintain consistent ELM-driven heat transport.

*cite**clarify**reward*

In light of the substantially different physics of the I-mode pedestal and energy confinement compared to H-modes, it is useful to construct a power-law confinement fit using I-mode data. It is strongly emphasized that such a fit would be only preliminary, as fits using data from a single machine lack the range of parameter values needed to fully constrain the fit. Even so, it is illustrative to examine the results of I-mode under an analogous approach, indicative of the potential benefits of I-mode operation when extrapolated to larger devices. I-mode energy confinement times are fitted in a least-squares sense to the general form

$$\tau_{\text{I-mode}} = C I_p^{\alpha_{I_p}} B_T^{\alpha_{B_T}} \bar{n}_e^{\alpha_{n_e}} R^{\alpha_R} \varepsilon^{\alpha_\varepsilon} \kappa^{\alpha_\kappa} P_{\text{loss}}^{\alpha_P} \quad (5.1)$$

to find free exponents α_j for plasma current I_p in MA, toroidal field B_T in T, line-averaged density \bar{n}_e in 10^{20} m^{-3} , major radius R in m, inverse aspect ratio ε , elongation κ , and loss power P_{loss} in MW (see eq. (1.26)). To extend the quantity of data and range of parameters available for this assay, the high-resolution pedestal data used in the bulk of this thesis is supplemented by older I-mode datasets containing both reversed-field LSN and forward-field USN I-mode cases. Although these data lack the high-resolution edge data necessary for pedestal structure and stability studies, they are nevertheless suitable for scalings based on global parameters. Although the net power P_{net} (see eq. (1.27)) has been demonstrated to be the more accurate parameter, rather than P_{loss} , these older data contain inconsistent measurements of the radiated power, necessitating the use of loss power in its stead (and in any case, this is consistent with previous confinement scaling studies).

cite, clarify

Table 5.1: Parameters for power-law scalings of the I-mode energy confinement time τ_E , along with R^2 coefficients of determination for the fit. Blank entries indicate parameters that were omitted from that fit. Note that fit #5 utilized a fixed $R^2\sqrt{\varepsilon}$ size dependence rather than taking the size to be a free fitting parameter. Parameters are in the given units: I_p in MA, B_T in T, \bar{n}_e in 10^{20} m^{-3} , R in m, and P_{loss} in MW. Elongation κ and aspect ratio ε are dimensionless.

	#1	#2	#3	#4	#5
C	0.040 ± 0.066	0.007 ± 0.002	0.014 ± 0.002	0.014 ± 0.002	0.056 ± 0.008
I_p	0.686 ± 0.074	0.696 ± 0.073	0.685 ± 0.076	0.692 ± 0.073	0.676 ± 0.077
B_T	0.698 ± 0.075	0.697 ± 0.071	0.768 ± 0.072	0.773 ± 0.071	0.767 ± 0.072
\bar{n}_e	-0.077 ± 0.055	-0.050 ± 0.048	0.017 ± 0.048		0.006 ± 0.048
R	4.219 ± 4.623				2^*
ε	0.127 ± 1.144				0.5^*
κ	1.686 ± 0.398	1.501 ± 0.350			
P_{loss}	-0.197 ± 0.048	-0.220 ± 0.043	-0.286 ± 0.042	-0.281 ± 0.039	-0.275 ± 0.042
R^2	0.713	0.711	0.685	0.684	0.683

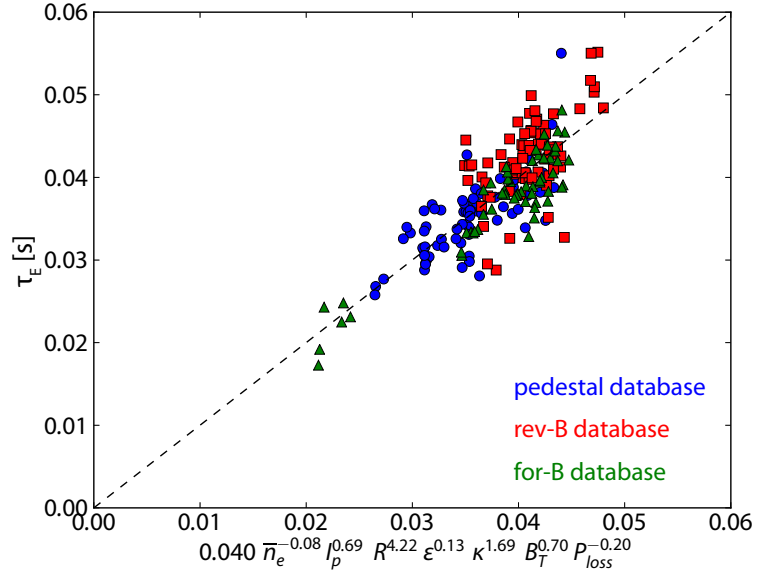
Results from a number of scaling studies are shown in table 5.1, containing the values and standard deviations for each exponent value, the scale factor C, and the R^2 coefficient of determination. We begin with the full parameter list used in the ITER98y2 scaling, shown as fit #1 in table 5.1, with results shown in fig. 5.23. However, it is immediately obvious that the size scalings, dependent on major radius R and inverse aspect ratio ε , are not properly captured (denoted by the extreme errorbars on these parameters). This is to be expected – absent meaningful variation in R and ε in the dataset (which requires multiple machines to produce) these parameters are not well-constrained, and result #1 is over-fitted.

For simplicity, we reduce our consideration to an effective single-machine scaling, omitting these parameters (indicated by blank entries in table 5.1). Under this fit, shown as #2 in table 5.1, the power applied to the elongation κ is elevated compared to that expected from the ITER98y2 scaling, with the relatively large deviation expected from the somewhat restricted range of shapes found in these studies. Omitting this fitting parameter results a minimum-complexity fit,

$$\tau_{\text{I-mode}} = 0.014 \times I_p^{0.685} B_T^{0.768} \bar{n}_e^{0.017} P_{\text{loss}}^{-0.286} \quad (5.2)$$

with a coefficient of determination of $R^2 = 0.685$ (also shown as #3 in table 5.1). The correspondence between experimental τ_E and the modeled confinement time is shown in fig. 5.24. The density dependence in τ_E is quite weak, and may be omitted (fit #4) with minimal alteration to the result; however, this may not capture effects on the

Figure 5.23: Power-law fit for I-mode energy confinement time τ_E , fitted using the full ITER98y2 parameter set (fit #1 in table 5.1). Both the high-resolution pedestal database and older reversed-field LSN and forward-field USN I-mode databases are used. While the fit is generally good, lack of variation in certain parameters – particularly the size parameters R and ϵ (as expected for a single-machine scaling), and elongation κ mean that the true variation with these parameters is not accurately captured. However, the expected weak degradation of τ_E with heating power is captured.



transport at higher Greenwald fraction, and requires additional experiments.

*physics arguments
for this scaling?*

As an illustrative exercise, we restore a fixed size dependence of the form $R^2\sqrt{\epsilon}$ (as is found in ITER98y2) to the fit, shown as #5 in table 5.1, with the correspondence to experimental τ_E shown in fig. 5.25. This enables extrapolation of the result to larger devices, with example predictions for DIII-D, ASDEX Upgrade, JET, and ITER shown in fig. 5.26. Due to the weakened power degradation ($\tau_E \sim P^{-0.2}$), I-mode operation on ITER (in the putative $Q = 10$ scenario with 100 MW of alpha heating) projects to a ~ 8 s energy confinement time, well in excess of the expected τ_E for H-mode.

*refine wording,
details?*

Again, we emphasize that single-machine scalings are of limited reliability for extrapolative purposes. However, this illustrates the potential gains in performance in the application of I-mode to larger devices, while correctly capturing the observed physics in I-mode (e.g., the degradation in τ_E is, to within uncertainty, consistent with the observed strong dependence of the stored energy and pedestal pressure on heating power).

*ASDEX I-mode
times?*

5.5 CONCLUSIONS

★

Figure 5.24: Power-law fit for I-mode energy confinement time τ_E , fitted with the size parameters R and ε , and elongation κ excluded due to the lack of variation in these variables in the available data (fit #3 in table 5.1). Both the high-resolution pedestal database and older reversed-field LSN and forward-field USN I-mode databases are used.

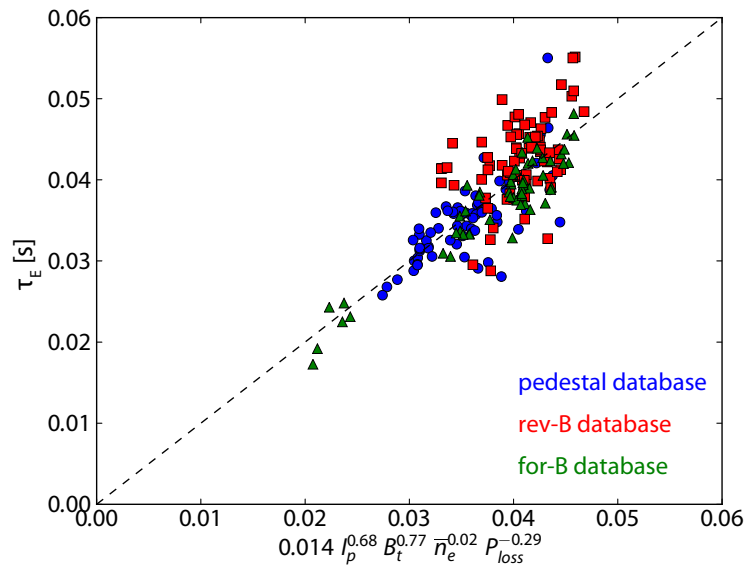


Figure 5.25: Power-law fit to I-mode energy confinement time τ_E , with the ansatz of an $R^2\sqrt{\varepsilon}$ size scaling fixed (fit #5 in table 5.1). Both the high-resolution pedestal database and older reversed-field LSN and forward-field USN I-mode databases are used. Note the expected weak degradation of τ_E with heating power.

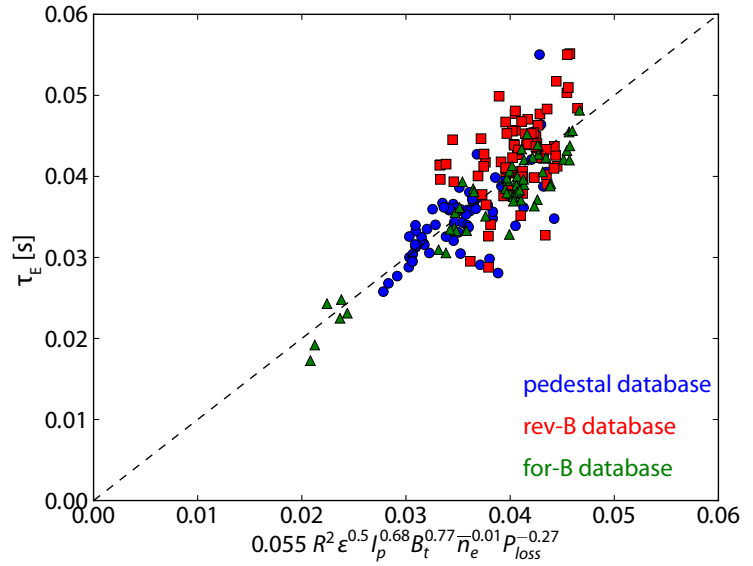
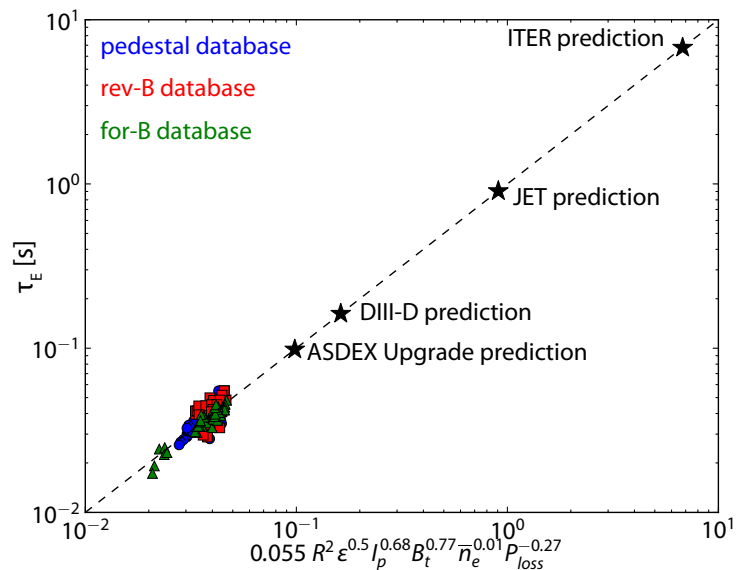


Figure 5.26: Modeled energy confinement time τ_E with the fixed $R^2\sqrt{\epsilon}$ size scaling (fit #5 in table 5.1, extrapolated to DIII-D, ASDEX Upgrade, JET, and ITER. Modeled energy confinement times are competitive with H-modes, both the measured τ_E for existing machines and the expected ITER98y2 prediction for ITER H-modes.



BIBLIOGRAPHY

- [1] D.G. Whyte, A.E. Hubbard, J.W. Hughes, B. Lipschultz, J.E. Rice et al. **I-mode: an H-mode energy confinement regime with L-mode particle transport in Alcator C-Mod.** *Nuclear Fusion*, 50(10):105005, 2010.
- [2] A. E. Hubbard, D. G. Whyte, R. M. Churchill, I. Cziegler, A. Dominguez et al. **Edge energy transport barrier and turbulence in the I-mode regime on Alcator C-Mod.** *Physics of Plasmas*, 18(5):056115, 2011.
- [3] A. Loarte, B. Lipschultz, A.S. Kukushkin, G.F. Matthews, P.C. Stangeby et al. **Chapter 4: Power and particle control.** *Nuclear Fusion*, 47(6):S203, 2007.
- [4] ITER Physics Expert Group on Confinement, Transport and ITER Physics Expert Group on Confinement Modelling and Database and ITER Physics Basis Editors. **Chapter 2: Plasma confinement and transport.** *Nuclear Fusion*, 39(12):2175, 1999.
- [5] J.E. Kinsey, G.M. Staebler, J. Candy, R.E. Waltz and R.V. Budny. **ITER predictions using the GYRO verified and experimentally validated trapped gyro-Landau fluid transport model.** *Nuclear Fusion*, 51(8):083001, 2011.
- [6] A. E. Hubbard, R. L. Boivin, R. S. Granetz, M. Greenwald, I. H. Hutchinson et al. **Measurements of the high confinement mode pedestal region on Alcator C-Mod.** *Physics of Plasmas*, 5(5):1744–1751, 1998.
- [7] W. Suttrop, A. Herrmann, F. Ryter and J. Stober. **Chapter 6: H-mode and pedestal physics in ASDEX Upgrade.** *Fusion Science and Technology*, 44(3):636–649, November 2003.
- [8] T N Carlstrom, K H Burrell and R J Groebner. **Comparison of a VB drift effect model with measured H-mode power thresholds.** *Plasma Physics and Controlled Fusion*, 40(5):669, 1998.
- [9] R J Groebner and T N Carlstrom. **Critical edge parameters for H-mode transition in DIII-D.** *Plasma Physics and Controlled Fusion*, 40(5):673, 1998.
- [10] J.R. Walk, P.B. Snyder, J.W. Hughes, J.L. Terry, A.E. Hubbard et al. **Characterization of the pedestal in Alcator C-Mod ELMing H-modes and comparison with the EPED model.** *Nuclear Fusion*, 52(6):063011, 2012.

- [11] R.J. Groebner, C.S. Chang, J.W. Hughes, R. Maingi, P.B. Snyder et al. Improved understanding of physics processes in pedestal structure, leading to improved predictive capability for ITER. *Nuclear Fusion*, 53(9):093024, 2013.
- [12] H Urano, W Suttrop, L D Horton, A Herrmann, J C Fuchs et al. Energy and particle losses during type-I ELMy H-mode in ASDEX Upgrade. *Plasma Physics and Controlled Fusion*, 45(9):1571, 2003.
- [13] A. E. Hubbard, R. L. Boivin, R. S. Granetz, M. Greenwald, J. W. Hughes et al. Pedestal profiles and fluctuations in C-Mod enhanced D-alpha H-modes. *Physics of Plasmas*, 8(5):2033–2040, 2001.
- [14] A.E. Hubbard, D.G. Whyte, R.M. Churchill, A. Dominguez, J.W. Hughes et al. Threshold conditions for transitions to I-mode and H-mode with unfavourable ion grad B drift direction. *Nuclear Fusion*, 52(11):114009, 2012.
- [15] Arturo Dominguez. *Study of Density Fluctuations and Particle Transport at the Edge of I-Mode Plasmas*. PhD thesis, Massachusetts Institute of Technology, 2012.
- [16] J. W. Connor, R. J. Hastie and J. B. Taylor. Shear, periodicity, and plasma ballooning modes. *Physical Review Letters*, 40:396–399, Feb 1978.
- [17] C.F. Maggi. Progress in understanding the physics of the H-mode pedestal and ELM dynamics. *Nuclear Fusion*, 50(6):066001, 2010.
- [18] M. N. A. Beurskens, T. H. Osborne, P. A. Schneider, E. Wolfrum, L. Frassinetti et al. H-mode pedestal scaling in DIII-D, ASDEX Upgrade, and JET. *Physics of Plasmas*, 18(5):056120, 2011.
- [19] T. Onjun, G. Bateman, A. H. Kritz and G. Hammett. Models for the pedestal temperature at the edge of H-mode tokamak plasmas. *Physics of Plasmas*, 9(12):5018–5030, 2002.
- [20] Istvan Cziegler. *Turbulence and Transport Phenomena in Edge and Scrape-Off Layer Plasmas*. PhD thesis, Massachusetts Institute of Technology, 2011.
- [21] I. Cziegler, P. H. Diamond, N. Fedorczak, P. Manz, G. R. Tynan et al. Fluctuating zonal flows in the I-mode regime in Alcator C-Mod. *Physics of Plasmas*, 20(5):–, 2013.
- [22] A.E. White, P. Phillips, D.G. Whyte, A.E. Hubbard, C. Sung et al. Electron temperature fluctuations associated with the weakly coherent mode in the edge of I-mode plasmas. *Nuclear Fusion*, 51(11):113005, 2011.

- [23] T H Osborne, R J Groebner, L L Lao, A W Leonard, R Maingi et al. **H-mode pedestal characteristics, ELMs, and energy confinement in ITER shape discharges on DIII-D.** *Plasma Physics and Controlled Fusion*, 40(5):845, 1998.
- [24] P. B. Snyder, R. J. Groebner, A. W. Leonard, T. H. Osborne and H. R. Wilson. **Development and validation of a predictive model for the pedestal height.** *Physics of Plasmas*, 16(5):056118, 2009.
- [25] P.A. Schneider, E. Wolfrum, R.J. Groebner, T.H. Osborne, M.N.A. Beurskens et al. **Analysis of temperature and density pedestal gradients in AUG, DIII-D and JET.** *Nuclear Fusion*, 53(7):073039, 2013.
- [26] P.N. Yushmanov, T. Takizuka, K.S. Riedel, O.J.W.F. Kardaun, J.G. Cordey et al. **Scalings for tokamak energy confinement.** *Nuclear Fusion*, 30(10):1999, 1990.
- [27] J.P. Christiansen, J.G. Cordey, K. Thomsen, A. Tanga, J.C. DeBoo et al. **Global energy confinement H-mode database for ITER.** *Nuclear Fusion*, 32(2):291, 1992.
- [28] P.B. Snyder, K.H. Burrell, H.R. Wilson, M.S. Chu, M.E. Fenstermacher et al. **Stability and dynamics of the edge pedestal in the low collisionality regime: physics mechanisms for steady-state ELM-free operation.** *Nuclear Fusion*, 47(8):961, 2007.

6

I-MODE PEDESTAL STABILITY MODELING

Large, uncontrolled Edge-Localized Modes (ELMs – see section 2.1) in ITER-scale operation are expected to drive unacceptable levels of pulsed heat loading and erosion damage to plasma-facing materials [1, 2]. As such, avoiding or mitigating large ELMs is a major focus of research in high-performance regimes: approaches include active ELM control in H-mode (section 2.1.3) and inherently ELM-suppressed regimes (section 2.3). To these we add the I-mode (section 2.4), which appears to be naturally stable against large, deleterious ELMs in addition to its other beneficial properties (see chapter 5).

Confidence in plans for high-performance operation on ITER- and reactor-scale devices requires a predictive model for the pedestal structure and stability, to optimize fusion performance and ELM control or avoidance. Recent cooperative efforts among theory, modeling, and experiment [3] have resulted in such a model for ELMy H-modes, termed EPED [4, 5], detailed in section 3.4. The EPED model combines constraints from peeling-balloonning MHD stability (section 3.2) [6, 7, 8] and kinetic-balloonning turbulence (section 3.3) [9, 10, 11]. The EPED model has been successfully implemented in ELMy H-mode on a number of machines, including DIII-D [4, 5], JT-60U [4], C-Mod [12], and KSTAR [13], as well as in QH-mode [14]; small/no-ELM regimes (EDA H-mode, type-II and type-III ELMy H-modes) have been shown to be stable against the drive identified in the EPED model [4].

cites?

In this chapter, we apply the EPED approach to I-mode, examining the stability of the I-mode pedestal against peeling-balloonning MHD and kinetic-balloonning turbulence [15]. This is compared to the observed lack of large ELMs in I-mode, with a goal of examining the parameter space in which stationary ELM-free operation with I-mode is possible. We also examine the stability and edge behavior of cases in which small, intermittent ELM-like events are observed in I-mode operation.

•

6.1 MHD STABILITY – ELITE

The triggering of large ELMs in H-mode has been identified with the interaction between pressure-driven balloonning and current-driven edge kink/peeling MHD instabilities (the latter is typically referred to as a “peeling” mode to distinguish it from similarly current-driven core kink modes) in the pedestal [6, 7, 8]. Numerical studies of these instabilities using the ELITE code [6, 16], detailed in section 3.2.3,

have proven quite successful in capturing the physics of the ELM trigger.

6.1.1 ELITE Implementation

At its simplest, a single pass in ELITE calculates the growth rate of the peeling-balloonning instability at fixed toroidal mode number n for a given plasma profile (to wit, the pressure gradient and current density in the pedestal) and equilibrium [17]. This requires a reconstructed magnetic equilibrium with sufficiently high point density to capture the rapid variation in flux surfaces near the edge – all results in this chapter were prepared using high-resolution EFIT [18] reconstructions constrained by kinetic profiles – and high-resolution diagnostics to generate accurate profile measurements in the pedestal. To fully capture the physics of the pedestal, however, it is beneficial to visualize the pedestal relative to the full stability boundary (see fig. 3.4 for a schematic illustration), typically expressed in terms of the pressure-gradient and current-density drive terms.

Beginning from the experimental result, the profiles are scaled at fixed pedestal width, such that the pressure pedestal height or peak current density is increased or decreased relative to the original by a scalar factor, after which a self-consistent EFIT reconstruction is attempted. This effectively fills in a grid in $\alpha_{\text{MHD}} - j$ space (a practice commonly termed “varyped”). Horizontal slices scaling the pressure pedestal height (and therefore gradient) at fixed current, and vertical slices scaling the current density at fixed ∇p – although ELITE does not explicitly distinguish between density and temperature profiles, these slices implicitly vary density and temperature relative to each other (for example, increased bootstrap current at fixed ∇p in a vertical slice requires increased density and decreased temperature, and vice versa for horizontal slices) [17]. Note that the practice described in section 3.4 of increasing pressure (and pressure gradient) at fixed width to find the maximum ELM-stable pressure as a function of width is essentially a diagonal slice through the grid: only the pressure profile is explicitly scaled, with the bootstrap current allowed to self-consistently vary, and will increase with increasing ∇p . At each point in the $\alpha_{\text{MHD}} - j$ grid, ELITE is run on a range of mode numbers (here $5 \leq n \leq 35$) to find the most unstable mode and its growth rate; this is normalized to diamagnetic stabilization effects by the threshold for instability onset, $\gamma_{\text{MHD}} > \omega_{*\text{eff}}/2$ where $\omega_{*\text{eff}}$ is the effective diamagnetic frequency accounting for variation in the pedestal, as implemented in EPED1.6 (see section 3.4.2).

how much of this in ch 3?

better ref for kinetic EFIT?

cite?

note low-n peeling, higher-n ballooning in ch 3

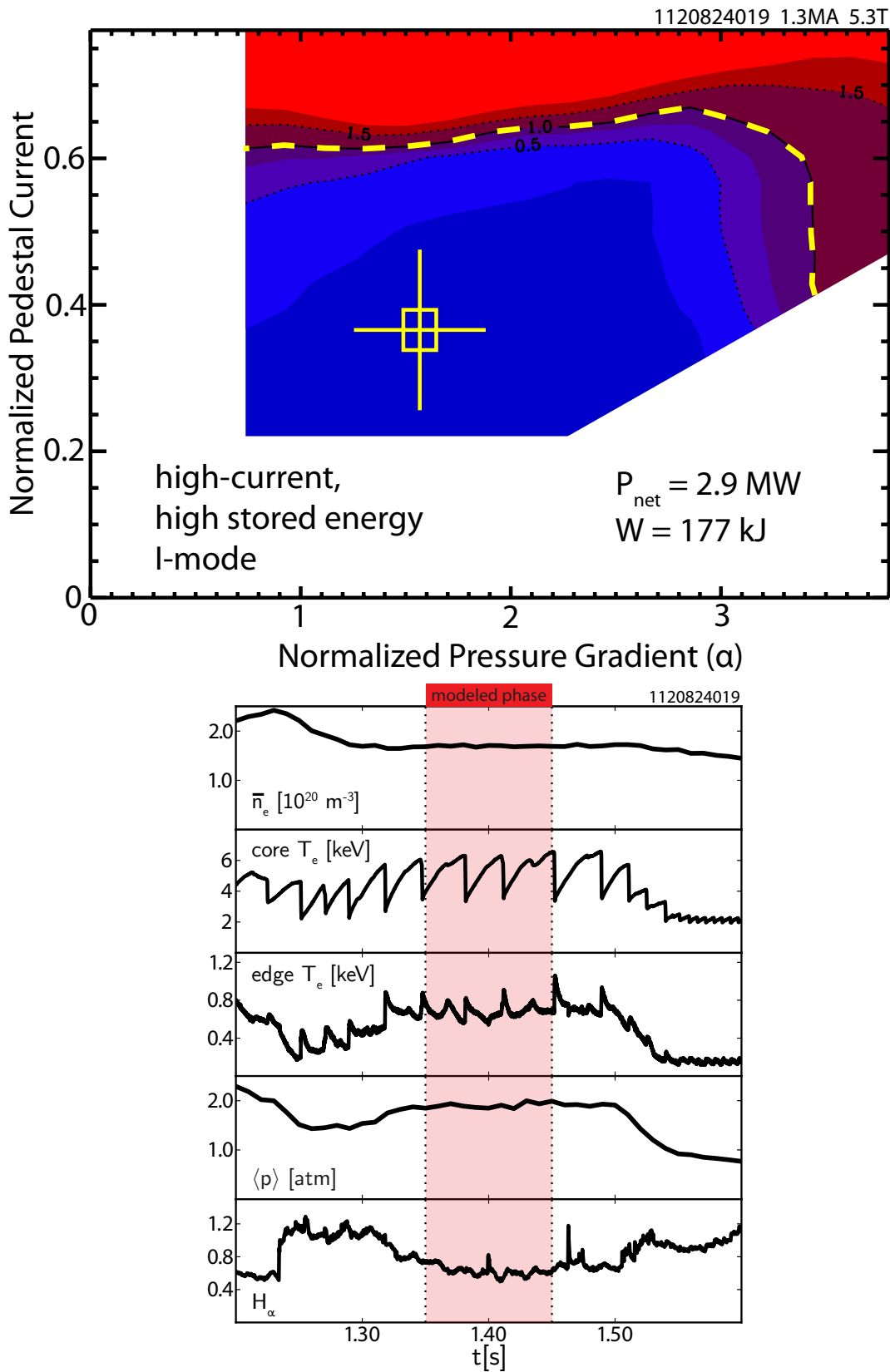
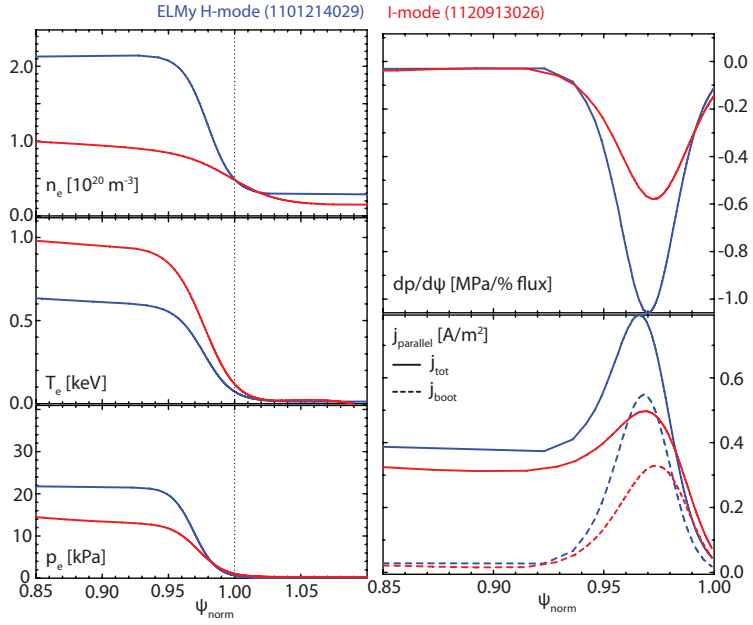


Figure 6.1: MHD stability contour for a high-current (1.3 MA), high-performance I-mode generated by the ELITE code. The experimental measurement is shown by the crosshair, with the stability boundary indicated by the yellow dashed line. Parameters for the modeled phase of the discharge are shown below. The I-mode pedestal is observed to be far from both the peeling and ballooning MHD stability boundaries.

6.1.2 I-Mode ELITE Calculations

An ELITE calculation for the I-mode pedestal is shown in fig. 6.1, along with parameters (line-averaged density, core and edge T_e , global-average pressure, and H_α emission) for the modeled phase of the discharge. The pedestal, indicated by the yellow crosshair, is far from both the peeling and ballooning MHD stability boundaries calculated by ELITE (indicated by the yellow dashed line, marking the $\gamma/(\omega_{\text{eff}}/2) = 1$ contour). This is consistent with the observed lack of large ELMs, even in higher-performance I-modes (both in the normalized sense, with $H_{98} = 1.02$ and $\beta_N = 1.0$, and in absolute terms, $W_{\text{MHD}} = 177 \text{ kJ}$ in the case in fig. 6.1). The calculated MHD stability is intuitively understood from the I-mode pedestal profile: the lack of a strong density pedestal reduces both the total pressure gradient, reducing the ballooning drive, and the edge current, reducing the peeling drive (recall from eq. (2.10) that ∇n_e is the dominant term setting the bootstrap current). A comparison of the pedestal profiles, with pressure gradient and edge current density, between I-mode and H-mode is shown in fig. 6.2:

Figure 6.2: Pedestal profiles in I-mode and ELMy H-mode. Due to the steep density gradient in the pedestal, the H-mode exhibits significant pressure gradient and edge current density, which drive the peeling-balloonning MHD instability associated with the ELM trigger. Despite this, the high edge temperature in I-mode allows it to reach an appreciable pedestal pressure.



Although I-mode is free of the regular, large ELMs typical of (type-I) ELMy H-mode, under certain conditions – particularly reduced toroidal field and plasma current – small (< 1% drop in stored energy) intermittent ELM-like events are occasionally observed in I-mode. However, when examined in ELITE (fig. 6.3) these cases are found to still be far from the peeling-balloonning boundary. These intermittent events occur in conjunction to sawtooth heat pulses reaching the edge, visible on the fast ECE T_e signal, indicating that the events are potentially triggered by transient modification of the pedestal by the

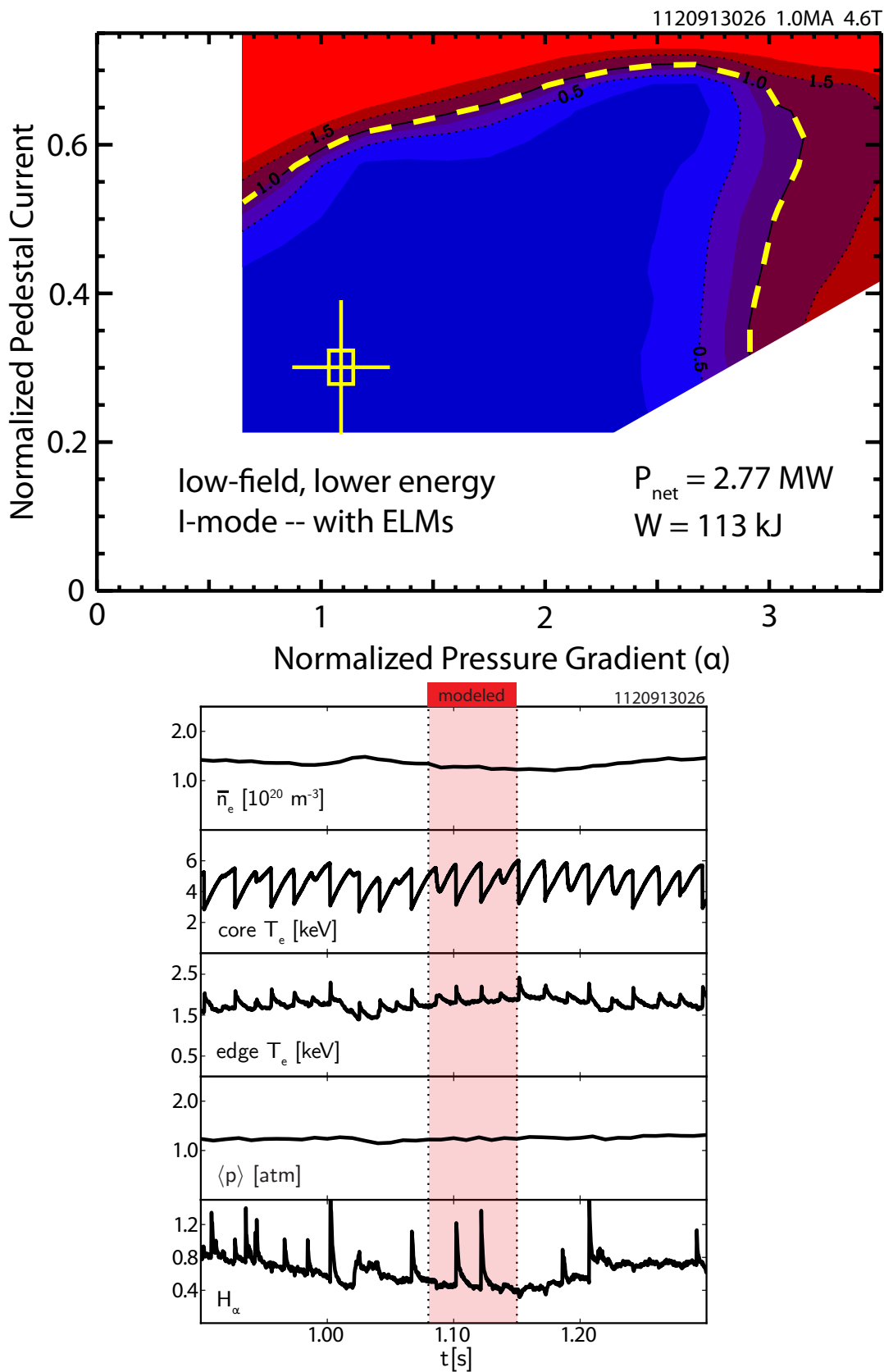


Figure 6.3: MHD stability contour for a low-field, lower-energy I-mode generated by the ELITE code. The experimental measurement is shown by the crosshair, with the stability boundary indicated by the yellow dashed line. Parameters for the modeled phase of the discharge are shown below. This case exhibited small, intermittent ELM-like events, but is still calculated to be peeling-ballooning stable.

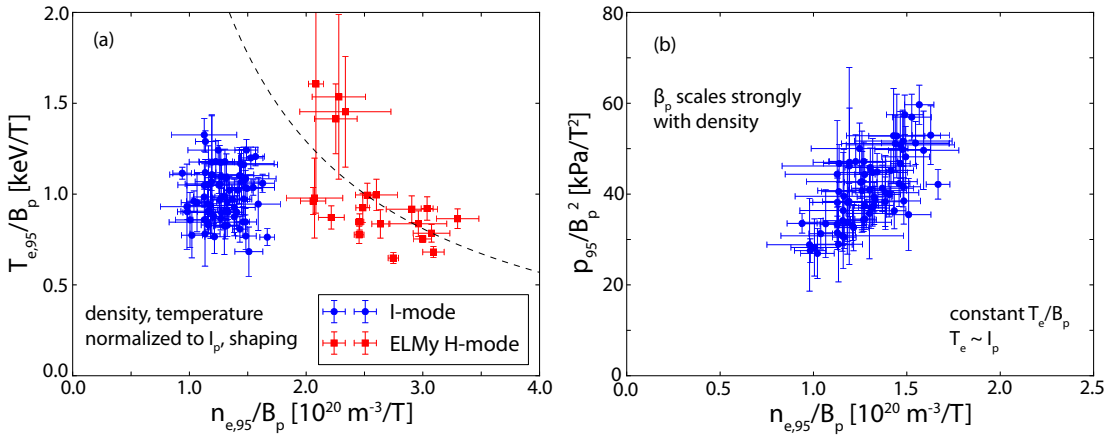


Figure 6.4: Pedestal temperature (left) and pressure (right) versus pedestal density. Parameters are normalized to the edge poloidal field – this accounts for plasma-current variation in the datapoints, as well as allowing a natural representation of MHD boundaries. (a) Pedestal temperature vs. density for I-mode and ELM My H-mode. Due to the poloidal-field normalization, hyperbolae in the parameter space are curves of constant $\beta_{p,ped}$. ELM My H-modes lie, to lowest-order approximation, on a $\beta_{p,ped}$ -limited curve (indicated by the dashed line) with the expected inverse relationship between density and temperature; I-mode n_e and T_e , however, are uncorrelated. (b) Normalized pedestal pressure versus density in I-mode. Pedestal poloidal beta trends linearly with (normalized) density, rather than lying on the $\beta_{p,ped}$ -limited line expected for MHD-limited pedestals, consistent with the strong response of the I-mode pedestal to fueling (see section 5.2.2). I-mode data lie on a line of constant T_e/B_p , consistent with the observed $T_{e,ped} \sim I_p$ seen in section 5.2.1.

heat pulse – however, these events are not consistently triggered on each sawtooth crash under similar conditions. More study is required on this front, with initial results shown in section 6.3.

move this to later section?

footnote this?

Examination of the I-mode pedestal is also illuminating from the perspective of MHD stability. To lowest order approximation, MHD-limited pedestals, as are found in ELM My H-mode, are limited in the attainable poloidal beta at the pedestal top (a limit arising from the limit on α_{MHD} from ballooning instability coupled with the weakly-varying pedestal width on a given tokamak – *cf.* section 2.1.2). This is illustrated in fig. 6.4(a), showing the pedestal density and temperature normalized to poloidal field (accounting for variation in plasma current). Due to the normalization to B_p , hyperbolae in the parameter space are curves of constant β_p . ELM My H-mode data lie on such a curve (note that, since the β_p limit is shaping-dependent, only ELM My H-mode cases with approximately matched shape are shown on the single hyperbolic curve), with the expected inverse relationship between pedestal density and temperature. I-mode pedestal density and temperature, on the other hand, are uncorrelated, consistent with the pedestal not being limited by MHD stability constraints. I-mode pedestal pressure, similarly normalized, is shown against normalized pedestal density in fig. 6.4(b). Where MHD-limited pedestals would show a flat trend due to the limit on poloidal beta, I-mode β_p instead exhibits a linear trend with density. This is consistent with the strong response of pedestal performance with increased fueling

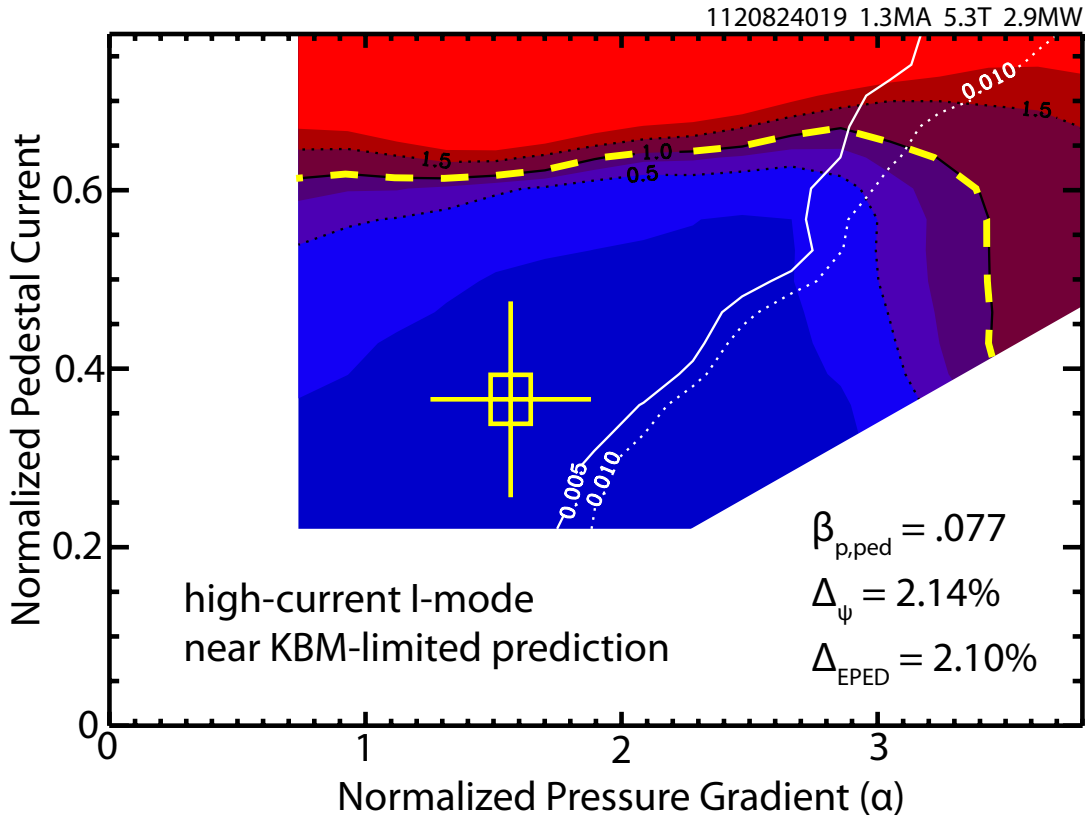


Figure 6.5: Infinite- n ballooning MHD results calculated by BALOO, overlaid on the ELITE results for the same case (see fig. 6.1). The Infinite- n ballooning threshold is taken as a surrogate for the onset of KBM turbulence. Due to the local nature of the infinite- n constraint, BALOO calculates the width in flux space that is locally ballooning-critical – when this reaches half of the pedestal width, the KBM is triggered. This case is near the KBM-predicted pedestal width Δ_{EPED} , but is nevertheless modeled to be KBM-stable (for $\Delta_\psi \sim 0.02$, the half-width threshold is the 0.01 contour).

(described in chapter 5, particularly section 5.2.2) provided sufficient heating power to maintain the pedestal. The slope of this trend is a line of constant $T_{e,95}/B_p$, consistent with the observed $T_e \sim I_p$ as well (see section 5.2.1).

6.2 KINETIC-BALLOONING MODE STABILITY

Edge turbulence in I-mode is characterized by the strong reduction of mid-frequency turbulence corresponding to the reduced energy transport after the L-I transition. In its place, the I-mode pedestal exhibits a broad higher-frequency (200 – 400 kHz) fluctuation, the *Weakly-Coherent Mode* [19, 20, 21] (see section 2.4.3). Due to its prominence in the I-mode edge and functional similarity to the Quasi-Coherent Mode (QCM) in EDA H-mode [22] (see section 2.3.2), the WCM is thought to play a role in regulating the I-mode pedestal, particularly by driving enhanced particle flux [23]. While the WCM is fairly well-characterized experimentally, the underlying physics of the mode re-

reword?

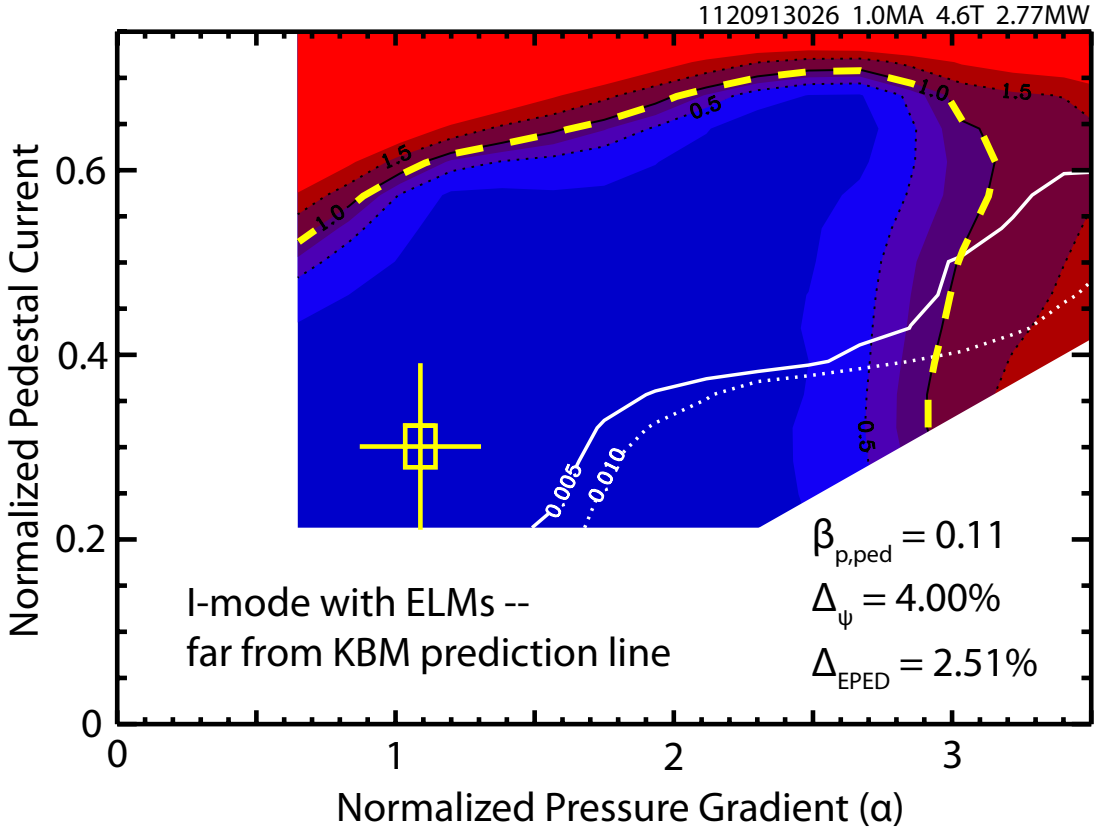


Figure 6.6: Infinite-n ballooning MHD results calculated by BALOO, overlaid on the ELITE results for the same case (see fig. 6.3). This case exhibited sawtooth-triggered ELM-like events. This case is substantially wider than the KBM-predicted pedestal width Δ_{EPED} , and is modeled to be strongly KBM-stable – in fact, the BALOO assay could not calculate enough ballooning-unstable rational surfaces to draw the contour for the BCP-predicted threshold of 0.02.

main an open question. From the standpoint of both turbulence characterization and ELM stability, the kinetic-ballooning mode (KBM) is a valuable starting point for comparing the WCM to the turbulent behavior in more conventional H-modes. *reward?*

Computational modeling of the KBM is possible using infinite-n ideal ballooning MHD as a surrogate for the turbulence threshold [4, 10, 11] (see section 3.3). The localized constraint from the KBM (and perfectly-localized infinite-n ideal MHD) is applied to the entire pedestal via the “ballooning-critical pedestal” technique, described in section 3.3.1, in which the KBM threshold is identified as the point at which half of the pedestal (typically the “middle half” where the pressure gradient is steepest) is locally at or beyond criticality to the MHD surrogate. This is calculated using the BALOO code [24, 25]; at each point in the varyped grid, the number of rational surfaces that are unstable to infinite-n ballooning modes and subsequently the width in poloidal flux space covered by these surfaces is calculated, drawing contours of pedestal half-width corresponding to the KBM threshold.

I-mode pedestals exhibit little trend in width (in poloidal flux space) with pedestal poloidal beta (see fig. 5.12), as is expected for pedestals limited by KBM turbulence. We may compare cases spanning the range in pedestal width Δ_ψ against the KBM-limited prediction for the width, $\Delta_\psi = 0.076\beta_{p,\text{ped}}^{1/2}$, from EPED1 (see section 3.4.1), herein termed Δ_{EPED} . The case near the EPED1 prediction line is shown in fig. 6.5 (overlaid on the ELITE result for the same case, fig. 6.1). For $\Delta_\psi = .021$, the expected KBM threshold based on the BCP half-width calculation is the 0.01 contour – the pedestal is calculated to be stable compared to this threshold. The case far from the EPED1 prediction line is shown in fig. 6.6 (overlaid on the ELITE result for the same case, fig. 6.3). At $\Delta_\psi = 0.04$, the expected KBM threshold is the 0.02 contour – however, the BALOO assay could not calculate enough ballooning-unstable rational surfaces to even draw this contour. Suffice to say that the pedestal is far from the KBM onset threshold as calculated from infinite-n MHD. Notably, the former case ($\Delta_\psi \sim \Delta_{\text{EPED}}$) was a relatively high-performance case, and did not exhibit ELM-like events, while the latter ($\Delta_\psi \gg \Delta_{\text{EPED}}$) exhibited ELM-like events. The indication from both experimental observation and computational modeling, then, is that the KBM is not responsible for limiting the pedestal in I-mode. •

6.3 INTERMITTENT ELMS IN I-MODE

Given the importance of controlling or avoiding large ELMs on ITER- and reactor-scale devices, a firm understanding of the physics underlying the ELM trigger is essential for planned ITER operation. While I-mode is typically observed to be naturally free of large, damaging ELMs, there are nevertheless cases in which small, intermittent ELMs (or ELM-like events) are observed. It is to these cases that we now turn our attention.

ELMs in I-mode are generally observed to be small (< 1% perturbation to the stored energy), and are sporadic, rather than occurring in a regular cycle as in the canonical type-I ELMy H-mode. These events occur shortly following the sawtooth heat pulse reaching the edge, based on timing from fast ECE T_e measurements in the pedestal. This indicates a possible trigger for the event due to transient modification of the pedestal structure. An example case of this is shown in fig. 6.7. The sawtooth heat pulse does not perturb the density profile, but drives a significant transient increase in the temperature pedestal (data masked to the first 25% of the sawtooth cycle after the heat pulse reaches the edge shown in red). Calculations in ELITE and BALOO for this case are shown in fig. 6.8 for both the time-averaged pedestal profile, and the masked data to the sawtooth cycle. While the sawtooth synchronization does drive a measurable perturbation to the pedestal in stability space – the effect is predominantly in the pres-

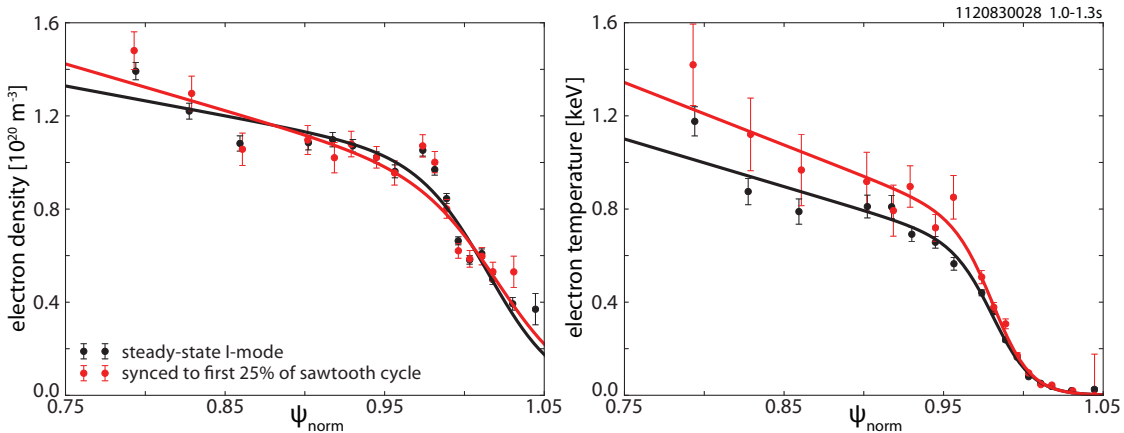


Figure 6.7: Profiles of n_e and T_e in the I-mode pedestal, with the full ensemble-averaged data (black) compared to data masked to the first 25% of the sawtooth cycle following the heat pulse reaching the edge. The Sawtooth does not meaningfully perturb the density profile, but triggers a measurable transient increase in the temperature pedestal.

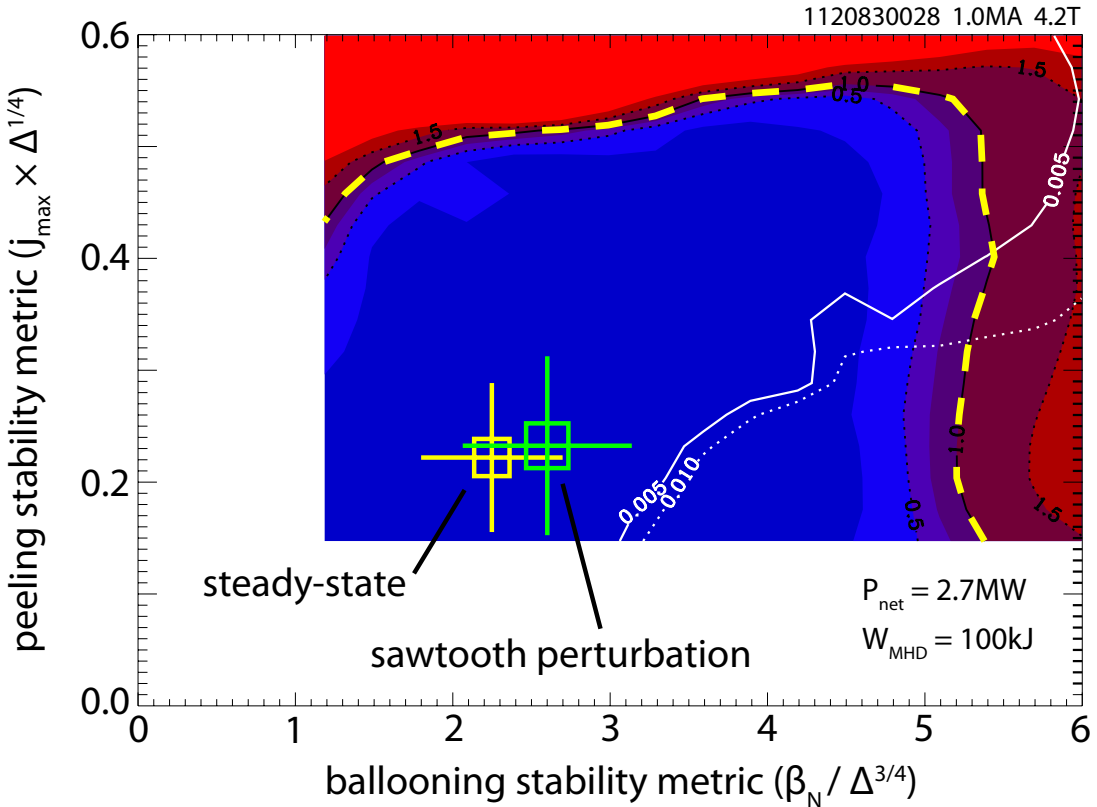


Figure 6.8: Peeling-ballooning MHD stability calculated by ELITE and KBM thresholds calculated by BALOO for an I-mode case, comparing the time-averaged data against pedestal profiles prepared with data masking to the first 25% of the sawtooth cycle following the heat pulse reaching the edge (see fig. 6.7). Note that, to directly compare two separately-calculated equilibria, we replace the α_{MHD} and j_{\parallel} axes with stability metrics arising from peeling and ballooning MHD. While the sawtooth heat pulse does measurably perturb the pedestal in stability space, it is insufficient to reach either the peeling-balloonning or KBM threshold.

sure gradient, rather than the current density, due to the weaker effect of the temperature gradient on the bootstrap current – the effect is insufficient to reach either the peeling-balloon MHD or the KBM turbulence threshold. Note that, in order to compare two separately-computed equilibria, we use alternate axes in fig. 6.8: rather than directly using α_{MHD} and the (normalized) edge current density, the parameter space is presented in terms of ballooning and kink-peeling stability parameters, $\beta_N/\Delta^{3/4}$ and $j_{\max}\Delta^{1/4}$. The first encapsulates the $p_{\text{ped}} \sim \Delta^{3/4}$ trend expected from ballooning stability, when accounting for the nonlocal effects – at broader Δ , wider low- n modes destabilize more easily, reducing the maximum α_{MHD} , as described in section 3.2 – and current stabilization. The second accounts for the trend in the total current, $\int j \, d\psi \sim \Delta^{3/4}$; however, the maximum current density and total pedestal current may be related by $\int j \, d\psi \sim j_{\max}\Delta \rightarrow j_{\max} \sim 1/\Delta^{1/4}$, thus the current-driven kink/peeling stability may be expressed in terms of the normalized $j_{\max}\Delta^{1/4}$.

elaborate in ch 3

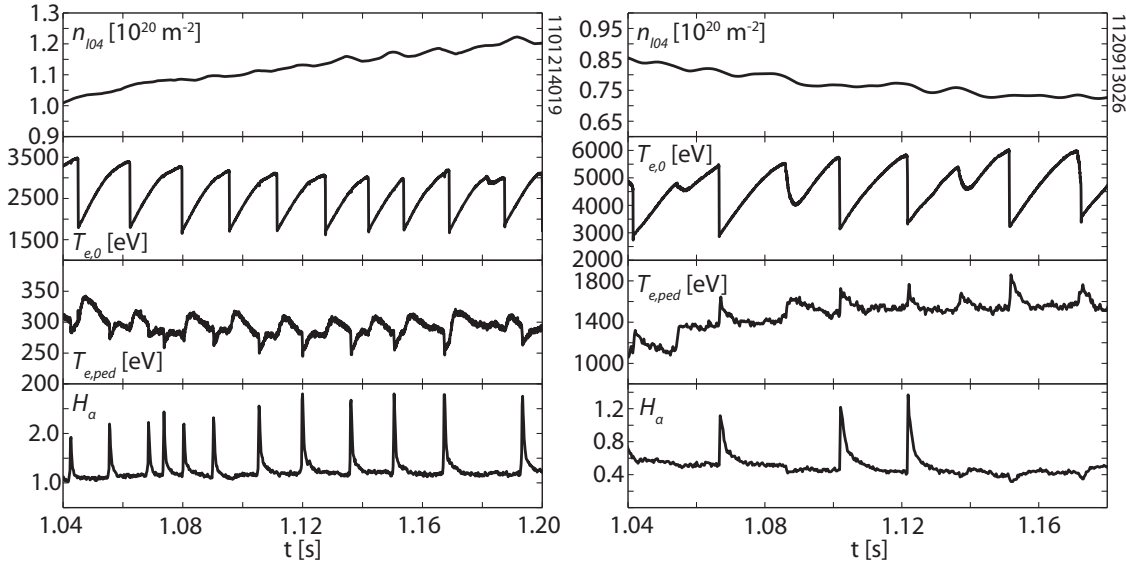
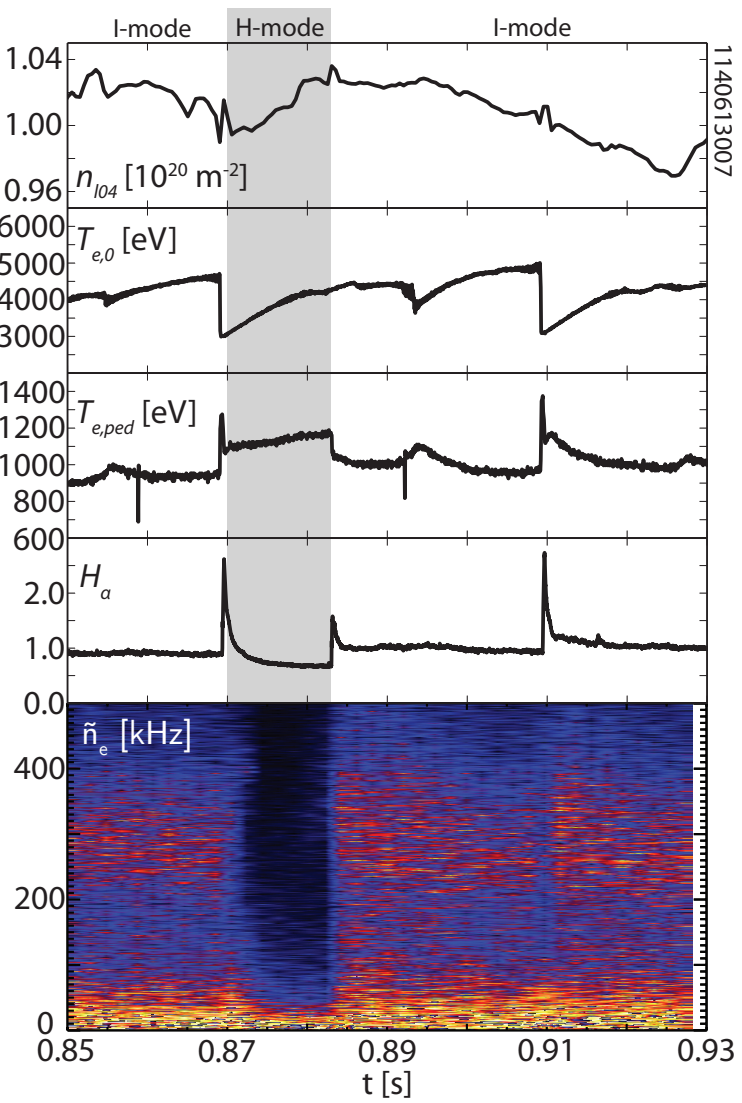


Figure 6.9: Traces of n_{l04} , core and edge T_e , and H_α for ELMMy H-mode (left) and I-mode (right). ELMs in H-mode (visible on the H_α trace) are independent of the sawtooth cycle, and drive perturbations to the edge temperature and line-integrated density, as both energy and particles are expelled from the plasma by the ELM crash. This is particularly clear on the edge temperature, which exhibits a clear increase with the sawtooth heat pulse and a separate crash with the ELM. I-mode, in contrast, exhibits ELMs (or ELM-like events) that are tied to sawtooth heat pulses reaching the edge, as visible on the ECE T_e signal. No visible crash in edge temperature is visible following the ELM, nor is there a significant perturbation to the density.

In light of the observed stability of I-mode to peeling-balloon MHD – even in cases where the perturbation of the putative sawtooth trigger for ELMs is accounted for – it is worthwhile to examine the behavior of the ELMs in I-mode compared to those found in more conventional H-modes. Traces from a type-I ELMMy H-mode and an I-mode are shown in fig. 6.9. The ELMMy case (left) exhibits behavior typical of a type-I ELM cycle: discrete, regular ELMs (visible on the

Figure 6.10: Traces of n_{104} , core and edge T_e , and H_α for an I-mode exhibiting ELM-like events. The sawtooth heat pulse at ~ 0.87 s triggers an I-H transition, indicated by the drop in H_α and suppression of turbulence visible on the \tilde{n}_e plot. This H-mode terminates with a non-sawtooth-triggered ELM with visible edge temperature crash and density perturbation, dropping back into I-mode. The I-mode phase also exhibits sawtooth-triggered ELM-like events with no visible density perturbation or temperature crash.



H_α trace), with crashes in density and edge temperature as the ELM expels energy and particles into the SOL. The effects of the sawteeth are distinct from the ELM, with a spike and subsequent relaxation in edge temperature from the heat pulse visible on the edge ECE T_e separate from the sharp temperature-pedestal crash due to the ELM. The sporadic sawtooth-triggered events in I-mode (right), despite a similar trace in H_α , do not exhibit the characteristic crash in edge temperature associated with an ELM – rather, only the spike in T_e from the sawtooth heat pulse is visible, followed by a relaxation to the steady pedestal temperature.

The distinction between the two edge perturbations is visible in a single case, shown in fig. 6.10. The sawtooth heat pulse at 0.87 s triggers an I-H transition, indicated by the reduction in H_α light following the pulse from the sawtooth, and the sudden reduction in turbulence visible in the \tilde{n}_e spectrogram (both destroying the WCM fluctuation at ~ 300 kHz, and further reducing the mid-frequency

broadband turbulence). Such a transition is not unheard-of – recall that the L-I transition is tied to sawtooth heat pulses as well. This H-mode terminates with a non-sawtooth-triggered ELM at 0.885 s, with the customary crash in edge temperature and H_α spike. After the H-mode terminates, the plasma drops back into I-mode, with a further sawtooth-triggered event at 0.91 s, which lacks a temperature crash.

It is possible that the sawtooth heat pulse modification to the pedestal is sufficient to trigger a conventional ELM instability. However, given that (a) the sawtooth-triggered events constituting the majority of ELMs in I-mode exhibit distinct edge behavior from more customary ELMs and (b) there is little distinction between cases with and without ELMs in terms of computed MHD stability, it is possible that the sawtooth-triggered events are a distinct phenomenon from large ELMs, independent of peeling-balloonning instability. A plausible explanation is that the sawtooth does not trigger an instability in the edge, but instead propagates into the scrape-off layer. The heat pulse then creates a propagating ionization front as it encounters the cold plasma and neutral gas in the SOL. The burst of H_α light and subsequent exponential decay is due to this sudden pulse energizing neutrals in the edge. Fundamentally, the H_α spike from a conventional ELM is driven by the same cause – a sudden influx of ions and energy into the SOL, as well as a similar ionization front in the neutrals in the far SOL. However, unlike the measurable expulsion of energy and particles from the pedestal by the ELM, the sawtooth-triggered events found in I-mode do not appear to significantly perturb the pedestal, and are evidently not tied to a major MHD instability.

These sawtooth-triggered events, which do not appear to perturb the pedestal in a deleterious sense, comprise the majority of ELM (or ELM-like) events in I-mode. A minority of these events do, however, exhibit the edge T_e crash expected from a conventional ELM. Peeling-balloonning stability analysis of such a case is presented in fig. 6.11, with additional KBM analysis in BALOO in fig. 6.12. In this case, a single ELM is visible at 1.1 s, independent of the sawtooth cycle – rather, the characteristic crash is visible in the edge temperature after relaxation of the temperature from the sawtooth heat pulse (note, however, that the ELM does not significantly perturb the stored energy/global-averaged pressure). When modeled in ELITE and BALOO, however, the steady I-mode phase around the ELM is nevertheless found to be well into the stable region both for infinite-n ballooning modes and finite-n coupled peeling-balloonning modes. While it is possible that a transient effect drove the pedestal near the classical ELM stability boundary in this case, the stationary state for the plasma is evidently stable to the expected ELM triggers. ●

*distinction from
grassy / type-II,III
ELMs?*

merge these figures?

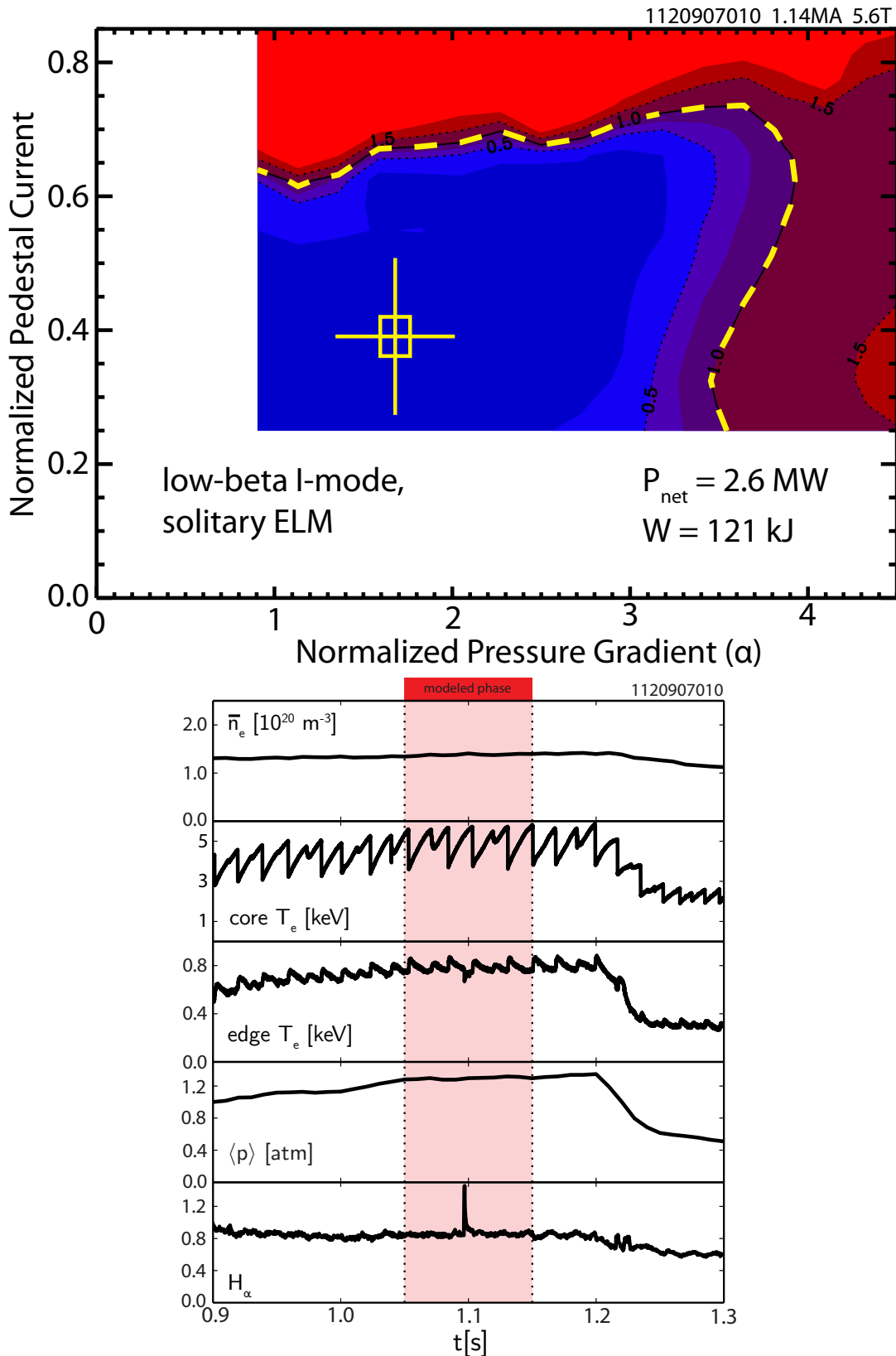


Figure 6.11: MHD stability contour for I-mode generated by the ELITE code. The experimental measurement is shown by the crosshair, with the stability boundary indicated by the yellow dashed line. Parameters for the modeled phase of the discharge are shown below. This case exhibited a solitary ELM not triggered by the sawtooth heat pulse, with the characteristic edge temperature crash of a canonical ELM. However, the I-mode phase around the ELM is calculated to be peeling-balloonning stable.

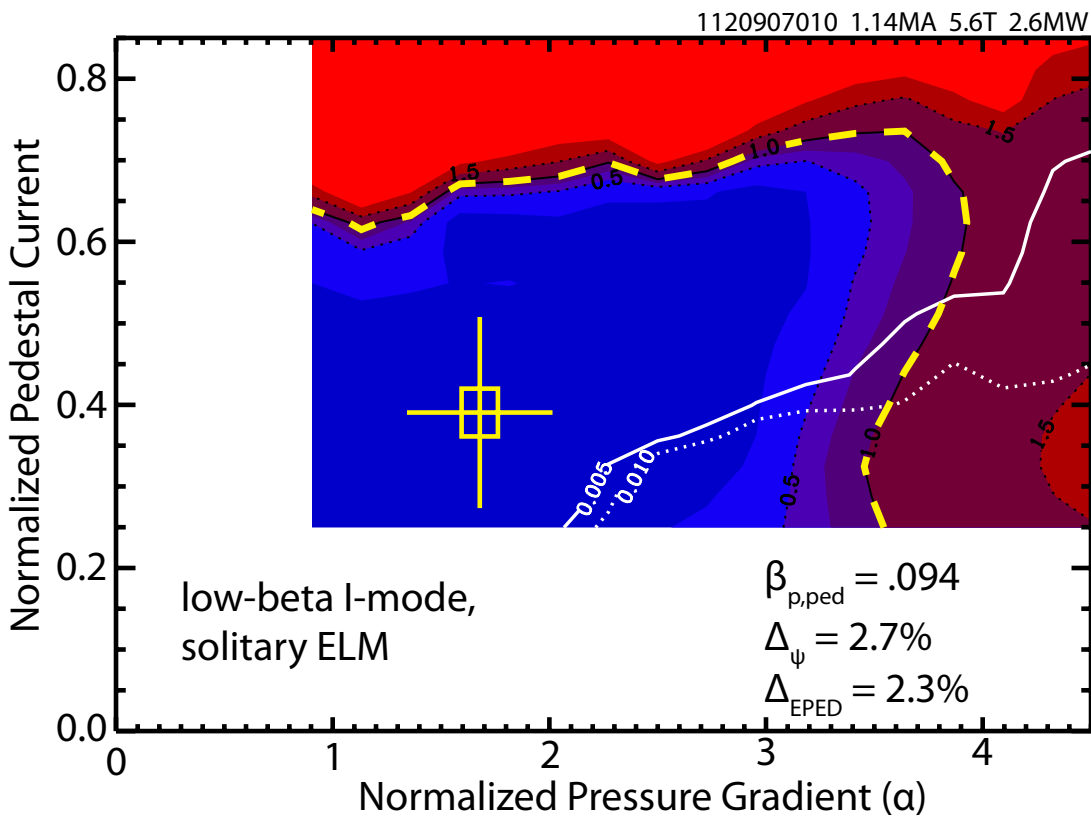


Figure 6.12: Infinite- n ballooning MHD results calculated by BALOO, overlaid on the ELITE results for the same case (see fig. 6.11). This case is modeled to be far from the KBM threshold, and is wider than the EPED₁-like prediction despite the presence of the ELM.

6.4 SUMMARY & DISCUSSION

Models for the trigger of large, deleterious ELMs based on coupled peeling-balloonning MHD instabilities [6, 7, 8, 16] and kinetic-balloonning turbulence [9, 10, 11] have been particularly successful in capturing the physics underlying the ELMy H-mode pedestal. This approach is applied to the I-mode pedestal. The majority of I-mode cases are naturally free of ELMs, and are modeled to be strongly stable both to coupled peeling-balloonning MHD modes and to KBM turbulence (calculated by way of the infinite- n ideal-balloonning MHD surrogate). Under certain conditions, particularly reduced plasma current and magnetic field, the I-mode exhibits small, intermittent ELM-like events evidently tied to the sawtooth heat pulse reaching the plasma edge. These cases are similarly modeled to be stable to the ELM trigger, even when the data is treated to account for transient modification of the temperature pedestal by the sawtooth. The edge behavior of these events appear to be distinct from that expected of ELMs, in that they do not present the expected crash in edge temperature (taken from fast ECE T_e measurements in the pedestal) from the expulsion of energy and particles by the ELM. This, coupled with the computed

stability of these pedestals, suggests that the phenomenon in I-mode is distinct from a traditional ELM, with the measured spike in H_{α} light (customarily indicative of an ELM) possibly driven by an ionization front in the SOL from the sawtooth heat pulse. A small minority of ELM events in I-mode, however, do exhibit the characteristic crash in temperature from the ELM, which are in these instances also not evidently triggered by the sawtooth heat pulse. The steady I-mode phases around these events, however, are also modeled to be stable, indicating a possible transient event driving the ELM.

This assay into the computed stability of I-mode is consistent with the observed absence of large, deleterious type-I ELMs in I-mode. The minority of I-mode cases exhibiting ELMs are still evidently stable in the stationary state against the ELM trigger, with small, intermittent ELMs triggered by transient events in the pedestal – the majority of these events do not appear to significantly perturb the pedestal and do not expel energy and particles into the plasma exhaust as expected for an ELM, possibly indicating that they are a fundamentally different (and less dangerous) phenomenon. Moreover, the I-mode cases exhibiting ELMs are typically the *lower* performance cases, with less aggressive fueling and heating power, reaching lower absolute (in terms of stored energy) and normalized (pedestal beta) performance. The conclusion, then, is that the existing I-mode parameter space is naturally stable against large (type-I) ELMs, as is desired for a putative reactor regime.

★

*discuss expansion to
higher fueling here,
or in conclusion
chapter?*

BIBLIOGRAPHY

- [1] A Loarte, G Saibene, R Sartori, D Campbell, M Becoulet et al. **Characteristics of type I ELM energy and particle losses in existing devices and their extrapolation to ITER.** *Plasma Physics and Controlled Fusion*, 45(9):1549, 2003.
- [2] G Federici, A Loarte and G Strohmayer. **Assessment of erosion of the ITER divertor targets during type I ELMs.** *Plasma Physics and Controlled Fusion*, 45(9):1523, 2003.
- [3] R.J. Groebner, C.S. Chang, J.W. Hughes, R. Maingi, P.B. Snyder et al. **Improved understanding of physics processes in pedestal structure, leading to improved predictive capability for ITER.** *Nuclear Fusion*, 53(9):093024, 2013.
- [4] P. B. Snyder, R. J. Groebner, A. W. Leonard, T. H. Osborne and H. R. Wilson. **Development and validation of a predictive model for the pedestal height.** *Physics of Plasmas*, 16(5):056118, 2009.
- [5] P.B. Snyder, R.J. Groebner, J.W. Hughes, T.H. Osborne, M. Beurskens et al. **A first-principles predictive model of the pedestal height and width: development, testing and ITER optimization with the EPED model.** *Nuclear Fusion*, 51(10):103016, 2011.
- [6] H. R. Wilson, P. B. Snyder, G. T. A. Huysmans and R. L. Miller. **Numerical studies of edge localized instabilities in tokamaks.** *Physics of Plasmas*, 9(4):1277–1286, 2002.
- [7] P.B. Snyder, H.R. Wilson, J.R. Ferron, L.L. Lao, A.W. Leonard et al. **ELMs and constraints on the H-mode pedestal: peeling-ballooning stability calculation and comparison with experiment.** *Nuclear Fusion*, 44(2):320, 2004.
- [8] H R Wilson, S C Cowley, A Kirk and P B Snyder. **Magneto-hydrodynamic stability of the H-mode transport barrier as a model for edge localized modes: an overview.** *Plasma Physics and Controlled Fusion*, 48(5A):A71, 2006.
- [9] Philip B. Snyder. *Gyrofluid Theory and Simulation of Electromagnetic Turbulence and Transport in Tokamak Plasmas*. PhD thesis, Princeton University, 1999.
- [10] J. Candy. **Beta scaling of transport in microturbulence simulations.** *Physics of Plasmas*, 12(7):–, 2005.

- [11] P. B. Snyder and G. W. Hammett. Electromagnetic effects on plasma microturbulence and transport. *Physics of Plasmas*, 8(3):744–749, 2001.
- [12] J.R. Walk, P.B. Snyder, J.W. Hughes, J.L. Terry, A.E. Hubbard et al. Characterization of the pedestal in Alcator C-Mod ELMing H-modes and comparison with the EPED model. *Nuclear Fusion*, 52(6):063011, 2012.
- [13] Hyunsun Han, Ohjin Kwon and J. Y. Kim. Predictive modeling of pedestal structure in KSTAR using EPED model. *Physics of Plasmas*, 20(10):–, 2013.
- [14] P. B. Snyder, T. H. Osborne, K. H. Burrell, R. J. Groebner, A. W. Leonard et al. The EPED pedestal model and edge localized mode-suppressed regimes: Studies of quiescent H-mode and development of a model for edge localized mode suppression via resonant magnetic perturbations. *Physics of Plasmas*, 19(5):–, 2012.
- [15] J. R. Walk, J. W. Hughes, A. E. Hubbard, J. L. Terry, D. G. Whyte et al. Edge-localized mode avoidance and pedestal structure in I-mode plasmas. *Physics of Plasmas*, 21(5):–, 2014.
- [16] P B Snyder and H R Wilson. Ideal magnetohydrodynamic constraints on the pedestal temperature in tokamaks. *Plasma Physics and Controlled Fusion*, 45(9):1671, 2003.
- [17] Philip B. Snyder. personal communication, August 2013.
- [18] L.L. Lao, H. St. John, R.D. Stambaugh, A.G. Kellman and W. Pfeiffer. Reconstruction of current profile parameters and plasma shapes in tokamaks. *Nuclear Fusion*, 25(11):1611, 1985.
- [19] D.G. Whyte, A.E. Hubbard, J.W. Hughes, B. Lipschultz, J.E. Rice et al. I-mode: an H-mode energy confinement regime with L-mode particle transport in Alcator C-Mod. *Nuclear Fusion*, 50(10):105005, 2010.
- [20] A. E. Hubbard, D. G. Whyte, R. M. Churchill, I. Cziegler, A. Dominguez et al. Edge energy transport barrier and turbulence in the I-mode regime on Alcator C-Mod. *Physics of Plasmas*, 18(5):056115, 2011.
- [21] I. Cziegler, P. H. Diamond, N. Fedorczak, P. Manz, G. R. Tynan et al. Fluctuating zonal flows in the I-mode regime in Alcator C-Mod. *Physics of Plasmas*, 20(5):–, 2013.
- [22] A. E. Hubbard, R. L. Boivin, R. S. Granetz, M. Greenwald, J. W. Hughes et al. Pedestal profiles and fluctuations in C-Mod enhanced D-alpha H-modes. *Physics of Plasmas*, 8(5):2033–2040, 2001.

- [23] Arturo Dominguez. *Study of Density Fluctuations and Particle Transport at the Edge of I-Mode Plasmas*. PhD thesis, Massachusetts Institute of Technology, 2012.
- [24] J. W. Connor, R. J. Hastie and J. B. Taylor. **High mode number stability of an axisymmetric toroidal plasma**. *Proceedings of the Royal Society of London. A. Mathematical and Physical Sciences*, 365(1720):1–17, 1979.
- [25] R.L. Miller and J.W. Van Dam. **Hot particle stabilization of ballooning modes in tokamaks**. *Nuclear Fusion*, 27(12):2101, 1987.

7

CONCLUSIONS

•

BIBLIOGRAPHY

A

DIAGNOSTICS

The dedicated pedestal experiments, both in I-mode and ELMy H-mode, presented here required an extensive suite of diagnostics to characterize pedestal behavior. Broadly, these diagnostics may be broken down into three categories:

THOMSON SCATTERING

Details the edge Thomson scattering diagnostic, from which the high-resolution profile data used for the bulk of this thesis was gathered.

FAST DIAGNOSTICS

Details the Electron-Cyclotron Emission (ECE) and H_{α} line radiation diagnostics used to track sawtooth crashes and ELM events in the plasma edge.

FLUCTUATION DIAGNOSTICS

Details Gas-Puff Imaging (GPI), Reflectometry, and other diagnostics used to characterize the mid-frequency fluctuations found in I-mode pedestals.

•

A.1 THOMSON SCATTERING

Due to the steep gradients in density, temperature, and pressure found in the pedestal, accurate characterization of plasma profiles in this region requires diagnostics capable of very fine spatial resolution. Measurements based on the Thomson scattering [1] of laser light off of electrons in the plasma provides the high-resolution pedestal profiles used in this thesis: Thomson scattering is a near-direct measurement of electron temperature and density, independent of bulk plasma parameters (i.e., it is unaffected by the cutoffs or reflections found in other diagnostics, and produces no significant perturbation to the plasma). Measurement via Thomson scattering produces an effective “snapshot” of the plasma parameters at each measurement point, with spatial resolution limited only by collection optics geometry, and time resolution limited by repetition rate on the lasers. Despite significant technical difficulties – for example, the high-powered lasers and sensitive collection optics needed to capture the weak scattered light and the necessity for careful calibration of density measurements – Thomson scattering diagnostics remain a versatile and powerful tool for plasma pedestal measurement, and provided the bulk of the profile data used in this thesis.

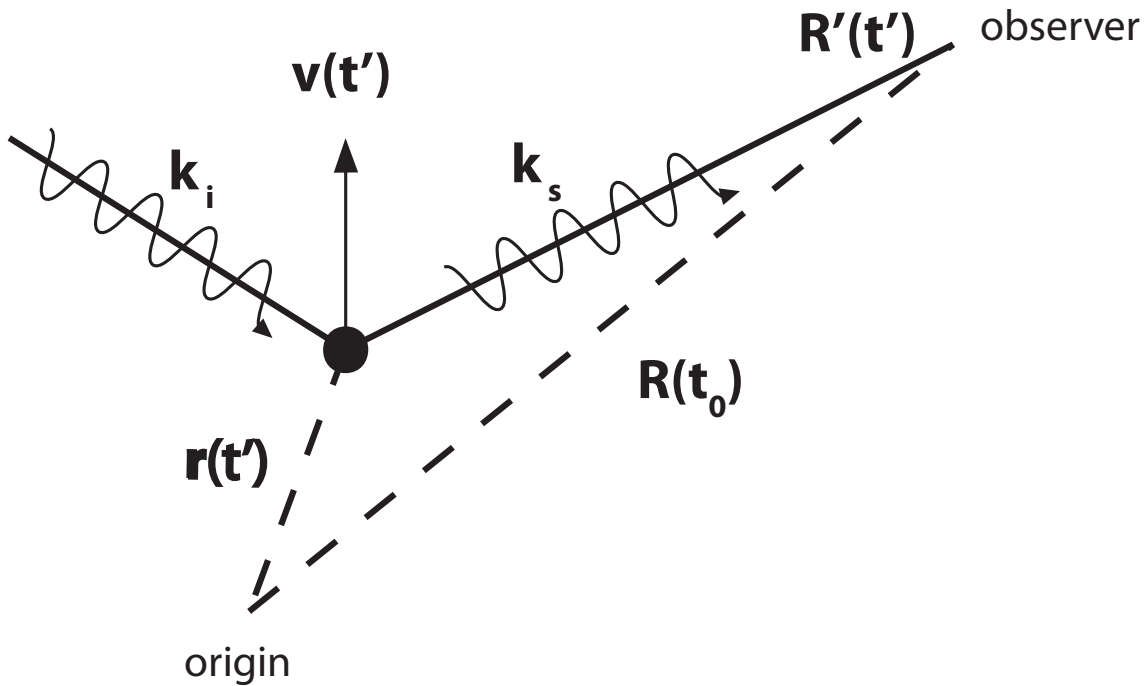


Figure A.1: Coordinate system considered for Thomson scattering, with the incident wave of wavenumber \vec{k}_i incident on a particle at $\vec{r}(t')$ for retarded time t' . The scattered wave \vec{k}_s is drawn to an observer at $\vec{R}'(t')$.

A.1.1 Principles of Thomson Scattering

An intuitive picture of the Thomson scattering phenomenon may be obtained by the consideration of a stationary, free electron with an EM wave impinging on it. The particle will be accelerated by the wave (approximately sinusoidally for E-field-dominated acceleration at nonrelativistic speeds), causing it to radiate. Any motion of the electron will cause Doppler shifting in the scattered radiation – motion relative to the incident wave shifts the incident frequency ω_i , at which the particle oscillates, while motion relative to an observer shifts the scattered wave. This geometry for general positions of the particle and observer is given in fig. A.1.

The scattered electric field from a generally-accelerated electron moving at $\beta = \vec{v}/c$ is given from the Lienard-Wiechert potentials [2, §7],

$$\vec{E}_s = \frac{-e}{4\pi\epsilon_0} \left[\frac{1}{\kappa^3 R c} \hat{s} \times \left((\hat{s} \times \vec{\beta}) \times \dot{\beta} \right) \right]_{t'} \quad (A.1)$$

$$\kappa = 1 = \frac{\vec{R}' \cdot \vec{v}}{R' c} = 1 - \hat{s} \cdot \vec{\beta}, \quad t' = t - \frac{R'}{c}$$

where \hat{s} indicates the unit vector along the scattering direction, $\vec{R} = R\hat{s}$ is the vector to the observer, κ is a relativistic scale factor, and t' is the relativistic retarded time. The apostrophe indicates a parameter

evaluated at the retarded time, i.e., $R' = R(t')$; the bracketed term in eq. (A.1) likewise is evaluated at t' . The scattered power per solid angle is given by

$$\begin{aligned}\frac{dP_s}{d\Omega} &= R^2 \vec{S} \cdot \hat{s} = R^2 \frac{1}{\mu_0} (\vec{E} \times \vec{B}) \cdot \hat{s} \\ &= R^2 \epsilon_0 c (\vec{E}_s \times (\hat{s} \times \vec{E}_s)) \cdot \hat{s} = R^2 c \epsilon_0 |E_s|^2\end{aligned}\quad (\text{A.2})$$

Relativistically, the electron motion (which in turn sets the field determined by eq. (A.1)) is given by

$$\dot{\beta} = \frac{d}{dt} (\gamma m_e \vec{v}) = -e (\vec{E}_i + \vec{v} \times \vec{B}_i) \quad (\text{A.3})$$

where $\gamma = (1 - \beta^2)^{-1/2}$ is a relativistic scale factor. Thus

$$m_e \gamma \dot{\beta} + \gamma^3 m_e \beta (\vec{\beta} \cdot \vec{\beta}) = -e \left(\frac{\vec{E}_i}{c} + \vec{\beta} \times \vec{B}_i \right) \quad (\text{A.4})$$

Dotting $\vec{\beta}$ into this and substituting,

$$\dot{\beta} = -\frac{e}{m_e \gamma} \left(\frac{\vec{E}_i}{c} - \frac{\vec{\beta} \cdot \vec{E}_i}{c} \vec{\beta} + \vec{\beta} \times \vec{B}_i \right) \quad (\text{A.5})$$

The general relativistic solution to eqs. (A.1) and (A.2) with the above is rather intractable, although full relativistic treatments have been undertaken [3, 4, 5, 6]. However, the radiated field may be simplified substantially in the nonrelativistic limit – in the limit of $\beta \ll 1$, the acceleration is simply

$$\dot{\beta} = -\frac{e}{m_e c} \vec{E}_i \quad (\text{A.6})$$

and the scattered field is

$$\vec{E}_s = \frac{e^2}{4\pi\epsilon_0 m_e c^2} \left[\left[\frac{1}{R} \hat{s} \times (\hat{s} \times \vec{E}_i) \right] \right]_{t'}, \quad (\text{A.7})$$

Recalling the classical electron radius,

$$r_e = \frac{e^2}{4\pi\epsilon_0 m_e c^2} \quad (\text{A.8})$$

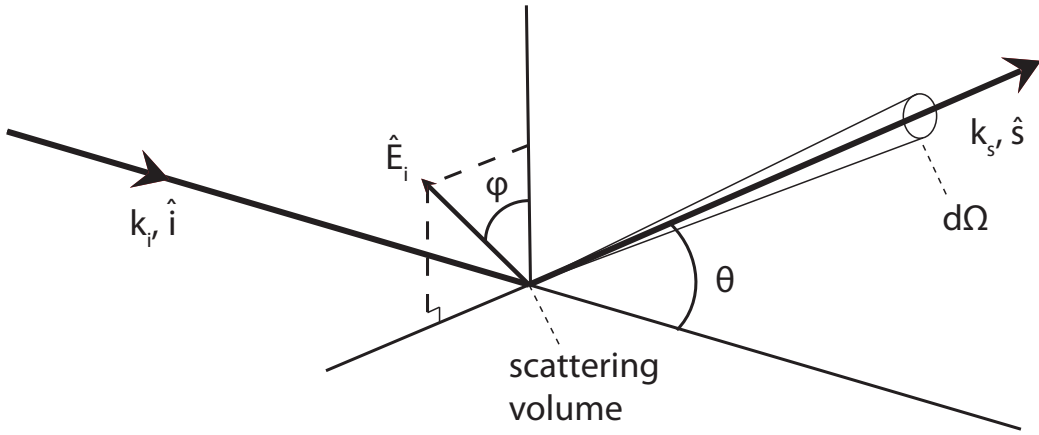


Figure A.2: Definitions of the angular dependences in the Thomson scattering geometry: namely, the angle θ between the incident wave direction \hat{i} and scattering direction \hat{s} , and the polarization angle ϕ of the incident electric field \hat{E}_i with respect to the projection of \hat{s} into the polarization plane.

the radiated power is given by

$$\frac{dP_s}{d\Omega} = r_e^2 c \epsilon_0 E_{i0}^2 \llbracket \hat{s} \times (\hat{s} \times \hat{E}_i) \rrbracket^2 \cos^2(\vec{k}_i \cdot \vec{r}' - \omega_i t') \quad (\text{A.9})$$

separating the magnitude, direction, and phase (evaluated at t') of the incident field.

We may first consider the scattering direction dependence,

$$\llbracket \hat{s} \times (\hat{s} \times \hat{E}_i) \rrbracket_{t'}^2 \quad (\text{A.10})$$

Defining the angular geometry as in fig. A.2 for the scattering angle θ between the incident wave direction \hat{i} and scattering direction \hat{s} , and the polarization angle ϕ (defined between \hat{E}_i and the projection of \hat{s} into the polarization plane), this reduces to (cf. [1, §1.7])

$$\llbracket \hat{s} \times (\hat{s} \times \hat{E}_i) \rrbracket^2 = 1 - \sin^2 \theta \cos^2 \phi \quad (\text{A.11})$$

Since the incident power flux is given by

$$S_i = c \epsilon_0 E_{i0}^2 \cos^2(\vec{k}_i \cdot \vec{r}' - \omega_i t') \quad (\text{A.12})$$

We may separate the incident flux and scattering by

$$\frac{dP}{d\Omega} = S_i \frac{d\sigma_t}{d\Omega} \Rightarrow \frac{d\sigma_t}{d\Omega} = r_e^2 [1 - \sin^2 \theta \cos^2 \phi] \quad (\text{A.13})$$

defining a scattering cross-section σ_t . Integrating over $d\Omega$,

$$\sigma_t = \frac{8\pi}{3} r_e^2 = 6.65 \times 10^{-29} \text{ m}^2 \quad (\text{A.14})$$

The extremely small cross-section for Thomson scattering necessitates high-powered lasers and sensitive collection optics – for example, the fraction of photons scattered from a segment along the laser beam path of length L with electron density n_e is given simply by $L n_e \sigma_t$. For $L = 1 \text{ mm}$ and $n_e = 1 \times 10^{20} \text{ m}^{-3}$, Thomson scattering faces an attenuation factor on the order of $\sim 10^{-11}$ to the incident photon count from the laser.

The phase of the scattered wave is determined by a retarded-time evaluation of the incident phase, $\vec{k}_i \cdot \vec{r}(t') - \omega_i t'$. Substituting $\vec{r}(t') = \vec{r}_0 + \vec{v}t'$, and assuming $R(t') \approx R(t_0)$ (which holds for observers far from the scattering volume, $R \gg r$) we may rewrite the retarded time as

$$t' = \frac{1}{1 - \hat{s} \cdot \vec{\beta}} \left(1 - \frac{R}{c} + \frac{\hat{s} \cdot \vec{r}_0}{c} \right) \quad (\text{A.15})$$

Substituting, the phase argument becomes

$$k_i \frac{1 - \hat{i} \cdot \vec{\beta}}{1 - \hat{s} \cdot \vec{\beta}} R - \omega_i \frac{1 - \hat{i} \cdot \vec{\beta}}{1 - \hat{s} \cdot \vec{\beta}} t - k_i \frac{1 - \hat{i} \cdot \vec{\beta}}{1 - \hat{s} \cdot \vec{\beta}} \hat{s} \cdot \vec{r}_0 + \vec{k}_i \cdot \vec{r}_0 \quad (\text{A.16})$$

where \hat{i} is the incident wave propagation direction. We have naturally arrived at the Doppler-shifted frequency,

$$\begin{aligned} \omega_s &= \frac{1 - \hat{i} \cdot \vec{\beta}}{1 - \hat{s} \cdot \vec{\beta}} \omega_i \\ \vec{k}_s &= k_i \frac{1 - \hat{i} \cdot \vec{\beta}}{1 - \hat{s} \cdot \vec{\beta}} \hat{s} = \frac{\omega_s}{c} \hat{s} \end{aligned} \quad (\text{A.17})$$

so the phase is

$$\vec{k}_i \cdot \vec{r}' - \omega_i t' = k_s R - \omega_s t + (\vec{k}_s - \vec{k}_i) \cdot \vec{r}_0 \quad (\text{A.18})$$

Alternately, we may define

$$\begin{aligned} \vec{k} &= \vec{k}_s - \vec{k}_i \\ \omega &= \omega_s - \omega_i = \vec{k} \cdot \vec{v} \end{aligned} \quad (\text{A.19})$$

We may establish the frequency spectrum of the scattered radiation by taking the Fourier transform of the scattered field,

$$\vec{E}_s(\omega_s) = \int \vec{E}_s(t) e^{i\omega_s t} dt \quad (\text{A.20})$$

At retarded time, $dt = \kappa' dt'$, and

$$\vec{E}_s(\omega_s) = \frac{r_e}{R'} \int \kappa' \Pi \cdot \vec{E}_i(\vec{r}', t') e^{-\omega_s (t' + \frac{R'}{c} - \frac{\hat{s} \cdot \vec{r}'}{c})} dt' \quad (\text{A.21})$$

Here, for generality we use the polarization tensor Π , which includes relativistic effects – in the nonrelativistic limit $\Pi = \hat{s}\hat{s} - \mathbf{I}$ such that $\Pi \cdot \vec{E}_i = \hat{s} \times (\hat{s} \times \vec{E}_i)$. Using $\vec{E}_i(\vec{r}, t) = \vec{E}_{i0} \exp(i(\vec{k}_i \cdot \vec{r} - \omega_i t))$ and eq. (A.19),

$$\vec{E}_s(\omega_s) = \frac{r_e}{R'} e^{ik_s R'} \int \kappa' (\Pi \cdot \hat{E}_i) E_{i0} e^{i(\omega t' - \vec{k} \cdot \vec{r}')} dt' \quad (\text{A.22})$$

Integrating and substituting $\omega_s = 2\pi\nu_s$,

$$\vec{E}_s(\nu_s) = \frac{r_e}{R'} e^{ik_s R} 2\pi \kappa (\Pi \cdot \vec{E}_{i0}) \delta(\vec{k} \cdot \vec{v} - \omega) \quad (\text{A.23})$$

We may thus construct the scattered power per solid angle per unit frequency

$$\frac{d^2 P}{d\Omega d\nu_s} = r_e^2 |\Pi \cdot \hat{E}_i|^2 (c\epsilon_0 E_{i0}^2) \delta \left(\nu_s - \frac{1 - \hat{i} \cdot \vec{\beta}}{1 - \hat{s} \cdot \vec{\beta}} \nu_i \right) \quad (\text{A.24})$$

So we have established the scattered power spectrum in solid angle and frequency of a single electron as a function of scattering direction (encoded in $\Pi \cdot \hat{E}_i$) and incident laser energy (in the incident Poynting flux $\langle S_i \rangle = c\epsilon_0 E_{i0}^2$). The scattered spectrum locked to a single frequency by the Dirac delta function, forcing the scattered spectrum to radiate strictly at the Doppler-shifted frequency set by the electron motion.

To consider the spectrum from a population of electrons, we must consider the interactions between nearby electrons. On length scales comparable to the electron Debye length λ_{De} (eq. (1.1)), electrons in the plasma screen out incident electric fields – this organized motion leads to interference in the scattered radiation, referred to as *collective*

or *coherent scattering*. The full solution for the scattered spectrum (see [1, §3]) may be expanded in a series in the factor

$$\alpha = \frac{1}{k\lambda_{De}} \quad (\text{A.25})$$

Coherent effects are negligible in the limit of $\alpha \ll 1$, at which the scattering is said to be *incoherent* or *noncollective* – the radiation from a population of electrons is simply the sum of each individual contribution. For the effective scattering wavevector, $\vec{k} = \vec{k}_s - \vec{k}_i$ (eq. (A.19)),

$$\begin{aligned} |\vec{k}| &= \sqrt{k_s^2 + k_i^2 - 2k_s k_i \cos \theta} \\ &\approx \sqrt{2} k_i \sqrt{1 - \cos \theta} = \sqrt{2} k_i \sqrt{2 \sin^2 \left(\frac{\theta}{2} \right)} \end{aligned} \quad (\text{A.26})$$

assuming $k_s \approx k_i$. Thus the noncollective requirement reduces to

$$\frac{1}{2k_i \sin(\theta/2)\lambda_{De}} \ll 1 \Rightarrow \frac{\lambda_i}{\lambda_{De}} \ll 4\pi \sin \left(\frac{\theta}{2} \right) \quad (\text{A.27})$$

This condition is readily satisfied at near-perpendicular scattering ($\theta \approx 90^\circ$, where the scattering amplitude is maximized) and with laser wavelengths much smaller than the Debye length ($\lambda_{De} \sim 10 - 100 \mu\text{m}$ at tokamak conditions, compared to the $\lambda_i \sim 1 \mu\text{m}$ IR lasers commonly used for Thomson scattering photon sources).

Thus, the incoherent scattered spectrum is simply the sum of contributions from each electron in the scattering volume – the spectrum from a population described by the distribution function $f_e(\vec{r}, \vec{v})$ is

$$\frac{d^2P}{d\Omega dv_s} = 2\pi r_e^2 \int_V \langle S_i \rangle \int |\Pi \cdot \hat{E}_i|^2 f_e(\vec{r}, \vec{v}) \kappa^2 \delta(\vec{k} \cdot \vec{v} - \omega) d^3v d^3r \quad (\text{A.28})$$

For small scattering volumes, the electron distribution function is approximately uniform in space. In the nonrelativistic limit, $\Pi \cdot \hat{E}_i$ is independent of velocity, thus the spatial contribution may be separated out:

$$\int_V \langle S_i \rangle |\Pi \cdot \hat{E}_i|^2 d^3r \quad (\text{A.29})$$

encoding the incident photon flux (from the Poynting vector of the laser) and the scattering direction dependence. The velocity integral (noting $\kappa \approx 1$ in the nonrelativistic case) is

$$\int f(\vec{v}) \delta(\vec{k} \cdot \vec{v} - \omega) d^3 \vec{v} \quad (\text{A.30})$$

Splitting the velocity into components parallel and perpendicular to \vec{k} , \vec{v}_\perp , \vec{v}_k , this is

$$\int f(\vec{v}_\perp, \vec{v}_k) \delta(kv_k - \omega) d^2 \vec{v}_\perp dv_k = \int f_k(v_k) \delta(kv_k - \omega) dv_k \quad (\text{A.31})$$

utilizing the normalization required for $f(\vec{v})$ to solve the integrals over \vec{v}_\perp . For a Maxwellian (eq. (1.5)) the distribution along the effective wavevector \vec{k} is

$$f_k(v_k) = n_e \frac{1}{v_t \sqrt{\pi}} e^{-v_k^2/v_t^2} \quad (\text{A.32})$$

thus the above is solvable,

$$\int f_k(v_k) \delta(kv_k - \omega) dv_k = \frac{1}{k} f_k \left(\frac{\omega}{k} \right) \quad (\text{A.33})$$

Substituting into eq. (A.28),

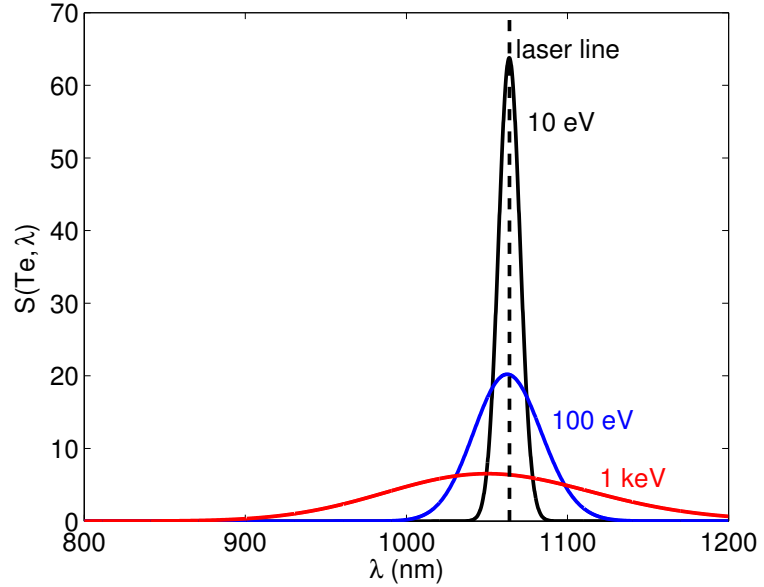
$$\begin{aligned} \frac{d^2 P}{d\Omega dv_s} &= 2\pi r_e^2 \left[\int_V \langle S_i \rangle |\hat{s} \times (\hat{s} \times \hat{E}_i)|^2 d^3 \vec{r} \right] \times \\ &\quad \frac{1}{\sqrt{\pi k}} \frac{n_e}{v_t} \exp \left(-\frac{\omega^2}{k^2 v_t^2} \right) \end{aligned} \quad (\text{A.34})$$

Substituting $k \approx 2k_i \sin(\theta/2) = (4\pi/\lambda_i) \sin(\theta/2)$, the exponent is

$$-\frac{(\omega_s - \omega_i)^2}{4 \frac{4\pi^2}{\lambda_i^2} \sin^2(\theta/2) v_t^2} \approx -\frac{c^2 (\lambda_s - \lambda_i)^2}{4 \lambda_i^2 v_t^2 \sin^2(\theta/2)} \quad (\text{A.35})$$

Converting from a frequency to a wavelength spectrum, and assuming the scattering volume to be sufficiently small that the scattering angle and incident Poynting flux are uniform (thus $\int \langle S_i \rangle d^3 \vec{r} =$

Figure A.3: Spectral functions normalized to density and laser power, evaluated at $\theta = \phi = \pi/2$. The spectrum spreads farther from the laser line at higher temperature, as well as blue-shifting due to relativistic effects.



$\langle S_i \rangle AL = P_i L$ for laser cross-section A , scattering volume L , and laser power P_i) the nonrelativistic scattering spectrum is

$$\frac{d^2P}{d\Omega d\lambda_s} = P_i r_e^2 n_e L |\hat{s} \times (\hat{s} \times \hat{E}_i)|^2 S(T_e, \theta, \lambda_s)$$

$$S(T_e, \theta, \lambda_s) = \frac{1}{2\sqrt{\pi} \sin(\theta/2)} \frac{c}{\lambda_i v_t} \exp\left(-\frac{c^2(\lambda_s - \lambda_i)^2}{4v_t^2 \lambda_i^2 \sin^2(\theta/2)}\right) \quad (\text{A.36})$$

This expression is a Maxwellian centered at $\lambda = \lambda_i$ with a spread determined by the electron temperature T_e (manifesting in the thermal velocity v_t) and the scattering angle θ . Recalling the angle ϕ defined between the incident polarization \hat{E}_i and the scattering direction \hat{s} (see fig. A.2), $|\hat{s} \times (\hat{s} \times \hat{E}_i)|^2 = \sin^2 \phi$ is maximized for scattering perpendicular to the incident laser polarization.

This analysis breaks down for relativistic electron populations. However, relativistic effects (see [1, §9]) may be expressed as a polynomial correction to eq. (A.36),

$$S_{\text{rel}}(T_e, \theta, \lambda_s) = S(T_e, \theta, \lambda_s) \left[1 - \frac{3.5(\lambda_s - \lambda_i)}{\lambda_i} + \frac{c^2(\lambda_s - \lambda_i)^3}{4v_t^2 \lambda_i^2 \sin^2(\theta/2)} \right] \quad (\text{A.37})$$

The relativistic correction breaks the symmetry of the Maxwellian spectrum, introducing a net blue shift to the spectrum. Physically, this is due to “relativistic headlighting,” in which the radiation from an accelerating relativistic particle is biased forward of its motion – The radiated power is stronger from particles moving toward the observer

(thus with a blue Doppler shift to their emissions). The spectral form factor $S(T_e, \theta, \lambda_s)$ is shown in figure fig. A.3, illustrating the width dependence of the spectrum on the electron temperature and the blue shifting evident in the spectrum even at relatively low plasma temperatures.

Examination of eqs. (A.36) and (A.37) readily illustrates the method for extracting n_e and T_e measurements from the Thomson scattering spectrum – the spread of the spectrum of scattered radiation is directly tied to the electron temperature, while the integrated amplitude gives electron density (as the total scattered power is linearly proportional to n_e). Assumptions regarding the Maxwellian distribution of the electrons allows accurate measurement of the electron profile with relatively simple hardware, detailed in the next section.

A.1.2 Edge Thomson Scattering on C-Mod

High-resolution density and temperature measurements on C-Mod are achieved with the core [7, 8] and edge [9, 10, 11] Thomson Scattering systems. While extracting density and temperature from the general Thomson-scattered spectrum (eq. (A.28)) for an arbitrary electron distribution $f_e(\vec{r}, \vec{v})$ is intractible, the spectrum for a thermal electron distribution is well-characterized (see eqs. (A.36) and (A.37)) and can be measured with a relatively simple system.

Both the core and edge TS systems measure light scattered from a pair of neodymium-doped yttrium-aluminum garnet (Nd:YAG) lasers with $\lambda_i = 1064 \text{ nm}$ fired vertically through the plasma at $R \sim 69 \text{ cm}$ such that it passes roughly through the magnetic axis. The lasers are each fired at 50 Hz 180° out of phase, such that the pair produce one hundred $\sim 5 \text{ ns}$ pulses per second, taking effective “snapshots” of the plasma profile. Each pulse provides $\sim 1 \text{ J}$ of laser energy, corresponding to roughly 5×10^{18} photons per laser pulse, ensuring sufficient collected photons even after the significant attenuation inherent in Thomson scattering. Focusing optics mounted at the vertical entrance port constrict the beam to a $\sim 2 \text{ mm}$ width through the plasma.

The scattered photons are focused through a Cooke triplet with 1:2 demagnification mounted at an outboard-midplane access port onto an array of fiber-optic collectors mounted on an actuated plate (see fig. A.4). Dedicated edge-viewing fibers are mounted in an adjustable block at the base of the plate, viewing the upper plasma at a scattering angle of $\theta \sim 80^\circ$. While the $\sim 1 \text{ cm}$ spot size of the core fibers is sufficient to resolve the core plasma profile, the small radial extent of the pedestal on C-Mod necessitates the millimeter resolution provided by the edge fibers.

The edge collection fibers deliver the scattered light to a filter polychromator array with 25 available spatial channels divided into four spectral bands. The spectral bandpasses, shown in fig. A.5, are de-

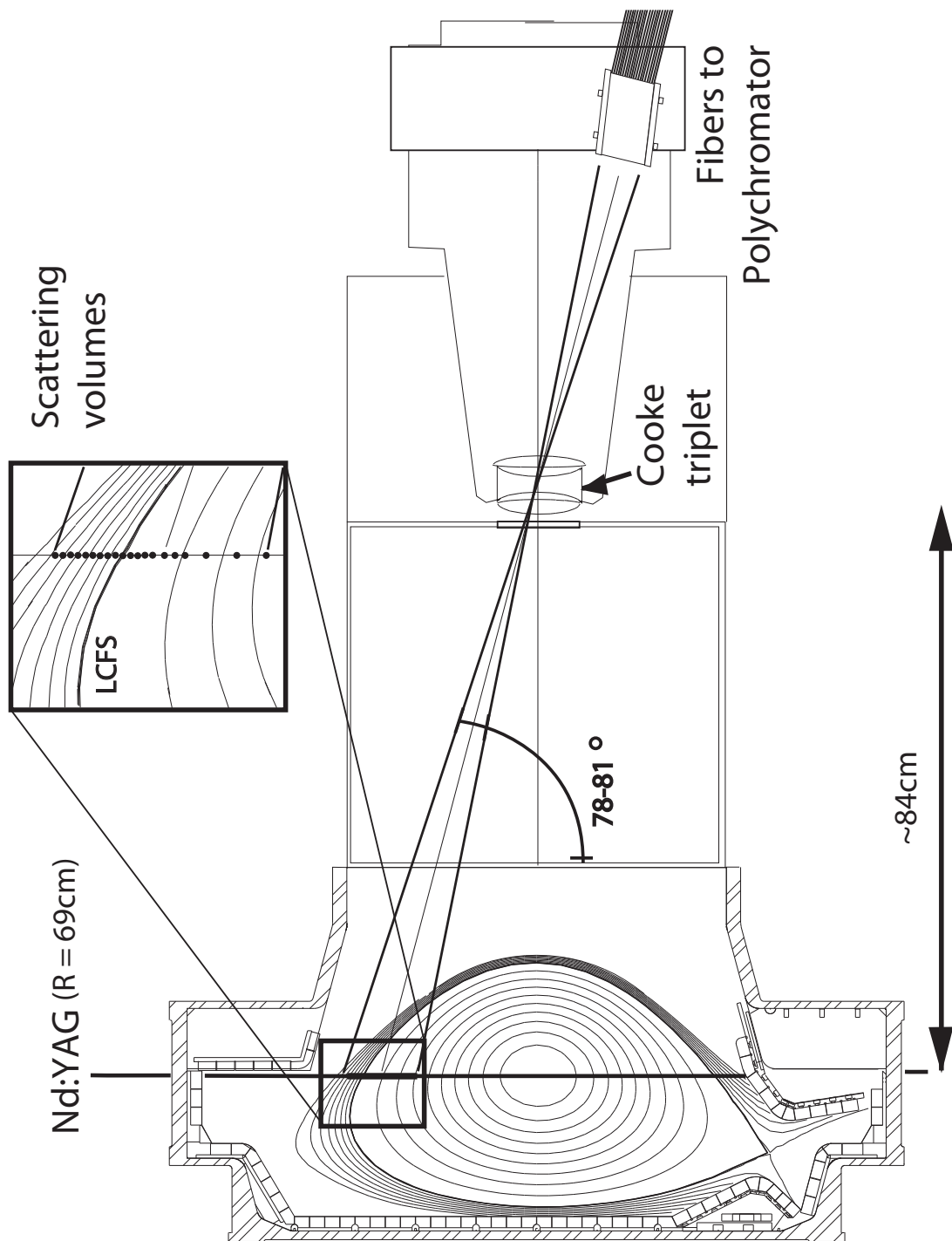
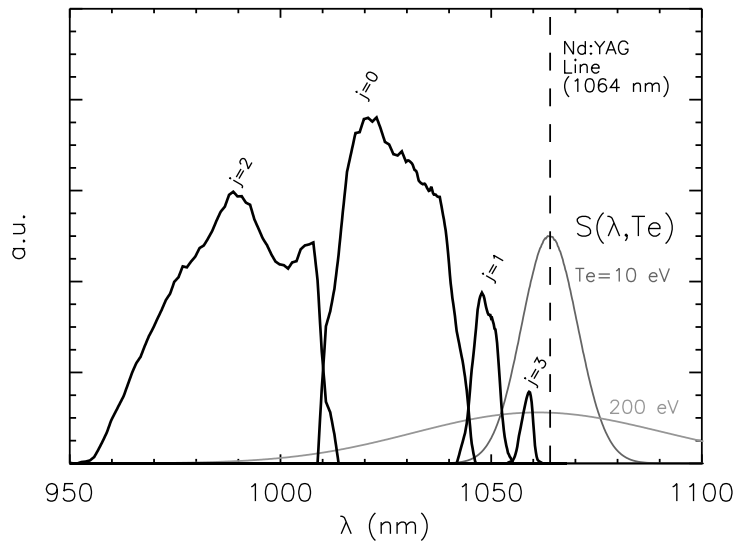


Figure A.4: Layout of collection optics for the core and edge Thomson scattering diagnostics on Alcator C-Mod. Two Nd:YAG lasers are fired vertically through the plasma near the magnetic axis, with the scattered light focused through a Cooke triplet at the outboard midplane onto an array of fiber optics. The positions of the high-resolution edge scattering volumes are highlighted in the inset.

Figure A.5: Normalized spectral response functions of the edge TS polychromator bandpasses, compared to characteristic scattered spectra at 10 eV and 200 eV.



signed such that the laser line is excluded from the captured light (reducing noise from reflected laser light incident on the fibers) while covering the expected spread in the scattered spectrum across a range of temperatures. Extracting n_e and T_e for each spatial channel is conceptually straightforward – the total signal in all spectral channels is analogous to the integrated area under the scattered spectrum (and thus n_e), while the relative signal strengths between spectral channels is set by the spread in the spectrum (thus T_e). For temperatures below ~ 50 eV (with the true lower bound dependent on the local density), the scattered spectrum is largely restricted to the $j = 3$ channel, setting a lower bound on the temperature measurement. Similarly, for $T_e \gtrsim 800$ eV the spectral response in $j = 1$ and $j = 3$ is flat, limiting the effectiveness of those spectral bandpasses in constraining the temperature measurement.

Although the n_e and T_e measurements from Thomson scattering require careful calibration and sensitive IR optics, the edge TS system provides reliable high-resolution profile measurements across a range of parameters found in the C-Mod edge. Further details on the edge TS hardware, calibration, and data analysis procedures is available in [11, §3].

A.2 FAST DIAGNOSTICS

In addition to the high spatial resolution necessary to diagnose the pedestal profile – provided by the edge Thomson Scattering system – a suite of diagnostics with high time resolution is desirable to capture rapid variations in plasma parameters near the pedestal. For our purposes, we focus on the electron-cyclotron emission (ECE) and H_α emission diagnostics. ECE provides fast measurement of local elec-

tron temperature, useful to track the impact of transient events like ELM crashes or sawtooth heat pulses on the pedestal temperature. H_{α} line emission in the plasma edge provides a measurement of density expelled into the plasma exhaust, marking both the particle transport changes during high-confinement modes and transient density bursts into the SOL during ELM crashes.

A.2.1 Electron-Cyclotron Emission

Electron-cyclotron emission, or ECE [2, §5.2], arises from the radiation driven by gyro motion of electrons in a magnetized plasma. Relativistically, the electron motion is described by

$$\frac{d}{dt}(\gamma m_e \vec{v}) = -e(\vec{v} \times \vec{B}) \quad (\text{A.38})$$

resulting in gyro-motion at the (relativistic) cyclotron frequency

$$\omega_c = \frac{eB}{\gamma m_e} \quad (\text{A.39})$$

While it is conceptually straightforward to substitute this motion into the Lienard-Wiechert potentials, eq. (A.1), the complexity of the motion results in a rather intractible general form for the radiation even for a single electron, requiring an infinite sum of Bessel functions to characterize the harmonics of the radiation. Fortunately, ECE systems may exploit the trait that electrons undergoing gyro-motion will also *absorb* radiation at the same frequency as their emitted radiation. Over a given path s through the plasma, the absorption is governed by the absorption coefficient $\alpha(\nu)$ (fractional absorption per unit path length), with which the radiated intensity $I(\nu)$ is given by

$$\frac{dI}{ds} = j(\nu) - I\alpha(\nu) \quad (\text{A.40})$$

where $j(\nu)$ is the frequency-dependence emissivity. For two points s_1 , s_2 along a path, this is solved by

$$I(s_2) = I(s_1)e^{\tau_1 - \tau_2} + \int_{s_1}^{s_2} j(\nu)e^{\tau - \tau_2} ds \quad (\text{A.41})$$

$$\tau \equiv \int_s \alpha(\nu) ds$$

for the optical depth τ . When the optical depth for a given path $\tau_{21} \equiv \tau_2 - \tau_1$ satisfies $\tau_{21} \gg 1$, the plasma within the path absorbs all

radiation incident upon it – it may then be treated as optically black, with the radiation given by the blackbody intensity

$$I(\nu) = \frac{\nu^2}{c^2} \frac{h\nu}{e^{h\nu/T} - 1} \approx \frac{\nu^2 T}{c^2} \quad (\text{A.42})$$

with the approximation holding for $h\nu \ll T$. In a broad range of tokamak plasma conditions, the first few harmonics will be optically thick, meaning that the intensity of those harmonics is a direct, straightforward measurement of the electron temperature.

This analysis must be modified somewhat to account for a spatially-varying magnetic field (for example, the $B_T \sim 1/R$ variation in a tokamak). Fortunately, for a given frequency ν_0 the emission is only strong close to the position of exact resonance. Through this resonance layer at location s_0 , the optical depth for a given harmonic m is given by

$$\tau_m = \frac{\alpha_m(s_0)}{m |d\omega_c/ds|} \quad (\text{A.43})$$

with the emission given by

$$I(\nu_0) = \frac{\nu_0^2 T(s_0)}{c^2} (1 - e^{-\tau_m}) \quad (\text{A.44})$$

Thus electron-cyclotron emission in a tokamak allows easy measurement of electron temperature. By observing emission within a given frequency band, the measurement may be localized to a resonance layer, the location of which is calculated by the known magnetic field variation $d\omega_c/ds$.

High time resolution ECE measurements are provided by a suite of diagnostics on C-Mod. Two grating polychromator systems (GPCs) view the plasma from the outboard midplane with coverage through the radial plasma profile on the high-field and low-field sides, though the spatial channel locations depend on the magnetic field and wavelength settings of the gratings [12]. The original nine-channel system, (GPC1) was originally developed for the MTX tokamak [13]. This is complemented by a second system, GPC2 [14], which adds 19 spatial channels at the midplane. These systems provide good frequency resolution, $\Delta f/f < 1\%$, with 10 μs time resolution and $\sim 10 \text{ eV}$ noise levels for the signal. However, due to geometric effects and frequency broadening, the system is only capable of $\sim 1 \text{ cm}$ spatial resolution [12]. An additional heterodyne ECE system developed by the Fusion Research Center for C-Mod [15, 16], is capable of higher spatial and temporal resolution measurements – the off-midplane viewing angle, when mapped to the outboard midplane, provides $\sim 4 \text{ mm}$ radial resolution, with $\sim 100 \text{ ns}$ time resolution, capable of resolving local

check!!!

temperature fluctuations with low noise levels.

The spatial resolution provided by these systems is more than sufficient to resolve core T_e profiles, and has historically been used for temperature pedestal measurements by sweeping the toroidal field (and therefore channel position) in otherwise steady plasmas [17]. However, the spatial resolution of the system is not, on its own, sufficient to resolve the sub-centimeter pedestal on C-Mod. Rather, ECE measurements from channels near the pedestal top are utilized in this thesis to track rapid perturbations to the pedestal temperature from sawtooth heat pulses or ELM crashes. These perturbations occur at frequencies typically in the range of 10 – 100 kHz, comparable to the framerate of the Thomson Scattering system, such that TS datapoints are effectively randomized in their timing relative to the perturbation cycle. ECE data is used to prepare specialized profiles, with TS datapoints masked for a particular phase of the perturbation cycle.

A.2.2 H_α Emission

•

A.3 FLUCTUATION DIAGNOSTICS

A firm understanding of plasma fluctuations is necessary to characterize high-performance regimes. Turbulent fluctuations drive enhanced transport of energy and particles out of the plasma, and it is the suppression of these fluctuations, particularly in the plasma edge, that defines high-performance operation. Conversely, beneficial fluctuations regulate the pedestal to allow stationary ELM-free operation (e.g., in EDA H-mode, QH-mode, and I-mode). Thus, an extensive suite of diagnostics to measure global and local fluctuation levels are maintained on C-Mod, a few of which are detailed here.

A.3.1 Reflectometry

As plasmas are composed of freely-interacting charged particles, electromagnetic waves interact quite strongly with the plasma. The dispersion relation for a wave of frequency ω and wavevector \vec{k} (alternately, refractive index $N = \vec{k}c/\omega$) is characterized (in the cold plasma approximation) by the Appleton-Hartree formula [2, §4],

$$N^2 = 1 - \frac{X(1-X)}{1-X - \frac{1}{2}Y^2 \sin \theta \pm \left[\left(\frac{1}{2}Y^2 \sin^2 \theta \right)^2 + (1-X)^2 Y^2 \cos^2 \theta \right]^{1/2}} \quad (\text{A.45})$$

where $X = \omega_p^2/\omega^2$, $Y = \omega_c/\omega$, and θ is the angle between \vec{k} and the background magnetic field \vec{B}_0 . For waves propagating perpendicular to the field ($\theta = \pi/2$), this reduces to two solutions:

$$\begin{aligned} N^2 &= 1 - X \\ N^2 &= 1 - \frac{X(1-X)}{1-X-Y^2} \end{aligned} \quad (\text{A.46})$$

which are called the *ordinary* or *O-mode*, and *extraordinary* or *X-mode* respectively. We primarily consider the O-mode propagation. Recall that the plasma frequency ω_p characterizes a natural “ringing” rate at which the plasma rearranges itself in response to a changing electric field – this screens out electromagnetic waves with frequencies $\omega < \omega_p$. As the wave propagates inward from the edge the plasma density increases, such that $X \rightarrow 1$. Above this point, the *cutoff*, the wave is evanescent with imaginary N and will reflect from the cutoff layer. The cutoff density n_c is trivially obtained from the above,

$$n_c = \frac{m_e \epsilon_0}{e^2} \omega^2 = \left(\frac{f}{89.8} \right)^2 \quad (\text{A.47})$$

where n_c is in 10^{20} m^{-3} and f is in GHz. Measurement of the reflected wave yields a wealth of information about the density profile – simple phase-delay measurements at a variety of frequencies produce a non-perturbative measurement of the density profile, as for each input frequency the density at the cutoff layer (the location of which is derived from the phase delay) must be equal to $n_c(f)$.

A.3.2 Gas-Puff Imaging

★

BIBLIOGRAPHY

- [1] J. Sheffield. *Plasma Scattering of Electromagnetic Radiation*. Academic Press, 1975.
- [2] I.H. Hutchinson. *Principles of Plasma Diagnostics*. Cambridge University Press, 2005.
- [3] J. Sheffield. The incoherent scattering of radiation from a high temperature plasma. *Plasma Physics*, 14(8):783, 1972.
- [4] T. Matoba, T. Itagaki, T. Yamauchi and A. Funahashi. Analytical approximations in the theory of relativistic Thomson scattering for high temperature fusion plasma. *Japanese Journal of Applied Physics*, 18(6):1127–1133, 1978.
- [5] A. C. Selden. Simple analytic form of the relativistic Thomson scattering spectrum. *Physics Letters A*, 79(5-6):405 – 406, 1980.
- [6] O. Naito, H. Yoshida and T. Matoba. Analytic formula for fully relativistic Thomson scattering spectrum. *Physics of Fluids B: Plasma Physics*, 5(11):4256–4258, 1993.
- [7] Reich Watterson and Kuo-In Chen. Status of the Alcator C-Mod scanning two-dimensional Thomson scattering diagnostic. *Review of Scientific Instruments*, 61(10):2867–2869, 1990.
- [8] D. A. Mossessian, A. Hubbard and J. Irby. Performance of Alcator C-Mod core Thomson scattering system. *Review of Scientific Instruments*, 70(1):759–762, 1999.
- [9] J. W. Hughes, D. A. Mossessian, A. E. Hubbard, E. S. Marmar, D. Johnson et al. High-resolution edge Thomson scattering measurements on the Alcator C-Mod tokamak. *Review of Scientific Instruments*, 72(1):1107–1110, 2001.
- [10] J. W. Hughes, D. Mossessian, K. Zhurovich, M. DeMaria, K. Jensen et al. Thomson scattering upgrades on Alcator C-Mod. *Review of Scientific Instruments*, 74(3):1667–1670, 2003.
- [11] Jerry W. Hughes. *Edge Transport Barrier Studies On the Alcator C-Mod Tokamak*. PhD thesis, Massachusetts Institute of Technology, 2005.
- [12] N. Basse, A. Dominguez, E. Edlund, C. Fiore, R. S. Granetz et al. Diagnostic systems on Alcator C-Mod. *Fusion Science and Technology*, 51(3):476–507, 2007.

- [13] S. K. Guharay, D. A. Boyd, R. F. Ellis, F. J. Stauffer and C. J. Lasnier. **A 19channel fast grating polychromator for ECE measurements in the MTX tokamak.** *Review of Scientific Instruments*, 61(11):3520–3523, 1990.
- [14] G. Taylor, C. K. Phillips, G. Schilling, J. R. Wilson, A. E. Hubbard et al. First measurements with a 19-channel ECE polychromator on C-Mod. In *Bulletin of the American Physical Society*, volume 43, 1998.
- [15] J. W. Heard, C. Watts, R. F. Gandy, P. E. Phillips, G. Cima et al. **High resolution electron cyclotron emission temperature profile and fluctuation diagnostic for Alcator C-Mod.** *Review of Scientific Instruments*, 70(1):1011–1013, 1999.
- [16] R Chatterjee, P.E Phillips, J Heard, C Watts, R Gandy et al. **High resolution ECE radiometer for electron temperature profile and fluctuation measurements on Alcator C-Mod.** *Fusion Engineering and Design*, 53(1-4):113–121, 2001.
- [17] A. E. Hubbard, R. L. Boivin, R. S. Granetz, M. Greenwald, J. W. Hughes et al. **Pedestal profiles and fluctuations in C-Mod enhanced D-alpha H-modes.** *Physics of Plasmas*, 8(5):2033–2040, 2001.

B

HIGH-RESOLUTION PEDESTAL DATABASE

For the work presented in this thesis, a subset of recent I-mode experiments on Alcator C-mod was prepared with high-resolution pedestal data. These data are stored in an SQL database under the C-Mod “logbook” system. Use of an SQL table enables easy cross-platform access to pedestal data in a format ideal for data mining, and allows for easy extensibility for additional experiments. The database stores time phases in which plasma parameters (e.g., temperature, stored energy, density, heating power) are steady – usable phases last at least ~ 100 ms (~ 10 TS frames), over which data is averaged (described in section 4.1). For each phase, the SQL database stores a variety of physics and engineering parameters, and scalar fitting parameters from high-resolution pedestal fits (defined using the $mtanh$ function, eq. (4.1)). The fits are defined in normalized poloidal flux space (denoted ψ_n in the units below). The table also stores analogous data from H-modes (EDA and ELM_y), as well as ELM-synchronized data from the ELM_y H-mode experiments in chapter 4, for direct comparison to I-mode. A parameter list for the SQL database is shown in table B.1. Parameters are organized as follows:

KEY PARAMETERS

The set of these keys is sufficient to uniquely identify an entry in the database.

PHASE FLAGS

Searchable flags for the phase type, specifiers for the pedestal profile MDS tree.

MEASURED PARAMETERS

Plasma measurements apart from the pedestal profiles.

EFIT PARAMETERS

Calculated parameters from the EFIT reconstruction.

HEATING POWER, STORED ENERGY, AND CONFINEMENT

Stored values for power source and sink terms, stored energy, and energy confinement (both dimensional and normalized).

PEDESTAL PROFILES

Fitting parameters and calculated values from the high-resolution pedestal profiles in electron density, temperature, and pressure.

WCM FLUCTUATIONS

I-mode-specific parameters storing fitted values from WCM fluctuation measurements.

★

Table B.1: SQL database parameters, with datatype, units, and description. These parameters store data from the EFIT reconstruction and global metrics, as well as parameters for the pedestal fits.

<i>SQL database key parameters</i>			
<i>column</i>	<i>type</i>	<i>units</i>	<i>description</i>
SHOT	long		C-Mod shot number
TA	long	ms	start time of phase
TB	long	ms	end time of phase
MODE	string		type of phase in window, e.g., 'IMODE', 'ELMY', 'EDA', 'LMODE', 'ELMBIN'
<i>time window flags</i>			
ELMS	int		binary flag, = 1 for ELMs in phase
LH	int		binary flag, = 1 for LHCD in phase
WCM	int		binary flag, = 1 for WCM fluctuation in phase (I-mode only)
TREE_PATH	string		path to branch in pedestal-profile MDS tree
TREE_SHOT	long		shot number flagged in pedestal-profile MDS tree, used to differentiate sub-branches of a single shot
SEED_SPC	string		gas seeding species (Ne, N, Ar) - None for no gas seeding
<i>measured parameters</i>			
NLo4	float	m^{-2}	line-integrated density from TCI
NLo4_ERR	float	m^{-2}	error in NLo4
NEBAR	float	m^{-3}	line-averaged density from TCI
NEBAR_ERR	float	m^{-3}	error in NEBAR
ECE_To	float	eV	core electron temperature from ECE

<i>column</i>	<i>type</i>	<i>units</i>	<i>description</i>
ECE_TPED	float	eV	pedestal electron temperature from ECE (channel nearest 95% flux surface)
NEo	float	m^{-3}	core density from TS
NEo_ERR	float	m^{-3}	error in NEo
TEo	float	eV	core temperature from TS
TEo_ERR	float	eV	error in TEo
NUSTAR	float		pedestal collisionality at 95% flux surface
RHOSTAR	float		pedestal normalized gyroradius at 95% flux surface
ZEFF	float		average effective charge
ZEFF_ERR	float		error in ZEFF measurement
<i>EFIT parameters</i>			
KAPPA	float		plasma elongation κ (see fig. 1.6)
KAPPA_ERR	float		error in KAPPA
DELTA_U	float		plasma upper triangularity (see fig. 1.6)
DELTA_U_ERR	float		error in DELTA_U
DELTA_L	float		plasma lower triangularity (see fig. 1.6)
DELTA_L_ERR	float		error in DELTA_L
IP	float	MA	plasma current
IP_ERR	float	MA	error in IP
DIDT	float	$MA \cdot s^{-1}$	change in plasma current dI_p/dt
DIDT_ERR	float	$MA \cdot s^{-1}$	error in DIDT
BT	float	T	axial toroidal field
BT_ERR	float	T	error in BT
BP	float	T	flux-surface averaged edge poloidal field
BP_ERR	float	T	error in BP

<i>column</i>		<i>type</i>	<i>units</i>	<i>description</i>
Qo		float		axial safety factor q_0
Qo_ERR		float		error in Qo
Q95		float		edge safety factor q_{95}
Q95_ERR		float		error in Q95
R		float	cm	major radius
A		float	cm	outboard-midplane minor radius
SSEP		float	cm	X-point position: ~ 1 is USN, ~ -1 is LSN, 40 is limited
BETAT		float		global toroidal beta, $\langle \beta_t \rangle$
BETAP		float		global poloidal beta, $\langle \beta_p \rangle$
BETAN		float	$m \cdot T \cdot MA^{-1}$	global normalized beta, $\beta_N = \langle \beta \rangle / (I_p/aB_t)$
TAU_MHD		float	s	MHD energy confinement time, τ_E
TAU_MHD_ERR		float	s	error in TAU_MHD
<i>heating power, stored energy, & confinement</i>				
PLASMA_W		float	J	plasma stored energy
PLASMA_W_ERR		float	J	error in PLASMA_W
DWDT		float	MW	change in stored energy, dW_{plasma}/dt
DWDT_ERR		float	MW	error in DWDT
P_ICRF		float	MW	absorbed ICRF heating power
P_ICRF_ERR		float	MW	error in P_ICRF
P_OHM		float	MW	Ohmic heating power
P_OHM_ERR		float	MW	error in P_OHM
P_LH		float	MW	absorbed lower-hybrid heating power
P_LH_ERR		float	MW	error in P_LH
P_RAD		float	MW	radiated power from bolometry
P_RAD_ERR		float	MW	error in P_RAD
P_SOL		float	MW	net power through SOL, eq. (1.27)
P_SOL_ERR		float	MW	error in P_SOL

<i>column</i>	<i>type</i>	<i>units</i>	<i>description</i>
P_THRES	float	MW	H-mode threshold power, eq. (2.7)
P_THRES_ERR	float	MW	error in P_THRES
H	float		ITER98y2 H-mode confinement scaling, $H_{98} = \tau_E / \tau_{98y2}$
H_ERR	float		error in H
H89	float		ITER89 L-mode confinement scaling, $H_{89} = \tau_E / \tau_{89}$
H89_ERR	float		error in H89
<i>parameters for high-resolution pedestal profiles</i>			
NEPED_H	float	m^{-3}	density pedestal height
NEPED_H_ERR	float	m^{-3}	error in NEPED_H
NEPED_B	float	m^{-3}	density pedestal baseline
NEPED_B_ERR	float	m^{-3}	error in NEPED_B
NEPED_D	float	ψ_n	density pedestal half-width
NEPED_D_ERR	float	ψ_n	error in NEPED_D
NEPED_Ro	float	ψ_n	density pedestal midpoint
NEPED_Ro_ERR	float	ψ_n	error in NEPED_Ro
NEPED_ALPHA	float		density pedestal inboard-slope parameter
NEPED_ALPHA_ERR	float		error in NEPED_ALPHA
NEPED_HEIGHT	float	m^{-3}	density at NEPED_Ro - NEPED_D
NEPED_GRAD	float	$m^{-3} \cdot \psi_n^{-1}$	peak density pedestal gradient (pedestal midpoint)
NEPED_GRAD_ERR	float	$m^{-3} \cdot \psi_n^{-1}$	error in NEPED_GRAD
NEPED_LGRAD	float	ψ_n	peak density pedestal gradient scale length
NEPED_LGRAD_ERR	float	ψ_n	error in NEPED_LGRAD
NEPED_95	float	m^{-3}	density at 95% flux surface
NEPED_95_ERR	float	m^{-3}	error in NEPED_95
TEPED_H	float	eV	temperature pedestal height

<i>column</i>	<i>type</i>	<i>units</i>	<i>description</i>
TEPED_H_ERR	float	eV	error in TEPED_H
TEPED_B	float	eV	temperature pedestal baseline
TEPED_B_ERR	float	eV	error in TEPED_B
TEPED_D	float	ψ_n	temperature pedestal half-width
TEPED_D_ERR	float	ψ_n	error in TEPED_D
TEPED_Ro	float	ψ_n	temperature pedestal midpoint
TEPED_Ro_ERR	float	ψ_n	error in TEPED_Ro
TEPED_ALPHA	float		temperature pedestal inboard-slope parameter
TEPED_ALPHA_ERR	float		error in TEPED_ALPHA
TEPED_HEIGHT	float	eV	temperature at TEPED_Ro - TEPED_D
TEPED_GRAD	float	$eV \cdot \psi_n^{-1}$	peak temperature pedestal gradient (pedestal midpoint)
TEPED_GRAD_ERR	float	$eV \cdot \psi_n^{-1}$	error in TEPED_GRAD
TEPED_LGRAD	float	ψ_n	peak temperature pedestal gradient scale length
TEPED_LGRAD_ERR	float	ψ_n	error in TEPED_LGRAD
TEPED_95	float	eV	temperature at 95% flux surface
TEPED_95_ERR	float	eV	error in TEPED_95
PEPED_H	float	$m^{-3} \cdot eV$	pressure pedestal height
PEPED_H_ERR	float	$m^{-3} \cdot eV$	error in PEPED_H
PEPED_B	float	$m^{-3} \cdot eV$	pressure pedestal baseline
PEPED_B_ERR	float	$m^{-3} \cdot eV$	error in PEPED_B
PEPED_D	float	ψ_n	pressure pedestal half-width
PEPED_D_ERR	float	ψ_n	error in PEPED_D
PEPED_Ro	float	ψ_n	pressure pedestal midpoint
PEPED_Ro_ERR	float	ψ_n	error in PEPED_Ro
PEPED_ALPHA	float		pressure pedestal inboard-slope parameter
PEPED_ALPHA_ERR	float		error in PEPED_ALPHA
PEPED_HEIGHT	float	$m^{-3} \cdot eV$	pressure at PEPED_Ro - PEPED_D

<i>column</i>	<i>type</i>	<i>units</i>	<i>description</i>
PEPED_GRAD	float	$m^{-3} \cdot eV \cdot \psi_n^{-1}$	peak pressure pedestal gradient (pedestal midpoint)
PEPED_GRAD_ERR	float	$m^{-3} \cdot eV \cdot \psi_n^{-1}$	error in PEPED_GRAD
PEPED_LGRAD	float	ψ_n	peak pressure pedestal gradient scale length
PEPED_LGRAD_ERR	float	ψ_n	error in PEPED_LGRAD
PEPED_95	float	$m^{-3} \cdot eV$	pressure at 95% flux surface
PEPED_95_ERR	float	$m^{-3} \cdot eV$	error in PEPED_95
ALPHA	float		peak normalized pressure gradient α_{MHD}
ALPHA_ERR	float		error in ALPHA
PROF_SHIFT	float	ψ_n	radial shift (in norm. poloidal flux) in TS profiles to satisfy power balance through SOL
EPED_WID	float	ψ_n	EPED-predicted pedestal width in normalized poloidal flux
EPED_P	float	kPa	EPED-predicted pressure pedestal height

WCM fluctuation measurements

WCM_AMP	float		normalized peak amplitude of WCM from reflectometry
WCM_FREQ	float	kHz	centroid frequency of WCM from reflectometry
WCM_WID	float	kHz	spectral width of WCM determined by $\pm\sigma$ of Gaussian fit on reflectometry
WCM_AMP_PCI	float		normalized peak amplitude of WCM from PCI
WCM_FREQ_PCI	float	kHz	centroid frequency of WCM from PCI
WCM_WID_PCI	float	kHz	spectral width of WCM determined by $\pm\sigma$ of Gaussian fit on PCI

COLOPHON

This document was typeset using `classicthesis` developed by André Miede (although aspects were changed to comply with the MIT thesis standards and the author’s personal preferences). The style was inspired by Robert Bringhurst’s seminal book on typography “*The Elements of Typographic Style*”. `classicthesis` is available for both L^AT_EX and L^AT_EX:

<http://code.google.com/p/classicthesis/>

Hermann Zapf’s *Palatino* and *Euler* type faces (Type 1 PostScript fonts *URW Palladio L* and *FPL*) are used. The “typewriter” text is typeset in *FPL*, originally developed by Bitstream, Inc. as “Bitstream Vera”. (Type 1 PostScript fonts were made available by Malte Rosenau and Ulrich Dirr.)